Secular changes in Earth's shape and surface mass loading

D. P. A. Booker

Thesis submitted for the degree of Doctor of Philosophy

Newcastle University

July 2012

Abstract

The changing distribution of surface mass (oceans, atmosphere, hydrology and cryosphere) causes detectable changes to the solid Earth's shape on timescales from hours to millennia. Transient changes in Earth's shape can be readily identified, but the tectonic plate movements and Glacial Isostatic Adjustment (GIA) will also influence the secular trends of Earth's shape. To analyse secular trends in surface mass loading, these two confounding factors must be quantified.

A suite of GPS-derived surface loading models, including both secular and transient terms is presented. Raw velocities are estimated from over 10 years of high quality combined global GPS position solutions, submitted as part of the first International GNSS Service (IGS) reprocessing campaign. A fiducial-free network approach is used with attention to estimating linear offsets and periodic signals. Consideration is given to realistic formal errors for station coordinates. A robust method is used for estimating horizontal and vertical linear velocities for all stations. Tests of the reprocessed data quality show that there is a dramatic improvement of the RMS of the weekly combined global network in comparison to the operational data used previously. The estimated Helmert transformations, when aligning the reprocessed frame to the IGS05 reference frame also show the stability and homogeneity of the new dataset. This permits a more precise estimate of individual station velocities, ~75% reduction to variability of Helmert parameters.

Several a priori GIA models are applied to produce corresponding plate velocity estimates, leaving a range of computed residual surface displacements. Present-day surface mass loading is estimated from these residuals, using gravitationally consistent mass-conserving basis functions. GIA models are assumed to be error-free, so only nominal formal errors, with a white noise assumption, can be calculated, these will be adjusted to produce a realistic uncertainty value. Surface mass loading estimates show significant secular mass loss in Alaska and Greenland. The Greenland values (-140Gt/yr, 1999-2010) fall within published GRACE gravity mission values (-66 to -248Gt/yr, 2002-2009).

Acknowledgements

I am indebted to the supervision of Pete Clarke throughout the four years of this study, especially stepping in as my primary supervisor. I would also like to thank Dave Lavallée for his advice at both Newcastle University during his stay as my primary supervisor and my various trips over to TU Delft to tap the wealth of knowledge especially regarding the bowels of the TANYA software and the modifications made to date.

Thanks must go to Fiona Smith and Chris Booker for proof reading this work.

Finally I would like to acknowledge all the contributing members and institutions of the IGS reprocessing campaign. Who without the continued effort to produce high quality data and the concerted effort to provide freely accessible data this study would not even have been conceivable.

This work was funded by a Natural Environmental Research Council (NERC) studentship

Content

List of Figures

List of Tables

Glossary

AC	Analysis Centre
BIH	Bureau International de l'Heure
BIFROST	Baseline Inferences for Fennoscandian Rebound Observations, Sea-level, and Tectonics
BP	Before Present
BSF	Block Scaling Factor
CC	Combination Centre
CDDIS	Crustal Dynamics Data Information System
CE	Centre of mass of solid Earth
CF	Centre of Earth Figure
CM	Centre of Mass of Earth system
CN	Coloured Noise
CNSS	Council of National Seismic Systems
COD	Centre for Orbit Determination Europe (Switzerland)
DOF	Degrees of Freedom
DORIS	Doppler Orbitography and Radiopositioning Integrated by Satellite
ECCO	Estimating the Circulation and Climate of the Ocean
ECMWF	European Centre for Medium-Range Weather Forecasts
EMR	IGS AC at Natural Resources Canada (Canada)
ENSO	El-Nino/Southern Oscillation
ESA	IGS AC at the European Space Agency (Germany)
EOP	Earth Observation Parameters
ERP	Earth Rotation Parameters
FFT	Fast Fourier Transform
FN	Flicker Noise
GC	Geocentre
GIA	Glacial Isostatic Adjustment
GFZ	IGS AC at GeoForschungZentrum (Germany)
GMF	Global Mapping Function
GMT	Generic Mapping Tool
GTZ	IGS TIGA AC at GeoForschungZentrum (Germany)

GLONASS	GLObalnaya Navigatsionnaya Sputnikovaya Sistema
GNAAC	Global Network Associate Analysis Centre
GNSS	Global Navigation Satellite System
GPS	Global Positioning System
GRACE	Gravity Recovery And Climate Experiment
IB	Inverse Barometer
ICRS	International Celestial Reference System
ICRF	International Celestial Reference Frame
IERS	International Earth Rotation Service
IGN	Institute Geographique National (France)
IGS	International GPS Service
IGSCB	IGS Central Bureau at http://igscb.jpl.nasa.gov
IMF	Isobaric Mapping Function
IPCC	Intergovernmental Panel on Climate Change
ITRF	International Terrestrial Reference Frame
ITRS	International Terrestrial Reference System
IUGG	International Union of Geodesy and Geophysics
JPL	IGS AC at the Jet Propulsion Laboratory (USA)
LAD	Land Dynamics
LGM	Last Glacial Maximum
LLH	Latitude, Longitude, Height
LM	Lower Mantle
LOD	Length of Day
LS	Least Squares
LVZ	Low Velocity Zone
MLE	Maximum Likelihood Estimation
MIT	IGS AC at the Massachusetts Institute of Technology (USA)
NCEP	National Centre for Environmental Prediction
NEU	North, East, Up
NGDC	National Geophysical Data Centre
NGS	IGS AC at National Geodetic Survey (USA)
NMF	Neill Mapping Function
NNR	No Net Rotation

NNT	No Net Translation
NRCan	Natural Resources Canada
OTL	Ocean Tide Loading
PDR	IGS AC at GeoForschungZentrum/Potsdam & Technical University of Dresden (Germany)
POLENET	Polar Earth Observing Network
PREM	Preliminary Reference Earth Model
PDMT	Present Day Mass Trends
RMS	Root Mean Square
RW	Random Walk
SBL	Special Bureau for Loading
SINEX	Solution Independent Exchange Format
SIO	IGS AC at Scripps Institution of Oceanography (USA)
SLE	Sea Level Equation
SLR	Satellite Laser Ranging
SSR	Sum of Square Residuals
TANYA	Type two Analysis New Year Attempt
TIGA	Tide Gauge
TRF	Terrestrial Reference Frame
TRS	Terrestrial Reference System
TUM	Technical University Munich
ULR	IGS TIGA AC at University of La Rochelle (France)
UM	Upper Mantle
UT	Universal Time
VLBI	Very Long Baseline Interferometry
VMF	Vienna Mapping Function
WGS84	World Geodetic System 1984
WN	White Noise
WRMS	Weighted RMS
XPO(R)	X Pole(Rate)
XPOR	X Pole Rate
XYZ	Cartesian Coordinate system
YPO(R)	Y Pole(Rate)

Chapter 1. Introduction

The continual variation in the global distribution of surface masses (atmosphere (van Dam et al. (2010), Tregoning and van Dam (2005b)), hydrology (Crowley et al. (2008), Tamisiea et al. (2001), van Dam et al. (2001), Dong et al. (1997)) and oceans (Chambers et al. (2004), van Dam et al. (1997))) loads and deforms the solid Earth causing changes in its shape on timescales from hours to millennia that are detectable using Global Navigation Satellite System (GNSS) data. These redistributions also introduce changes to the Earth's gravity field which cannot be directly detected using GNSS; however missions, such as the Gravity Recovery And Climate Experiment (GRACE) (Tapley et al. (2004)) can be used to measure these changes (Wahr et al. (2004)). If the redistributions can be accurately detected and quantified then additional inferences can be made about large scale mass redistribution and the Earth's elastic response to them. These inferences will affect how the terrestrial reference frame is produced, with implications for all space geodetic missions (altimetry, Satellite Laser Ranging (SLR) and GNSS), Glacial Isostatic Adjustment (GIA) and sea level determination, amongst other applications.

Although there have been previous studies into surface mass loading (Clarke et al. (2007), van Dam et al. (2007), Wu et al. (2003)), plate tectonics (Argus et al. (2010), Kogan and Steblov (2008), Sella et al. (2002), Larson et al. (1997)) and GIA (Ivins and James (2005), Paulson et al. (2005), Peltier (2004), Mitrovica et al. (2001)) there is still debate as to the accuracy of some of the reference models used, for example continental water storage (CWS) (Fiedler and Doll (2007)) and GIA (King et al. (2010)), which are very difficult to model accurately. One of the drivers behind these investigations is to gain a better understanding of the effects of climate change on the redistribution of surface masses (IPCC report 2007 (Solomon et al. (2007))).

This study utilises data from the US Global Positioning System (GPS). GPS satellites are tracked by ground stations whose position on the Earth can then be calculated on a regular basis. Regular calculation of station positions allows for the interpretation of station movements to be made. Since 1994 the International GNSS Service (IGS) has been collating data submitted by Analysis Centres (ACs) and organising processing strategies. Each week to the present, an official global network has been produced; however, clear systematic

processing errors are visibly present in this operational data set Ray et al. (2008).

The main issues to be addressed by this work are twofold: the first subject is the comparison of the original operational GPS solutions with the newly released reprocessed data set, detailed in section (3.6). The second focus is the level of precision and accuracy to which secular changes in the shape of the solid Earth, caused by surface mass loading, can be detected using a modern geodetic space technique such as GPS, section (6.4). Highlighted in the first issue are the implications for the Terrestrial Reference Frame (TRF), as distinct differences between the origin and orientation of the operational and reprocessed data sets have already been observed (Collilieux et al. (2011), Steigenberger et al. (2006b)). By comparing the two data sets it should be possible to highlight areas where significant geophysical signals or model deficiencies have been resolved or may still exist. To achieve this the second part of this project uses the reprocessed GPS data to develop an integrated loading model combining the secular effects of plate tectonics and GIA.

Potential error sources can be found at the very fundamental level of the data that I am proposing to use; GPS data relies heavily upon both its chosen frame of reference for the determination of its orbits and the processing model chosen. Any error or change in the reference frame definition will filter down, contaminating the coordinates of the receiving stations, especially their heights. Periodically a new official release of the International Terrestrial Reference Frame (ITRF) is created (Altamimi et al. (2011), Altamimi et al. (2007), Altamimi et al. (2002)); this combines information from GPS, Satellite Laser Ranging (SLR), Doppler Orbitography and Radiopositioning (DORIS) and Very Long Baseline Interferometry (VLBI). Even though its creation is based on the same principles each new release will have slight differences, in part due to changes in the observation analysis models used, section (3.3).

Over the last two decades several different TRFs and processing models were used as part of the operational GPS processing which led to an inhomogeneous coordinate time series full of systematic offsets and discontinuities, which hindered studies into long term changes in the Earth system. This was identified and in 2005 a complete reprocessing of all the GPS data was proposed by the IGS (Steigenberger et al. (2006a)) with the aim of producing a new homogeneous data set aligned to the most recent release of the ITRF, or its

GPS only realisation, the IGS05 (Ferland (2006)). This has since been superseded by the ITRF2008 and IGS08. The reprocessing was carried out by several ACs around the globe and part of the aim of this project is to create a new TRF from this reprocessed data series (Steigenberger et al. (2006b)). The reprocessed frame can be compared to previous frames; thus highlighting problems and model changes which have occurred with previous frames. Any issues that do arise will have wide ranging implications for many users, especially those that require the high level of precision of the ITRF.

The IGS reprocessing campaign aims to remove some of the doubts in the data sets and it is the intention of this work to develop a framework from which secular change in the Earth's shape caused by surface mass loading can be observed. Once this framework has been rigorously tested the result will be used to produce GPS derived coefficients of the Earth's deformation and converted into an equivalent mass change.

"Secular period" for geophysical studies usually refers to changes which are multi-decadal and greater, as described in Figure 1.

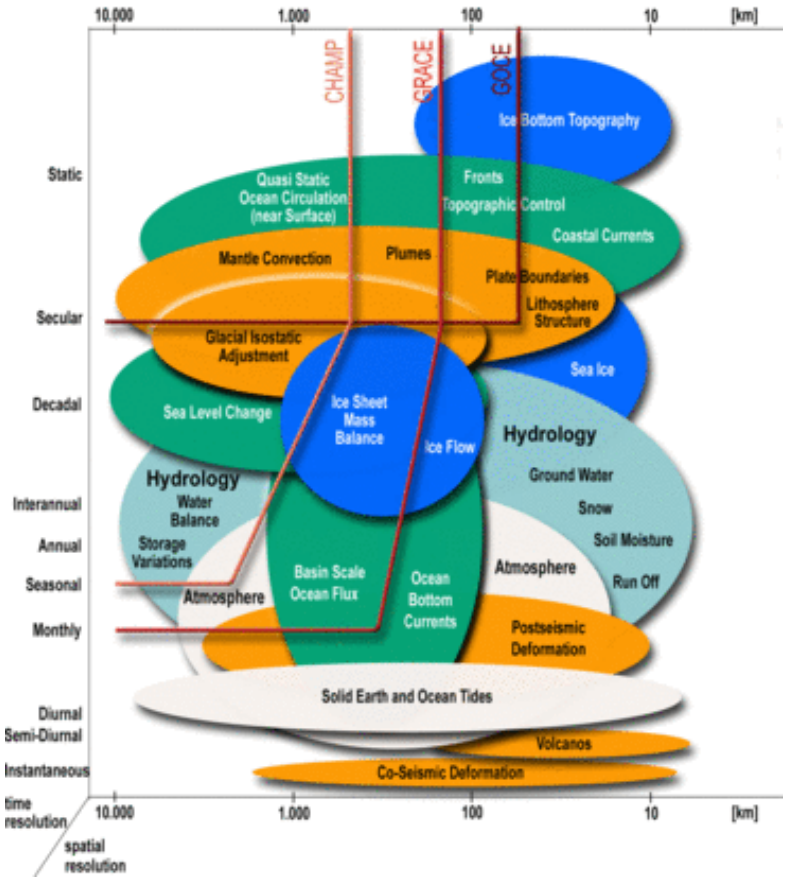

Figure 1: Spatial and temporal scales for gravity field changes; surface displacements behave similarly. From Ilk et al. (2005)

1.1 Aims of the Study

In this study I aim to validate and use the homogeneous IGS Reprocessing data set to develop a better understanding of surface mass loading unaffected by GPS processing model changes, e.g. the adoption of a new TRF or the switch from relative to absolute satellite antenna phase centre offsets/variations (Schmid et al. (2005)). By removing modelled GIA and estimated plate tectonic rotations, which are the two identified primary sources of secular motion, from the estimated station velocities, I will attempt to quantify the remaining secular motion caused by present day surface mass loading. In terms of this study, “secular” will be limited by the 10 years of GPS data used but long term trends will be inferred from this data.

As part of this study I have taken over the running of the Global Network Associate Analysis Centre (GNAAC) combining the operational AC solutions into a weekly combined solution. Newcastle has been part of the IGS operational combination as a GNAAC since 1995 (Davies and Blewitt (1995)). With the advent of the reprocessing campaign Newcastle agreed to be a GNAAC again. Newcastle uses TANYA which is a bespoke piece of software developed at Newcastle by Lavallee (2000), Davies (1997) and various other authors. TANYA is a combination software which uses Least Squares (LS) to produce a unified single solution of all the individual AC weekly submissions. For a full description of TANYA see Lavallee (2000) and Davies (1997).

Using the combined solution produced at Newcastle it will be possible to estimate a velocity for each reference frame station. These velocities result from a combination of factors including the redistribution of surface masses, plate tectonics and GIA. The amount of data available as part of the IGS reprocessing campaign begins in 1994, submitted by a subset of ACs, (4 as of NC1 combination), but I have used March 1999 to February 2010 (GPS weeks 1000 – 1570) as this contains all data from all 11 participating ACs and covers over a 10 year time period. This also bridges between the reprocessing and operational data sets, at GPS week 1459.

I aim to separate out the signals in the data that are the indicators of surface loading by producing a combined GIA and plate tectonic velocity estimate. The confounding factors which have been extensively researched are GIA (Ivins and James (2005), Paulson et al. (2005), Peltier (2004), Johansson et al. (2002)) and tectonic motion (Argus et al. (2010), Kogan and Steblov (2008), Altamimi et

al. (2007), Sella et al. (2002), Larson et al. (1997)) which assigns vertical station motions to GIA and surface mass loading and horizontal motions to plate tectonics, GIA, surface mass loading and many other negligible effects which are not considered in this work.

There are several processes that occur on the surface of the Earth which can influence the weekly estimate of any chosen site:

1. The site is located upon the plate interior and moves with the tectonic plates.
2. The site is contaminated by plate boundary movements.
3. The site is located upon the plate interior, but is subject to intra-plate deformation.
4. Site contains vertical and horizontal motion due to GIA.
5. The site is insufficiently attached to the rigid plate.
6. There is a change in surface mass loading.

This is a brief summary of the main causes of a station's apparent velocity. Alternatively the velocity of a station may be influenced by measurement errors, for example antenna/receiver changes. I aim to mitigate the effects of (1, 2, 3 and 4) as described below. I will disregard (5) as all IGS sites should have good quality monuments IGSCB (2012). Factors (1-3) can be assessed using geological observations of tectonic faults, seismology, topography, seafloor mapping and by excluding sites within the known plate boundary deformation zones. I will attempt to account for (4) by employing a GIA model. There are several GIA models in circulation (Ivins and James (2005), Schotman and Vermeersen (2005), Peltier (2004)) all of which attempt to reconstruct the geometry of the last ice age and the resulting adjustment of the solid Earth during and after glaciation. These GIA models contain potentially large scale regionally correlated errors and are likely to poorly model the magnitude of horizontal motion (King et al. (2010)). By employing different families of GIA models and comparing their output I hope to assess the effects of these errors.

Once the velocity due to GIA has been removed (4) the residual velocities should be due to plate tectonics (1-3) and any other secular loading (6). Recent publications show that plate motions can now reliably be estimated from GPS data (Kogan and Steblov (2008)) by estimating an absolute Euler pole and the magnitude of the rigid body rotation about that pole. Developing a fully integrated model comprising the modelled GIA and estimated plate velocities

will leave residuals caused by present day surface mass loading trends and model error.

1.2 Reference Systems and Frames

None of the above would be possible without a high quality and stable TRF. Nearly all geodetic applications rely upon a chosen reference frame. Any reference frame is based upon a set of ideals defined by the reference frame's associated reference system.

1.2.1 *Reference Systems*

A reference system is a spatial model which fits the motion of the Earth in a theoretical space. The reference system definition contains the origin and scale of the coordinate axis and the orientation of the frame with respect to the Earth. In the wider global geodetic community the system defined by the International Earth Rotation Service (IERS) is recognised as the reference system of choice, known as the International Terrestrial Reference System (ITRS), although there are several other Terrestrial Reference Systems (TRS) such as the ETRS and GTRS (Boucher (2001)). Focussing on the ITRS, the origin is defined as being the centre of mass (CM) of the Earth system, including the Earth and all the mass that is on the exterior of the Earth surface (atmosphere, oceans, hydrology and ice). The scale of the ITRS is defined by the SI unit of the metre. Finally the orientation of the TRS is equatorial with the Z-axis passing through the Earth's surface at the IERS Reference Pole (IRP) which is a position equivalent to an average historic location of the North Pole. The X-axis is set to 0° Longitude (Greenwich Meridian) with the Y-axis perpendicular to the X-axis completing the right hand system. These definitions are laid down in the IERS Conventions 2003 (McCarthy and Petit (2004)).

1.2.2 *Reference Frames*

With the complete definition of the TRS, in this case the ITRS, it becomes possible to realise a TRF, or the ITRF from the ideals of the ITRS (Altamimi et al. (2007)). The ITRF is reference frame which is fundamental to all space geodetic applications (GPS, VLBI, SLR and DORIS). There are three stages in the realisation of the ITRF:

1. Aligning the Cartesian axes of the ITRS to the model of the Earth through a series of rotations, translations and scaling of geodetic observations.
2. Definition of the unit of length
3. Fitting an estimation of the Earth's surface to the axes.

(1) creates a physical connection between the CM of the Earth to the origin of the TRF axes; this is not a simple procedure as the CM of the Earth is constantly changing due to the dynamic nature of surface masses. Every release of the ITRF includes the location of the origin at the chosen reference epoch and its evolution in time, e.g. ITRF2005 is defined over 1995-2005. The origin of the ITRF is defined as the CM from an average of the SLR time series which for the ITRF2005 was 13 years long (Altamimi et al. (2007)).

(2) defines the scale of the frame; the SI metre is the chosen scale (McCarthy and Petit (2004)). Although this should be a repeatable measurement each technique has slightly different systematic errors and calibrations which cause slight variations to its definition. This variability means that the absolute scale of the ITRF is the weakest part of the realisation.

(3) drapes an approximated surface of the shape of the Earth over the frame and allows coordinates to be described in geographic coordinates (latitude, longitude and height (llh)) which are much easier to interpret than Cartesian coordinate (XYZ). A best approximation of the Earth is an ellipsoid defined by the semi-major (North Pole) and semi-minor axes (equatorial).

1.3 Surface Mass Loading

Surface mass loading is caused by a body of water resting upon the surface of the Earth (or as near-surface groundwater) causing deformation of the solid Earth. It is extremely important that the temporal and spatial distributions of these surface masses be quantified to be able to understand their effects on the solid Earth. Fluids on the Earth exist in three states: solid, liquid and gas. The effect of surface mass loading and redistribution affects not only the shape of the Earth but also its rotation (axis and rate) and the gravity field.

Water that is frozen can predominantly be found at high latitudes and high altitudes in glaciers and ice caps. The long-term change in the mass balance of ice stored in glaciers is a relatively stable process, which is calculated by snow fall (input) minus melt (output) which can take several years for any major secular changes (trends) to become apparent. In comparison seasonal snow

fall is very difficult to measure and is a weakness of hydrology models (Wouters et al. (2011)). The secular growth and retreat of glaciers causes surface loading upon vast swaths of the Earth, the resulting adjustment after deglaciation is known as GIA, section (2.4).

Most GIA models incorporate ice change until ~3-4kyr ago (Peltier (2004)); any ice change after this period is relatively small in comparison to the LGM and will not be modelled; therefore this is a potential signal in our residuals. Table 1 summarises the observed ice changes over the last ~10 years, it is changes such as this that this study hopes to be able to detect.

Table 1: Estimated ice mass change in recent times

Location	Mass Change (Gt/yr)	Time period
Continental Glaciers	-148±30 (Jacob et al. (2012))	Jan2003-Dec2010
Greenland	up to -230±33 (Velicogna (2009))	Apr2002-Feb2009
Antarctica	-143±73 (Velicogna (2009))	Apr2002-Feb2009

Liquid water is stored in oceans, lakes, rivers and groundwater. The amount of water stored in land can be modelled using a combination of soil moisture and hydrological models e.g. Land Dynamics (LaD) (Milly and Shmakin (2002)) but these are inaccurate as global grids are interpolated from a small number of finite point records (Tregoning et al. (2009b)). Water stored in continental lakes, rivers and wetland areas accounts for less than 0.25% of the total on the surface, but the redistribution of this stored water causes noticeable signals in station time series at a seasonal and secular period (Chao et al. (2008)). Of all water mass redistribution Continental Water Storage (CWS) is the least understood due to the difficulties in making accurate recordings. Studies by Tregoning et al. (2009b), Lavallee et al. (2007), Wahr et al. (2004), Wu et al. (2003) and van Dam et al. (2001) begin to formulate ideas on how the deformation due to terrestrial water is a combination of factors.

The main drivers of mass redistribution in the oceans and seas are waves, currents and tides. Waves are driven by surface winds (Tolman (2008)) introducing energy into the surface layer of the oceans. These waves have very high frequency and have a negligible influence upon loading and will not be discussed further. The ocean currents drive a massive flow of water from one area to another; these currents are caused by changes in the temperature, salinity or the wind moving small quantities of mass. However the largest

causes of ocean mass redistribution are the ocean tides. The gravitational attraction of bodies in the solar system, the Sun and the Moon having the largest effects, causes a bulge in the oceans and the Earth's interior at the point of shortest distance. There are several ocean tide models to fit different requirements and this decision of which model to implement has always been handled by the ACs and the International GNSS Central Bureau (IGSCB), section (3.3.7). For the first round of reprocessing all ACs have to use FES2004 (Lyard et al. (2006)) in the CM frame, (Reprocessing (2012)) to remove the effects of short-period ocean tidal loading. The choice of model is important as their coverage varies globally and some of the shallow seas are neglected in some models.

Finally water in its gaseous state mostly lies within the lowermost layer of the atmosphere known as the troposphere and contributes to atmospheric pressure. Atmospheric pressure causes a load upon the surface of the Earth and this varies with the movement of high pressure systems and short period synoptic storms passing over an area (van Dam and Wahr (1998)). van Dam et al. (2010), Tregoning and van Dam (2005b), Tregoning and van Dam (2005a), van Dam et al. (1997) and van Dam et al. (1994) have all studied the effects of atmospheric pressure upon station coordinates and have concluded that the effect is dependent upon a station's latitude, with the effects being greater at higher latitudes as at low latitudes the variation in atmospheric pressure is very small (van Dam and Wahr (1998)).

The quantification of the surface displacement caused by surface mass loading is achieved via Love number theory which is discussed in section (2.2).

1.4 Glacial Isostatic Adjustment

GIA is caused by a secular change in ice mass on the surface and is characterised by the redistribution of mass in the Earth's interior causing uplift and horizontal motion of the surface of the Earth around areas where large glaciers were located. In the long term the deformation is driven by the slow viscous creep of mantle material. Assuming the material in the Earth's interior to be in isostatic equilibrium then any change in surface loading will disrupt this equilibrium. During an ice age, large areas of the Earth's surface are covered by ice; during the Last Glacial Maximum (LGM) large ice sheets covered Fennoscandia, Laurentia and Antarctica with smaller ice sheets covering UK,

Siberia and Patagonia. The weight of the ice pressing down deforms the crust of the Earth which in turns increases the internal pressure of the mantle. Movement of mantle material will occur from this induced area of high pressure to the surrounding areas of low pressure in an attempt to restore isostatic equilibrium. This movement causes a deficit below the surface and additional subsidence of the crust.

Currently the Earth is in an interglacial period which means that the large glaciers and ice sheets have receded and most of the surface of the Earth is ice free. However, the redistribution of mantle materials is not instantaneous as the mantle is highly viscous ~10^{20}-10^{22}Pas (Sabadini and Vermeersen (2004)). As such, GPS observations are still recording the effects of the LGM, ~26-20kyr (Clark et al. (2009)) caused by the slow creep of material back into its original location (Peltier (2004)). Vertical trends of up to 10mm/yr (Sella et al. (2007)) and 8mm/yr (Bevis et al. (2009)) have been measured in GPS time series at stations in close proximity to the old ice domes. There is not only vertical motion associated with GIA, generally much smaller horizontal trends (Sella et al. (2007), Johansson et al. (2002)) can be seen in affected time series. This is caused by the movement of mantle material, lithospheric flexing and the collapse of the glacial forebulge (Fjeldskaar (1994)) which is a feature of glaciation, Figure 2.

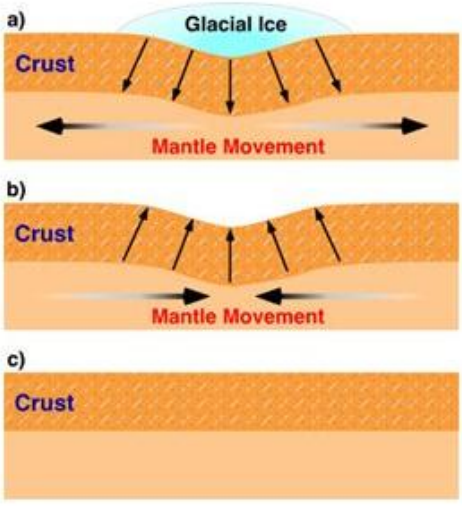

Figure 2: Stages of isostasy, (a) load present, crustal deformation (b) load removed, uplift experienced caused by mantle repositioning (c) equilibrium restored. [Physical Geography.net]

GIA not only affects surface displacements; the large accumulation of ice had an associated effect upon the oceans. The amount of water in the Earth system

can be thought as being a constant. The growth of glaciers causes a fall in global sea levels and a reduced load upon the ocean bottom. With glacial retreat the stored water migrated back to the oceans, causing subsidence over the oceans basins due to the increased mass of water.

The sheer size of the LGM glaciers disrupts the local gravity field (Trupin (1993)) drawing the mobile fluids in the oceans towards them causing a secondary increase in loading. GIA also affects the rotation of the Earth and the location of the rotation axis. The displaced mantle moved away from the poles towards the equator slowing down the rotation rate, and increasing the Length of Day (LOD). This effect is reversed during the interglacial period as mantle material returns towards the poles (Argus and Peltier (2010)). The position of the Earth rotation axis was also disrupted. This can be seen by the slow drift of the pole towards ~80° West which happens to be the centre of the old Laurentian ice complex (Peltier (1984)).

1.5 Plate Tectonics

Plate tectonic theory, developed during the 20th century, took great steps in unifying the study of Earth sciences. Alfred Wegener proposed his theory of continental drift in 1912 (Wegener (1912)); this outlined methods with which the continents were able to move relative to one another. This theory took steps to explain why some continental coastlines appeared to interlock for example South America and the west coast of Africa. Modern day plate tectonics arises from the combination of Wegener's theory with the later theory of seafloor spreading (Hess (1962)) which explains how new crust is created at ridges under the oceans as they drift apart. It is known that the outer part of the Earth is comprised of lithospheric plates which are ~100km thick and it is assumed that they behave rigidly in the plate interior. Tectonic plates are able to move on the surface of the sphere at the rate of 10cm/yr (Plag et al. (2006)). Where tectonic plates meet, plate boundary processes are the primary driver in the creation and destruction of the lithosphere (Condie (1997)). It is at the boundary zones that the vast majority of earthquakes of magnitude five and above on the Richter scale occur; there is a striking pattern which delineates the plate boundaries, Figure 3.

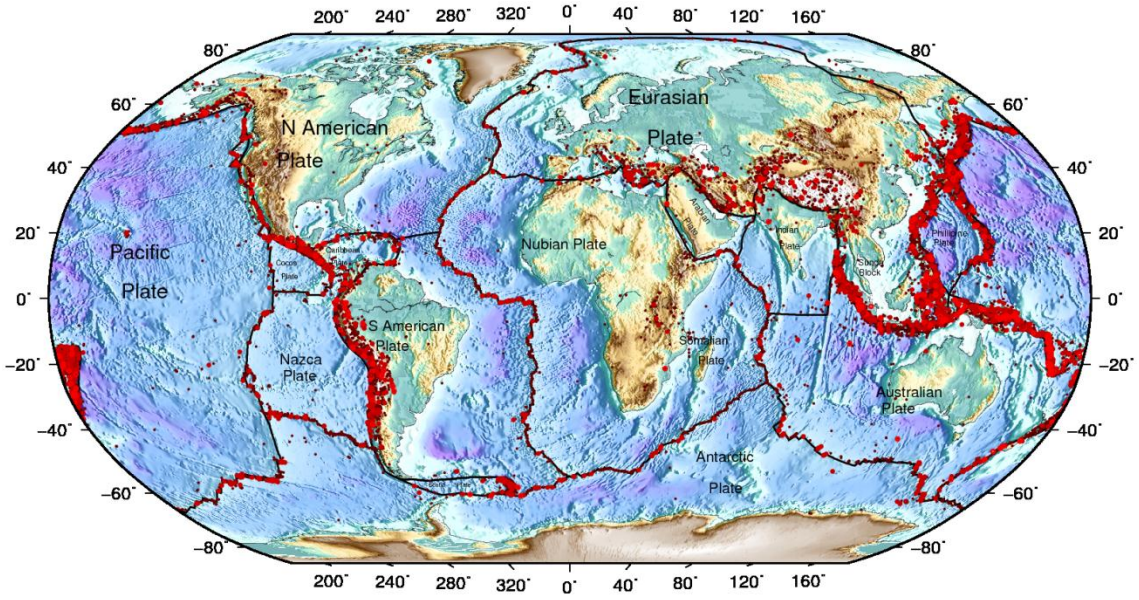

Figure 3: Red dots represent major earthquakes of magnitude five or greater, the increasing size and redness represent larger earthquakes. Earthquakes cover the period 1994 to 2011 and are taken from the Council of National Seismic Systems catalogue http://www.ncedc.org/cnss/. Topographic data are from the National Geophysical data Centre (NGDC). All maps are produced using the Generic Mapping Tools (GMT) software. Plate boundaries are from Demets et al. (1990).

There have been several attempts to calculate the velocities and rotations of the separate tectonic plates (Bullard (1965), Hess (1962)). The standout model which has been used by hundreds of studies is the NUVEL-1 Model (Demets et al. (1990)) and its updates. The choice of plate model is fundamental to so many applications that require a precise definition of plate movements and evolution. Prior to space geodetic techniques, plate motion was calculated using sea floor spreading rates averaged over millions of years and earthquake slip vectors from seismic measurements (DeMets et al. (2010), Demets et al. (1990)).

Space geodetic techniques present an alternative method which does not have to make the assumption to average millions of years into a single velocity. Such is the accuracy and precision of spaceborne measurements that only a few years of data are required to calculate the plate motions. Blewitt and Lavallee (2002) determined that 2.5 years would be sufficient to estimate site motions in the presence of seasonal signals. Sites that fall within the plate boundary deformation zones are not included, as plate boundary processes can bias estimates of relative plate motions (Kreemer et al. (2003)).

The main limitation of space geodetic measurements is the availability of land on oceanic plates such as the Pacific where there are limited islands on which

tracking stations can be located. Many different space geodetic techniques have been used to estimate plate motions. VLBI, SLR and DORIS data historically have been used to develop plate models. In the late 20th Century GPS became the forerunner in tectonic plate modelling as the number of stations in the tracking network vastly increased and global solutions soon became a reliable possibility. The success of densification has been due to the improvements in portability, the cost of the GPS receivers and the immense work of the IGS densification project (Blewitt and Lavallee (1999)), section (3.1).

1.6 Issues of GIA / Tectonic Separation

The separation of GIA and tectonically induced velocities forms a large portion of the work undertaken in this thesis. Steps have been taken to identify all the causes of horizontal and vertical trends. Current methods (Klemann et al. (2008), Sella et al. (2007), Johansson et al. (2002), Cretaux et al. (1998), Argus and Heflin (1995)) assign vertical velocities to GIA and present day surface mass loading and horizontal velocities to plate tectonics and to a lesser extent GIA and surface mass loading, meaning that there is not a clear divide between the two. By ensuring that study stations are located upon the rigid plate interior it is possible to ensure that plate tectonics does not contribute to vertical velocities (Lavallee (2000)). This is further defended by Euler's theorem (Palais et al. (2009)) which states that rigid bodies can only move horizontally over the surface of the Earth rotating around an absolute Euler pole and therefore cannot contribute to the vertical velocity component. The horizontal component is a more complex situation; as mentioned most of the horizontal velocity comes from plate rotations, but some horizontal motion is driven by GIA and surface mass loading. Most Earth models used in GIA modelling are composed of a 1D layered Earth which varies viscosity only with depth, for example VM2 (Peltier (2004)). This is a major limiting factor to the accuracy with which the horizontal velocity can be estimated as current stratified Earth models describe each layer as having homogeneous viscosity and lithospheric thickness. If the lateral viscosity of the Earth varies (Paulson et al. (2005)) then current models will not be able to accurately represent the observed horizontal velocity. This unaccounted for velocity will introduce a bias into any velocity estimation. Steps have been taken to adapt a stratified model by introducing areas of varying viscosity within each layer and varying the thickness of the lithosphere (Paulson et al. (2005)), but these models are still in their infancy (Davis et al. (2008),

Klemann et al. (2008), Latychev et al. (2005b), Kaufmann et al. (2000)). I will attempt to mitigate these GIA model shortcomings by implementing a suite of different GIA models developed around different Earth models and ice histories.

1.7 Summary

By using the newly published reprocessed IGS data set there is opportunity to study the long term deformation of the Earth. After accounting for plate tectonics and GIA, the residual velocity will be caused by present day surface mass loading trends. In the following chapters I will explain the various interpretations of GIA and how plate tectonic velocities are estimated. Chapter 3 will explain the combination of AC network solutions and modifications made to improve accuracy and inclusion of additional parameters. The final Chapters will highlight the results of the combination and how they are interpreted to quantify present day surface mass loading.

This work extends previous knowledge by using the IGS's reprocessing campaign and presents new GPS derived loading coefficients of secular mass change. By using basis functions (Clarke et al. (2007)) and a suite of global GIA models I aim to provide several estimates of surface mass loading which can be compared against other studies, such as Wu et al. (2010), which employs an ocean model to constrain the estimation and a compilation of GIA models, or GRACE estimates (Baur et al. (2009), Velicogna (2009), Luthcke et al. (2008), Wouters et al. (2008), Chen et al. (2006b), Velicogna and Wahr (2005)). Previously only Lavallee et al. (2007) used the basis functions but that study was concerned with extracting low degree harmonics, I am more concerned with the highest maximum level attainable and thus the finest spatial resolution.

These new results are not immune to GPS errors but they are less susceptible than the original operational data set. For example, tropospheric errors have been considered but 2nd order ionospheric effects are not included in the first IGS reprocessing campaign. There are still GPS orbit errors which affect all GPS station positions but compared with the operational data set massive improvement is shown. With respect to loading, the homogeneous nature of reprocessing allows the study of real secular signals as there should no contribution to the long term from processing models.

Chapter 2. Geophysical Causes of Secular Deformation

Deformation of the Earth occurs over a range of time scales, from the very high frequency sub daily (tidal) to the extremely long spanning centuries to millennia. There are very strong seasonal signals caused by the redistribution of surface masses (Wouters et al. (2011), Bos et al. (2010), Bennett (2008), Lyard et al. (2006), Chambers et al. (2004), Cretaux et al. (2002), Shmakin et al. (2002), Blewitt et al. (2001), van Dam et al. (2001), van Dam and Francis (1998), van Dam and Wahr (1998)) with vertical deformation magnitudes up to around 20mm due to the atmosphere, 30mm from Continental Water Storage (CWS) and <10mm due to non-tidal ocean loading (Williams and Penna (2011)); inter-seasonal variation caused by co/post seismic processes and volcanism (Arriagada et al. (2011), Chen et al. (2011), Reddy et al. (2011)) which typically has a magnitude of 1-2mm/yr; and finally secular motion (linear over human time scales) (Khan et al. (2008), Klemann et al. (2008), Sella et al. (2007), El-Fiky and Kato (2006), Kreemer et al. (2003), Sella et al. (2002), Tamisiea et al. (2002), Wahr et al. (2001), Mitrovica and Peltier (1993)), typically this includes plate tectonics (<50mm/yr horizontally) and GIA (10mm/yr vertically and 2-3mm/yr horizontally) with very small trends from fluid mass loading on the surface (van Dam et al. (2001)).

The focus of this study is the secular signals present in GPS coordinate time series; the short term and inter-seasonal variation can be removed during the analysis by estimating a linear trend, section (4.1), and seasonal signals will average down to zero after 2.5 years of observations (Blewitt and Lavallee (2002)), leaving only the secular deformation.

In this chapter I will discuss secular deformation; of which the two primary drivers are plate tectonics and GIA. I aim to treat these two signals as errors (biases) in the reprocessed station time series which can be quantified and removed. The linear trend of the residual coordinates, if any, will be indicative of present-day secular deformation due to surface mass loading or other processes which I will consider to be negligible. First we must consider the construction of the solid Earth and its properties as this will dictate how it reacts to surface loading.

2.1 General Earth Structure

The physical and chemical structure of the Earth has been estimated using a variety of seismological techniques (Miller et al. (2009)). By defining the layers of the Earth by their rheological properties (deformation type and strength) instead of physical and chemical properties we can begin to explain the process of plate tectonics.

The structure of the Earth can be broken down into distinct physical layers, briefly these are the crust (70km thick), mantle (2800km), outer core (2300km) and inner core (1200km). However by the rheological properties the crust and mantle can be broken down into three distinct layers (Miller et al. (2009)). The lithosphere is the outer most part of the solid Earth, comprising of the crust and part of the upper mantle, it is approximately 100km thick but this varies with the type and age of the lithosphere (Van Der Pluijm and Marshak (2004)). The lithosphere is divided into tectonic plates; there are approximately 15 major and several other minor/micro plates (Altamimi et al. (2007)). The lithosphere has a finite strength and will rupture when placed under stress where the tectonic plates collide (Frisch et al. (2010)). Away from these rupture zones the lithosphere can be treated as elastic (Anderson (2007)) where the lithosphere is able to flex under loading. Beneath the lithosphere is a layer known as the asthenosphere, this layer is approximately 180km thick (Low Velocity Zone (LVZ) for Earthquakes) (Condie (1997)). Kearey et al. (2009) defined the root of the asthenosphere as being the beginning of the seismic transition zone. Due to the immense pressure and temperature in the asthenosphere the mantle material is ductile and it is involved in both the process of plate tectonics and GIA. Below the asthenosphere is the mesosphere, this is the portion of the mantle between the asthenosphere and the outer core (2900km depth). Although the mesosphere is part of the mantle the increased pressure makes it much less deformable (Poirier (2000)). The Earth structure is summarised in Figure 4.

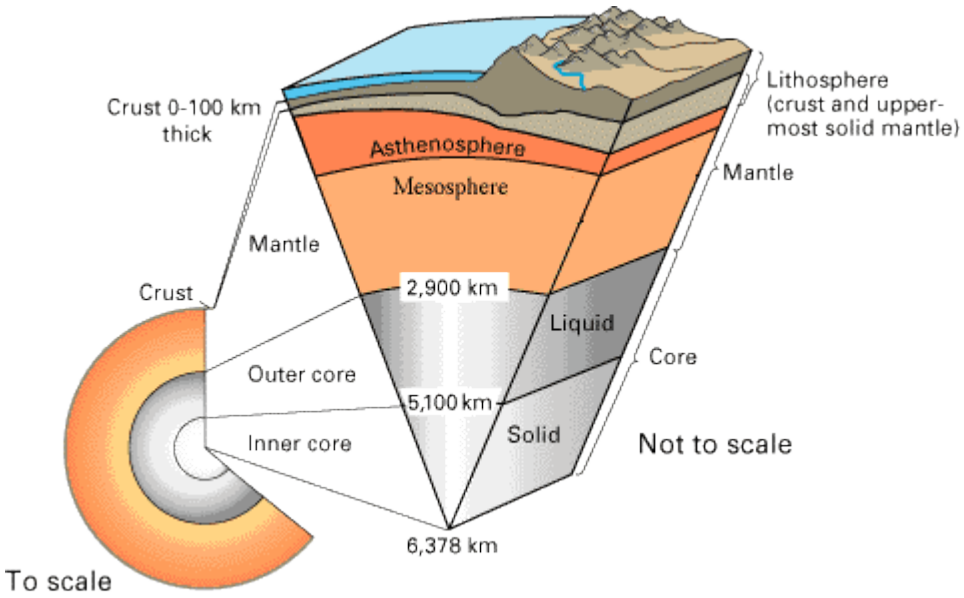

Figure 4: Internal Structure of the Earth (approximate values, USGS)

2.2 Elastic Deformations of the Solid Earth

The movement of surface masses on an elastic Earth will induce horizontal and vertical deformations (Farrell (1972)). The change in shape of the Earth due to the masses' gravitational and loading pressure is described by the load Love numbers (Blewitt (2003), Love (1909)).

Love number theory is used to calculate the response of the solid Earth to the disturbing forces of surface masses and luni-solar gravitation. There are two forms of Love numbers, tidal (interactions with the Sun and Moon) and loading (surface masses). The Earth's surface moves tidally by as much as 50cm per day due to the gravitational attraction of the Sun and Moon (Lennon and Baker (1973)). However this study is more concerned with the effects of surface mass loading so I will detail the load Love numbers. The (dimensionless) load Love numbers are a measure of how much a planet's surface and interior deforms in response to surface mass loading (Love (1909)). The general formula for calculating the load Love numbers is laid out in Farrell (1972). There are three different Love numbers which account for: radial displacement h', the additional gravitational potential k' and the horizontal displacement l' due to the load. If a planetary body is fully rigid then these values should all equal zero, but as the propensity of a body to deform increases then the load Love numbers increase (Love (1909)). Farrell (1972) developed a series of load Love numbers for different scenarios of Earth rheology.

Blewitt (2003) building on the summary of Bomford (1980) used load Love numbers to explain the expected surface deformation due to surface mass redistribution. The change to the Earth's gravitational potential at any location (Ω) is:

$$V(\Omega) = \sum_n V_n(\Omega) = \frac{4\pi R_E^3 g}{M_E} \sum_n \sum_m \sum_\Phi \frac{\sigma_{nm}^\Phi Y_{nm}^\Phi(\Omega)}{(2n+1)} \tag{2.1}$$

Where g is the acceleration due to gravity, σ_{nm}^Φ is spherical harmonic magnitude, Y_{nm}^Φ are the surface spherical harmonic functions, R_E,M_E are the radius and mass of the Earth respectively. The surface deformation in local height $\Delta s_h(\Omega)$ and lateral $\Delta s_l(\Omega)$ directions are:

$$\begin{aligned} \Delta s_h(\Omega) &= \sum_n h_n' V_n(\Omega) / g \\ \Delta s_l(\Omega) &= \sum_n l_n' \hat{l}(\Omega).\nabla V_n(\Omega) / g \end{aligned} \tag{2.2}$$

Where $\hat{l}(\Omega)$ is the unit vector in the horizontal plane and V_n is the induced gravitational potential due to the surface load (Blewitt (2003)). There is an additional loading potential which is associated with the redistributed mass on and in the Earth:

$$\Delta V(\Omega) = \sum_n k_n' V_n(\Omega) \tag{2.3}$$

Using (2.1)-(2.2), the net loading potential can be shown as:

$$U(\Omega) = V(\Omega) + \Delta V(\Omega) = \sum_n (1 + k_n') V_n(\Omega) \tag{2.4}$$

This section discusses the Love numbers for an elastic Earth, however the Earth is not purely elastic and the load Love number theory can be extended to incorporate a viscoelastic Earth.

2.3 Surface Mass Loading

Surface mass loading induces deformation to the solid Earth which is recorded by GPS stations and can be described as a weekly (or daily etc.) displacement. It has been shown that the inversion of geodetic displacement data can be used to infer surface mass loading by fitting a set of spherical harmonic coefficients (Blewitt and Clarke (2003), Wu et al. (2003)). Using the conventions from Clarke et al. (2007) it is possible to express the total load on the surface of the Earth,

T , in equivalent terms of a column of sea water with density ρ_s , as a function of location, Ω .

$$T(\Omega) = \sum_{n=1}^{\infty} \sum_{m=0}^{n} \sum_{\Phi}^{\{C,S\}} T_{nm}^{\Phi} Y_{nm}^{\Phi}(\Omega) \tag{2.5}$$

Where T_{nm}^{Φ} are the spherical harmonic coefficients and Y_{nm}^{Φ} are the surface spherical harmonic functions as above. The summation in (2.5) begins at degree $n = 1$, as conservation of mass dictates that the degree-zero term should be zero and hence disappear. The vertical and lateral elastic displacements caused by $T(\Omega)$ can be calculated using the appropriate load Love numbers Love (1909), see section (2.2). The change in height of any location is:

$$H(\Omega) = \frac{3g\rho_s}{\rho_E} \sum_{n=1}^{\infty} \sum_{m=0}^{n} \sum_{\Phi}^{\{C,S\}} \frac{h_n^{'}}{n+1} T_{nm}^{\Phi} Y_{nm}^{\Phi}(\Omega) \tag{2.6}$$

Where g is the gravitational acceleration at the surface and $h_n^{'}$ are the height load Love numbers for degree n . Likewise the lateral displacements of the surface are:

$$\begin{aligned} E(\Omega) &= \frac{3\rho_s}{\rho_E} \sum_{n=1}^{\infty} \sum_{m=0}^{n} \sum_{\Phi}^{\{C,S\}} \frac{l_n^{'}}{2n+1} T_{nm}^{\Phi} \frac{\partial_\lambda Y_{nm}^{\Phi}(\Omega)}{\cos\varphi} \\ N(\Omega) &= \frac{3\rho_s}{\rho_E} \sum_{n=1}^{\infty} \sum_{m=0}^{n} \sum_{\Phi}^{\{C,S\}} \frac{l_n^{'}}{2n+1} T_{nm}^{\Phi} \partial_\varphi Y_{nm}^{\Phi}(\Omega) \end{aligned} \tag{2.7}$$

(2.7) uses $h_n^{'}$ and $l_n^{'}$ which are the height and lateral load Love numbers. Equations (2.5)-(2.7) use the standard spherical harmonic functions.

Blewitt (2003) developed the theory of Earth loading and calculated different load Love numbers in a variety of different frames of reference, see section (2.7.1).

There is an imbalance of GPS observations, with areas such as North America and Western Europe being saturated with observations whereas the Pacific Ocean and other areas are very sparse in observations. This imbalance causes higher degree estimation to become unstable as the required number of coefficients rapidly increases (Wu et al. (2002)). The standard spherical harmonic functions do not distinguish between oceans and continents and so the spherical harmonic estimate of the load will leak from the land mass to the oceans. This led to the development of an alternative method to standard

spherical harmonics, (Clarke et al. (2007)), which uses a set of basis functions to constrain the loading estimation to continental land mass; this is described in section (2.3.1).

2.3.1 *Development of Basis Functions*

It has been shown that fitting a load using the standard spherical harmonic coefficients is inefficient as it suffers from the imbalance of tracking stations distribution (Clarke et al. (2007)), as the spherical harmonic estimation is calculated evenly over the entire globe, whereas geodetic observations are mostly confined to the continental land mass. Continental land is predominantly located in the Northern Hemisphere limiting the availability of stable land in the Southern Hemisphere to locate tracking stations (e.g. GPS, SLR or DORIS). This bias increases the uncertainties in areas which are sparse in observations or allows data sparse areas to have unrealistic values to ensure a smooth fit elsewhere.

The inverse barometer (IB) assumption Wunsch and Stammer (1997) describes how the oceans will redistribute from one geopotential surface to another by redistributing the load across the entire basin over longer time periods (greater than a few days). As such Clarke et al. (2007) strove to develop a gravitationally consistent, mass-conserving set of basis functions as an alternative to the spherical harmonic functions. These basis functions enable the estimation of realistic surface loads within the coastline, with the only signal over the oceans being the mass conserving tidal response. Clarke et al. (2007) achieved this by taking the original spherical harmonic functions and masking them with an ocean function $C(\Omega)$ which is zero over land and unity over the oceans.

$$B'_{nm}(\Omega) = \{1 - C(\Omega)\} \cdot Y^{\Phi}_{nm}(\Omega) \tag{2.8}$$

As it stands (2.8) is no longer mass conserving so in the final stages of basis function development an oceanic term is introduced.

$$\begin{aligned} B^{\Phi}_{nm}(\Omega) &= B'_{nm}(\Omega) + S^{\Phi}_{nm}(\Omega) \\ S^{\Phi}_{nm}(\Omega) &= C(\Omega) \cdot \{[V(\Omega) + \Delta V]/g - H(\Omega)\} \end{aligned} \tag{2.9}$$

In the updated (2.9) the $S^{\Phi}_{nm}(\Omega)$ term contains the ΔV component which ensures that mass is conserved and the remaining parameters ensure obedience of the Sea Level Equation (SLE) Farrell and Clark (1976), where

$H(\Omega)$ and $V(\Omega)$ are the Earth's response to the total load $B(\Omega)$ and is required to fulfil the SLE. The SLE accounts for the spatially varying term (change in the shape of the geoid) and a spatially constant term accounting for the total change in ocean mass.

The modified basis functions, which account for the SLE, will constrain the surface load to the continents in this case without accounting for the evolution of the coastlines. For small changes in surface mass load this evolution is negligible, in contrast to GIA modelling where coastline changes are significant. To avoid confusion through this study I will use the term "level" to refer to the level of basis functions, i.e. n on LHS of (2.8) and "degree/order" to refer to the spherical harmonic degree and order more generally, i.e. n on RHS of (2.8).

In this study the basis function are evaluated as spherical harmonics and truncated at degree 45. For a full description of the development of the basis functions see Clarke et al. (2007) who truncated them at level 30. The number of terms evaluated at a given basis function level is simply:

$$N = (n+1)^2 \tag{2.10}$$

Where N is the number of parameters and n is the basis function level. By varying the level of basis function it is possible to vary the spatial resolution of the weekly estimation to isolate specific loads, see introduction (Chapter 6), in particular the low degree harmonics.

2.4 Glacial Isostatic Adjustment

GIA is caused by response of the solid Earth to the changing surface loading caused by the growth and retreat of major ice-sheets and glaciers. With the growth of the ice-sheets come an associated fall in relative sea-levels of ~130m (Latychev et al. (2005b)). During the last major ice age, areas of North America, Fennoscandia, Antarctica and other parts of Northern Europe and South America were covered by ice, (Latychev et al. (2005b)) as illustrated in Figure 5.

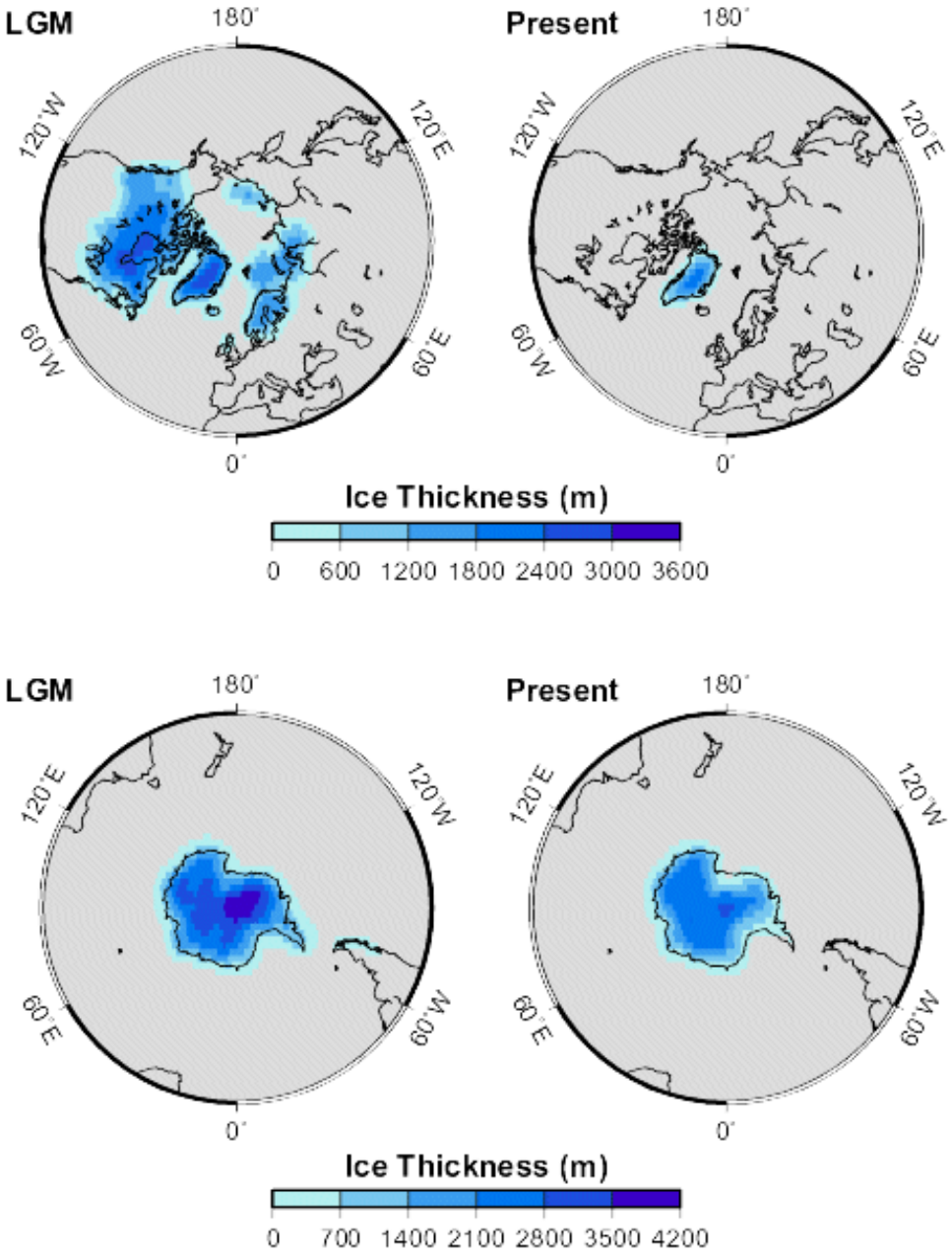

Figure 5: Representation of ice sheet coverage during the last ice age (Milne (2012))

The glacial cycle describes the growth and retraction of glaciers on the surface of the Earth, the associated drop in sea levels and the effect upon the solid Earth, Figure 6.

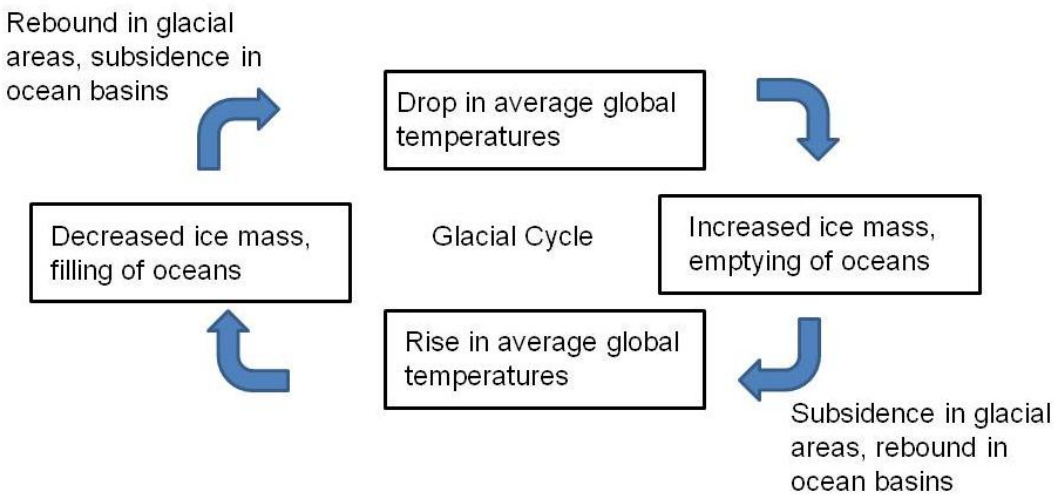

Figure 6: Simplified glacial cycle

Modelling GIA is an extremely complex process; the response of the Earth to the variation in ice load is not instantaneous, thus GIA does not occur synchronously with the (de)glaciation of the Earth. The interior of the Earth is a highly viscous fluid (near solid) and therefore the flow of material in the mantle takes thousands of years. The rate of this flow of materials decreases as the time increases from the unloading event but it can be considered as constant over human time scales, thus the Earth is still undergoing GIA today (Clark et al. (2009)).

GIA models attempt to determine the magnitude of deformation caused by previous glaciation (Spada et al. (2006), Ivins and James (2005), Schotman and Vermeersen (2005), Peltier (2004)). The effect of GIA can be observed through three parameters:

- Changes to the Earth's gravity field (Lambert et al. (2001), Larson and van Dam (2000))
- Deformation of the Earth's surface (Sella et al. (2007), Johansson et al. (2002))
- Variations to the Earth's rotation (Argus and Peltier (2010))

Any one or combination of these observations can provide additional constraints upon the internal structure of the Earth and the history of previous glaciations. Other than the direct effect of the massive loading due to glaciation there is an associated change to the localised gravity potential which varies the level and distribution of the oceans. This variation in the oceans causes an additional surface load which must be modelled (Whitehouse (2009)). By measuring rates

of change of gravity and crustal deformation in previously glaciated areas it is possible to calculate constraints on the Earth's viscoelastic structure.

The uplift/subsidence of land will cause a change to the local gravity field which is detectable using absolute gravimeters; which measure the acceleration of mass in a vacuum. Repeated measurements can be used to infer the secular changes in the local gravity field, such as those caused by the change in volume/quantity of mantle mass in areas of previous glaciation (Lambert et al. (1989)). The accuracy or precision with which absolute gravity rates can be determined is 0.5*μGal*/yr ≈1.5mm/yr (Larson and van Dam (2000)) and more recently 0.5mm/yr (Van Camp et al. (2005)).

It is possible to measure the rate of surface displacement using space geodetic techniques such as GPS, via tracking stations attached to the solid Earth (Lidberg et al. (2010), Lidberg et al. (2007), Sella et al. (2007)) or levelling networks e.g. in Fennoscandia (Fjeldskaar et al. (2000)). Current observed rates of GIA vertical displacement have been measured at over 10mm/yr (Sella et al. (2007), Johansson et al. (2002)) in Hudson Bay and 8mm/yr in the Antarctic (Bevis et al. (2009)).

Finally, any surface deformation, redistribution of surface mass or internal structure will affect the Earth's rotation, as this induces a deformation due to centrifugal potential. For example, if a glacier forms away from the polar axis then the rotation axis would drift away from the centre of mass (as can be seen in the present day drift of the rotation pole towards Hudson bay, ~80°W (Mitrovica et al. (2005), Paulson et al. (2005)).

As this study uses GPS observations of surface deformation (with potential for future incorporation of GPS Earth Orientation Parameters (EOP)), any conclusions made will be based on the measurable surface deformation caused by GIA.

2.4.1 *Current GIA Estimation*

When completing any geodetic study it is vital that GIA is considered as either an error or a valid signal in the data. In this study I will treat GIA as a source of error which can be modelled and successfully removed from GPS observations.

To be able to accurately model the effects of GIA via surface observables, a sufficiently dense and long data set in tectonically stable areas is required. Only recently with the densification of GPS networks in Fennoscandia, see Baseline

Inferences for Fennoscandian Rebound Observations, Sea-level, and Tectonics (BIFROST) (Johansson et al. (2002)) and the North American network (Sella et al. (2007)) are there data sets that can begin to constrain the models using geodetic measurements. Antarctica still suffers from poor data coverage due to the cost and inaccessibility of GNSS campaigns which is why models of Antarctica GIA are currently poorly constrained. The POLENET project (www.polenet.org) is in the process of installing new permanent GNSS receivers in Antarctica and Greenland. It will be several years before any reliable estimates of secular velocities can be made from these receivers. Current GIA models comprise an estimated glaciation (ice) history and a modelled rheology of the Earth built from geological records. Several models have been produced over the last two decades; these models predominantly have been constrained to maximise the accuracy of vertical motions (Sella et al. (2007)). Dietrich et al. (2004) determines that GPS observations provide valuable insight into recent crustal movements in Antarctica; the results are limited however by the quality of the reference frame at the time and the limited tracking stations. Thomas et al. (2011) and Bevis et al. (2009) extends this research by using an extensive GPS network which shows that model GIA uplift is often over-estimated and that recent mass loss estimates may be systematically biased, with many being too high.

2.4.2 *Theoretical GIA Loading*

The Earth is deformed in response to a change in surface loading, the effect that a load has on the Earth is described by the load Love numbers, section (2.2) to develop a finite size time evolution of the surface loads. The total surface load is a combination of ice and ocean loads:

$$T\left(\Omega,t\right)=L_i\left(\Omega,t\right)+L_o\left(\Omega,t\right) \tag{2.11}$$

Where $t=\text{time}$, $\Omega=\text{location}$, L_i and L_o are the surface loads associated with changes to the weight of ice sheets and oceans respectively.

GIA models attempt to reconstruct the historical load due to ice and oceans in a single present day estimation. Below is a short introduction of the theory; for a comprehensive explanation please refer to Whitehouse (2009). The elastic term of the same theory can be applied to present day surface mass loading which could be the driver behind any present day secular deformation, if the load change is itself secular.

2.4.2.1 Ice Load

The theoretical variation to the thickness of ice $I(\Omega,t)$ can be described as:

$$I(\Omega,t) = D(\Omega,t) - D_0(\Omega) \tag{2.12}$$

Where $D(\Omega,t)$ is the thickness of ice at Ω on the Earth at the epoch t and $D_0(\Omega,t)$ is the thickness at the reference epoch. Using this information it is possible to estimate the ice load L_i:

$$L_i(\Omega,t) = \rho_i I(\Omega,t) \tag{2.13}$$

Where $\rho_i =$ ice density. By defining the ice load within a finite boundary then:

$$L_i(\Omega,t) = \sigma(\Omega) f(t) \tag{2.14}$$

Where $\sigma(\Omega) =$ spatial distribution of the load and $f(t)$ is the load time history.

2.4.2.2 Ocean Load

As the ice sheets increase and decrease in size this is accompanied by variation to global sea levels as a decreasing/increasing amount of water is stored as ice on land. At any ocean point $P(\Omega)$ for a chosen epoch t the sea level SL can be calculated by:

$$SL(\Omega,t) = r_g'(\Omega,t) - r_i'(\Omega,t) \tag{2.15}$$

Where $r_g' =$ distance between the Earth's CM and the instantaneous equipotential surface and $r_i' =$ distance between the Earth's CM and the surface of the solid Earth. By calculating the sea level then it is possible to calculate the change in sea level from a chosen reference epoch. The resulting change in sea level will change the ocean load, this can be calculated by:

$$L_o(\Omega,t) = \rho_o \Delta S(\Omega,t) O(\Omega) \tag{2.16}$$

Where $\rho_o =$ density of water, $O(\Omega) =$ ocean function and $\Delta S(\Omega,t) =$ change in sea level. Any change in sea level (2.15) results from a change in the volume of the ocean basin, variation to the surface topography caused by vertical displacements, alterations to the geoid or changes to the amount of water contained within the ocean basins. The spatial evolution of sea level is described by the SLE (Farrell and Clark (1976)). The SLE has become a fundamental part of studying GIA and surface mass loading in recent times

(Paulson et al. (2005)). In simple terms the SLE describes the evolution of the ocean level required to keep the sea surface at an equipotential, with the influx and draining of the ocean basins during the formation and collapse of glaciers. The movement of mass from continental water storage to the ocean basins is not always instantaneous; it is highly dependent upon the surrounding topography, for example in Antarctica it can be modelled as instantaneous but continental loads in North America have many stages of intermediate storage in lakes and river, and this effect must be accounted for in a step wise manner.

Any change to the mass of water in the oceans $m_i(t)$ causes a change in eustatic sea level over the entire ocean area, A_o, which can be identified by a distinct spatially varying fingerprint (Mitrovica et al. (2009)).

$$S(\Omega,t) = -\frac{m_i(t)}{\rho_o A_o} O(\Omega) \tag{2.17}$$

Following on from (2.11) the ocean load will change uniformly:

$$L_o(\Omega,t) = -\frac{m_i(t)}{A_o} O(\Omega) \tag{2.18}$$

2.4.3 *Construction of Models*

For a GIA model to be considered fully consistent then it must account for the self-gravitation of the deformation and loads, the variation of surface ice, the distribution of the oceans and the interaction between the load and Earth's rotation. This is achieved by creating a comprehensive ice history and Earth rheology.

The ice history is compiled by studying the locations of the historical ice fronts at selected time intervals from geological records (Whitehouse (2009)) and the ice thickness are also determined from geological records (Tushingham and Peltier (1991)). The amount of ice globally is assumed from the observed global relative sea level (RSL), as the amount of ice is proportional to RSL. Ice histories are an inversion of historic relative sea level histories and therefore rely upon the quality of these records; these are supplemented by estimations implied from geological observations and rely upon inferences made from these. The maximum extent of the glaciers can be determined well from geomorphological evidence; uncertainties occur when determining ice thickness and the advance of glaciers as most evidence is destroyed with glacial retreat.

Our knowledge of the Earth's rheology plays an equally important role as the ice sheet. Lateral changes in the lithosphere are predominantly influenced by the motions and compositional variations of the plates (Paulson et al. (2005)). Vertical changes are principally due to the variation of temperature as depth increases (Mitrovica and Forte (2004)). A rheological model attempts to describe how the mantle will respond to changes in local stress and strain. It is important to accurately parameterise the interior of the Earth as this will determine the behaviour of the rocks to loading. Due to the complexity of modelling most GIA models only vary the rheology in the radial direction. Initial values are taken from an Earth model, such as the Preliminary Reference Earth Model (PREM) (Dziewonski and Anderson (1981)), which provides a comprehensive Earth model calculated from seismological studies measuring the elastic properties of the Earth.

Mantle viscosity variations are strongly linked with depth and temperature gradients and it is this heat which enables the slow creep of materials. The models described above assume that viscosity varies only with depth, however this is incorrect, there are noticeable variations in the lateral viscosity profile of the Earth, which previously have not been modelled (Paulson et al. (2005)). The station rates interpolated from the GIA models represent the effects of glaciation as a single linear value, which is only true for the short observation period of geodetic systems. In reality the rate of adjustment is reducing from the initial unloading; there was a period of elastic adjustment initially during the unloading, after this there is an extended period of viscoelastic adjustment which rate decreases with time. The variation of mantle viscosity dictates the relaxation time of the mantle after the unloading event. The reader should also be aware of the effect of defining the depth of each layer in the Earth model, a thinner lithosphere will decrease the far-field influence of the local ice sheet, but increase the amount of localised vertical deformation (Paulson et al. (2007), Zhong et al. (2003)). Studies have shown that the assumed 120km lithospheric thickness over the British Isles is too great and that this should actually be reduced to 90km (Milne et al. (2006)).

The majority of trends expected due to GIA are in the vertical direction; however there is some discussion as to the magnitude of GIA in the horizontal plane (Kollo and Vermeer (2010), Teferle et al. (2009), Klemann et al. (2008), Milne et al. (2006), Paulson et al. (2005)). In places the glacial forebulge/hinge line

horizontal velocities can exceed the vertical (Sella et al. (2007)). There is evidence that current models underestimate this effect (Lidberg et al. (2010), Sella et al. (2007), Paulson et al. (2005)).

It is well documented that the strength of the GNSS system is in the determination of horizontal positions, with vertical estimates approximately three times less precise (Leick (1995)). For 1D GIA it is the vertical estimates which have the higher accuracy in comparison to the horizontal due to the construction of the Earth model (Whitehouse (2009)). It should be possible to harness the high precision of the GNSS measurements to evaluate the accuracy of the horizontal GIA estimates and highlight areas of potential mis-modelling (Dietrich et al. (2004)).

The choice of reference frame is important when defining the velocity caused by GIA; most GIA models use the CE for the definition of model geocentre. Alternative frames such as CM are used, these different models are comparable assuming that there is no on-going surface mass exchange, (Tamisiea and Mitrovica (2011)); however this is an incorrect assumption which introduces uncertainties in model comparisons due to incorrectly matching data and reference frame differences. These errors can be mitigated by ensuring that the origins of respective models match. Tanaka et al. (2011) states that for any surface loading the CM will move towards the load and the geocentre will move in the opposite direction; the resulting displacement will move the CM away from the load. After loading, the CM initially moves away from the loaded area before moving back towards the initial load centre. It is important to have a consistent and well defined reference frame origin. For a full description of origin choice see section (2.7.2).

Although in this study I am treating GIA as a source of noise in the data there is no absolute “true” model; in an attempt to mitigate this I will use a suite of 1D GIA models and compare the results to see which models are able to best model deformation in the vertical, horizontal and a combination of both components.

2.4.4 *Global Models Used in Thesis*

I have available two families of global GIA models, Peltier’s ICE5G ice history with VM2 and VM4 Earth rheologies (Peltier (2004)) and Schotman’s two models based in ICE3G ice history (Schotman et al. (2008), Schotman and

Vermeersen (2005)). These models were provided by the authors as part of a call by the IERS Special Bureau for Loading (SBL) (http://www.sbl.statkart.no.project/pgs, accessed June 2009, now defunct) and are presented below in a summarised form, Table 2. Displacements are provided as 3 dimensional vectors on a specified regular grid. These models have various parameters settings see below. The expected displacement of each model is achieved by convolving the ice history, section (2.4.4.1) with the Earth model, section (2.4.4.2).

Table 2: Global GIA models

Author	Ice History	Earth Model
Peltier	ICE5G	VM2
Peltier	ICE5G	VM4
Schotman	ICE3G	Modified PREM
Schotman Alternative	ICE3G	Modified PREM

2.4.4.1 Ice Histories

The ice history of a GIA model describes the extent and thickness of glacial ice from the LGM until the end of the glacial period. These are provided as a regular global grid at a specified time step. Both of Peltier's models use his ICE5G ice history which covers 122-3kyr BP.

- Ice history covers 122-3kyr BP (Peltier (1996), Peltier (1994))
- Maximum ice thickness 3km around Hudson Bay (Peltier (2004))
- Major deglaciation ends at 3kyr BP (Peltier (2004))
- 121kyr-LGM set at LGM extent with only height varying (Peltier (2004))

Schotman began with the ICE3G history (Tushingham and Peltier (1991)) and made the following modifications:

- LGM occurring at ~21.5kyr BP
- Increase ice volume by ~20% at LGM
- Linear glaciation phase of 90kyr BP, beginning at 120kyr BP
- Constant ice volume from 30-22kyr BP
- Major deglaciation ends 4kyr BP
- No rotational feedback

Although deglaciation has an absolute point in these models this does not mean that the Earth is ice free, however the deglaciation point is an indication of a halt in significant mass loss. There will be continual small changes in the amount and location of ice on the Earth but these are relatively small and therefore not included in the ice histories mentioned above. However these small changes are the focus of this study and will be discussed later.

2.4.4.2 Earth Model

The Earth model in a GIA model describes the elasticity, viscosity and internal thickness of the Earth at a regular spatial interval. Peltier (2004) provides two Earth models, VM2 and VM4, convolved with the ICE5G history and Schotman Schotman and Vermeersen (2005) provides two alternate models (Table 2). All of the Earth models used assume that the viscosity of the Earth only depends upon depth i.e. there is no lateral variation. Both of Peltier's models are far too detailed to cover in one table, with viscosity profiles at 162 irregular steps from the core to the lithosphere (Figure 7, summarised in Table 3).

Table 3: Brief overview of VM2 and VM4 Earth models, for a full description please see www.sbl.statkart.no/projects/pgs/authors/peltier. The layer depths stated are approximate changes of viscosity bands.

Layer/Radial Bands(km)	Thickness (km)	VM2 Viscosity (Pas)	VM4 Viscosity (Pas)
Lithosphere/ $6371-6281$	90	1×10^{43}	1×10^{43}
Upper Mantle & Transition Zone/ $6281-5700$	579	$1.5-7\times10^{20}$	$3-7\times10^{20}$
Lower Mantle/ $5700-3485$	2215	$1-3.6\times10^{21}$	$9\times10^{20}-3.2\times10^{21}$
Core/ $3485-0$	3485	1×10^{-43}	1×10^{-43}

Table 4 describes the values used by Schotman's primary GIA model; this is a very basic stepwise model which only defines the viscosity at 5 distinct bands in the Earth.

Table 4: Schotman Earth model

Layer/Depth Bands (km)	Thickness (km)	Viscosity (Pas)
Lithosphere/ $6371-6256$	115	1×10^{50}
Upper Mantle/ $6256-5791$	285	5×10^{20}
Transition Zone/ $5971-5701$	270	5×10^{20}
Lower Mantle/ $5701-3480$	2221	5×10^{21}
Core/ $3480-0$	3480	1×10^{-43}

There is on-going debate to the true viscosity; Schotman provides an alternative Earth structure. The alternative Earth structure varies from

Table 4 by:

- A thinner lithosphere 98km
- Uniform mantle viscosity $1x10^{21}$Pas

The variation in the lithospheric thickness will dictate the spread and depth of deformation and the increase in viscosity will delay the characteristic time scale. Schotman notes that his changes are not warranted by any data observations but they are provided as source of comparison.

Peltier's extensive Earth models (Peltier (2004)) should provide a much more precise description of the response of the Earth to glaciation due to the greater detail of layering. These different rheologies are displayed in Figure 4.

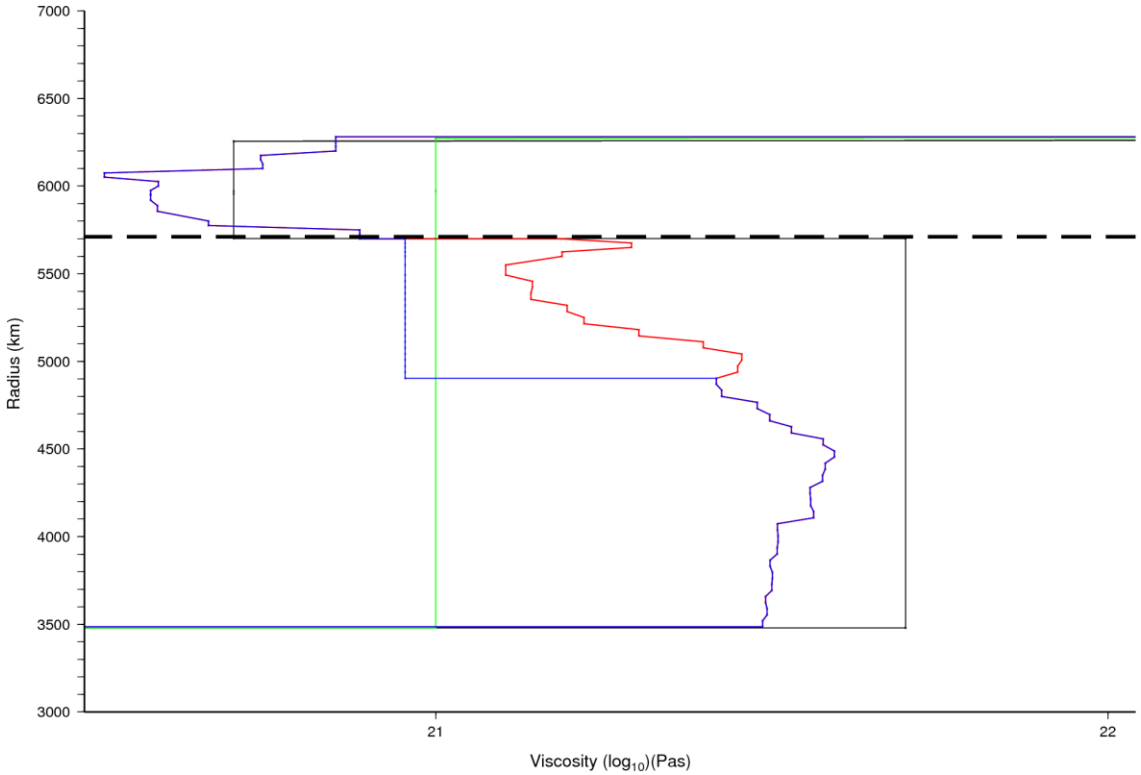

Figure 7: Viscosity profiles, VM2 (red), VM4 (blue), Schotman (black) and Alternative (green). Dashed black line separates the UM (above) and the LM (below) on the 660km discontinuity.

Below (Figure 8-Figure 9) are representations of the vertical and horizontal displacements for each of the GIA models considered.

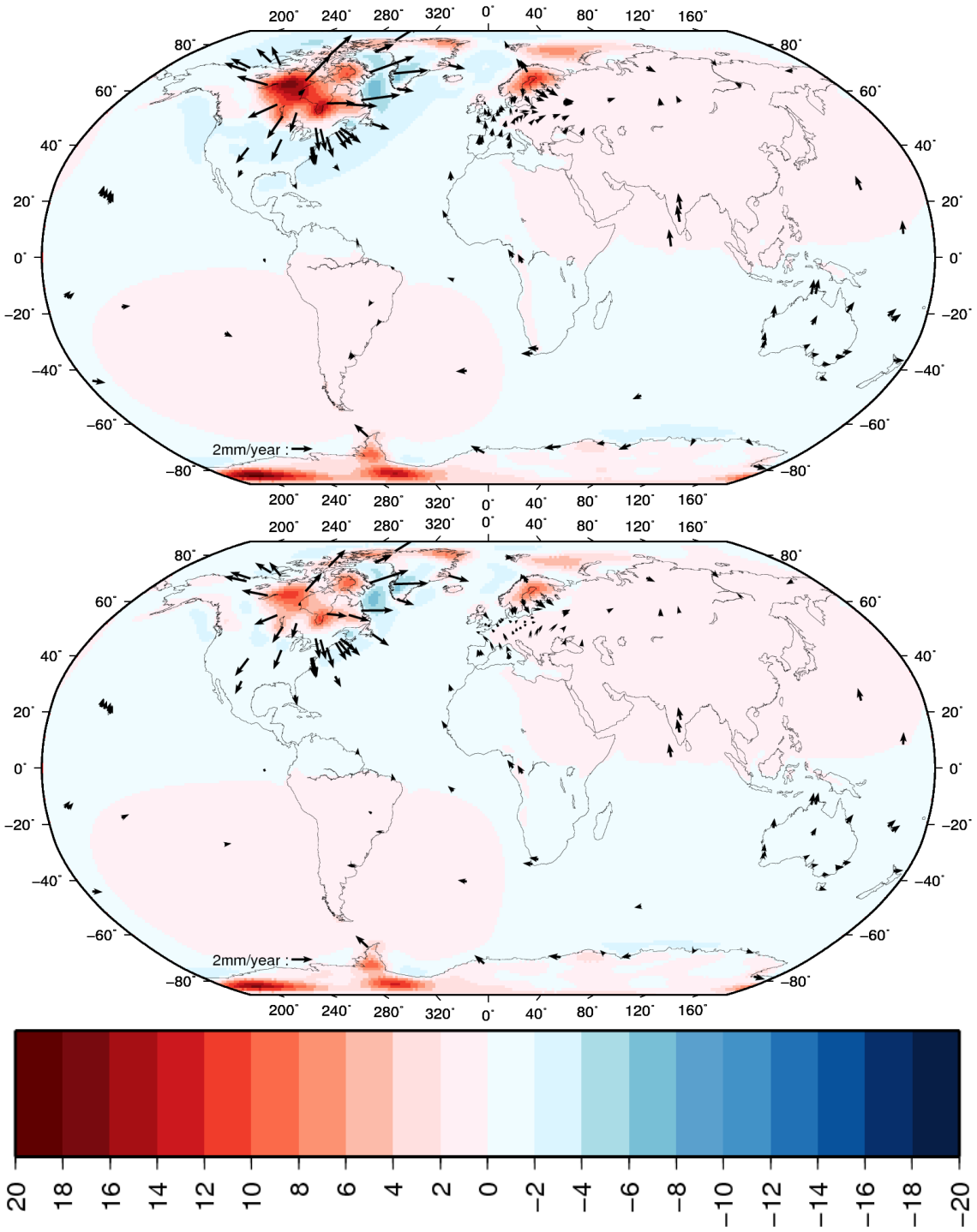

Figure 8: Global GIA models, horizontal (arrows, at GPS sites) and vertical (colour) rates mm/yr, top ICE5G-VM2, bottom ICE5G-VM4.

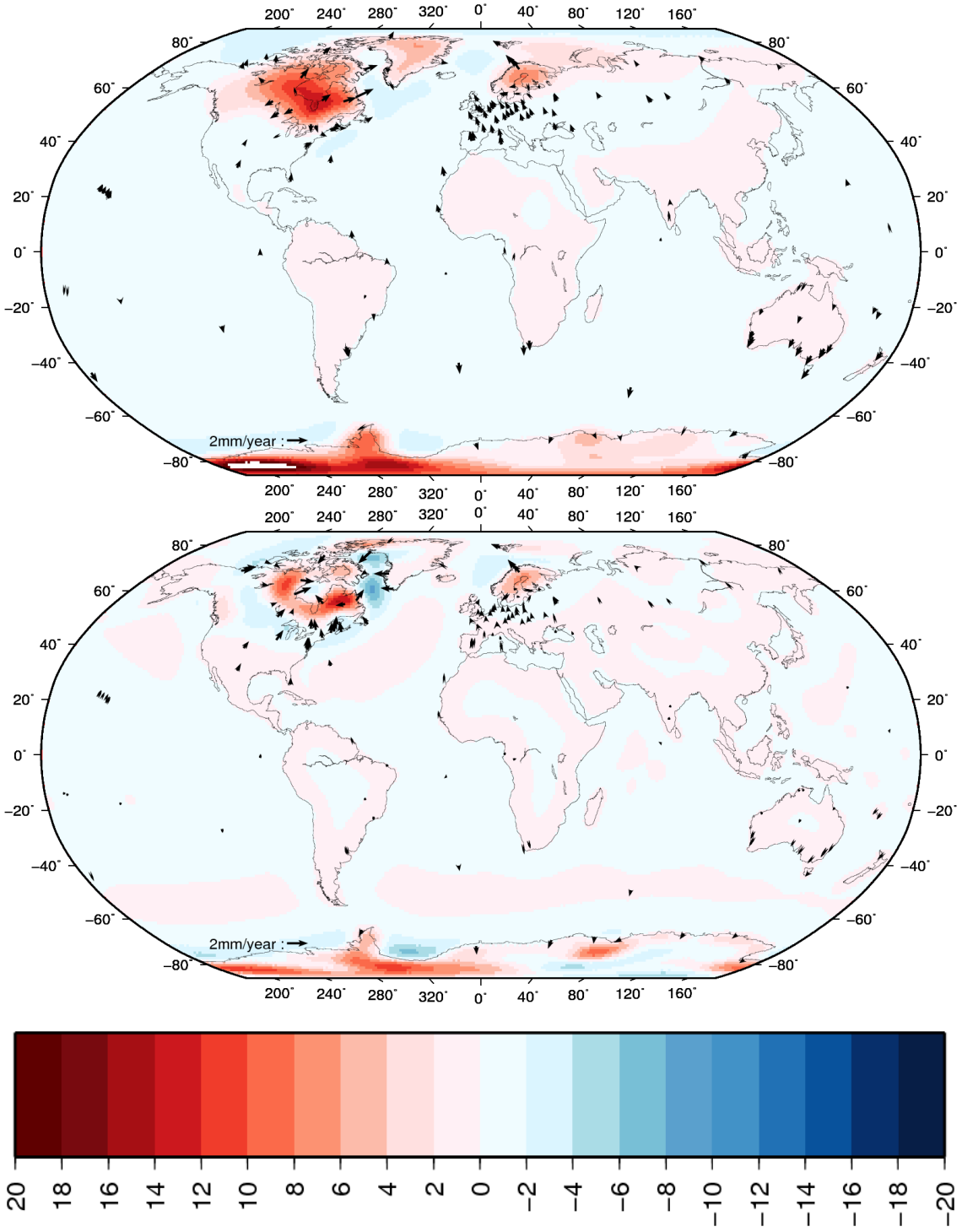

Figure 9: Global GIA models, horizontal (arrows, at GPS sites) and vertical (colour) rates mm/yr, top Schotman, bottom Schotman alternative

These models (Figure 8 and Figure 9) are all plotted to the same scale; although there are differences to the magnitude of uplift the spatial pattern is generally in agreement. The centres of uplift are located in the areas of the old ice domes (Peltier (2004)); these are around Hudson Bay in North America, the Gulf of Bothnia in Fennoscandia and near to the Antarctic Peninsula. The largest differences in the vertical velocities occur in the areas of greatest uplift,

most noticeably in Antarctica and Greenland. The main cause of differences witnessed is the due to the choice of mantle viscosity profiles which leads to different relaxation periods. The current estimated relaxation times are 3.4kyr in SE Hudson, 4.2kyr in Gulf of Bothnia (Peltier (2004)).

Visual examination of the pattern of horizontal velocities highlights differences between the models that are much greater than for the vertical velocities. The horizontal velocities are significantly smaller than the vertical rates but these can still produce substantial variations to velocity estimation.

Each of the figures shown in section (2.4.4) are the different models used in this study. Horizontally both of Peltier's models (Figure 8) show a distinct secular deformation radiating away from the Hudson Bay area which is not present in either of the Schotman models (Figure 9). These differences will be discussed in section (5.1.4).

2.4.5 *1D versus 3D GIA Modelling*

Lateral heterogeneities in the structure of the Earth result from plate tectonics, temperature gradients in the lithosphere and compositional changes in the mantle (King et al. (2010)). The main focus of 1D models has been to best-fit the vertical deformation with little regard to the horizontal (Sella et al. (2007)), yet the horizontal response is just as sensitive to the variations in the viscosity of the upper mantle (Sella et al. (2007)). It is however possible that improvement in 3D velocities will improve understanding of both the ice history and Earth models. Over the last decade, studies have been investigating the effects of laterally heterogeneous (3D) Earth models, i.e. viscosity varies with depth and location (Davis et al. (2008), Klemann et al. (2008), Kendall et al. (2006), Latychev et al. (2005a), Paulson et al. (2005)). It should be noted that during processing no 3D model was available for comparison but below is a discussion of the potential influences of using a 3D model instead of the standard 1D rheology.

3D rheological models are formulated using seismic shear wave velocities which can be converted via a velocity to density scaling algorithm (Latychev et al. (2005b)). These values are converted into a temperature field which it is assumed that the viscosity field is dependent upon. Latychev et al. (2005b) calculated that for North America 50% of model elements have a viscosity ~1 order of magnitude around the Lower Mantle (LM) value of $5x10^{21}$Pas and 95%

are within ~2 orders of magnitude. For the whole Upper Mantle (UM) the viscosity value is slightly more limited (factor of ~2 in log-space), but with are large variations in the upper UM (the asthenosphere).

By varying the thickness and viscosity of the different elements and introducing lateral heterogeneities different authors have been able to produce a variety of 3D Earth models (Zhong et al. (2003), Kaufmann and Wu (2002), Kaufmann et al. (2000)). The standard 1D reference model used is generally a variation on a spherically symmetric, viscoelastic Earth using the elastic structure of PREM (Dziewonski and Anderson (1981)), with an elastic lithospheric thickness of 120km, UM viscosity of ~$5x10^{20}$Pas and LM viscosity of ~$5x10^{21}$Pas, convolved with an ice history, e.g. ICE3G ice history (Tushingham and Peltier (1991)), this produces rates similar to those shown Figure 8.

3D models vary the thickness of the lithosphere or the viscosity of the mantle; both have their own distinct effects upon GIA rates. Latychev et al. (2005a) introduces large scale variations to the lithosphere, (220km – 70km) but with an weighted average of 120km. Radial rates can be affected by as much as ±2mm/yr with horizontal motions spreading throughout the continents, perturbing rates by ~1mm/yr. Davis et al. (2008) produced four Earth model scenarios following work from Latychev et al. (2005b) convolved with the ICE5G-VM2 history (Peltier (2004)).

- 1D-VM2 elastic lithosphere of 120km and radial profile from VM2 Peltier (2004)
- 3D-LT global variation of lithospheric thickness (adapted from Zhong et al. (2003))
- 3D-UL UM viscosity and lithospheric thickness variation
- 3D-LM LM viscosity variation

Davis et al. (2008) found that there is very little difference between the 1D-VM2 and 3D-LT models, whereas the 3D-UL model shows a net reduction of ~0.5mm/yr between 37°N-43°N from the 1D-VM2 model and the 3D-LM model produces a significant but constant shift (~0.3mm/yr) to values compared against the 1D-VM2 values.

Paulson et al. (2005) postulated whether localised data would be sufficient to infer mantle viscosity or an accurate description of the Earth's structure can be determined from a single localised observation such as GIA rates. Using a 3D

model with 76800 lateral elements (dimension ~80km) and 48 radial elements (dimension ~20-110km) and a 1D model of lithospheric thickness, 120km, UM viscosity of 10^{21}Pas and LM viscosity of $2x10^{21}$Pas convolved with ICE3G, Paulson et al. (2005) concluded that GIA rates depend most upon the viscosity of the mantle below the load. If the observations are in made in the same place as the load (e.g. GPS) then the 3D model agrees closely with the 1D model. Localised observations in the far-field of a deglaciation area, (e.g. sea-levels along eastern seaboard) cannot be explained by the 1D as accurately as the 3D model for the Laurentian deglaciation. For truly global observations such as GRACE or $\dot{J}_2$, results lean towards a best fit from a 3D model but with a heavily weighted structure beneath the local load (Paulson et al. (2005)). Alternatively Sella et al. (2007) used a network of 223 GPS sites located on the rigid interior of the North American plate; by removing an estimate of rotation due to plate motion the residual horizontal velocity was assumed to be due to GIA. Observations of residual velocities generally match published GIA model rates, but with some differences; it is noted that there may be a small amount of bias to the horizontal velocities caused by the absorption of GIA rates into the plate rotation estimate.

It is not only the influence on GIA rates that are affected; there is an additional influence upon the determination of plate rotation. Klemann et al. (2008) defined various UM viscosities with a constant LM value of $1x10^{22}$Pas, with an elastic lithosphere of various thicknesses. Comparing the location and rotation rate of the North American Euler pole from ITRF2005 with 1D and 3D models, Klemann et al. (2008) concluded that the induced motion is ~10% of the plate motion and is greater than the precision of the plate motion determination; this is summarised in Table 5.

Table 5: Effect of 1D and 3D GIA model on North American Euler pole and rotation rate (taken from ITRF2005)

Case	Longitude (°)	Latitude (°)	Rotation °/Myr
ITRF2005	-87.4±0.6	-4.3±0.9	0.192±0.002
1D	+1.1	-0.0	+0.002
3D	+2.4	+3.6	+0.008

2.4.1 *Observations of GIA*

After many years of study using 1D GIA models there is a general consensus that a 3D model is required for GIA studies, however the exact detail of a 3D model and the influence its adoption will have are still cause for research. For 3D models there is evidence for strong influence of lateral viscosity changes on uplift, present day velocities and gravity anomalies. Lateral mantle heterogeneities have been shown to have a large effect upon predicted GIA rates (Wang et al. (2008), Sella et al. (2007), Steffen et al. (2006), Gasperini and Sabadini (1990), Gasperini and Sabadini (1989)) and lithospheric thickness variation determines the radial extent of an ice sheet and its influence in the far-field (Latychev et al. (2005a), Chen and Wilson (2003)). Whitehouse et al. (2006) determined that for Fennoscandia the differences between 1D and 3D model values exceed the horizontal observational uncertainties, with lateral variations in both the near- and far-field in the lithosphere and UM having a big effect upon horizontal velocities.

The change from 1D to 3D can potentially cause a 7mm/yr difference vertically and 1-2mm/yr horizontally (Latychev et al. (2009)). However it is noted that these 3D models still require study e.g. BIFROST observations still best fits a 1D model with 2-7mm/yr uplift differences for various 3D models (Steffen et al. (2006)). Davis et al. (2008) concludes that the model rate change from 1D to 3D is significant enough to warrant further investigations into lateral variations of Earth structure. Although 3D models are likely to make some difference to my results, as there were none yet available publically I have had to use the more readily accessible 1D models. Paulson et al. (2005) recommends that for localised observations in-situ to the load 1D≈3D model accuracy, otherwise a 3D model would provide more realistic values. By using a suite of 1D models it should be entirely possible to determine a good ball park estimate of the influence and removal of GIA from GPS velocities for studying present day secular mass rates.

2.5 Tectonics

One of the main driving forces in the Earth system is the movement of the tectonic plates. It is assumed that the tectonic plate move with a regular velocity over millions of years (DeMets et al. (2010)). To fully understand present day secular loading it is vital to precisely estimate and completely remove any secular motion due to the motion of the tectonic plates. A good understanding of the structure of the Earth is therefore required, section (2.1). Plate tectonics is concerned with the two outermost layers, the lithosphere and the asthenosphere. The lithosphere is able to move over the asthenosphere due to the viscous properties of the lower layer. However the relative movement of the lithospheric plates is hampered by frictional forces at the plate boundaries (Silverstein et al. (2009)). Release of lithospheric friction occurs via brittle deformation in the form of an earthquake (Silverstein et al. (2009)). If the locations of these earthquakes are plotted, Figure 10, they delineate the positions of the plate boundaries. The plate boundaries encircle an area of lithosphere and these enclosed areas have become known as the tectonic plates. Although there is not a consensus as to the exact number of plates it is believed that there are approximately 15 major plates (Altamimi et al. (2007)) and several minor/micro plates (DeMets et al. (2010)). Argus et al. (2011) develops a model, MORVEL, modelling 25 major and minor plates accounting for ~95% of the Earth surface but also including 31 micro plates from Bird (2003) which accounts for a further ~2.8% of the surface. Figure 10 plots the locations of major earthquakes which delineates the major plates (labelled).

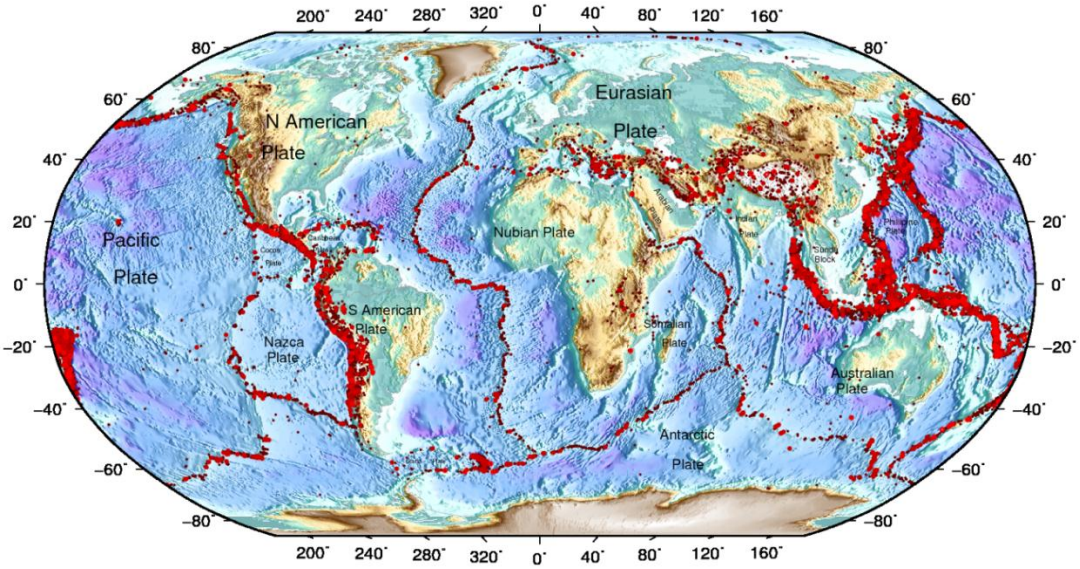

Figure 10: Location of Earthquakes with magnitude of greater than 5 taken from http://www.ncedc.org/cnss/

Tectonic lithosphere includes continental crust, oceanic crust or a mixture of both. This study makes the assumption that the tectonic plates are rigid (Gordon and Stein (1992)) and the interiors do not deform readily and the only seismic deformation occurs at the plate boundaries. There is some evidence of intraplate deformation. Banerjee et al. (2008) found that there is potentially 4-7mm/yr of southern motion on the Shillong plateau on the north east of the Indian plate, but the majority of this falls within the plate boundary deformation zones. Studies of strain in central and Eastern US show a potential 1mm/yr recorded by local strainmeter observations (Calais (2012)) but this has proven difficult to detect via GPS observations. Calais et al. (2010) find there is no appreciable deformation in the New Madrid Seismic zone on the Eastern seaboard of the US. Nocquet et al. (2001) find that the ITRF97 velocities of several European stations fit a rigid plate hypothesis, however they also identified a northward motion of sites located in Italy, suggesting internal deformation of the Adriatic block and a significant westward motion of the western extreme of Europe of ~1-2mm/yr relative to central Europe; however this interpretation is limited by the number of sites and accuracy of the ITRF1997. Although there is evidence of intra-plate earthquakes these should have a very little impact upon this work as the majority of events are very small and would be difficult to detect with GPS observations, i.e. negligible velocity biases.

At the plate boundaries the tectonic plates are subjected to the plate boundary processes, which can be destructive, constructive or transform faults (Kearey et al. (2009), Silverstein et al. (2009)). The driver behind the movement of tectonic plates is convection cells in the mantle; these cells occur as hotter less dense materials rise up from deep in the Earth displacing the cooler materials which moves aside before sinking, where it then heats up and continues the cycle (Kearey et al. (2009)).

2.5.1 *Plate models*

There are two methods used to estimate the motions of the tectonic plates: the first uses geodetic observations and the second uses geological measurements. With the rapid development of geodetic systems over the last two decades there has been a large number of new plate estimates published (Argus et al. (2010), Altamimi et al. (2007), Sella et al. (2002), Lavallee (2000),

Cretaux et al. (1998), Larson et al. (1997), Argus and Heflin (1995)). Over time, as data spans increase, more detailed models estimating a greater number of plates become available which helps to increase the overall accuracy of the solution. The second method is geological models (DeMets et al. (2010), Demets et al. (1990), Gripp and Gordon (1990)) which use geological records such as earthquakes slips (decadal – centuries), transform rates (millennial) and spreading rates (~3.16Ma) to produce an averaged estimation of the motion of the plates.

There is general agreement between geodetic models and geological models, such as NUVEL-1A, within 95% confidence. However there are uncertainties in both the geodetic observations and the geological models, i.e. omission of some minor plates or assumption that there have been no changes to plate motions over the last 3 Ma (DeMets et al. (2010), Sella et al. (2002)) which is unlikely. Sella et al. (2002) estimate that the decade of geodetic observations is representative of plate motions for the previous 10,000yrs.

The continual movement of the tectonic plates constantly changes the location of the tectonic plates in relation to one another. Any plate model attempts to describe the relative movements between plates as well as the absolute movements of individual plates. There is no method to determine the absolute orientation of the Earth's crust in inertial space as the movement of the tectonic plates is not the only motion of the Earth's crust (Steinberger and Torsvik (2008)) and therefore the absolute location of each tectonic plate is unknown; however it is possible to define an arbitrary orientation such as the No Net Rotation (NNR) model (Argus and Gordon (1991)). NNR-NUVEL-1A is an example of a NNR reference frame. NNR defines that the summation of all the plate velocities yields zero over the Earth's surface (Argus and Gordon (1991)). By aligning geodetic models to a NNR geological model it is possible to estimate the "absolute" Euler pole of the tectonic plates. As a by-product of this study I will produce a geodetic plate velocity model which I can compare to other models, section (5.2.1).

2.5.2 *Euler Poles*

To enable any examination of plate tectonic movements it is important to be able to describe how each plate moves across the surface of the Earth. Euler's rotation theorem states "Any displacement of a rigid body, such that the

geometry of the rigid body remains unchanged, is equivalent to a single rotation about a chosen axis that runs through the fixed point" (Palais et al. (2009)). Using this theory it is possible to model the movements of the tectonic plates around a series of fixed points (poles) on the surface of the Earth.

With the development of GPS and other GNSS it is possible to measure the velocity of the tectonic plates from a few years of continuous data at tracking stations (Kearey et al. (2009), Johansson et al. (2002), Lavallee (2000), Larson et al. (1997)). Stations that are attached to the rigid interior of a plate will have an angular velocity owing to the movement of the plate; it is therefore a simple process to estimate the common rotation component of the plate for each station. The location of the Euler pole is at the intersection of the great circles perpendicular to the velocity of each of the stations on the plate. As only the station's horizontal component is used in the estimation then a minimum of two stations are required to provide enough information to estimate the Euler pole. The precision of estimation is improved by both increasing the number and distribution of stations on a plate (Cretaux et al. (1998)).

2.5.3 *Estimation of Euler Poles*

The determination of the absolute Euler pole location plus the angular velocity of the plate can be used to determine the plate velocity component of each station; as the distance of the station from the pole increases then the rotational velocity of the site increases. The absolute Euler pole is (Altamimi et al. (2007)):

$$\Omega_A = \omega e \tag{2.19}$$

Where $\omega = |\Omega_A|$ is the estimated rotation rate and e is the unit vector along the direction of the rotation axis. For any station at position r on plate A the velocity v can be calculated using the vector product:

$$v = \Omega_A \wedge r \tag{2.20}$$

The associated speed $|v|$ can also be calculated using the station's latitude φ:

$$|v| = \omega R \sin\varphi \tag{2.21}$$

The motion of any plate is dependent upon the angular velocity described in (2.19); this is known as the Euler vector. The unit vector e can be computed from the estimated Euler pole, this represents the Euler pole's rotation axis between the geocentre and the Euler pole location on the surface.

$$e = \begin{pmatrix} \cos\varphi\cos\lambda \\ \cos\varphi\sin\lambda \\ \sin\varphi \end{pmatrix} \tag{2.22}$$

This theory applies to estimates on a spherical Earth, however the Earth is not a sphere and the best approximation is an ellipsoid. Lavallee (2000) determined that the difference between the two for a tectonic velocity of 100mm/yr never exceeds 0.02mm/yr. This error is well below the level of noise and can therefore be disregarded.

It is a very simple process to determine the relative velocities between two plates by holding the velocity of one plate stationary and measuring the relative motion of the second plate (Cretaux et al. (1998)). This method is useful for estimating global plate circuits and fulfilling the NNR condition of the reference frame (Kreemer et al. (2006), Argus and Gordon (1991)). To calculate the relative rotation of plate A with respect to plate B we can use:

$$_A\Omega_B = \Omega_B - \Omega_A = -_B\Omega_A \tag{2.23}$$

Ω_B and Ω_A from (2.19). Although it is very simple to estimate the relative motions of the plates, it is not possible to directly calculate the absolute Euler poles from observations so all studies rely of the accuracy of the reference frames which employ a NNR condition (e.g. ITRF2005, NNR-NUVEL-1A) (Altamimi et al. (2007), Argus and Gordon (1991)).

2.5.4 *Forming the Model*

A least squares system can be formed for each station m_i on an individual plate j with an estimated velocity $\dot{x}_j$ and the modelled residual v_j. The linearised form looks as:

$$\dot{x}_j = D_i\Omega_j + v_j \tag{2.24}$$

Where D_i is a 3×3 rotation matrix. This can be solved for p plates (Davies and Blewitt (2000)). This model only accounts for the common horizontal motion of the plate as vertical motion is assumed to be zero. There will be vertical motion input into the system caused by GIA and surface mass loading, this will not affect the estimation but it will affect the calculated unit variances.

2.5.5 *Station Classification*

The stability of the local area around the GPS tracking station is crucially important to the robustness of the station coordinate time series used in this study. It is assumed that the interior of any tectonic plate can be modelled as a rigid body (Gordon and Stein (1992)). Any station which lies within ~100km of plate boundary tends to show signs of non-rigid motion, most likely caused by the build-up of seismic strain (Kreemer et al. (2003)).

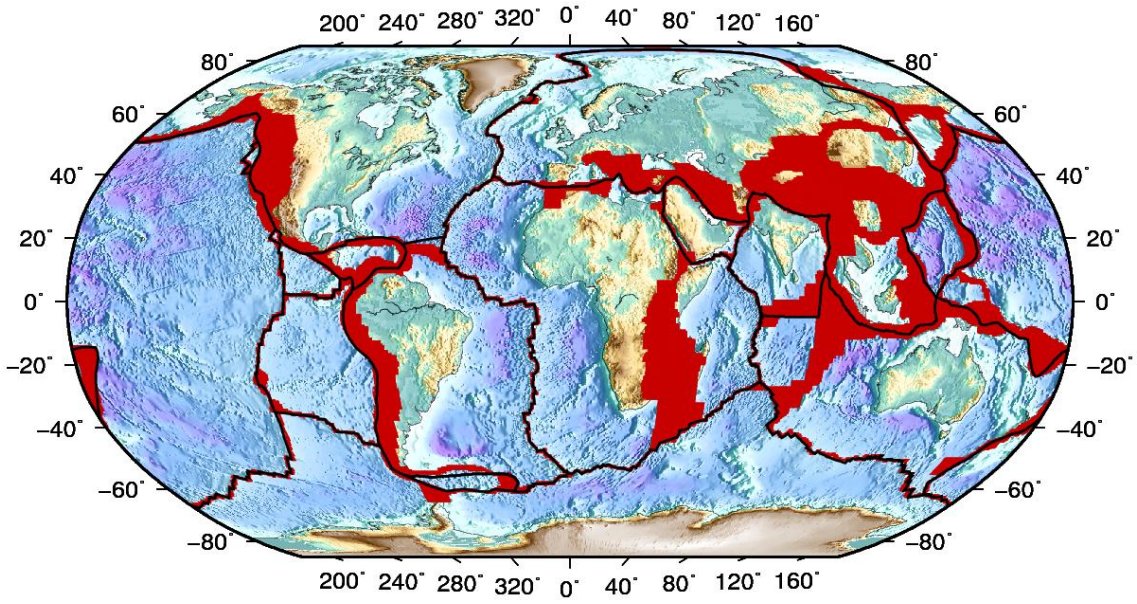

Figure 11: Estimated plate deformation zones in red with estimated plate boundaries in black (Kreemer et al. (2000)).

Although the actual plate boundaries shown in black in Figure 11 are very narrow, several of the deformation zones shown in red spread over large areas around the plate boundaries. Kreemer et al. (2000) determined that for a globally dense and evenly distributed station network that an individual station's classification does not matter greatly when attempting to calculate a global plate circuit. To date no study has been able to implement a network of sufficient density to be able to use deformation zone stations in global circuit studies. Even with the increased number of reprocessed stations used in this study it still falls short of the globally dense network stated by (Kreemer et al. (2000)). Therefore it is of paramount importance that the distinction between stable and boundary sites is made so that the sites used in the plate velocity estimations are free from plate boundary discontinuities.

Although it may be possible that a boundary site has a sufficient period of clean data to precisely estimate an accurate plate rotation it cannot be included with any confidence due to post-seismic deformation or pre-seismic strain build up.

In this study once I have selected the stations which fulfil criteria of data span (>2.5 years) (Blewitt and Lavallee (2002)) and number of observations (>104 observations) (Lavallee et al. (2006)), I will reject any sites that are likely to be contaminated by plate boundary processes (section (4.2.2)).

2.6 Expected Present-Day Mass Changes and their Observations

The focus of the discussion above has primarily been on secular changes due to GIA and tectonics and their influence upon GPS observations. However there are other geophysical causes which could be a source of secular mass change and other geodetic systems which can observe this.

2.6.1 *Predicted Mass Changes*

On a secular time scale the main areas of Present Day Mass Trends, (PDMT), are areas of large scale glaciation (e.g. Greenland, Alaska and Antarctica (Velicogna (2009), Wouters et al. (2008), Luthcke et al. (2006))), river basins or groundwater storage, for example in the Congo (Crowley et al. (2006)), India (Tiwari et al. (2009)) and the Amazon (Chen et al. (2009b)).

2.6.2 *Previous Studies of Surface Mass Loading*

Using very low degree spherical harmonics, Blewitt et al. (2001) found that winter loading from surface fluids induces a degree-one deformation of the Earth, compressing the poles by up to 3mm and expanding the equator by approximately 1.5mm. This deformation is reversed with the changing of the seasons. Wu et al. (2002) argue however that higher degree ($n \geq 2$) signals could alias into the low degree coefficients due to the uneven network distribution. Again using spherical harmonics but with an a priori model of atmosphere, oceans and CWS to aid ocean mass constraint Wu et al. (2003) determined that inversion of GPS displacements can accurately determine features of large-scale seasonal mass variation. This method demonstrates that GPS observations agree with the models in Eurasia, North America and Australia but disagree within South America, Africa and Antarctica, Wu et al. (2003) suggested that this is due to model deficiencies and poor coverage of GPS stations which are unable to constrain local mass distribution in the inversion process. Using forward modelling, van Dam et al. (2001) compared GPS displacements corrected for atmospheric pressure with a model of continental water storage. Their findings were that although the GPS observations contain

systematic errors, they also showed real seasonal and secular geophysical signals due to continental water loading.

Wu et al. (2010) is the stand out study which attempts to predict PDMT using GRACE, Geodetic Observations (SLR, VLBI and GPS), the ECCO Ocean Bottom Pressure (OBP) model and an a priori GIA model (ICE5G with VM2 and IJ05). This is the closest alternative method to the one described in this thesis. Wu et al's methods follow a different line of investigation in that they attempt also to estimate the GIA contribution, but ultimately aim to end up with an estimate of secular PDMT as we do. Using the above data sets, Wu et al. estimate the PDMT, (Figure 1 of Wu et al. (2010)); the results show mass loss in areas including South and West Alaska, coastal Greenland, Svalbard and West Antarctica (Amundsen Sea and Whillans Ice Stream) with mass gain in the Greenland interior and West Antarctica (Kamb Ice Stream). Wu et al. presented two mass change values, one which utilises all available data with a GIA model estimated and atmospheric mass re-added, and a second value which is solely based on GRACE with an a priori GIA correction; these values will be compared with the NC1 predicted solution, section (6.5). In addition to the PDMT values, Wu et al also attempts to calculate the contribution to observations due to GIA (Figure 2 of Wu et al. (2010)) using the computed covariance of a suite of models to constrain the bounds of the solution about an a priori model, which highlights two significant areas of disagreement between the a priori GIA model and the estimated GIA model. This suggests new evidence for additional historic ice over Greenland (additional net past ice accumulation) and significant ice melt over Alaska (effects of little ice age (Larsen et al. (2004))) which are not present in the ICE5G-VM2 model; however, no physics-based GIA modelling is done to confirm this possibility and is controversial (Olaizola et al. (2011)).

In conclusion Wu et al suggests that the kinematic method allows for the simultaneous prediction of PDMT and GIA but the inversion is sensitive to the GIA and atmospheric model used as well as the GRACE data period, especially for the low degree harmonics. These results suggest that present GIA models contain large uncertainties in previously identified areas of weakness, e.g. Antarctica, with values overstated in Greenland and significant differences over Alaska.

The above studies utilise observations from GPS and with the newly released IGS reprocessing campaign GPS should be able to provide new insight into present mass change dating back to the early 1990s. However there are other systems which can provide independent observations of global mass change.

2.6.3 *SLR*

Satellite Laser Ranging uses lasers to measure the distance from the surface of the Earth to orbiting satellites fitted with special reflectors. Measurements have been calculated with millimetric accuracy and have been used to determine accurate orbits and variations to the Earth's gravity field due to mass redistribution. SLR is the primary technique for determining and monitoring the geocentre and its variations. SLR has been active for over three decades now and has been used in numerous studies of the solid Earth and surface mass loading (Chen and Wilson (2008), Altamimi et al. (2007), Pearlman et al. (2005), Bianco et al. (2001)). The SLR system provides accurate observations as most of the satellites orbit at higher altitudes, this gives them longer life and are less sensitive to high degree spherical harmonic gravity changes (Chen and Wilson (2008)).

SLR has been used to infer changes in the low degree spherical harmonic coefficients of the Earth's gravity field for many years, particularly $J_2, \dot{J}_2$ (Earth oblateness). Long term negative trends have traditionally been attributed to the mass redistribution due to GIA (Mitrovica and Peltier (1993)). Yoder et al. (1983) showed that the $\dot{J}_2$ could be well determined from SLR observations at -2.5 to -3x$10^{-11}$$yr^{-1}$, this value has been confirmed by more recent studies (Chen and Wilson (2003), Cox and Chao (2002), Devoti et al. (2001)). This calculated rate was consistent until 1998 when several authors noted that the trend abruptly changed to a positive value (Earth becoming less oblate) (Chen and Wilson (2003), Cox and Chao (2002), Dickey et al. (2002)) which continued until 2002 where the trend shifted back to its original rate. This became known as the J_2 anomaly and suggested a large shift in mass redistribution able to mask the signal due to GIA. Cox and Chao (2002) suggested that this anomaly was due the El-Nino/Southern Oscillation, ENSO, affecting the ocean mass, continental water storage, the hydrological cycle and snow and ice sheets. Dickey et al. (2002) estimated that the ocean could account for ~1/3 of the J_2 anomaly and

suggests that the remaining redistribution could be caused by sub-polar melt. Chen and Wilson (2003) produced a combined model of the oceans including altimetry, OBP and the ECCO, using an observation window of 1979-2002 and accounting for GIA by removing a constant trend of -2.8×10^{-11} (from Cox and Chao (2002)) and concluded that the J_2 rate anomaly was triggered by the ENSO event and continued for several years due to the long relaxation time versus climatic and sea surface temperature observations. Observations of higher degree zonal harmonics J_3 and J_4 showed some small interannual variation but no large shift is present (Cox and Chao (2002)). Chen and Wilson (2008) used SLR amongst other methods to observe the low degree harmonics, for the degree 2 harmonics, all methods showed interannual variations with good agreement. However, Benjamin et al. (2006) suggested that this apparent anomaly may be due to mismodelling of the 18.6 year solid Earth tide in the SLR analysis. Lavallée et al. (2010) showed that using a loading model accounts for the anomaly in GPS observations but still leaves a residual in SLR observations which would suggest systematic SLR errors in J_2. It is not only long term trends of the gravity field (GIA) which affect SLR observations. Moore et al. (2005) used 30 years of SLR from Lageos and Starlette to calculate the annual and semi-annual variations (atmosphere, cryosphere, hydrosphere and oceans) of the low-degree spherical harmonics due to surface mass redistribution. The estimated values from SLR agree well with geophysical models on a 4x4 degree grid, but this agreement is not as strong when sampled on a 6x6 degree grid.

2.6.4 *DORIS*

DORIS is a Doppler system that has been included on many satellites put into orbit (Topex/Poseidon, Jason, Envisat and Cryosat) (Jayles et al. (2006)). Unlike GPS, the receiver is on the satellite and beacons attached to the Earth re-transmit the signal which is recorded by the satellite before being downloaded. This technique began use in 1990 and there are ~50 beacons distributed globally on all major plates, with positional accuracy of ~10cm (Altamimi et al. (2007)). Cretaux et al. (1998) used observations from DORIS to determine the velocities of 45 sites of 8 tectonic plates. It was shown that results in the stable plate interior agreed with other techniques, and the distribution of DORIS sites can improve the estimation of previously poorly

determined plates such as Africa. These plate rates were compared with the NUVEL-1A model and had very high correlation.

2.6.5 *GRACE*

The Gravity Recovery and Climate Experiment (GRACE) is an orbiting satellite pair which measures changes to the Earth gravitation field (Wahr et al. (2004)). The aim of the GRACE mission is to investigate secular and seasonal gravity changes due to GIA and present day mass changes (hydrology and cryosphere). GRACE has been shown to have a geoid height accuracy of 2-3mm at a spatial resolution of ~400km (Tapley et al. (2004)). GRACE is unable to distinguish between the GIA and present day mass change so, as with GPS, GIA must be accounted for before observations can be uses for present day mass change (Tamisiea et al. (2007)). GRACE observations are provided as monthly estimations of the Earth gravity field. This provides a perfect data set for observing seasonal and secular mass variation; however, GRACE is insensitive to the degree-1 harmonics (geocentre).

2.6.5.1 Seasonal

Tests of the ability of GRACE determination of annual loading signals have been conducted by comparing values to GPS estimates. Tapley et al. (2004) demonstrated that GRACE is able to observe the seasonal variation of the Amazon watershed and separate it from the smaller surrounding watersheds. Davis et al. (2004) showed good agreement between early observations, but van Dam et al. (2007) were unable to reproduce this good agreement, which was attributed to spurious signals in the GPS. However this lack of agreement seems to have been remedied by the GPS reprocessing campaign as both Tesmer et al. (2009) and Tregoning et al. (2009b) find better agreement than van Dam et al. (2007). The strength of GRACE is shown in that it is not sensitive to site specific errors which may be problematic for GPS observations.

2.6.5.2 Secular

Although hydrological signals are predominantly seasonal, some short term inter-annual changes, for example drought, will cause multi-year trends which are detectable by GRACE (Tregoning et al. (2009a)). Crowley et al. (2006) studied the water content of the Congo, and as well as the expected seasonal signal, there was an interseasonal trend of drying observed over the 4 year period equivalent to 17mm/yr. Crowley et al. (2008) conducted the same

investigation over the Amazon and found the expected annual signal but no evidence of drying.

One focus of this thesis is the assessment of present day secular mass loss using GPS. There have been many studies of mass loss using GRACE observation which have widely been accepted as realistic within GIA uncertainties. Over the last two decades there has been evidence of rapid acceleration of mass loss in Greenland (Velicogna and Wahr (2005)) and Antarctica (Velicogna and Wahr (2006b)). Previously these rates were determined using remote sensing, radar altimetry and ICEsat; however, these observations were limited by their temporal coverage. The GRACE mission provided a new data set with which to study glacial mass change (Chen et al. (2009a), Velicogna (2009), Chen et al. (2008), Ramillien et al. (2008), Wouters et al. (2008), Chen et al. (2006b), Luthcke et al. (2006), Velicogna and Wahr (2006a), Velicogna and Wahr (2006b), Velicogna and Wahr (2005)), summarised in Table 6. For a specific analysis of individual studies see section (6.5).

Table 6: Estimated range of GRACE mass change over Greenland and Antarctica from studies mentioned above, summarised from Cazenave and Chen (2010).

Area	Time Period	Mass Change Gt/yr
Antarctica	2002-2005	-104 to -144
	2006-2009	-220 to -246
Greenland	2002-2005	-137 to -159
	2006-2009	-267 to -286

Figure 7 of Cazenave and Chen (2010) displays the estimated trends of the surface of the Earth from GRACE. Mass losses averaged over large areas of up to 6cm/yr of surface water equivalent have been observed over Greenland, Alaska, West Antarctica and the Peninsula, with mass increase over Brazil.

As with GPS, GRACE cannot distinguish between GIA and present day loading trends so a GIA model must be removed before any estimate can be made. Tregoning et al. (2009a) demonstrated that although GRACE observations match ICE5G-VM2 (Peltier (2004)) well, over two of the three suggested ice domes (~12mm/yr uplift west of Hudson Bay), it is unable to detect the suggested uplift near Baffin Island, due to contamination by Greenland hydrology. Tregoning et al. (2009a) suggested ~12mm/yr of GIA uplift to the west of Hudson Bay. Mountain glaciers only account for a small percentage of

glaciated regions. Quantification of mass change is difficult due to the wide spread distribution of these glaciers and the low number observations. Total values of -288Gt/yr (1993-2003) (Lemke and Ren (2007)) and -390Gt/yr (2003+) (Meier et al. (2007)) have been estimated from GRACE, estimations of other large areas of glaciation have also been calculated, Table 7.

Table 7: Mass change in other glaciation regions

Area	Time Period	ΔMass Gt/yr	GIA model	Author
Alaska	$2002-2005$	-101 ± 22	ICE5G-VM2	Chen et al. (2006a)
Alaska	$2003-2008$	-71 ± 6	ICE5G-VM2	Luthcke et al. (2008)
Patagonia	$2002-2006$	28 ± 11	Ivins and James (2004)	Chen et al. (2007)
Himalaya	Recent years	-47 ± 12	Kaufmann (2005), Kaufmann and Lambeck (1997)	Matsuo and Heki (2010)

The above values will be used for comparison to the estimated GPS rates presented in this study.

2.7 Terrestrial Reference Frame

TRFs are regularly realised via observations from various space geodetic techniques. To establish a fully consistent reference frame several geodetic techniques are required as no single technique can fulfil all the required parameter definitions to the highest obtainable accuracy. For example GPS is highly dependent upon the quality of the atmospheric propagation models, the satellite orbit models and the antenna phase centre models used, whereas VLBI is not affected by orbit errors and observations are calibrated with water vapour radiometers and SLR is only affected by the dry tropospheric delay and has smaller orbit modelling errors due to the nature of the satellites. These factors mean that the origin of the ITRF has traditionally been defined from SLR measurements and scale defined from VLBI and SLR, except in the formation of the ITRF2005, as the SLR scale time series was shown to be piecewise in nature (Figure 4 of Altamimi et al. (2007)). This choice is due to the stability of the long term estimate being better than 4mm in origin and 0.5ppb in scale

(Angermann et al. (2005)). This study uses the ITRF2005 (Altamimi et al. (2007)) and its GPS-only realisation (IGS05) (Ferland (2006)). The ITRF2005 presents the coordinates X_0 of selected geodetic sites at the reference epoch t_0, (2000.0), and a corresponding linear velocity $\dot{X}_0$ which describes the temporal evolution of the station coordinates. It is possible to calculate the station's coordinates X_t at any given epoch t using:

$$X_t = X_0 + \dot{X}_0(t - t_0) \tag{2.25}$$

The movement of surface masses across the surface of the Earth will displace the stations' positions on seasonal and secular time periods. These displacements will manifest themselves as variations to the time series of station coordinates; which will distort the calculated weekly reference frame. These distortions will be visible in one or more parameters of a Helmert transformation estimated between the weekly combinations and the IGS05. Some signals that I would expect to observe are a seasonal signal in the translation along the Z-axis; forced by the seasonal mass transfer between Northern and Southern hemispheres (Kenyeres and Bruyninx (2006), Blewitt et al. (2001)) and an annual signal in the estimated scale parameter due to seasonal hemispheric loading combined with the non-uniform distribution of tracking stations. The solution in this study and any kinematic frame is described through Cartesian station coordinates and velocities. These observations allow for the definition of geocentric distances and angles as well as inter-station parameters. For any GPS only derived reference frame the origin definition is crucial and is described in more detail below section (2.7.1). All frames produced in this study are mapped to the IGS05 which is the GPS-only realisation of the ITRF2005. This frame has been in general use since November 2006 (GPS week 1400).

By aligning the solutions herein to the IGS05, which indirectly aligns it to the ITRF2005 (Altamimi et al. (2007)), we apply the NNR conditions (Argus and Gordon (1991), Demets et al. (1990)). This allows for the comparison of plate models published by different authors as there are all various realisations of the same TRS.

By definition the ITRF follows the principles of the ITRS and therefore the origin in should be CM, however as the ITRF does not include models of seasonal displacements this is only true over secular periods (1983-2005) as the

seasonal displacements average out. Therefore for any seasonal studies the ITRF should be viewed as having the Centre of Surface Figure (CF) as its origin and only CM in the secular (Dong et al. (2003)). The realisation of a CM origin is indirect and relies upon precise orbit modelling and processing models.

2.7.1 *Origin Definition of TRFs*

TRF's are vital to studies of geophysical processes, which has led to many studies of the importance of a TRF's definition, especially how the origin is realised (Tregoning and van Dam (2005b)). There are several different types of origin definition each of which has its benefits and drawbacks. Blewitt (2003) and Dong et al. (1997) discussed the main three frames considered in geophysical studies,

- Centre of Mass of the Solid Earth (CE) – theoretical geophysics
- Centre of Mass of entire Earth system (CM) – satellite geodesy
- Centre of Mass of Surface Figure (CF) – satellite geodesy and ground surveys.

In addition to this the Centre of Network (CN) is introduced by Dong et al. (2003). The above list attempts to define a geocentric origin and it is possible to calculate the origin transformation between the different types, known as geocentre motion. The actual realisation of CE is impossible from satellite observations alone. In practice it is very difficult to establish a true CM reference frame as this requires intimate knowledge of both surface masses and mass distribution of the Earth interior required to model the SLR satellite orbits. CF requires summation of entire surface including new crust created by tectonics, which is problematic (Dong et al. (2003)). Blewitt (2003) goes to great lengths to describe the three main reference frame origins, below is a brief summary of this.

The CE reference frame is fixed to the centre of the mass of the solid Earth only. However, CE is not directly accessible from geodetic observations. Initial observations (Dong et al. (1997)) describes the CE frame as a close approximation of the CF frame (see below).

CM is the centre of the mass of the solid Earth and all the surface masses in the hydrosphere. The CM is also the centre of orbit for satellites above the Earth. Therefore, satellite geodetic observations are naturally in the CM frame but solutions rely heavily on the accurate estimation of the satellite orbits which are

sensitive not only to gravitational perturbations but also non-gravitational effects such as solar radiation pressure. The internal geometry is very precise; however the external solution is less precise and is highly dependent upon the orbit modelling. A CM solution is usually transformed to a previously established CM frame by ensuring No Net Translation (NNT). Any CM solution depends upon the accuracy and temporal resolution to the frame which it is tied to, e.g. the ITRF is more suited to secular deformation but less so for seasonal loading.

Seasonal studies tend to adopt the CF (Trupin et al. (1992)), geometrically this means that the CF is defined as if the Earth's surface was covered in an infinitely dense array of points and it is the motion of these points which are taken into account. Realistically this is achieved by using a sufficiently dense global distribution of geodetic stations averaged over the globe. The origin of CF is such that the surface integral of the vector displacement field is zero (NNT).

CF is a suitable alternative for techniques which cannot realise a CM frame accurately, e.g. GPS as orbit modelling limiting factor and for VLBI as no satellites are used. CF≈CE (2%), CF approximates centre of mass of solid Earth (Dong et al. (1997)). A true CF origin would be difficult to realise as the surface of the Earth is constantly evolving with the creation and destruction in the plate tectonic deformation zones. This is where the Centre of Network (CN) frame is introduced, even though a sufficiently dense network is not possible a sufficiently dense global network of sites may be used to define a network origin.

Tregoning and van Dam (2005b) demonstrated via a simple diagram the effects of an uneven network on the determination of a CM, CF and CN frame origin.

Dong et al. (2003) suggested that with the improvement in geodetic observations CM and CF are no longer indistinguishable.

In the CM frame the motion of any point is caused by either surface deformation motions (plate tectonics, GIA, mass redistribution) or solid Earth motions due to mass balance changes.

2.7.2 *Geocentre Motion*

Conservation of momentum dictates that the redistribution of surface mass displaces CE relative to CM (Blewitt et al. (2001), Dong et al. (1997), Trupin et al. (1992)). Both the redistribution of surface and internal masses affects the

geocentre on seasonal timescales (Dong et al. (1997)), the focus is on surface mass change as internal changes are negligible on seasonal time scales.

In the CM frame every point on the surface of the Earth undergoes 2 types of motion,

- Plate tectonics, fault slip, GIA, body tide deformation (surface deformation)
- Solid Earth shift due to mass balance of atmosphere, oceans, ground water and internal masses

Currently the ITRF only models and removes the first of these effects. Investigations have shown that there is unlikely to be the presence of a significant secular drift between CF and CM (Dong et al. (2003)). Over periods less than 100 years GIA, sea level change and ice cover can generate an apparent secular drift between CF and CM. If there is an apparent secular drift of the geocentre then this can affect the estimation of site position which potentially causes a bias to loading estimates.

2.7.3 *Errors in the TRF Definition*

TRF scale should be repeatable for all techniques, but in reality there are several technique specific errors. GPS, for example, is highly dependent upon the ground and satellite antenna phase centre offsets/variations (Ge et al. (2005)).

The definition of the scale plays a very important role in the definition of the origin of the TRF. For example if there is an error in the scale of the GPS then this influences the ability to determine the true distance to the orbiting satellites. A scale rate systematically changes the heights of all stations equally. Due to the uneven distribution of oceans and continents (in general) this could alias into a translation rate error, e.g. if there was a negative shift of station heights globally, the greater number of sites in the northern hemisphere could lead to an “incorrectly” estimated negative T_z trend when calculating a Helmert Transformation.

In terms of loading if there is a negative trend of station heights then this would imply an increase in the amount of mass on the land/ decrease in ocean mass; this could bias the interpretation of any mass loading estimates.

Morel and Willis (2005) demonstrated that 1ppb error corresponds to 10^{-9} TRF scale and ~6.4mm height for stations. The shift from relative to absolute phase

centre antenna models was shown to produce a ~1.86ppb change to the IGS05 reference frame scale (Ferland and Piraszewski (2009)). It is not possible to completely remove any scale error, but by using the absolute phase centre offsets/variations (which are good, but not perfect) this effect can be minimised. This error can be identified when mapping the solutions to the TRF (IGS05), presuming VLBI and VLBI/SLR are accurate, as it would manifest as a scale rate in the solutions, this would also be true of translations is there was an error in T_X, T_Y or T_Z.

If there is an error in the TRF that the solution is mapped to then there is nothing that can be done to remedy this. An error would appear as a residual velocity and would result in a bias to one hemisphere or all stations moving uniformly up or down.

For example, previous comparisons of the Z-axis translation between ITRF2000 and ITRF2005 documented a drift of 1.8mm/yr, (Altamimi et al. (2007)); at the time this was attributed to the poor SLR network geometry, but in truth this was due to systematic errors. With the release of the ITRF2008 (Altamimi et al. (2011)) the translation rate between the ITRF2005 and ITRF2008 is 0.0mm/yr in all three components. Conclusions from these new calculations traced back to an error in the definition of the ITRF2000 origin which will only affect solutions in the operational campaign which used the ITRF2000. This would have introduced uncertainties into the solution influencing the ability to successfully remove vertical velocities due to GIA.

In theory any satellite derived TRF should be able to realise an origin centred on the centre of mass of the whole Earth as this is the focal point of the satellite orbits. This definition is highly dependent upon the satellite orbits and any mismodelling will affect the ability of the TRF to realise a true CM origin (Urschl et al. (2005)). Altamimi and Collilieux (2009) commented that the seasonal variation displayed in the T_Z component of the operational GFZ AC solution was most likely linked to an orbit mismodelling influence. Further analysis (Altamimi et al. (2008), Collilieux et al. (2007)) determined that the amplitude of the seasonal variations was too large to be true geocentre motion.

There is on-going debate as to the correct method as to the best origin for the TRF attached to the Earth and which ITRF realisation best realises this origin.

The first argument for the ITRF2005 is presented by Collilieux and Woeppelmann (2010) who showed that network geometry can propagate errors into the T_Z component by a factor of 50%. By introducing additional stations this effect was reduced to 10%. A forward model presented in this paper using tide gauge records found that the resulting reference frame showed a difference to the ITRF2005 origin of -0.44±0.22mm/yr whereas the rate to the ITRF2000 origin was 1.36±0.22mm/yr.

The argument presented by Collilieux and Woeppelmann (2010) is countered by work of Argus and Peltier (2010) and Argus (2007) who presented the case for the ITRF2000 origin to be closer to the true CM instead of the ITRF2005. The expected difference between the CE and CM is predicted to be no greater than 0.5mm/yr of which potential Antarctic deglaciation could explain ~0.4mm/yr of this (Argus (2007)). Argus calculated a reference frame with the origin at CE, as this is not strongly influenced by the choice of GIA model, using data from VLBI, SLR, GPS and DORIS corrected for GIA using Peltier (2004) and Peltier (1996). Predictions of CM-CE displacements indicate that Argus' method agrees with the ITRF2000 origin (-0.5mm/yr) better than the ITRF2005 origin (1.3mm/yr) as it gives a smaller CM-CE velocity. As there is no agreement over the correct realisation of the TRF origin then it can only be kept in consideration when interpreting GPS station data (Altamimi and Dermanis (2012)).

2.8 Noise

To be able to fully understand any estimates of station velocities then an accurate estimation of associated errors is required. GPS time series have been estimated over the last 10+ years and there are several sources of error which can influence the final (daily/weekly) position. Each individual station time series will have a unique error signature and especially during the operational campaign the sources of errors can evolve or change completely, e.g. Antenna/Receiver or processing model change (Mao et al. (1999)). This should be less of a problem with the reprocessed data set as although the error sources are still present as biases, those caused by model changes will not change with time. There are two types of noise present in the GPS time series, temporally uncorrelated White Noise (WN) and temporally correlated Coloured Noise (CN). WN has equal power at all frequencies and CN has varying power, greater at lower frequencies (Santamaria-Gomez et al. (2011)).

Sources of noise in GPS time series include:

- monument instability (King and Williams (2009))
- mismodelled satellite orbits (Griffiths and Ray (2009))
- reference frame errors (Argus et al. (1999))
- atmospheric loading and propagation mismodelling (Tregoning and Watson (2010))
- antenna phase centre model errors (Schmid et al. (2007))
- local station dependent factors (King and Watson (2010))
- systematic processing error (Amiri-Simkooei et al. (2007))

The noise in GPS time series can be described by the power-law process (Williams et al. (2004)), or in the time domain which has a power spectrum of:

$$P_x(f) = P_0\left(\frac{f}{f_0}\right)^k \tag{2.26}$$

Agnew (1992).

Where f is the temporal frequency, P_0 and f_0 are normalising constants and k is the spectral index. It is typical to expect naturally occurring processes to have greater power at lower frequencies and have values of k of $-3 < k < -1$ (Williams et al. (2004), Williams (2003a)). Specific cases of spectral indices have been identified: $k = -2$ is known of Random Walk (RW), $k = -1$ is known as Flicker Noise (FN) and pure Gaussian WN has a value of $k = 0$. All values $-1 < k < 1$ are classed as fractional WN (Amiri-Simkooei et al. (2007), Williams (2003a), Zhang et al. (1997)).

If the noise in the GPS time series is assumed to be uncorrelated then velocity uncertainties due to WN can be approximated using the sampling rate ΔT , providing there are a large number of observations, N :

$$\sigma_r^2 \approx \frac{12 \cdot a^2}{N \cdot T^2} = \frac{12 \cdot a^2}{\Delta T^2 \cdot (N^3 - N)} \tag{2.27}$$

where a is the WN amplitude and T is the time series length (Santamaria-Gomez et al. (2011)). Therefore by increasing the sampling interval or length of time series, through additional uncorrelated observations, the uncertainties due to WN are significantly reduced (potentially to unrealistic values).

For time correlated noise, specifically RW the uncertainties are:

$$\sigma_r^2 \approx \frac{b^2}{T} = \frac{b^2}{\Delta T \cdot (N-1)} \tag{2.28}$$

with b being the amplitude of RW (Bos et al. (2008), Williams (2003a)). Thus increasing the number of position estimates (extending the data span into the time series) has very little effect upon the uncertainties and changing the sampling interval has very little effect upon the uncertainties (Santamaria-Gomez et al. (2011), Mao et al. (1999)).

Bos et al. (2008) determined that for FN the uncertainties are:

$$\sigma_r^2 = \frac{8c^2}{\pi \Delta T^{3/2} \left(N^2 - N\right)} \tag{2.29}$$

where c is the amplitude of FN. This means that FN uncertainties are affected by the sampling rate and number of observations but not as sensitively as WN (2.27).

Noise type and amplitude can be determined using Maximum Likelihood Estimation (MLE) (e.g. Williams et al. (2004)), Spectral Index Analysis (Mao et al. (1999), Langbein and Johnson (1997)) or LS-Variance Covariance Estimation (LS-VCE) (Teunissen and Amiri-Simkooei (2008), Amiri-Simkooei et al. (2007)); most authors use the MLE method (Bos et al. (2008), Williams et al. (2004), Mao et al. (1999)).

TANYA amongst other software uses an estimation of the kinematic solution's χ^2/dof to estimate a goodness of fit to determine velocity uncertainties (Bos et al. (2008)). For a large number of observations this value should be ~1, if not then either the estimated models are incorrect or the assumed errors are too small. To improve this error estimate the initial uncertainties are scaled by the unit variance $\sqrt{\left(\chi^2 / (N-M)\right)}$, where $N =$ number of observations and $M =$ number of parameters. This method assumes that the data is temporally uncorrelated (Bos et al. (2008)), but as described here this is not the case.

Very early studies assumed that GPS time series only contained WN but this assumption was soon dismissed. Zhang et al. (1997) determined for a regional network of 10 sites that uncertainties would be 3-6 times greater when using WN+FN against WN model only. Mao et al. (1999) came to a similar conclusion except that for a globally distributed network of 23 sites the uncertainties are likely to be an order of magnitude greater for WN+FN opposed to WN only.

Calais (1999) determined that for a regional network in Europe that WN+FN is the best fitting model. Amiri-Simkooei et al. (2007) investigated individual station time series which all but one had 10 years of observation and a global network of 71 sites found that the best model to fit errors in GPS time series is WN+FN.

It has been noted that random walk is also present in GPS time series which has been attributed to monument instability. Johnson and Agnew (1995) found that RW error can be up to $3mm/yr^{1/2}$ but this can be mitigated by ensuring monuments are securely anchored to bedrock, reducing RW error to $0.4mm/yr^{1/2}$ (Johnson et al. (2000)) and therefore likely be masked by other CN sources.

Williams et al. (2004) used solutions from several different analysis centres which use much denser global networks and more modern data where no attempt had been made to reduce spatially correlated noise. Again WN+FN was clearly the dominant noise model, tested against WN+RW and WN only. Williams et al. (2004) extended the statistical testing and found that global networks were shown to generally be noisier than regional networks, southern hemisphere sites tend to be noisier than those in the northern hemisphere and comparing horizontal and vertical components found that the vertical WN+FN model is 2-3 times noisier than the horizontal components.

All authors attempt to calculate a “scaling factor”, a single value that can be applied to the calculated “uncorrelated” (WN) uncertainties. Bos et al. (2008) determined that the scaling factor of Mao et al. (1999) of 5-11 could grow to 6-13 taking into account Equation 32 of Bos et al. (2008). Argus and Peltier (2010) calculated using Equation 32 of Bos et al. (2008) that a WN linear estimation underestimates the true noise value by 5-25 times.

All of the studies mentioned above were carried out using operational GPS data solutions and derived position timeseries. Santamaria-Gomez et al. (2011) used GPS data from the University of La Rochelle (ULR) reprocessing campaign. The network contained 275 GPS sites which had 2.5+ years data span to avoid seasonal signal velocity bias (Blewitt and Lavallee (2002)) and underestimated uncertainties due to correlated noise of short time series (Bos et al. (2010), Williams et al. (2004)).

Santamaria-Gomez et al. (2011) found that even in the reprocessed time series a WN+CN model was superior to WN only, and further investigation into CN

found that FN was superior to RW. It is noted though that this does not disprove the existence of RW (station specific) only that it is either difficult to detect due to the shortness of time series or is masked by the more dominant FN in the global solution. More specifically as the spectral index and amplitude are affected by time series length then the primary noise source cannot be due to monument noise (RW) and that noise is affected predominantly by GPS processing, quality and quantity.

Williams (2003b) investigated offsets in station time series and what effect they have upon the estimation of station velocities. The amount it affects the estimation of velocity uncertainties depends upon the type of noise; if the noise is purely WN then an offset in the mid-point of the time series double the rate uncertainty. The rate uncertainty increases until some point between $-2 < k < -1$after which offsets have little effect upon the value of random walk, $k = -2$. Williams (2003b) determined that undetected offsets can mimic random walk noise.

The difference in noise content between the reprocessed and operational solutions should be highlighted here. Due to the nature of the reprocessed data the noise content would be expected to be lower compared to the operational data. In addition to the discussion above the difference between the two data sets can be highlighted by comparing the work of Williams et al. (2004) and Santamaria-Gomez et al. (2011). Both authors calculate the amplitude of WN and FN modelswhich best fits the operational (Williams et al. (2004)) and reprocessed (Santamaria-Gomez et al. (2011)).

Table 8: Comparison of estimated WN and FN amplitudes for the operational network (Williams et al. (2004)) and the and reprocessed network (Santamaria-Gomez et al. (2011))

	White Noise (mm/yr)			Flicker Noise (mm/yr$^{1/4}$)		
Author/Network	North	East	Up	North	East	Up
Williams/SOPAC	1.4	2.1	3.9	4.9	6.8	20.1
Williams/JPL	2.9	4.1	7.3	7.6	9.6	22.0
SM-G/UL1	N/A	N/A	2.0	N/A	N/A	6.0

What Table 8 demonstrates is the reduction in the amount of both white noise and flicker noise in the reprocessed solution in comparison to the operational solution which can be attributed to the model implementation and the increase in the network density.

Noise is not only time-correlated; observations have shown that GPS noise is spatially correlated. Mao et al. (1999) determined that there is a small increase in WN in the southern hemisphere and has a clear latitude dependence (greater at ±23° of equator) for the vertical component. Williams et al. (2004) determined that FN has a potential latitudinal dependence, being greater in the Southern Hemisphere. Santamaria-Gomez et al. (2011) confirms that this is also the case for the reprocessed data. Using this theory I will calculate a realistic scaling factor for the combined solution here at Newcastle, section (4.4.2).

2.9 Summary

In this chapter I have outlined the identifiable causes of secular deformation of the solid Earth, GIA and tectonics, and how they are measured and quantified. However there is continual debate as to the accuracy of models used especially in GIA studies. To date there have only been limited studies into the simultaneous estimation of GIA, plate tectonics and present day secular loading, e.g. Wu et al. (2010) and Wu et al. (2003). In the following chapters I will explain how the data I use in this study begins its process from raw AC input solutions to the final kinematic station velocity model. Using these station velocities I will remove a suite of estimated GIA and tectonic velocities, with the residual comprising of the present day secular mass loading. My technique differs from the study of Wu et al. (2010) as I will be using modified basis functions instead of an ocean model to constrain the loading to the continents and instead of using a composite GIA model I will consider several different a priori global GIA models and assess their strengths and weaknesses. The majority of current work on present day mass loss utilises data from the GRACE mission (Velicogna (2009), Velicogna and Wahr (2005)), but this data still relies upon model assumption and the removal of a GIA model, as in the case of GPS. The benefit of GPS over GRACE is the length of reliable data, GRACE 2004-2009 versus GPS 1994-2001. GPS is also able to study the geocentre and has greater sensitivity to the low degree harmonics, (especially n=2).

Chapter 3. Reprocessed GPS Data and Combination

Since the inception of the IGS and the completion of the GPS satellite constellation, various working groups have been striving to produce and publish a variety of products all derived from the GPS tracking data. Currently there are seven ACs producing a weekly global network solution for the operational processing campaign. In July 2005 it was agreed by the IGS Steigenberger et al. (2006a) that the catalogue of GPS and GLObalnaya Navigatsionnaya Sputnikovaya Sistema (GLONASS) data was sufficiently complete that it would be prudent to reprocesses the entire GPS data record. This decision was made due to the heterogeneous nature of the operational time series. During the history of GPS processing, new models and processing techniques were introduced; this meant that the overall time series was not homogeneous; i.e. it has systematic breaks and offsets which would affect how any signals were interpreted. The reprocessing campaign aimed to produce a systematically consistent homogeneous time series, using the most recent models and processing techniques. This should allow for the detection of long term geophysical signals which may previously have been masked by the systematic discontinuities introduced by model changes and noise. The reprocessing period covers GPS weeks 0730-1459; the latter is when the processing strategy coincides with the operational product from GPS weeks 1460-present. This study uses data covering GPS weeks 1000-1570; the earlier weeks were not utilised as at the time of processing some AC solutions were not available, thus limiting the number of stations available for combination.

3.1 The IERS and IGS

There are two bodies which oversee the running of geodetic applications; these are the IERS and the IGS which are briefly described below.

3.1.1 *The IERS*

The IERS is the governing body that serves the astronomical, geodetic and geophysical communities by producing the International Celestial Reference System, (ICRS), the International Terrestrial Reference System (ITRS) and their realisations along with EOP transformations between the ICRF and ITRF, plus all the standards, constants and models required for any geodetic processing. The ITRF produced by the IERS is indirectly accessed in this study by aligning solutions to the IGS's GPS only realisation of the ITRF (Ferland (2006)).

3.1.2 *The IGS*

The IGS is the scientific governing body of all GNSS operations; it comprises a collection of over 200 global centres that promote the exchange of permanent GNSS tracking station data to produce a variety of products. Although only one data product is explicitly used in this study, a large number of products are utilised in the steps taken to produce that product. All operations are overseen by the IGSCB which provides the recommendations and guidelines for all GNSS operations. Using various techniques these ACs, Table 9, used the raw data collected at GNSS tracking stations to produce a weekly global network based on a subset of tracking stations. These weekly solutions are deposited at a data store, Table 12. It is these weekly solutions that are combined forming the fundamental data set used in this study. Table 10 summarises the combination centres and the combination of the reprocessed data products.

Table 9: IGS ACs, tick indicates regular submission, cross indicated no solutions submitted and TIGA are the tide gauge solutions. The final column summarises the processing techniques used, UD – undifferenced, DD – Double differenced

AC Code	Full Name	Operational/ Reprocessed Network	S/W	GNSS	Type
COD	Centre for Orbit Determination Europe	√/√	Bernese v5.1	GPS GLONASS	DD
EMR	Natural Resources Canada	√/√	GIPSY-OASIS v5	GPS	UD
ESA	European Space Agency	√/√	NAPEOS v3.6	GPS GLONASS	UD
GFZ	GeoForschungs Zentrum	√/√	EPOS.P.v2	GPS	UD
GTZ	GeoForschungs Zentrum	X/TIGA	EPOS.P.v2	GPS	UD
JPL	NASA Jet Propulsion Laboratory	√/√	GIPSY-OASIS v5	GPS	UD
MIT	Massachusetts Institute of Technology	√/√	GAMIT/GLOBK v10.32	GPS	DD
NGS	National Geodetic Survey	√/√	Pages/gpscom	GPS	DD
PDR	GeoForschungs Zentrum/ Potsdam & TU Dresden	X/√	Bernese v5.1	GPS	DD
SIO	Scripps Institution of Oceanography	√/√	GAMIT/GLOBK v10.20	GPS	DD
ULR	University of La Rochelle	X/TIGA	GAMIT v10.34 /CATREF	GPS	DD

Table 10: Combination centres, which are part of the IGS reprocessing campaign

Combination Centre	Location	Product
NRCan	Natural Resources, Canada	SINEX combination
NCL	Newcastle University	SINEX combination
GFZ	GeoForschungsZentrum Potsdam, Germany	GPS orbits and ftp directories
NRL	Naval Research Laboratory, USA	Clock and timescale combination

3.1.3 *Precision and Accuracy*

One cause of the poor quality estimation of the station positions and velocities in previous combinations is undetected discontinuities in station time series (Williams (2003b)). Most discontinuities can be explained by changes to station hardware or Earthquakes. It is simple to account for station hardware changes as this usually appears as a single discontinuity in the time series which can be estimated as an XYZ shift, the main challenge is detecting these discontinuities. At present there is no standard automatic process for detecting offsets; the handling of offsets is discussed in section (4.3.2). A discontinuity caused by an Earthquake cannot be handled quite as easily; after a brittle failure of the Earth, station positions can shift by up to several metres. This however cannot always be modelled with the introduction of a single offset, as after an Earthquake there is usually an extended period of nonlinear post-seismic slip (El-Fiky and Kato (2006)). There are different methods for treating discontinuities. These include excluding data before the discontinuity or after dependent upon the position of the break in the time series, estimating two separate time series or in the case of post-seismic deformation excluding a section after the event or estimating a logarithmic decay function.

3.1.4 *Station Coordinate Time Series Quality*

The quality of the station coordinate time series is dependent upon several factors, including station location (visibility of sky and satellite geometry), monument stability, high quality equipment (antenna and receiver) and minimisation of multipath environment (King and Watson (2010)). In an attempt to minimise these factors the IGS guidelines ensure that station monuments are embedded into the bedrock away from any seismically active areas or local subsidence.

3.1.5 *Reference Frame Sites*

There are hundreds of sites globally that record and submit their data to the GPS data centres (Table 12). The ACs can choose any or all of these stations to be included in their solution. However when it comes to producing a reference frame the IGS has laid down some additional guidelines for station inclusion. They use the following criteria in addition to the standard IGS criteria. This will determine whether a site will be used as a reference frame site.

- Avoidance of closely-spaced sites
- Minimum 2.5 years of data
- Run by a recognised geodetic institute
- Part of an established regional network
- Collocation to other geodetic techniques

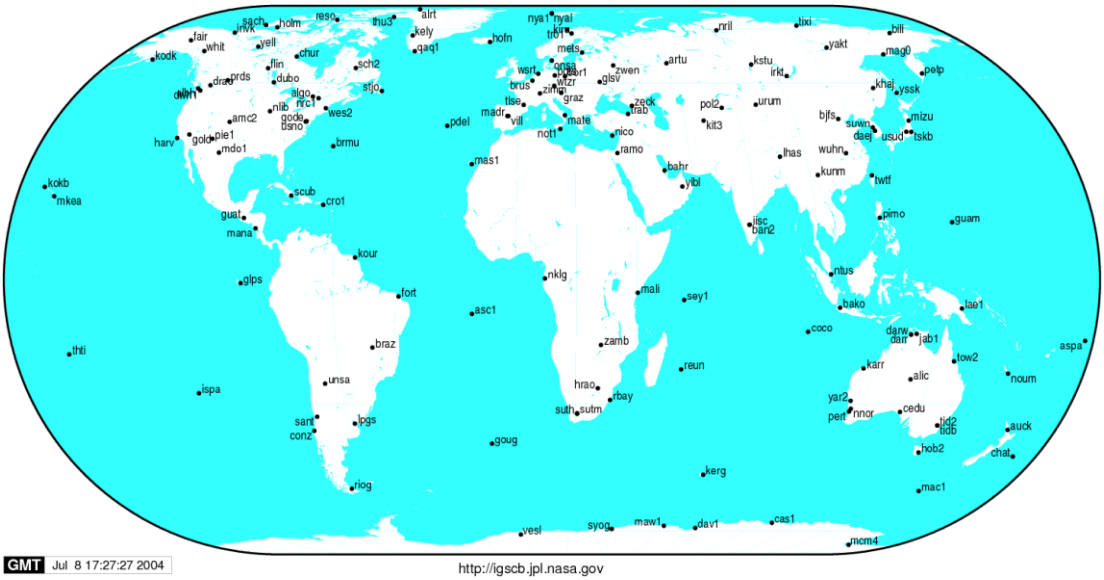

Figure 12: IGS05 core tracking stations, http:/igscb.jpl.nasa.gov (accessed 3rd August 2008)

3.1.6 *Infrastructure of Reprocessing Campaign*

Newcastle is a Global Network Associate Analysis Centre (GNAAC) along with Massachusetts Institute of Technology (MIT) and Natural Resources Canada (NRCan), with NRCan having the responsibility of producing the official weekly combination of station coordinates estimates produced by the ACs, (in Spring 2011 this responsibility passed to the Institut Geographique National (IGN), France). Each AC had a different processing and data handling technique and therefore their solutions have different systematic and random errors. It has been shown that by combining the individual AC SINEX files, the formal errors of the combined SINEX solution are less than any of the individual AC solutions,

(Davies and Blewitt (2000)). Ferland and Piraszewski (2009), Zerbini et al. (2007) and Ferland et al. (2000) show that by combining solutions it is possible to detect blunders and the random processing noise of each AC is averaged out. To avoid any confusion a specific naming regime for the different operational and reprocessing campaigns was agreed upon, Table 11.

Table 11: Designation of AC CODE for different processing campaigns

Campaign Name	AC Code
Operational	COD
1st round of reprocessing	CO1
2nd round of reprocessing	CO2

In 2010, the reprocessing ACs completed their reanalysis of the complete catalogue of GPS data from 1994 onwards. This is the first ever reanalysis of GPS data carried out by the IGS but several more campaigns are envisaged in the future as further model improvements are implemented. It is not only the station coordinates used in this study that are being reprocessed; the complete reprocessing campaign products are summarised below.

- Daily GPS orbits and respective satellite clocks
- Daily satellite and tracking station clocks
- Daily Earth rotation parameters
- Weekly terrestrial coordinate frames with daily ERPs

Other products such as ionospheric maps and tropospheric zenith path delays are not part of this first round of reprocessing. There are plans to include these and other products into future campaigns when new more robust models are available; improving the products provided for use by the wider geodetic community. Several standards were adhered to in the reprocessing campaign to ensure that all analysis centre reprocessed products were consistent, these guidelines are laid out in the position paper (Steigenberger et al. (2006a)). These recommendations will ensure that the reprocessed time series will contain little or no systematic error due to model changes; however temporal variations in station distribution back to 1994 are unavoidable, within the reanalysis period. Selected stations must meet the strict criteria laid down by the IGS (http://igscb.jpl.nasa.gov/network/guide_igs.html, maintained by the IGSCB). ACs were encouraged to reconsider the inclusion of stations which have been, are currently used in reference frame solutions, or which are

collocated with additional space geodetic methods such as DORIS, SLR and VLBI and Tide Gauge (TIGA) sites. In the reprocessing campaign there are two dedicated TIGA site solutions from GTX and ULR. These changes are discussed below in section (3.3).

3.2 TANYA Combination Software

The combination of data AC reprocessed SINEX solutions presented in this thesis is achieved using the bespoke software TANYA developed and used by Newcastle University for selected IGS operations. TANYA comprises a set of executable files written in C and is controlled by a set of front end scripts written in C Shell. These control the reading of weekly network files and writing of system-dependent files through a series of logic loops and branches. These scripts enable advanced users to create and access the full power of the TANYA modules, but there is also a set of predefined scripts for beginners; see Davies (1997) for a full description.

3.2.1 *TANYA Processing Data Flow*

There are several stages in the processing scheme from the raw input files to the combined solution. Raw solution files produced by ACs are delivered to the three IGS Global Data Centres listed in Table 12.

Table 12: Global data repositories as part of the IGS

Acronym	Name	Location
CDDIS	Crustal Dynamics Data Information Service	Maryland, USA
IGN	Institute Geographique Nationale	Paris, France
SIO	Scripps Institution of Oceanography	California, USA

All files are delivered by the ACs to the IGS Data Centres using the standardised SINEX (Solution INdependent EXchange) format which was devised by the IGS SINEX Working Group (Blewitt et al. (1994)). This format was developed to enable the transparent and seamless transfer of station coordinates, but also other important space geodetic parameters that are estimated concurrently with GPS and other space geodetic data processing. The standardised format of the SINEX file allows for data to be transferred to the TANYA file format. The fundamental structure used in the TANYA program is the data block; this consists of a set of files which have the same root

filename but a different three character extension, Table 13 . There are many file extension possibilities but only a few are of relevance here. All processing within the program requires three core extensions; in addition to these two other file extensions are used.

Table 13: File extensions used by the TANYA block format

Extension	Contents	Format	Optional
.hed	Agency , timestamp, number of stations in block, number of stations in catalogue, parameters per station, covariance scaling factor, block reference epoch	Single line	No
.sib	List of station reference numbers	List of integers	No
.vec	List of the vector of parameters	List of floating point numbers	No
.cov	Upper triangular covariance matrix of .vec vector	List of floating point numbers	Yes
.wgt	Upper triangular weight matrix of .vec vector	List of floating point numbers	Yes

Apart from the .hed format, each of the other blocks is designed to only contain integers or floating point numbers. Station estimates are written into the vectors block; if there is the respective a priori information then this is written to a separate block. The .sib file contains the station id, referring to the SINEX catalogue; TANYA stores these character ids as a separate list of numbers for internal processing but is readily interchangeable between internal catalogue numbers and four character name. The .vec file can contain station coordinates, station velocities or both, as defined in the .hed file. The expected number of values in the .vec file can be determined by multiplying the number of parameters, pps , by the number of stations, n_i in the input file.

$$pps \times n_i \tag{3.1}$$

Combination of the input data is achieved through pre written scripts, which call the TANYA routines to create the weekly combined solution. A combination

requires a minimum of three input files from different ACs. Each AC has a slightly different interpretation of the SINEX file format and because of this some files have slight formatting errors. Lavallee (2000) took great steps to correct known formatting errors prior to the formation of the blocks; further steps were required by the author to correct errors or inconsistencies in the reprocessed submissions. Once the errors are corrected the corresponding TANYA block can be constructed. Each AC will impose a certain level of constraint upon its solution file; in order to be able to produce a rigorous combination these constraints must be removed, known as loosening the block. The relevant constraint information is contained in the a priori block. The loosening of input solutions is achieved by subtracting the a priori block from the estimate block. At this time additional, arbitrary, rotational constraints can be applied to aid the inversion process (Blewitt (1997)).

Once the blocks are loosened, a Block Scaling Factor (BSF) is applied to the files' variance components; this determines the influence that each file has upon the final combined solution. The BSF is calculated from the AC unit variance:

$$\sigma_{i+1}^2 = \sigma_i^2 \left(d\left(\lambda - 1\right) + 1 \right) \tag{3.2}$$

Where σ_i^2 is the current week's BSF, σ_{i+1}^2 is the following week's estimate, λ is the unit variance estimate and d is the damping factor. The damping factor limits the influence that a week's variance can have in calculating the long term BSF. Davies (1997) suggests using a value of $d = 0.2$ which Lavallee (2000) also uses and I use here. This chosen weekly damping factor only allows a 20% influence on the calculation of the following week's BSF. A varying BSF will allow for the evolution of an AC's network solution which is not always an ideal situation as this may mask any transient errors in a particular AC solution, but this procedure is required for operational processing due to the changes in processing strategies and models. For the reprocessing solutions each AC will use the same software and models throughout the entire data set and as such the variance-covariance matrices should be homogeneous. This means that it is valid to use a calculated constant BSF for each input solution.

Once the blocks have been scaled they can be combined using the rigorous least squares combination routine in TANYA. This builds an observation and parameter model for the station coordinates that appear in at least three AC solutions and is solved by inverting the standard normal equations. Included

stations are put into the “g-network” solution. Any station that is rejected is put into the “a-network” solution which can be attached to the final combined solution but has no influence over the network estimation. Once completed the blocks are written in the SINEX format and are run through data quality testing. Rejecting a station which does not appear in a minimum of three ACs for any week prevents a rogue result from an individual AC from biasing the final velocity solution.

3.3 Current Models

The main source of heterogeneity in the operational time series was identified as the various model changes implemented throughout the history of the IGS processing (Ferland (2006)). The IGS reprocessing committee decided that the current operational models were of a sufficiently high precision to be suitable as models for the reprocessing campaign. Below is a summary of the main models implemented in the reprocessing campaign:

- Absolute satellite and receiver antenna calibrations
- IGS05 reference frame
- Updated Ocean Tide Loading (OTL) model i.e. FES2004
- No non-tidal loading displacements
- Updated tropospheric propagation delay models
- No higher order ionospheric effects applied
- Updated IGS catalogue to include historic and defunct IGS stations
- P1-C1 satellite code bias corrections

The updated IERS Conventions 2003 have been used; these summarise the numerical standards and frame definitions required for all IERS work (McCarthy and Petit (2004)) including the IGS.

3.3.1 *Absolute Antenna Phase Centre Variation/Offsets*

The model which made the biggest improvement to the precision of the global operational solution was the implementation of the absolute antenna calibrations in GPS week 1400. For short baselines with very little height change, GPS relative phase centre corrections are sufficient as the satellites in view are at a similar elevation; however this is not sufficient for global solutions (Schmid et al. (2005)). During 1996 relative GPS antenna phase centre corrections were applied by ACs to allow for a non-spherical phase response of GPS antennas (Schmid et al. (2007)). Phase centre corrections calculated

consisted of an offset between the electrical and physical reference points and a variation which was dependent upon the elevation angle of the tracked satellite (Schmid et al. (2007)). The relative corrections assumed that the phase centre variation of the reference antenna (Dorne Margolin choke ring) was zero (Schmid et al. (2007)) and other assumptions meant that there were systematic errors. In November 2006 it was decided to switch to the subsequently available absolute phase centre corrections which mitigated some of the issues inherent with using the relative corrections and would therefore not bias the solutions. Two corrections were calculated at GFZ and TUM for GPS satellite antennas for the different GPS blocks. The satellite PCV corrections are calculated at each institution using a calibrated robot rig and a Kalman filter. Differences between two different generations of satellite antenna patterns have been found to be approximately 4cm (Schmid et al. (2005)). It is therefore important that these antenna variations are estimated in the AC solutions. The satellites are tracked at a variety of inclinations and elevation cut off angles and values for absolute 3D offsets, elevation and azimuthal dependent phase centre variations are calculated. Field observations of absolute PCV show that the current operational elevation dependent corrections only account for ~10% of the actual effect (Wubbena et al. (2007)). These corrections are summed up in the updated igs05.atx file. This file contains the satellite specific z-offsets and satellite block specific x-/y-offsets as well as the block phase centre variations.

3.3.2 *IGS05 Reference Frame*

The IGS05 is the GPS only realisation of the ITRF2005, produced by the IGS (Altamimi et al. (2007)). This frame is aligned to the ITRF2005 via a 14-parameter Helmert transformation (Ferland (2006)) and is based on 132 sites. This frame is chosen because it is realised via GPS observations for use with GPS time series. The reference frame to which the reprocessed solution is aligned plays an important role in the precision of station locations and the global combined network. There have been many releases of the official reference frame to which the operational solutions are aligned to; Table 14 lists all the changes of reference frame solutions each of which introduced a systematic error in the operational time series. The first round of the reprocessing campaign uses the IGS05.snx throughout.

Table 14: Reference frame solution and data span covered

Reference Frame	Reference Epoch	Data Span GPS week
Core94.snx	1993.0	0815 – 0946
Core96.snx	1997.0	0947 – 1020
Core97.snx	1998.0	1021 – 1064
Core_IGS97.snx	1998.0	1065 – 1142
Core_IGSb00.snx	1998.0	1143 – 1400
IGS05.snx	2000.0	1400 – 1632
IGS08.snx	2005.0	1632 - present

3.3.3 *Atmospheric Mapping Functions and Tides*

The troposphere is a turbulent layer of the atmosphere which the GPS signal must pass through to reach the ground station. Of all the atmospheric layers the troposphere contains the highest water content which is highly variable. Several models have been created to map the effect of the hydrostatic and wet atmosphere path delay on the GPS signal such as the Isobaric Mapping Function (IMF) (Niell (2001)) and the Vienna Mapping Functions (VMF) (Boehm et al. (2006b), Boehm and Schuh (2004)). Of the total atmospheric path delay 90% due to dry delay is estimated fairly accurately; the remaining 10% from the wet delay is highly variable and is difficult to estimate accurately (Elgered et al. (1991)). Previously most ACs used the Niell Mapping function (NMF) (Niell (1996)) whose coefficients are empirically derived from site location and day of year. The NMF is created from data which only uses one year of northern hemisphere radiosonde profiles; this has been shown to contain latitudinal deficiencies which are at a maximum in southern hemisphere locations (Boehm et al. (2006a)). For this round of the reprocessing campaign the Global Mapping Function (GMF) developed by Boehm et al. (2006a) and derived from the European Centre for Medium-Range Weather Forecasts (ECMWF) numerical weather model was used by all ACs. The GMF uses coefficients ultimately derived from the VMF; input is kept simple and is similar to Neill's NMF. The GMF is based on mean values of model data. It reduces systematic errors, especially in the southern hemisphere which has been a large source of error in previous mapping functions (Boehm et al. (2006a)).

3.3.4 *Higher Order Ionospheric Corrections*

Published work Petrie et al. (2011), Fritsche et al. (2005) and Kedar et al. (2003) shows that higher order (2^{nd} and 3^{rd}) ionosphere corrections produce a small systematic change in the GPS processing results, however these corrections are not considered in this round of reprocessing.

3.3.5 *Atmospheric Tides and Non-Tidal Loading*

The S_1 and S_2 atmospheric tides have no accurate model and therefore have not been included; neither were the non-tidal loading effects of the atmosphere, ocean and hydrology (Tregoning and Watson (2011), Tregoning and Watson (2010)). As there is no consensus on these effects no corrections were implemented in this round of reprocessing (Williams and Penna (2011), van Dam et al. (1997)).

3.3.6 *Receiver Bias*

There are different receiver types regarding the code tracking on the L1 frequency. C1 receivers track the C/A code and P1 receivers directly track the P-code. Some receivers track P1/P2/C1, others track C1/P2. Each instrument will have a bias with respect to C1, P1 and P2. It is common to calculate the following differential biases: P1-P2 and P1-C1 (differential code bias) (Schaer (2006)). It is the second of these biases that is accounted for in the IGS reprocessing campaign Reprocessing (2012). The values for each satellite are different at the receiver, and monthly values are calculated at the CODE IGS AC and are updated each time a new satellite is launched (Steigenberger et al. (2006a)). The differential code biases are also calculated at TUM/TUD (Steigenberger et al. (2006b)) and these could potentially be used by the IGS. For the reprocessing campaign a single mean value was used instead of a monthly variable value, this is due to the noise level of the early weeks.

3.3.7 *Ocean Tide Loading Model*

Ocean Tide Loading (OTL) results in a deformation of the Earth due to the weight of water redistributed by the ocean tides. The ocean tides are caused by the gravitational attraction of the Sun and Moon, there are multiple periodicities due to the irregular orbits of the Sun and Moon and the ocean tides can be described as a sum of all these ocean tide periodicities (Cartwright (2000)). The summation is described by an OTL model; these usually summate the main (9-

11) periods. Various OTL models were used by ACs in the operational processing:

- GOT00.2 (Ray (1999))
- FES99 (Lefevre et al. (2002))
- NAO.99b (Matsumoto et al. (2000))
- CSR4.0 (Eanes and Schuler (1999))
- TPXO.6.1 (Egbert et al. (1994))

However for the reprocessing campaign it was decided that the FES2004 model (Lyard et al. (2006)), corrected for CM station motion, is globally the best model available.

3.4 IGS Tracking Network

The IGS tracking network is a dynamic list of GNSS stations which has changed dramatically over the history of the IGS. The IGS publish a catalogue SINEX file which includes all decommissioned and defunct stations. Each AC is free to choose which stations they include in their weekly solutions; in the operational solutions some perfectly functional tracking stations were not included as they were relatively new and did not meet the required data span recommended in the IGS guidelines. Some stations which are initially included drop out of the pool of stations as they are decommissioned or replaced. Hindsight is a great ally; with the advent of the reprocessing campaign, stations which were not initially used in the operational campaign, due to insufficient data span or offsets, now become available for use in the reprocessing solutions. The tracking network that an AC chooses to use each week aims to optimise the estimation of the global network, each AC has a different number and distribution of stations in their network. The importance of having a balanced geometry, especially along the Z-axis has been shown (Lavallee et al. (2006)). A perfectly optimal 50/50 split along all three axes has proven difficult to implement due to the continent rich northern hemisphere and the lack of required land and/or infrastructure in the southern hemisphere. Historically the African and South American continents have suffered from sparse data coverage of IGS quality tracking stations. This coverage is improving quickly but even in the reprocessing campaign there is still a bias of stations in the northern hemisphere, especially going back towards 1994.

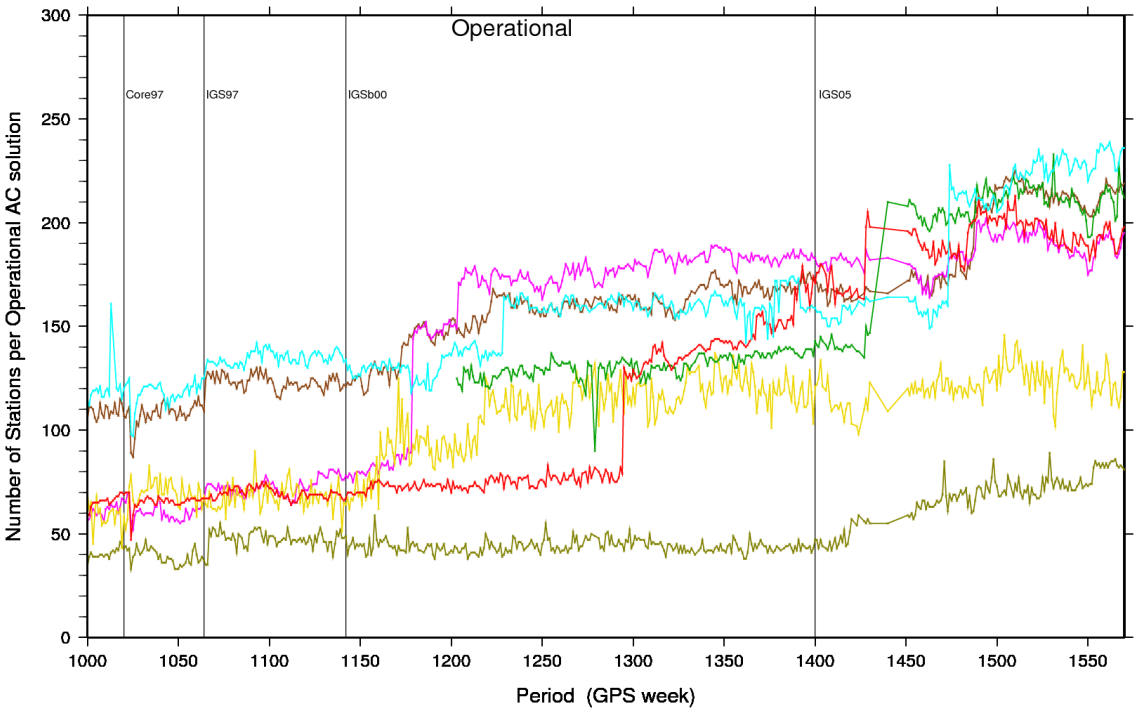

Figure 13: Number of stations included by each AC as part of the operational campaign. The black lines refer to the changes to the reference frame of choice, Table 14.

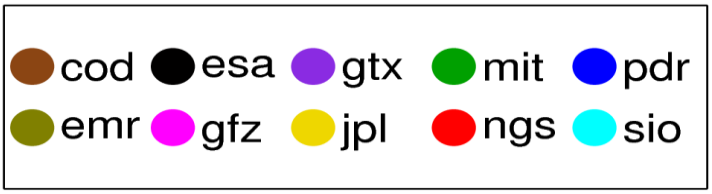

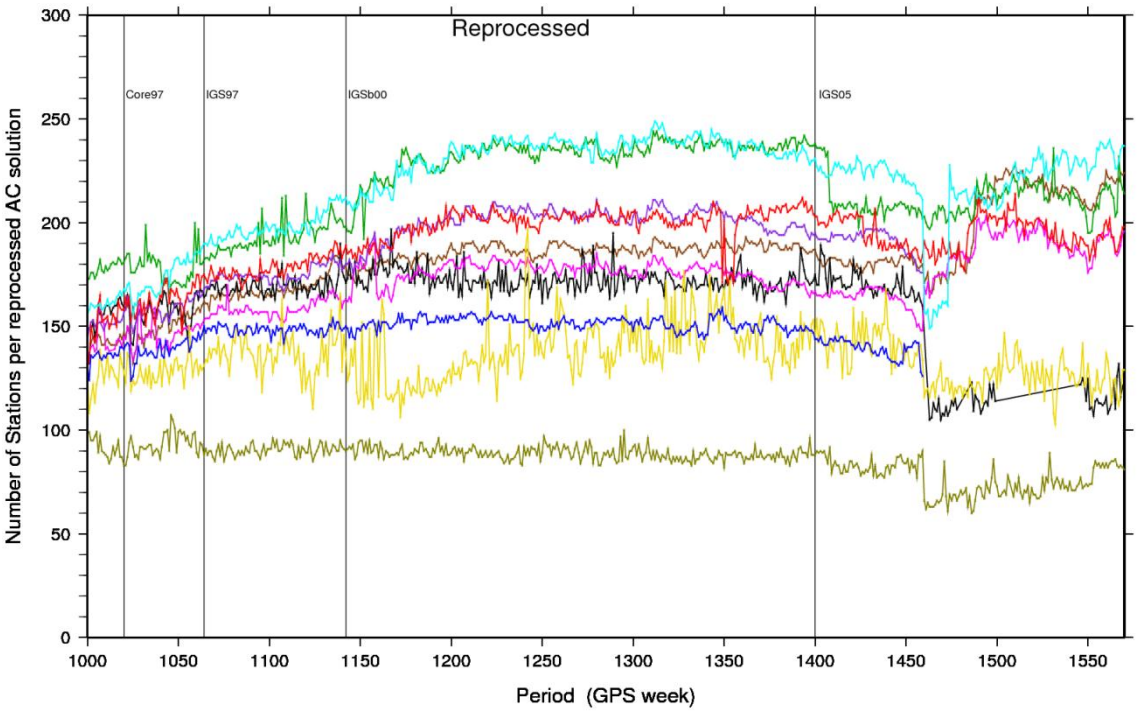

Figure 14: Number of stations included by each AC as part of the reprocessed campaign. The black lines refer to the changes to the reference frame of choice in the operational campaign Table 14, included here as a comparison.

Comparing the number of stations included by each AC in the operational campaign, Figure 13 and the reprocessing campaign, Figure 14, it becomes clear that the number of stations included, especially in the early weeks 1000-1300, increases dramatically. All ACs apart from EMR included over 100 stations in the reprocessing campaign whereas in the operational campaign, it is not until after week 1300 that there are consistently over 100 stations included in each solution. The number of stations included by any one AC peaks at over 300 stations. However this does not mean that the combined solution will include 300 stations. One of the criteria in the TANYA combination software stipulates that a tracking station must be included in at least three individual solutions. Therefore the number of stations included in the Newcastle combination varies as the geometry of a tracking station network changes, section (3.6.5). What the number of stations included is unable to tell us is the distribution of tracking stations along each of the coordinate axes. It is possible to calculate for each AC the weekly distribution of stations in the reprocessing campaign by examining the approximate coordinates of each network station.

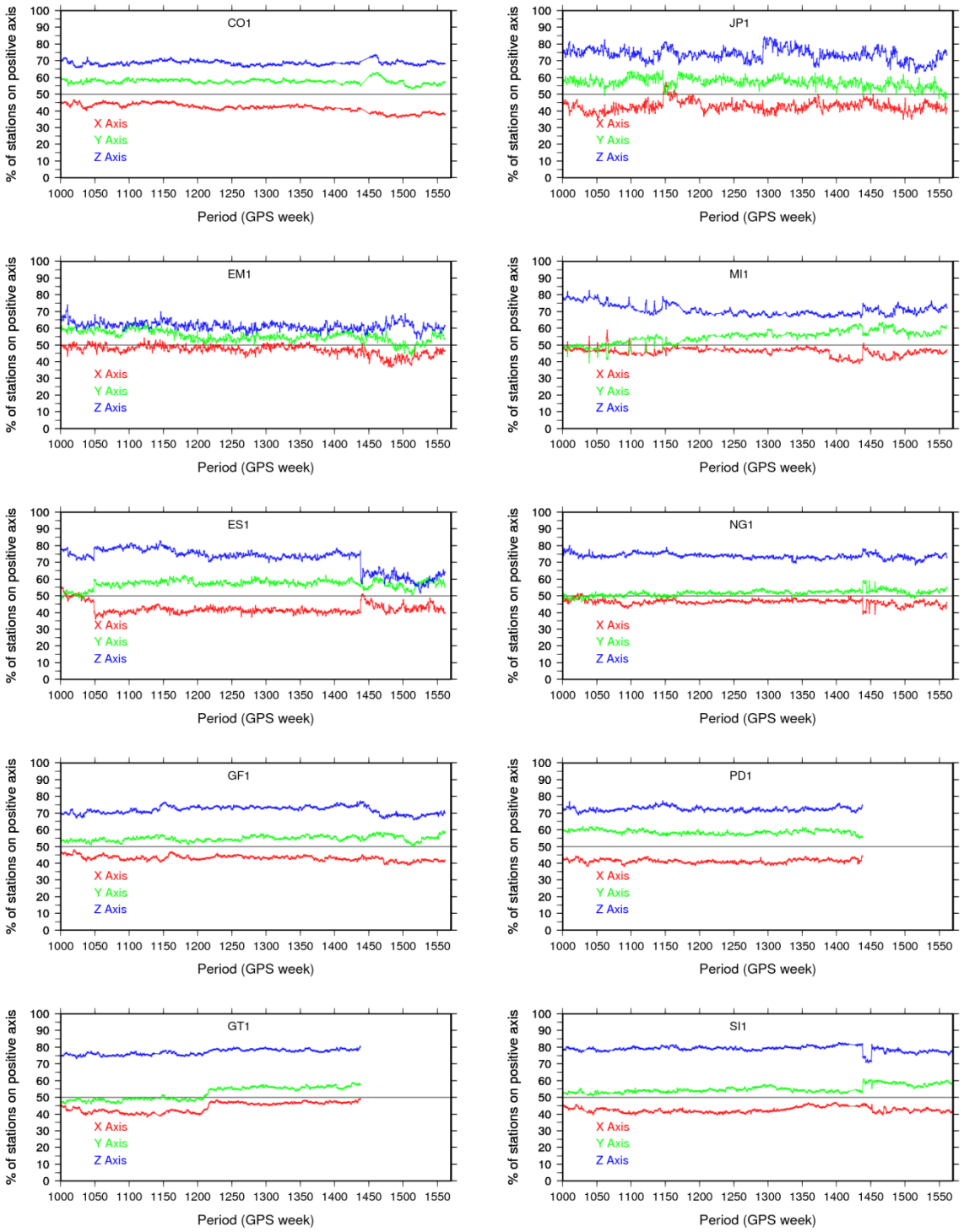

Figure 15: The percentage of stations distributed on each of the positive axes for all reprocessing AC solutions

Most ACs are able to balance the number of stations on the X and Y axes, however, as mentioned previously, global networks suffer from the continent rich nature of the northern hemisphere, this corresponds to the Z-axis shown by the blue lines in Figure 15. No matter what configuration of stations used there will nearly always be a bias towards the positive Z-axis.

3.5 Analysis Centre Combination Theory

There are a number of ACs committing solutions to both the operational and reprocessing campaigns. There are currently seven ACs in the operational campaign and eleven in the reprocessing, with two GNAACs. It is the role of the GNAACs to combine these network solutions into a unified rigorous solution to act as an independent comparison for the official IGS combination. Table 9 summarises each AC's contribution to the operational reprocessing campaigns. The IGS reprocessing campaign website contains full details of each of the contributing ACs processing strategy, http://acc.igs.org/reprocess.html. It is left to the discretion of the ACs to select methods for how they carry out the reprocessing analysis, within given guidelines and recommended models.

3.5.1 *AC Inclusion/Exclusion*

Initially all of the 11 ACs that submitted reprocessed solutions were considered; however there are only 10 actually used in this study. I have chosen not to include the TIGA solution of ULR as the residuals and estimated transformation parameters suggest that there are unstated constraints that have not successfully been removed during the combination process.

3.5.2 *Different Techniques Used*

Summarised in Table 9 are the different techniques implements by the ACs as part of the reanalysis campaign. Although there were constraints on the processing models used, ACs were free to choose what software and whether to use GPS or GPS+GLONASS. Combining all the solutions will exploit the slight variations to the processing techniques to our advantage, minimising any systematic processing noise or highlighting any particular problems with individual ACs. If all solutions were calculated using exactly the same techniques and station selection criteria then any error in station coordinates or systematic processing techniques would pass unnoticed into our solution biasing any estimation. One particular AC model/technique may be superior to those used by others but this would be difficult to determine and the variation of processing techniques highlight gross errors in certain methods. ACs are free to choose what stations they include in their solution apart from the stipulated 132 IGS05 sites, the newly release IGS08 contains 232 core sites. Each centre will supplement these sites with additional sites, which still must be a recognised geodetic quality GPS sites, to their weekly solutions.

3.5.3 *Helmert Transformation Estimation*

The parameters which are fundamental to any reference frame are the origin, orientation, scale, and their evolution with time. Uncertainties in the definition of the reference frame can propagate into the precision of the station coordinates and velocity estimations. In a perfect world free from any systematic errors, the origin and scale of the reference frame will be stable without any drift compared to the truth.

Each AC solution is defined in its own unique realisation and as such they cannot be directly compared. To be able to compare the solutions, first they must be transformed to a common reference frame of choice using a Helmert transformation. A Helmert transformation is a rigid body translation, rotation, plus scale change from one reference frame station coordinates, X to another X'.

$$X' = t + RX + sX \tag{3.3}$$

(3.3) is the basic Helmert transformation for a coordinate reference frame at a chosen epoch, it is comprised of three translation parameters t, a solid body rotation R around each axis and a single scale factor s. This is applicable for station coordinates; to calculate a transformation for station velocities then (3.3) must be modified:

$$\dot{X}' = \dot{t} + R\dot{X} + s\dot{X} + \dot{R}_X X + \dot{s}X \tag{3.4}$$

(3.4) accounts for the rates of the different parameters where $\dot{X}, \dot{X}'$ are station velocities in the two reference frames. The rotation parameters take the form of a 3x3 matrix.

$$R = \begin{bmatrix} 1 & -r_z & r_y \\ r_z & 1 & -r_x \\ -r_y & r_x & 1 \end{bmatrix} \quad \dot{R}_X = \begin{bmatrix} 0 & -r_z & r_y \\ r_z & 0 & -r_x \\ -r_y & r_x & 0 \end{bmatrix} \tag{3.5}$$

Davies and Blewitt (2000) describe how to estimate the Helmert transformation to align the solution to an existing frame. This method can also be used to remove orientation differences when calculating station residuals. Even though there is the need to estimate a rotation between the networks no analysis of these estimates is carried out as there is no relevant information to be gained. Rotations are loosely constrained in the combination as this parameter cannot be determined from GPS measurements. All rotations are arbitrarily defined.

3.6 Combination

The combination of AC solutions are completed at selected institutions, I will focus on two of these centres. The first combination I will examine is provided by the official IGS Combination Centre (CC). The second combination results are taken from the solution produced in-house at the Newcastle GNAAC (NC1).

3.6.1 *Combination of AC Files at the IGS*

The IGS CC, during this study, was part of NRCan; here the official IGS weekly combination was computed. As with Newcastle, the IG1 combination contains the weekly estimate of selected tracking stations; it also contains information on the Earth Rotation Parameters (ERPs). There is strong agreement between the global network coordinate solutions from NC1 and IG1; therefore I will not repeat the IG1 coordinate results here. The official IG1 solution contains ERPs which are not yet included in final the NC1 solution due to numerical instabilities in some of the input AC solutions, see section (3.6.2). I will focus on the Length of Day (LOD) and the coordinates of the instantaneous rotation pole. The pole rates provide no additional information that cannot be gathered from the pole coordinates, and the Universal Time (UT) parameter is not a truly unconstrained parameter and therefore not discussed.

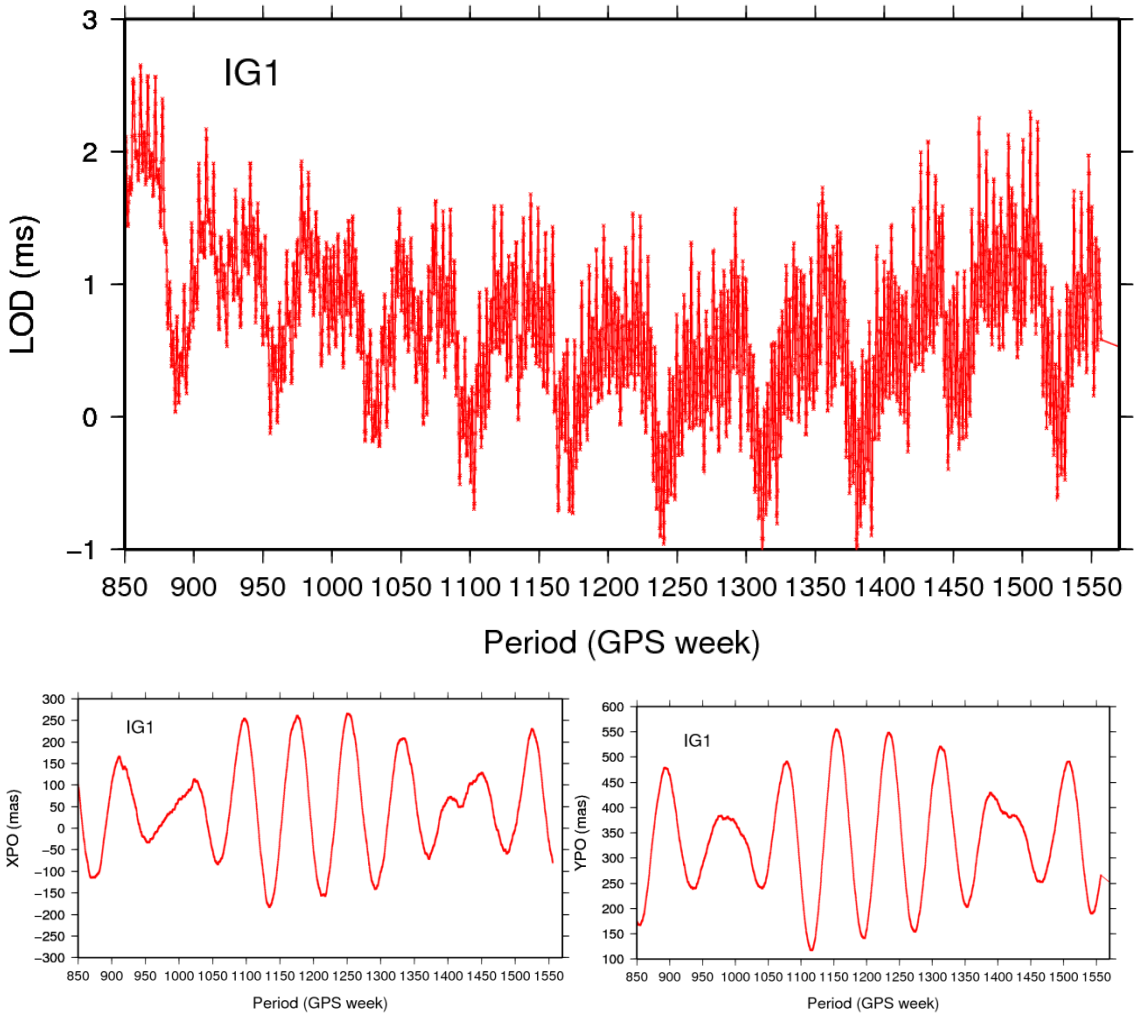

Figure 16: Earth rotation parameters, Top LOD, Bottom Left X Pole, and Bottom Right Y Pole. Produced from the IGS official combination.

Figure 16 is a full estimate of the temporal evolution of the LOD and pole coordinates using the reprocessed combination data from the GNAAC IG1. In the LOD parameter there is a regular annual repeating signal, the LOD increases during the summer months where surface masses at the poles are at a minimum and there is a shortening of the day during the winter. There is a hint of a very long, perhaps inter-decadal variation but without a more substantial data span one can only speculate about this. Inspection of the coordinates of the pole reveals a regular period to the pole location; these appear to have a consistent magnitude apart from two years where there is a significant deviation from the expected range. What is known is that the redistribution of mass will alter the moment of inertia of the Earth which alters the location of the rotation axis, this is a combination of seasonal variation and GIA (Klemann and Martinec (2009)). Figure 16 shows this variation of the rotation axis is synchronised with the changing of the seasons. Figure 17 shows the XY location of the pole and its change in position since 1997.

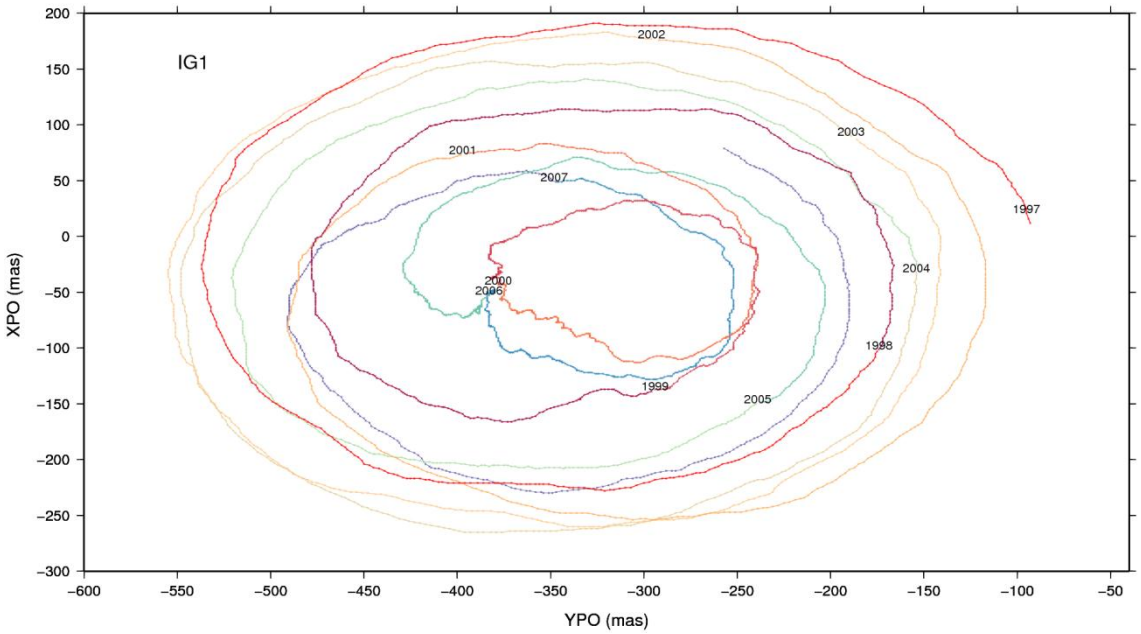

Figure 17: Daily variation of the rotation pole position YPO versus XPO.

It is possible to estimate the amplitude in each of the components (Figure 16) using a Lomb-Scargle periodogram (Press et al. (1992)). This method is used instead of the Fast Fourier Transformation (FFT) method as the FFT requires continuous data whereas the Lomb-Scargle method allows for breaks in the input data series; this is ideal for the nature of GPS data which contains some gaps due to outliers detection (Scargle (1982)).

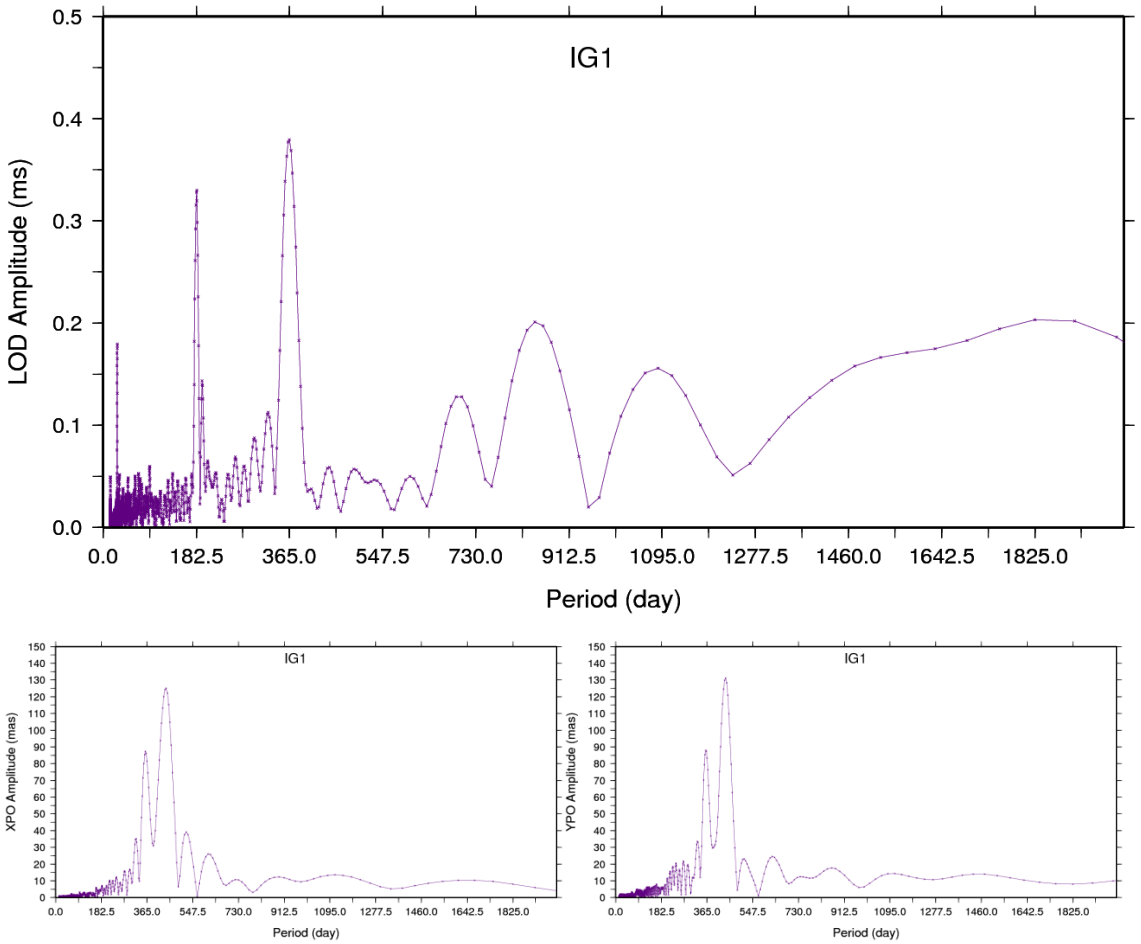

Figure 18: Amplitude in the ERPs for IG1, Top LOD, Bottom Left X Pole and Bottom Right Y Pole.

Figure 18 displays power in the periodogram at several periods. In the LOD there are the expected strong peaks at the annual and semi-annual component. Additionally there is a high frequency spike at 27.5 days which could suggest some mismodelling of sub-daily EOP. Penna et al. (2007) showed how tidal signals can alias into spurious lower frequency harmonics, with periods from 2 weeks to semi-annual. In the X and Y poles there are the two expected peaks which correspond to the annual circular motion and the Chandler Wobble of 433 days.

3.6.2 *Combination of AC Files at Newcastle*

As discussed previously the combination at Newcastle has been achieved via the bespoke software TANYA. Previously TANYA applied fiducial constraints to a sub set of core network stations, which has been shown to introduce errors into the global network estimation (Blewitt et al. (1992)). Fiducial analysis involves selecting a subset of stations and fixing their coordinates, these stations then provide a “truth” to tie the calculated network by altering the

calculated subset station position so they equal the fixed values, this can distort the network and introduce large errors. In the early stages of this study steps were taken to change the processing strategy from applying fiducial constraints to a subset of core stations, to a process of estimating and applying a Helmert transformation between the weekly solution and the chosen reference frame (IGS05). This prevents any error from being introduced from applying fiducial constraints. Section (3.5.3) describes the estimation of a 14 parameter Helmert transformation between the weekly solution and the chosen reference frame. What is not described there is the estimation of the ERP transformation. This was implemented using the techniques described by Altamimi et al. (2005):

$$\begin{aligned} X_i^{pole} &= X_{IGS05}^{pole} + R_y \\ Y_i^{pole} &= Y_{IGS05}^{pole} + R_x \\ \dot{X}_i^{pole} &= \dot{X}_{IGS05}^{pole} + \dot{R}_y \\ \dot{Y}_i^{pole} &= \dot{Y}_{IGS05}^{pole} + \dot{R}_x \\ UT_i &= UT_{IGS05} - \frac{1}{f} R_z \\ LOD_i &= LOD_{IGS05} + \frac{\Lambda_0}{f} \dot{R}_z \end{aligned} \tag{3.6}$$

Where i is the individual solution and $R, \dot{R}$ are the rotation and rotation rate respectively, $f = 1.002737909350795$ is the conversion factor from UT into sidereal time and $\Lambda_0 = 1$ at a daily basis. UT is shown here for completeness but is not considered in the solution as it is not a freely estimable parameter by GNSS.

Once the Helmert transformation between the chosen solution and reference frame has been estimated then the calculated rotations, translations and scale change must then be applied to the solution at each epoch to enable any comparison; these values are plotted in section (3.6.7). The rotational parameters are not included in the detailed analysis as they have no physical meaning.

A great amount of effort was taken to include the ERPs into the Newcastle combination. This was achieved and initially ERPs were included from a subset of AC's. However for some unknown reason, ACs which have a full a priori matrix of the ERPs proved numerically unstable during the inversion of the normal equations. It was decided that all ERP's should be excluded instead of rejecting three vital AC coordinate solutions. It should be made clear that all

stages of ERP combination have been put in place and preliminary results of selected ACs were evaluated and as a test of quality they were overlaid over the IGS weekly combination. The inclusion of ERPs into the combination does not affect how the combined stations' coordinates are calculated; the only difference in values will be very minor numerical instabilities which are inherent in the data inversion process. As a comparison of combination quality, the initial NC1 ERP's were plotted against the established routine of the IGS CC, Figure 19-Figure 20.

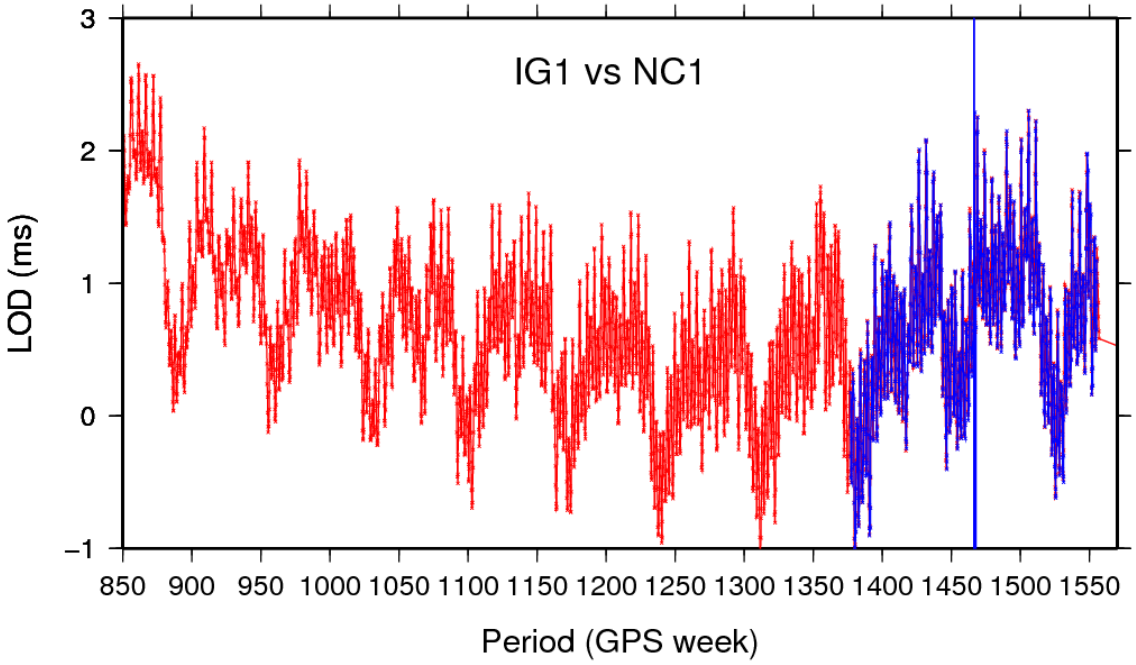

Figure 19: LOD combination: IG1 solution red, NC1 evaluation blue.

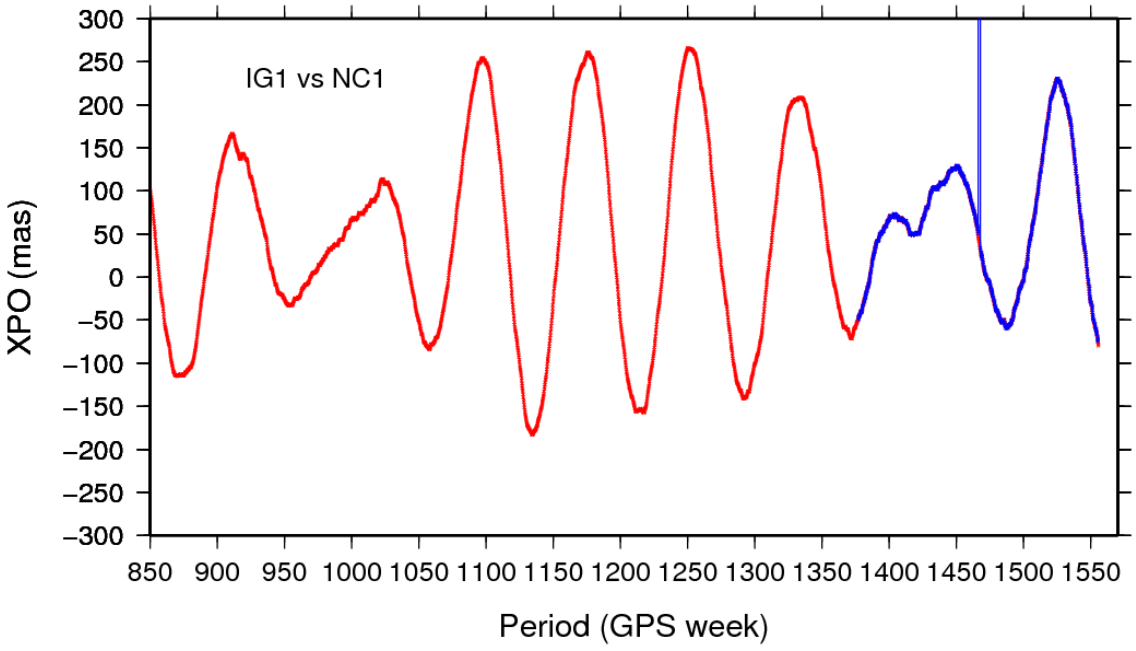

Figure 20: X Pole combination, IG1 solution red, and NC1 evaluation blue.

As discussed above, due to the instability of certain input files these parameters were not included in the final combination. However as Figure 19-Figure 20 show the NC1 combined ERPs are comparable with the IG1 combination.

3.6.3 *Combination of Operational and Reprocessed Results*

The operational global network campaign has been in existence since 1994, when the tracking network was sufficiently dense to produce a consistent global network solution. The raw data collected at these tracking stations are processed by ACs; they produce all the products stated above. This study is interested in the weekly global network computed via the weekly coordinates of selected IGS tracking stations. The fundamental model for these network solutions is the reference frame to which the GPS orbits are calculated and which the solutions are aligned to. This section briefly covers the combination of the operational processing, how the precision and parameters have changed with the adaptation of newly published models and reference frames and how they compare to the new reprocessed solutions. By calculating the Helmert parameters (Figure 27-Figure 29) and the goodness of fit of the AC (Figure 24-Figure 25) and combination solutions (Figure 26) to the chosen reference frame it is possible to begin to see the influence of model changes to the operational global network solution. It soon becomes apparent where new reference frames are implemented, this effect is compound with the introduction of the absolute phase centre antenna model in GPS week 1400, (Figure 29). Although this is not the only model introduced, the effect of this is very obvious. Other models will introduce offsets and inconsistencies into the time series which are not so apparent. There are several parameters which can be interrogated to test the quality of the input data and the quality of the combination. In the following sections (3.6.5-3.6.7) I will discuss the different statistical parameters (number of stations, WRMS and Helmert Parameters) of the operational, reprocessed and NC1 combined solutions respectively. For all operational plots the black vertical lines represent the adoption of a new reference frame, these lines do not appear on the reprocessed plots as they use IGS05 for the entire time series. The black lines appear on the combination plots but these only apply to the operational (red) time series and not the reprocessed (blue).

3.6.4 *Block Scaling Factors*

Block scaling factors are an attempt to scale the uncertainties of each AC solution by the AC's a priori estimation. During the operational processing these values were likely to change with the adoption of new processing techniques and models. However for the reprocessing campaign the estimates of a priori variances will remain relatively constant. The variation of BSF for each AC will iterate rapidly to a stable value, e.g. CO1 (Figure 21). Even after a clear slip in the estimation, most likely due to an outlier at ~110 weeks, the BSF soon iterates back to a stable level. There is a hint of a shift in the average BSF after GPS week 1459 which is the link between the reprocessed and current operational data set. This could suggest some slight systematic differences between the two "comparable" data sets.

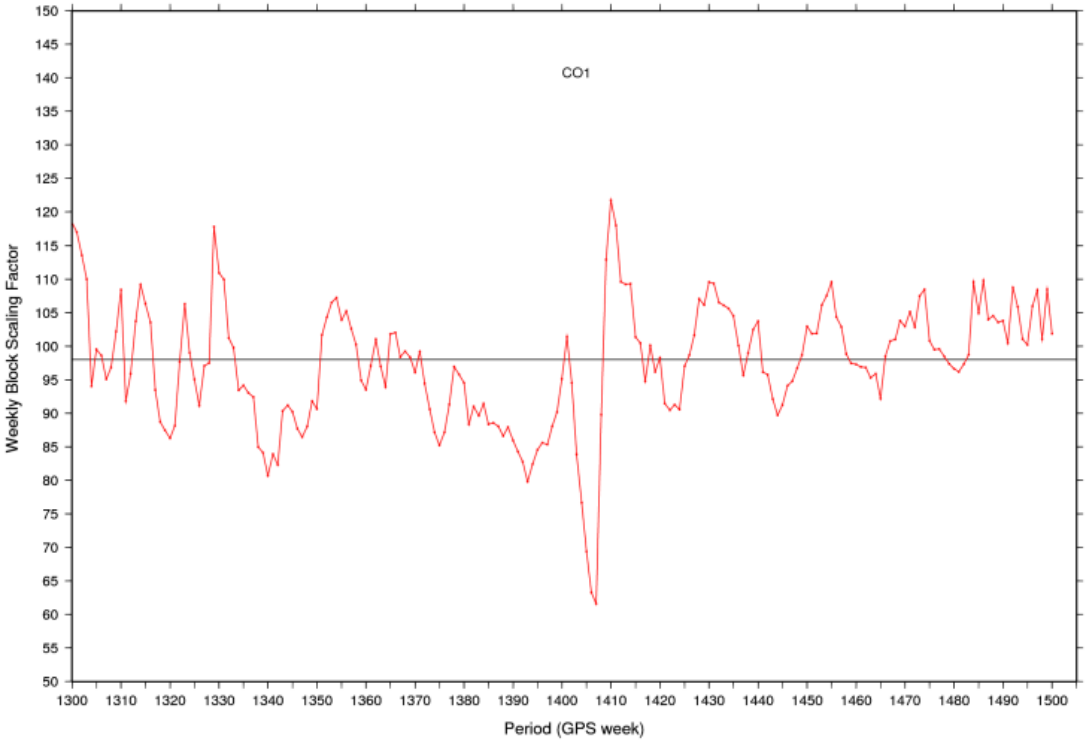

Figure 21: Time varying BSF for co1 (red) with mean line (black)

A constant value can be calculated for all ACs reprocessed data sets, Table 15.

Table 15: Calculated constant block scaling factor for each input AC

Analysis Centre	Block Scaling Factor
CO1	98.00
EM1	18.00
ES1	14.00
GF1	55.50
GT1	80.60
JP1	29.20
MI1	43.30
NG1	965.92
PD1	216.45
SI1	39.00

These values do not equal to 1 as each AC is free to set the a priori sigmas, which model the correlations between stations. The values differ between the different software packages and how the mathematical correlations are calculated by each ACs.

3.6.5 *Number of Stations in Combination*

The number of stations which are common to both the solutions and reference frame are important to a certain degree, as the number of stations increases so does the degree of freedom available to estimate a Helmert transformation. Figure 13 shows the number of stations included in each analysis centre operational solution; EMR and JPL are the only networks which have a consistent value with a gradual increase. The other ACs have large jumps which coincide with the introduction of new reference frames, most notably the largest jump occurs at week 1142 with the introduction of the IGS97. For most ACs there is an increase of approximately 50 stations included in this new frame. This is not the case for the reprocessed AC solutions Figure 14 and therefore the NC1 combined solution Figure 22 (blue line). All ACs have at least 100 stations from GPS week 1000 all the way through, most having an average value between 150-200 stations. When comparing the operational and reprocessed NC1 combination it is clear that the number of stations included have greatly increased, by nearly 100 stations each week right up until the convergence of solutions in GPS week 1459, Figure 22.

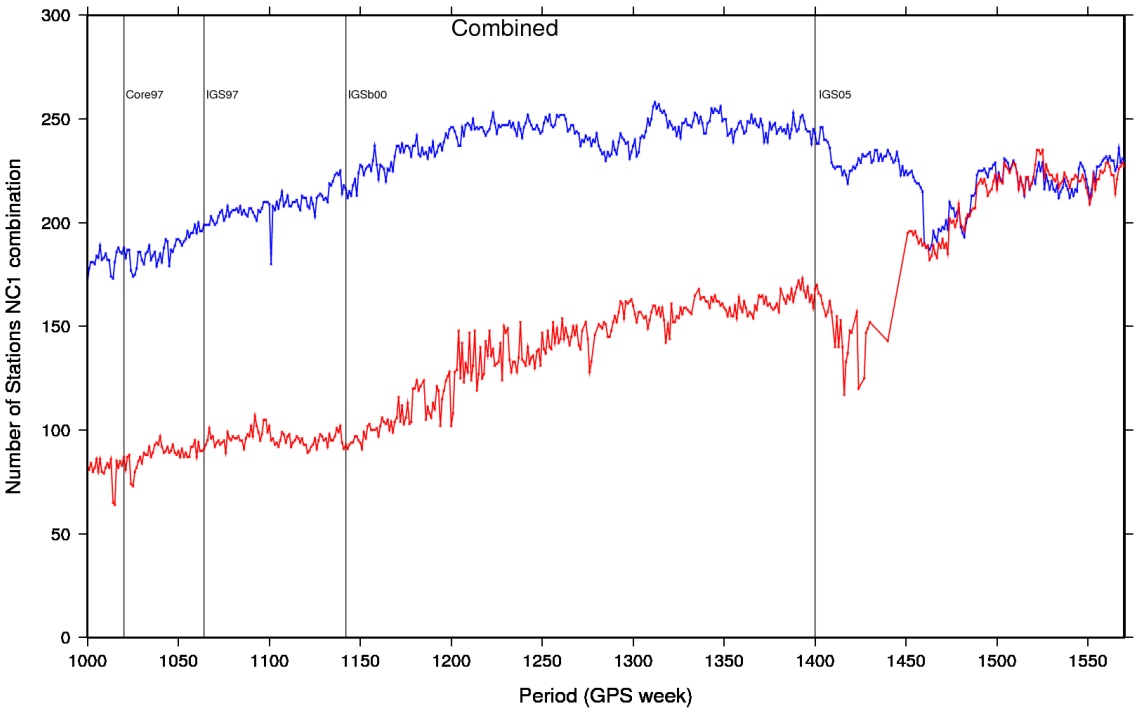

Figure 22: Comparison of the number of stations included in the NC1 combined solution: the red line is the original operational combination and the blue line is the reprocessing campaign. The black lines represent the change in operational reference frame, Table 14.

It is very clear in Figure 22 that the number of stations included in the combination is much greater in the reprocessed solution. This is due to the availability of additional IGS tracking stations. This is the first indication of the improvement to the weekly network solution. Only after week 1459 (where the reprocessed solution merges with the on-going operational solution) is there a convergence of the solutions. In theory the two solutions should be the same; the difference seen in Figure 22 is due to slightly different outlier rejection selection between the reanalysis and original weeks post 1459. Calculating the station distribution for the combined solution at Newcastle, Figure 23 demonstrates that the X and Y axes shows a station distribution of 50% ±5% which should limit the systematic errors due to station distribution bias (Collilieux and Altamimi (2009), Wu et al. (2002)). However, consistently the percentage of stations on the positive Z-axis is approximately 75%.

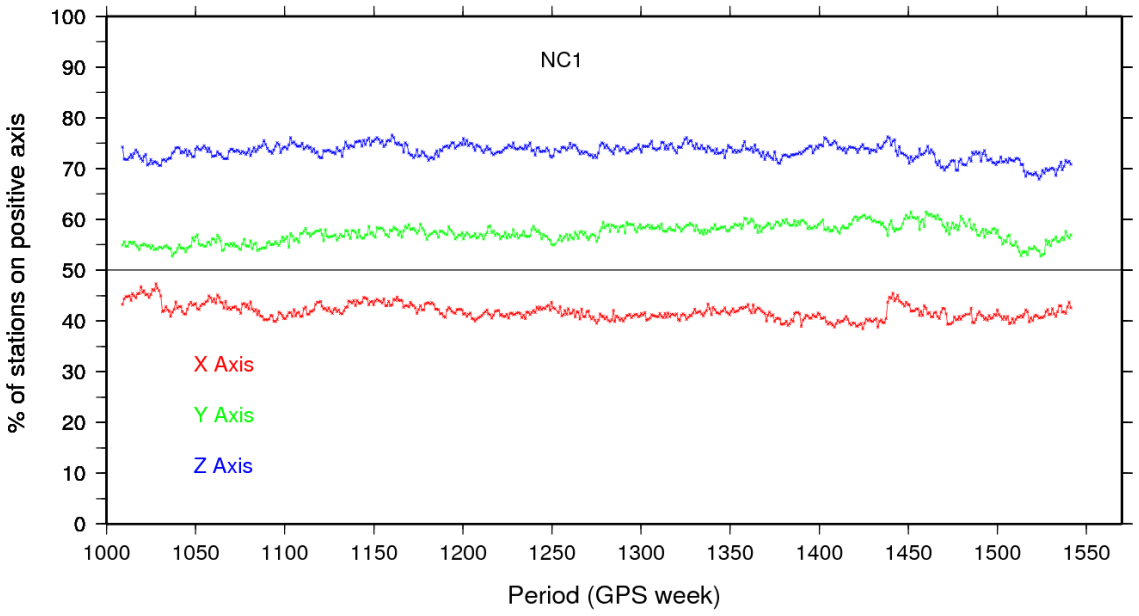

Figure 23: The percentage of stations distributed on each of the positive axes for the combined Newcastle solution, NC1.

Although it is not possible to get an idealised 50% split along each axis, especially the Z-axis, without thinning out several important stations, there can be at least be a fairly consistent inter-weekly distribution; which will minimise the error introduced by this uneven distribution (Collilieux and Altamimi (2009)).

3.6.6 *Root Mean Square error and Weighted RMS*

The Root Mean Square error (RMS) of a solution is the measure of the summation of observational scatter for station coordinates and velocities. It can also be thought of as the repeatability of the network. The RMS test statistic is defined by:

$$RMS = \sqrt{\sum_{i=1}^{m} \frac{v_i^2}{m}} \tag{3.7}$$

for m stations residuals v in the solution. Alternatively the weighted root mean square error (WRMS) accounts for the individual variances σ_i^2, which are the diagonal elements of the estimated residual covariance matrix $C_{\hat{v}}$. The WRMS is a modified version of the RMS and can be calculated by:

$$WRMS = \sqrt{\frac{\left(\frac{m}{m-1}\right)\sum_{i=1}^{m} \frac{v_i^2}{\sigma_i^2}}{\sum_{i=1}^{m} \frac{1}{\sigma_i^2}}} \tag{3.8}$$

Lavallee (2000) and Dixon (1991).

Figure 24 shows the WRMS of operational AC solutions fit to the chosen reference frame. There are several jumps in the time series which correspond to the introduction of new reference frames. The reduction in the WRMS is an accumulation of many factors including the increase in stations available to use in the solution and the improvement to the precision of reference models. However the increase in WRMS as the time series move towards the introduction of a new reference frame is due to the propagation of errors as time series moves away from the reference frame's reference epoch. There is a strongly likelihood that the number of critical TRF stations has fallen due to equipment changes or that some stations became redundant. Only after week 1400 does the WRMS regularly drop below 10mm and all ACs show a similar level of repeatability. Figure 25 is the WRMS of the reprocessing AC solutions, these all use the IGS05 and there are none of the large jumps seen in Figure 24. There is a much tighter clustering of the individual solutions throughout the time series and there is a reduction to the WRMS until approximately week 1400 before it increases; this is because the number of stations which are common to the AC and IGS05 solutions dwindles. This should be remedied by the publication of the new ITRF2008/IGS08 reference frame (Altamimi et al. (2011), Collilieux et al. (2011)) which includes a large number of active and historic stations not included in the IGS05 due to the insufficient occupation time. It should be noted that the y-axis scale of Figure 25 is three times smaller than Figure 24. The IGS05 was released for operational use in GPS week 1400, this is the frame epoch of optimal network distribution, this is why we see a reduction of the WRMS up between GPS week 1350-1400 and then the WRMS increase as we move further away from GPS week 1400.

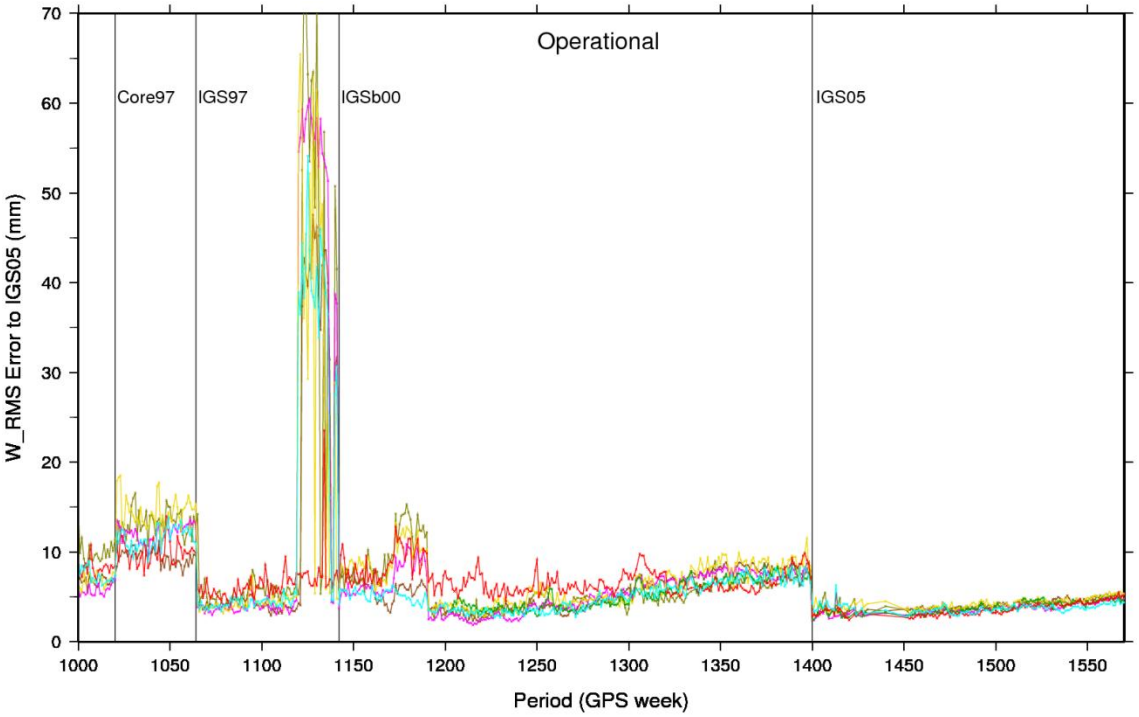

Figure 24: Weighted Root Mean Square error of operational AC solutions to the chosen reference frame. The vertical black lines correspond to different periods where reference frames are active, Table 14.

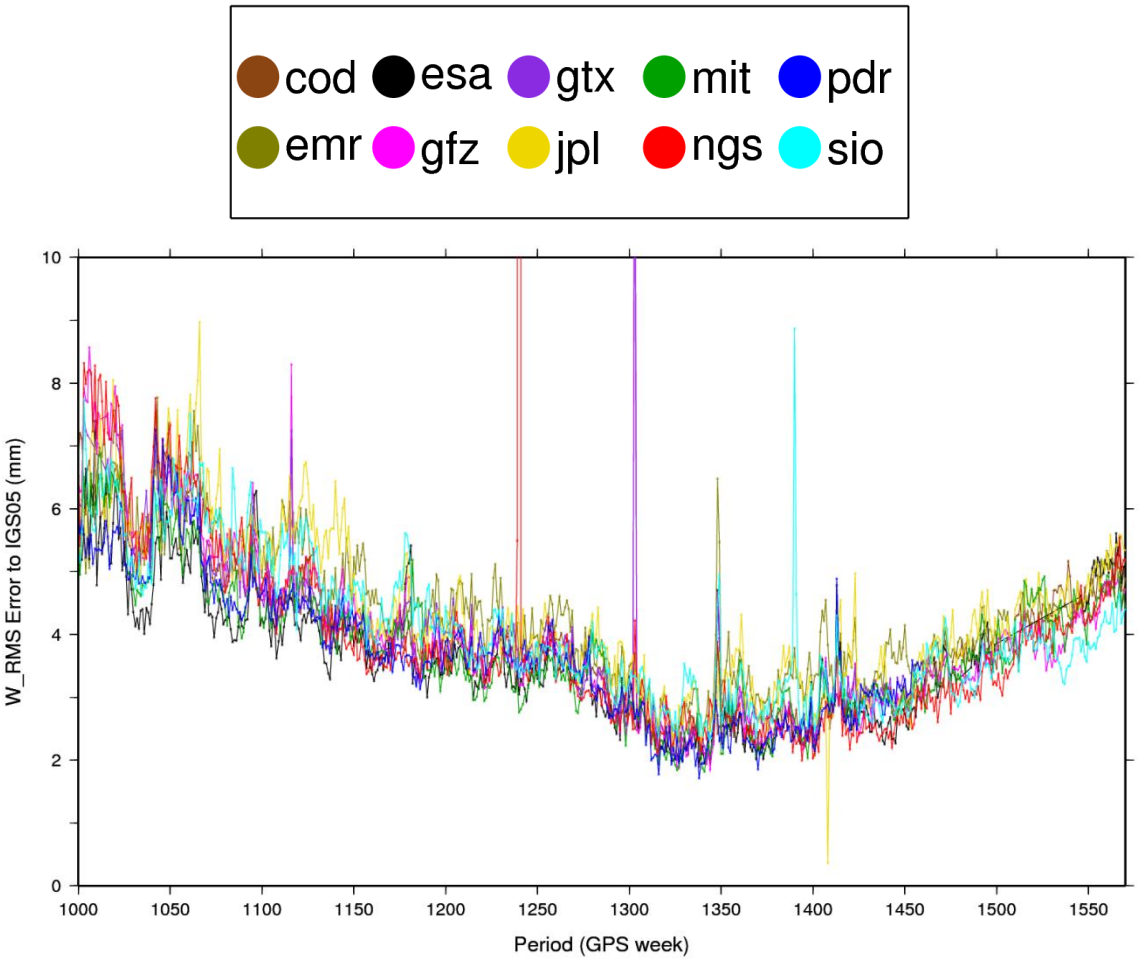

Figure 25: WRMS error of reprocessed AC solutions fit to the IGS05 solution, y-axis seven times smaller than Figure 24.

This improvement will also show in the combined NC1 solution.

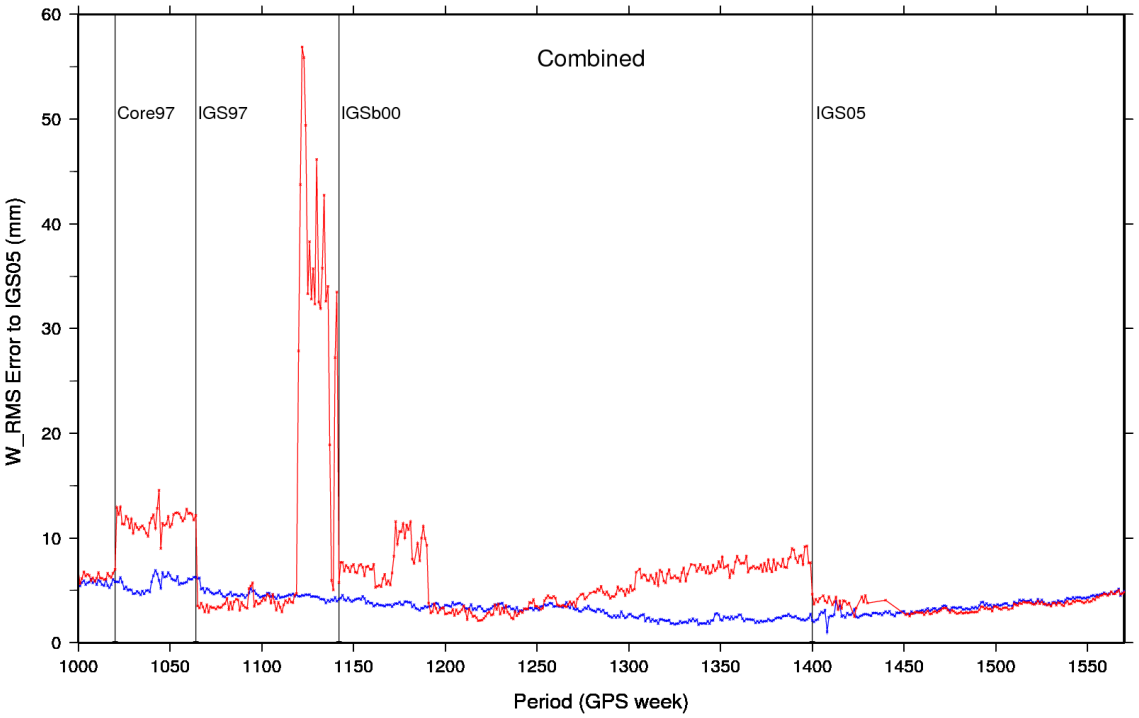

Figure 26: Comparison of operational (red) and reprocessed (blue) WRMS from combinations. The vertical black lines correspond to different periods where reference frames are active, Table 14.

Figure 26 plots the WRMS of the operational and reprocessed combined NC1 results. The improvement is striking; only after GPS week 1400 do the two solutions converge which is to be expected as the same processing models and TRF are utilised. There are none of the jumps in the residuals of the reprocessed solutions that are present in the operational residuals. On a small number of weeks the operational solution (red line) appears to show better repeatability than the reprocessed solution (blue line). This is most likely because the operational weekly network is tailor-made for the reference frame in question. For example if a site has multiple velocity estimates the operation frames have more freedom to match each section whereas the reprocessed frame (IGS05) has to fit a single velocity through the entire processing period. There is therefore the strong possibility that some periods of operational processing appear better than the reprocessing. In general the WRMS of each operational reference frame period degrades over time whereas the reprocessed solution consistently reduces the WRMS, until after GPS week 1400 without any significant spikes or offsets.

3.6.7 *Helmert Transformation Parameters*

There is a high level of inter-week variability in the operational estimated translation parameters, which may mask any shifts or signals that may be present in the data. Again there is the same pattern of offsets in the scale parameter, Figure 27, which corresponds to the introduction of the new reference frames. This is most notable at GPS week 1142 which is the date of the shift from the ITRF solution to the GPS only realisation and at GPS week 1400 which is when the IGS05 and absolute antenna corrections were introduced. The latter has an impact on the estimation of satellite orbits and therefore the scale of weekly solutions, section (2.7.3). Conversely this shift at 1400 does not appear in the translation parameters. Comparing this to the estimated transformation of the reprocessed AC solutions (Figure 28); there is a higher correlation between individual solutions and a reduced level of weekly variability (see Table 16), noting a different axis scale between Figure 27 and Figure 28. This reduction is most apparent when comparing the first 100 weeks of the operational solution to the last 100 weeks; this difference is dramatically reduced when observing the reprocessed solutions. It is clear that each solution has benefited from using the most up to date models over the entire processing period. None of the offsets in Figure 27 are seen and clear seasonal signals are evident in the Y and Z translations and scale parameters which I will investigate later on in section (3.7).

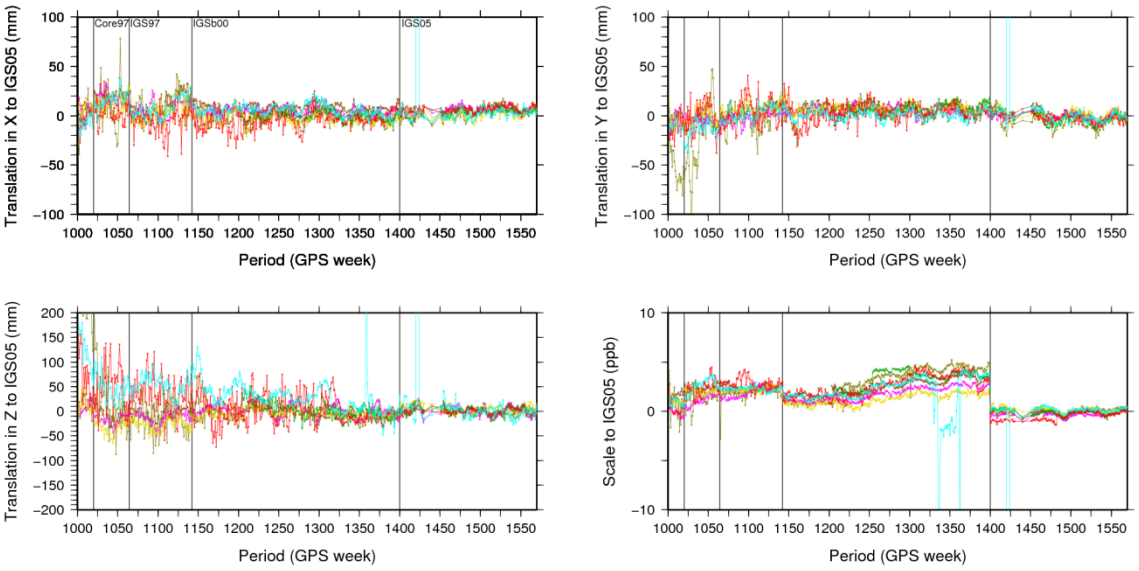

Figure 27: Detrended translation and scale parameters between operational AC solutions and the chosen IGS core solutions. The vertical black lines correspond to different periods where reference frames are active, please refer to Table 14.

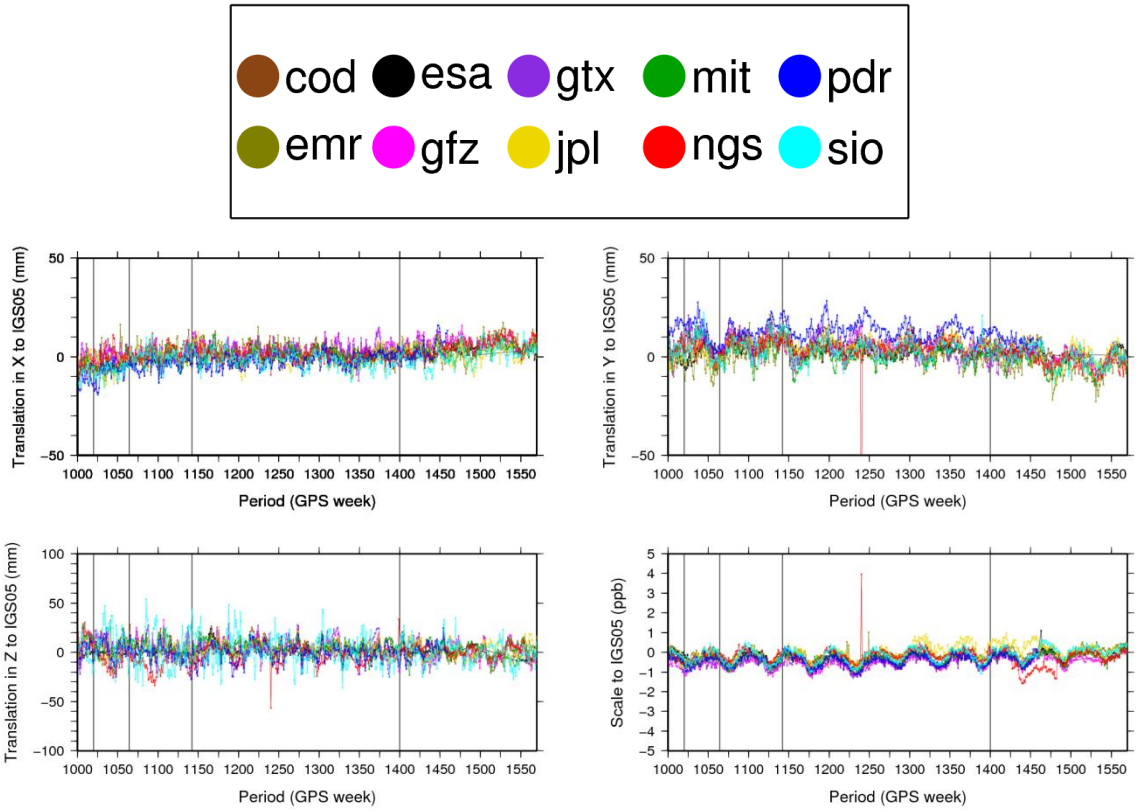

Figure 28: Detrended translation and scale parameters of the reprocessed AC solutions to the IGS05 solution. The vertical black lines correspond to different periods where reference frames are active, Table 14.

This reduction in variability will again benefit the combined solution, Figure 29,

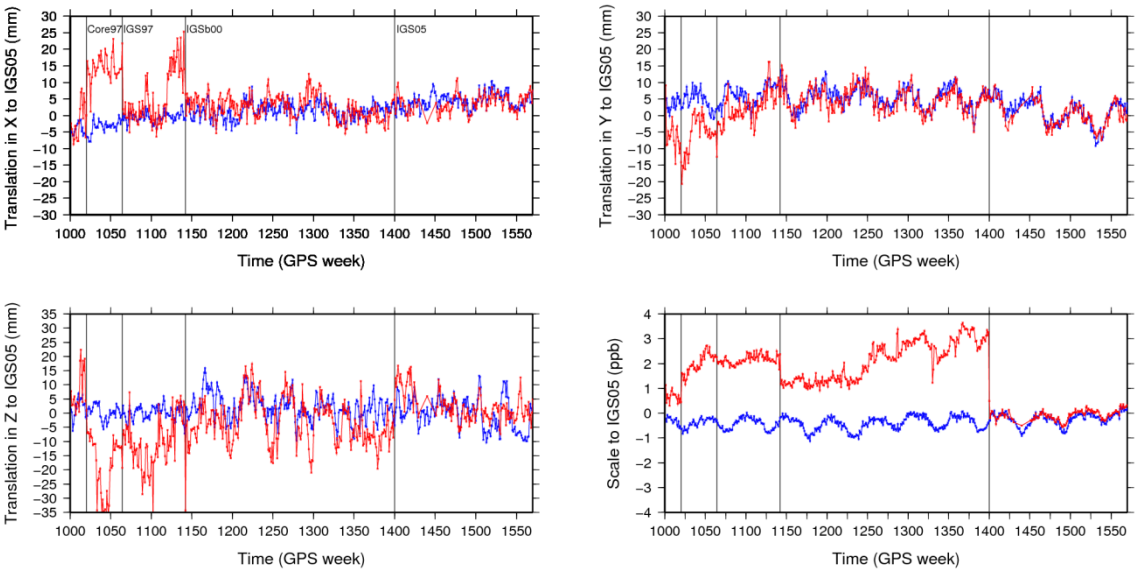

Figure 29: Combined operational (red) and reprocessed (blue) estimated Helmert transformation parameters. The vertical black lines correspond to different periods where reference frames are active, Table 14.

Figure 29 shows that although there are similar seasonal patterns in both the operational and reprocessed combinations there are no longer offsets present and the level of noise/variability is greatly reduced, Table 16. This seasonal variability and lack of trend suggests real geocentre variation on a weekly basis. This is because the IGS05/ITRF2005 doesn't represent the short term geocentre only its long term evolution.

Table 16: Average RMS of translation (mm) and scale parameters (ppb), first 100 weeks (1st) and final 100 weeks (final) of AC and NC1 Operational and Reprocessed solutions.

	Tx	Ty	Tz	Scale
Operational (1st)	28	13	42	0.78
Operational (final)	4	5	8	0.37
Reprocessed (1st)	5	5	10	0.28
Reprocessed (final)	4	4	8	0.23
NC1 Operational(1st)	8	6	13	0.60
NC1 Operational(final)	4	4	5	0.20
NC1 Reprocessed (1st)	2	3	3	0.20
NC1 Reprocessed (final)	2	3	4	0.20

3.7 Periodic Signal Estimation

It is not always possible to detect seasonal signals in a time series or estimated transformation parameters as they may be masked by undefined offsets or high levels of noise (Williams (2003b)). This has been a problem for the operational processing and one of the aims of the reprocessing campaign is to enable study into the seasonal behaviour of GPS free from processing errors. Strong periodic signals appear in many geophysical time series and this is apparent in the reprocessed/combined GPS time series used in this study, e.g. scale in Figure 29. The main period observed in the GPS time series occurs at the annual signal with a smaller but still significant semi-annual period. These periodic signals in the GPS time series have been documented (Kenyeres and Bruyninx (2006)). Periodic signals are not an issue for the estimation of linear trends as the effect of an annual signal averages down quickly after a minimum of 2.5 years (Blewitt and Lavallee (2002)). The annual signal in the GPS station time series can, to a large extent be explained by the seasonal variation of masses in the atmosphere, terrestrial water storage and atmospheric and hydrological loading (Crowley et al. (2008), van Dam et al. (2007), Heki (2003), Dong et al. (2002)).

Not all signals in the GPS time series are due to geophysical causes however. Non-loading signals have been identified in the GPS time series which is believed to be driven by systematic error combined with the repetition of the satellite geometry as it has not been found in SLR and VLBI time series (Collilieux et al. (2011), Ray et al. (2008)). The solar year has a period of 365.25 days, but the satellite geometry with respect to the Earth-Sun system repeats itself every ~351.2 days, known as the draconitic year (Ray et al. (2008)). This can manifest itself in the GPS time series producing a regular signal at the draconitic year rather than the solar year.

There has been discussion about the origin of the draconitic period (Tregoning and Watson (2010)):

- Local multipath due to the satellite-geometry repeating every sidereal day, for a 24 hour sampling period the alias period is the draconitic year (King and Watson (2010)).
- Mismodelling effect in the satellite orbits.
- Errors in the a priori IERS model for the sub-daily tidal EOP variation on GPS orbits.

It is not the aim of this thesis to investigate the source of this potential error, only to note that it is present in all IGS products.

3.7.1 *Identification of Periodic Signals*

Periodic signals appear in all station time series with a varying amplitude and phase; it is possible to identify the largest of the signals in some transformation parameters or GPS time series by a quick visual inspection. The largest signals appear as a sinusoidal wave; smaller signals will be present but may not be visible due their low amplitude compared to the larger signals. This will identify signals in the time series; even those which do not appear to have significant power to influence the time series. This technique will also demonstrate the level of noise present in the GPS time series and can be used to determine the type of noise present in the data. A Lomb-Scargle expansion comprises the fundamental frequency plus any number of harmonics. The fundamental frequency in a time series can be modelled by:

$$x_{t_i} = a\cos\left(2\pi f t_i - \varphi\right) + v_i \tag{3.9}$$

Any periodic signal will have an amplitude a at the given fundamental frequency f with a given phase lag φ and random errors v_i, in this work the Lomb-Scargle uses an oversampling factor of 10. Additional terms can be added to (3.9) as various harmonics. In the spectral domain any significant periods in the spatial time series will appear as distinct peaks in the power series. I would expect to see peaks at the annual and semi-annual periods of the solar year. Some peaks may be present at the draconitic periods and its multiples especially two, three and six (Ray et al. (2008)).

Due to the sampling frequency of the reprocessed submissions (weekly) it may not be possible to distinguish between the two periods as their periods are very close and can appear as the same signals due to the temporal resolution, Santamaria-Gomez et al. (2011) determined the resolution of distinguishable periods as 0.1cpy and Collilieux et al. (2007) determined 0.106cpy for the studies data span, although these values are not directly transferable to this study, it shows that it may not be possible to separate the draconitic and solar periods especially at the 1st and 2nd harmonics for ~10 years of GPS data.

3.7.2 *Periodic Signals in Calculated Parameters*

The first set of periodograms I present (Figure 30-Figure 31), will inspect the Helmert parameters of the operational and reprocessed AC solutions respectively, followed by the operational and reprocessed combined solutions (Figure 32-Figure 33), respectively.

Considering the operational solutions Helmert parameters of the AC solutions (Figure 27) there is not the expected prominence of the annual and semi-annual periods shown in Figure 30. The most likely reason for this is due to the offsets early in the operational time series GPS weeks (1000-1150) and the high level of variability in each AC solution. Some solutions (GFZ, JPL and NGS) show an annual period in the T_Y component but even these peaks have sidelobes due to aliased error.

Comparing Figure 30 with Figure 31, the latter which relates to the reprocessed AC solutions (noting the different y-scales), the emergence of geophysical signals becomes more apparent above the process noise. In the spectral domain there are more prominent spikes at the reprocessed annual periods for the T_Y and scale components with some ACs having an annual T_Z component. There are also smaller but still significant spikes at the semi-annual periods in the T_X,T_Z and scale components. What has become clear after comparing the operational to the reprocessed periodograms is that there are many more visible peaks in the reprocessed data than the operational data most likely due to the homogeneous nature of the time series and the reduced levels of high frequency and random noise.

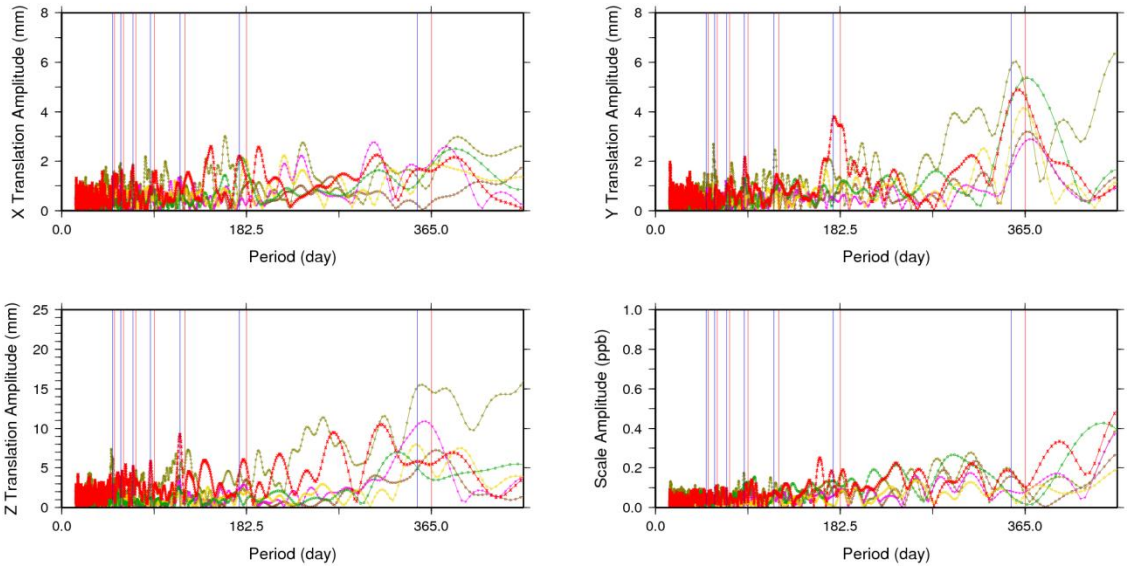

Figure 30: Helmert parameters in the spectral domain of the operational AC solutions. The blue lines represent the draconitic year and the red lines represent the solar year, each with its higher frequency harmonics.

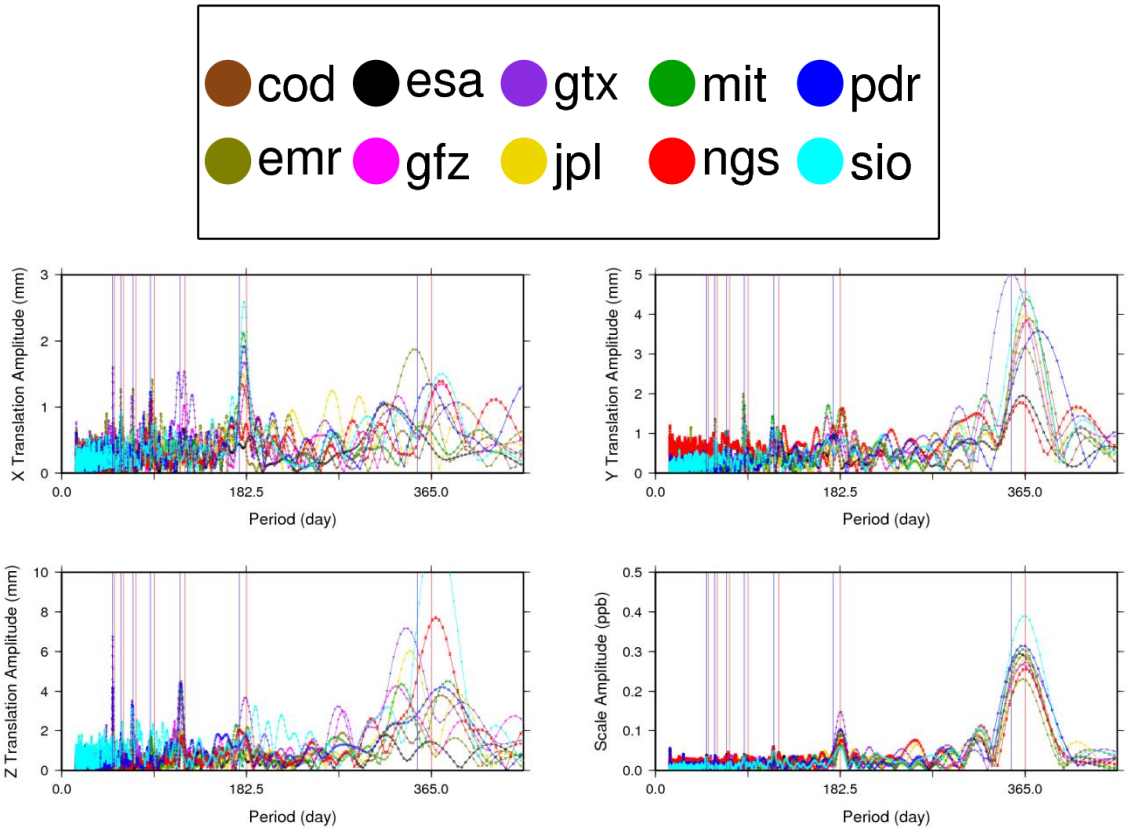

Figure 31: Helmert parameters in the spectral domain of the reprocessed AC solutions. The blue and red lines represent the draconitic and solar year respectively, each with corresponding higher frequency harmonics.

The annual peaks in the translation components ($T_{X,Y,Z}$) in Figure 31 could be linked to the movement of the geocentre (Moore and Wang (2003)); this geocentre motion is caused by the seasonal transportation of surface masses especially in the T_Z component (Lavallee and Blewitt (2002)). There are other

significant peaks (2^{nd}, 3^{rd}, 5^{th} and 7^{th}) present in some of the translation parameters. Ray et al. (2008) examines possible harmonics in a variety of geophysical loading models and geodetic time series and concludes that for geodetic observations it is not possible to distinguish between the 1^{st} and 2^{nd} harmonics of the solar and draconitic periods (1cpy and 1.04cpy) but the higher frequency peaks are almost certainly harmonics of the draconitic as these are not present in other geodetic techniques. From the loading models Ray et al. (2008) determines that the atmosphere has a distinct annual signal but very little power sub-seasonally. A hydrological model shows potential harmonics up until 8cpy for the solar period (1cpy) but Ray et al. (2008) concludes that the loading models show strong seasonal peaks but there is little to no evidence of sub-seasonal peaks as seen in the GPS spectra. This is further examined in section (4.5).

Considering the NC1 combined operational solutions, Figure 32, there is little evidence of distinct signals in any of the Helmert Parameters apart from T_Y where there is a spike at the annual period rising above the noise.

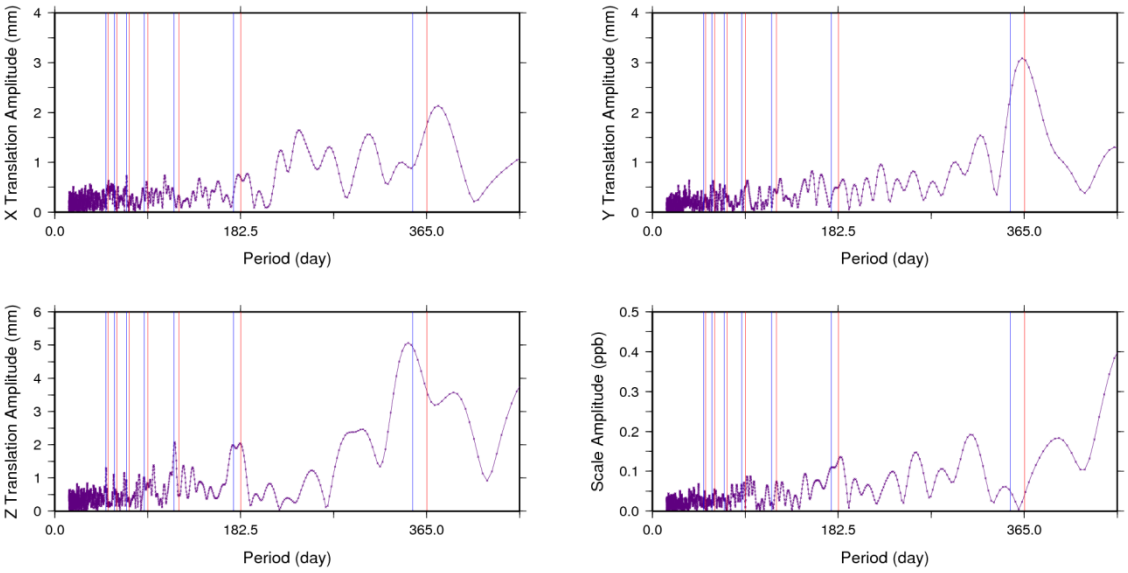

Figure 32: Helmert parameters of the combined NC1 operational solution. The blue and red lines represent the draconitic and solar year respectively, each with corresponding higher frequency harmonics.

What first becomes apparent by comparing Figure 32 with Figure 33 is the clear emergence of peaks at the annual period in the T_y and scale. This is not the case for the T_X and T_Z components as there is less coherence between AC solutions of both the amplitude and period of the annual signal even in the reprocessed data, Figure 31. There is still a certain level of base noise in the solution but this is dramatically reduced (~50%) compared to the combined operational solution.

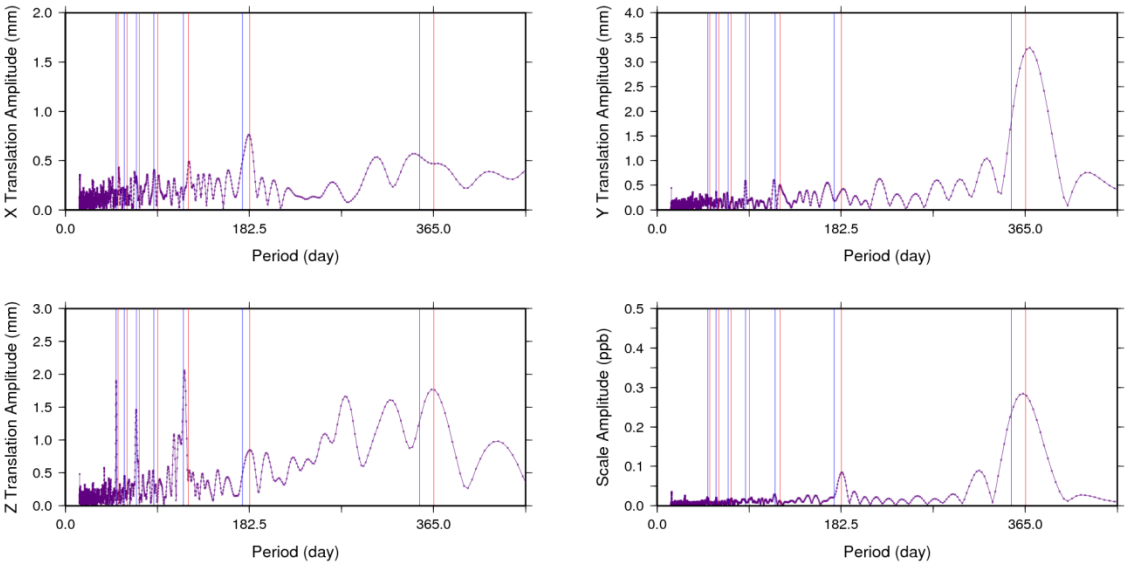

Figure 33: Helmert parameters of the combined NC1 reprocessed solution. The blue and red lines represent the draconitic and solar year respectively, each with corresponding higher frequency harmonics.

Through the reduced noise values there are clear spikes in T_x at the 2nd harmonic (2cpy or 2.08cpy), T_z has clear spikes at the 3rd, 5th and 7th harmonic of 1.04cpy and scale has a broad annual and a suggestion of the semi-annual (2cpy or 2.08cpy).

Even with the vast improvement shown in the combination of the reprocessed data versus the operational data there will always be unmodelled uncertainty in the individual station time series and in the weekly global network. Section (2.8) discusses the type and potential impact of noise on the solution and associated uncertainties.

3.8 Summary

In this section I have shown that the quality of the reprocessed solution is much better than the operational network as predicted and verified by Collilieux et al. (2011). There is still evidence of variability in some of the transformation parameters, section (3.7); this is due to the mapping of the weekly frames to a reference frame which only models the long term CM and not the weekly variability, network geometry changes and reduced residual systematic errors. The tests described above are only a measure of the AC and combined networks quality and stability. In Chapter 4 I will discuss the steps taken to produce a kinematic velocity model including individual station error detection.

Chapter 4. Combined Time Series

In the previous chapter I discussed the combination of AC weekly solutions into a weekly unified combined network. This is the first stage of a two stage process to estimate a kinematic reference frame containing station coordinates and velocities. The second stage combines these weekly Newcastle GNAAC solutions into a single kinematic solution, section (4.1). Kinematic solutions have been used to determine crustal deformation (Kreemer et al. (2000), Lavallee and Blewitt (2000), Blewitt and Lavallee (1999)), atmospheric loading (Tregoning and van Dam (2005b), Tregoning and van Dam (2005a), van Dam et al. (1997), van Dam et al. (1994)) and hydrological loading (Crowley et al. (2008), van Dam et al. (2007), Davis et al. (2004), van Dam et al. (2001), Dong et al. (1997)). This work builds on the previous work of Lavallee (2000); in his thesis Lavallee produces a global kinematic reference frame derived from GPS observations, in addition to this a set of plate rotation vectors were calculated. The frame was estimated using four years of global and regional GPS combinations which were combined using a free-network approach, estimating offsets and periodic signals. Lavallée uses a fractal white noise and random walk noise model when calculating his uncertainties.

4.1 Kinematic Model

The process of estimating the weekly combined solution is described below. The linear progression of any station's position at a chosen epoch t_i is a function of the station position X_{t_0} at the chosen reference epoch t_0, plus the estimated linear velocity for the chosen station, $\dot{X}$.

$$X_{t_i} = X_{t_0} + (t_i - t_0)\dot{X} \tag{4.1}$$

Both X and $\dot{X}$ are 3×1 linear matrices of the station's Cartesian components.

$$X = \begin{pmatrix} x \\ y \\ z \end{pmatrix} \qquad \dot{X} = \begin{pmatrix} \dot{x} \\ \dot{y} \\ \dot{z} \end{pmatrix} \tag{4.2}$$

Davies and Blewitt (2000).

The combined data set contains weekly coordinate estimates of selected sites, y_{t_i} which correspond to the epoch t_i. These weekly estimates comprise n_{t_i} station coordinate triplets X from (4.2).

$$y_{t_i} = \begin{pmatrix} X_{1,t_i} \\ X_{2,t_i} \\ . \\ . \\ X_{n,t_i} \end{pmatrix} \tag{4.3}$$

The number of stations in each epoch solution y_{t_i} varies week to week, with stations being decommissioned or added to the network. A reference position for all stations must be recorded; at the reference epoch t_0 there are m stations. The number of stations m at the reference epoch t_0 is greater than or equal to that at any chosen epoch t_i as all stations have a reference record but not all stations will be present in a particular week's solution. For m stations in the study there are m (3×1) positions at the reference epoch t_0 and their associated m (3×1) velocities. This forms the least squares model vector:

$$Y_{t_0} = \begin{pmatrix} X_{1,t_0} \\ X_{2,t_0} \\ . \\ X_{m,t_0} \\ \dot{X}_1 \\ \dot{X}_2 \\ . \\ \dot{X}_m \end{pmatrix} \tag{4.4}$$

The observed estimate of a station's position at epoch t_i takes the form $y_{t_i} = A_i Y_{t_0}$. The design matrix A_i has dimensions $3n \times 6m$ and its non-zero sub-matrices are 3×3 identity matrices selecting the station coordinates and 3×3 identity matrices multiplied by the time evolution from the reference epoch $(t_i - t_0)$ selecting the velocities. If a station from list m is not present in the weekly solution n then these sub-matrices are set to zero. For a single station the design matrix takes the form:

$$A_1 = \left[\begin{array}{ccc:ccc} 1 & 0 & 0 & 1(t_i - t_0) & 0 & 0 \\ 0 & 1 & 0 & 0 & 1(t_i - t_0) & 0 \\ 0 & 0 & 1 & 0 & 0 & 1(t_i - t_0) \end{array}\right] \tag{4.5}$$

(4.5) can be expanded to include the m stations in an epoch solution. It is possible to introduce multiple stations into A_i to produce the weekly design matrix (4.6).

$$A_i = \left[\begin{array}{cccc:cccc} I & 0 & \cdots & 0 & I(t_i - t_0) & 0 & \cdots & 0 \\ 0 & I & \cdots & 0 & 0 & I(t_i - t_0) & \cdots & 0 \\ \vdots & \vdots & \ddots & 0 & \vdots & \vdots & \ddots & 0 \\ 0 & 0 & 0 & I & 0 & 0 & 0 & I(t_i - t_0) \end{array}\right] \tag{4.6}$$

The combined solution is solved by sequential Least Squares (LS) (Cross (1992)). This method stacks (sums) the normal equation components for each weekly solution i. The sequential LS solutions take the form:

$$N = \sum_{i=1}^{i} A_i^T W_i A_i \quad p = \sum_{i=1}^{i} A_i^T W_i y_{t_i} \tag{4.7}$$

where W_i is the associated weight matrix. The final kinematic estimate and its variance covariance matrix can be found by:

$$\hat{Y}_{t_0} = C_{\hat{y}} p \quad C_{\hat{Y}} = N^{-1} \tag{4.8}$$

As discussed previously in section (3.5.3), each weekly solution is loosely constrained to the chosen reference frame. The initial orientation and the orientation rate of the system are loosely constrained via a priori values. Each weekly solution is aligned to the chosen reference frame, in this case the IGS05 (Ferland (2006)). To be able to estimate any absolute Euler pole in the kinematic reference frame then the NNR condition must be applied. By aligning the weekly solution to a NNR reference frame each week (IGS05) it therefore applies this condition to the final kinematic solution. A complete plate model should fulfil the condition that the summation of the estimated Euler vector weighted by the plate areas should equal zero. In practice the NNR condition is only calculated over the rigid plate area and therefore it is difficult to achieve exactly zero as the estimated plate areas do not equal the absolute surface area of the Earth due to the plate boundary zones (Argus et al. (2011)). However, Kreemer et al. (2006) determined these boundary zones to have an insignificant effect on the NNR estimation. Once solved, the LS system output is a kinematic reference frame which has an origin, scale and orientation aligned to the IGS05. It is this method that I will use to estimate station velocities by including the relevant parameters.

4.2 Study Data

The data used in this study is taken from the weekly reprocessed SINEX solutions combined here at Newcastle, NC1, into a unified weekly solution. The weekly solutions span from March 1999 (GPS week 1000) to February 2010 (GPS week 1570), which covers nearly 11 years. This is almost three times longer than the previous study of Lavallee (2000) who only uses 4.5 years. I choose to use the combined solution opposed to any individual AC solution as it is superior in precision, this is also confirmed by Collilieux et al. (2011) and Davies and Blewitt (2000). Lavallee (2000) attaches regional network solutions to the kinematic solution to densify the solution but I employ no such strategy as there are no regional networks available for the reprocessing campaign. Even without these attached regional networks the global solution in this study is substantially more dense (greater number of stations and shorter average inter-station distance within each plate) than that used by Lavallee (2000). All potential IGS tracking stations are listed in the IGS catalogue SINEX file; this file is regularly updated as new stations are added to the tracking network. As the Cartesian values do not lend themselves to easy interpretation all station parameters are converted to a local up, north, east system (Hoffman-Wellenhoff et al. (1994)).

4.2.1 *Processing Strategy*

For each week a single global combined solution is produced, with an associated rejected network comprising stations which do not appear in at least three individual solutions. Outlier detection is carried out on both of these networks as described in Davies (1997). The residual time series standard deviation is calculated for each station coordinate component in each weekly combination. Any parameter which has a residual *r* times greater than the standard deviation is rejected from the offending solution, and the combination is recalculated without the offending station. This is described in Table 17.

Table 17: Combination scenario, top row represents inclusion in the combined solution; bottom row represents inclusion in each of the three theoretical AC solutions. X is a station's successful inclusion in the weekly combination. O is a station's unsuccessful inclusion in the weekly combination, x represents an included station by an AC, and o represents a rejected station from an AC.

	Week 1 AC1/AC2/AC3	Week 2 AC1/AC2/AC3	Week 3 AC1/AC2/AC3	Week 4 AC1/AC2/AC3
Station 1	X x/x/x	X x/x/x	X x/x/x	X x/x/x
Station 2	X x/x/x	X x/x/x	O x/o/x	X x/x/x
Station 3	X x/x/x	O x/x/o	X x/x/x	X x/x/x
Station 4	X x/x/x	X x/x/x	X x/x/x	X x/x/x

Table 17 is a theoretical scenario where four stations' (rows) inclusion in a weekly solution (column) is designated by X. The first row of each cell is the weekly solution and the input ACs are on the second row. For each week there are up to ten AC input solutions which are combined to create the combined solution but only 3 theoretical ACs are shown. When detecting outliers in the weekly combination the data snooping routine is solely concerned with each input AC station's solution with respect to the weekly combined solution, treating each column as an independent solution from the next column (week1/week2/week3 etc.). If an outlier is found in any of the available AC input stations (little x) then it is excluded from the input and the combination is iterated. These exclusions are shown by (o) in Table 17. In this theoretical case if a station is excluded then it no longer appears in ≥3 AC solutions and the rejected station is not considered for the weekly combination, even though the other two AC solutions for that station would be accepted. Problems arise when all ACs submit the same station error; in this case the data snooping technique will be unable to detect the rogue station. Conversely if an AC correctly identifies an outlier and alters it in their solution, (e.g. station log error), but all other ACs submit an incorrect solution then the correct estimate will be rejected. In summary this method is able to detect gross outliers in an individual AC

solution, but it is unable to detect outliers if the same error is recorded by several ACs.

As discussed in section (4.1) each weekly combined solution is achieved by solving for (4.8). Following this combination each weekly combination can be combined again following (4.3)-(4.8) to produce a single kinematic solution. The LS combination method described in section (4.1), has regularly been used for combining weekly and kinematic network solutions.

4.2.2 *Tracking network*

As of 11th April 2012 there were 439 stations maintained in the IGS network available for weekly operational analysis by ACs, which are supplemented with many other geodetic quality stations determined by each AC. Over 900 stations were considered by at least one reprocessed AC solution; the IG1 reprocessed solution considers a maximum of 631 stations which have 2+ years of observations, the IG1 solution having slightly different selection criterion to NC1. Blewitt and Lavallee (2002) explain that 2.5 years and 104 observations (Lavallee et al. (2006)) are the minimal data criteria to estimate a linear trend which minimises the error from annual and semi-annual signals and dilution of precision if estimating these. Of the 900+ stations considered in the reprocessed data set, 377 appear in the required minimum of three independent estimates during the time series. 290 of these stations meet the minimum of 2.5 years of data and 104 observations, (Figure 34), which forms the reference epoch station set m.

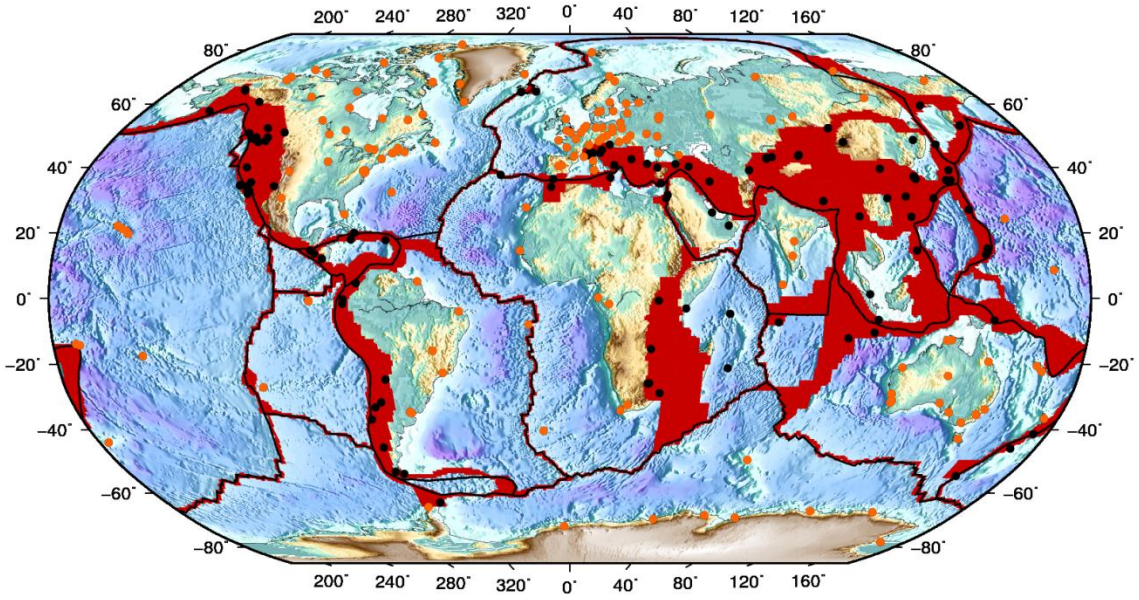

Figure 34: IGS stations that meet the requirement of appearing in a minimum of three AC solutions, 2.5 years of data and 104 observations. The areas of red are the predicted plate tectonic deformation zones (modified from Kreemer et al. (2000)). Orange dots represent stations used in this study; black dots represent stations which meet the data span criteria but fall within a plate boundary deformation zone.

The station coordinate time series represents the estimated combined weekly position from $t_{-i} < t_0 < t_{+i}$, where t_0 is the reference epoch and $t_{\pm i}$ is the earliest/latest week for each station. Gaps will appear in the station time series as they are included or rejected from each weekly combination. Any error in these station estimates will propagate through to the velocity estimate. Each coordinate position will have an associated error calculated from the diagonals of the covariance matrix.

The introduction of additional station coordinate observations into the velocity estimation will improve the precision of the plate estimates. There are some weekly deviations of station coordinates from the expected linear progression due to geophysical signals, modelling and systematic errors. Therefore, it is not possible to simply estimate a linear velocity for all included stations directly from the raw combined reprocessed data set. A full description of station offsets and outliers handling can be found in section (4.3). During the kinematic velocity estimation annual and semi-annual harmonic terms are estimated, however these are not removed as removal of these at this stage would influence the time series (Lavallee (2000)).

One geophysical cause of offsets in station time series are Earthquakes. Figure 35 shows the raw kinematic solution for the IGS site Conzception (conz) which

shows a clear offset, beside this is an example of a “clean” time series from the IGS site Potsdam (pots).

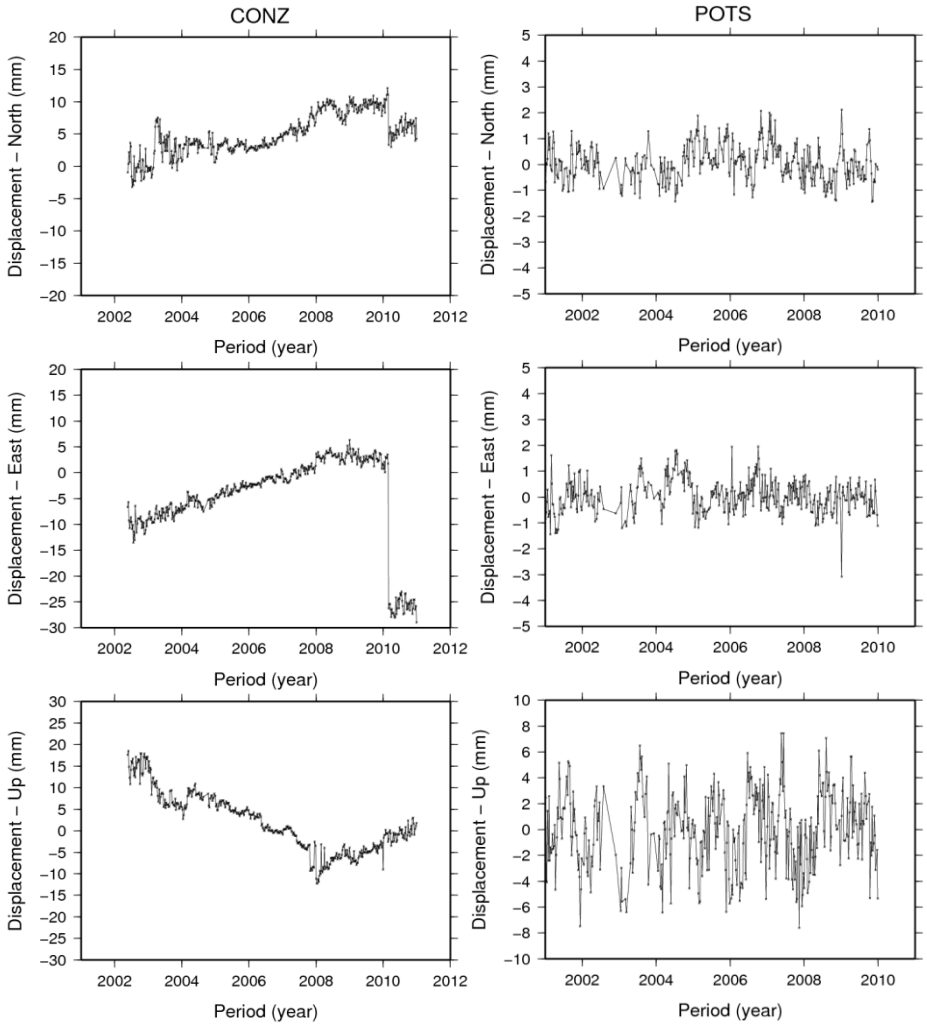

Figure 35: GPS time series of Conzception (left) and Potsdam (right), note different scales

The time series in Figure 35 have been iterated to remove gross outliers, section (4.3.1); however no remedial action has been taken to adjust the offsets (conz) at this stage. The offset in the (conz) time series at the beginning of 2004 causes a jump in the up component which is not as clear in the horizontal coordinate time series. This is most like due to an equipment change or other hardware alteration as the secular trend appears to be consistent either side of the offset; however there is no IGS station log recording any changes. The offset at the beginning of 2010 was caused by the magnitude 8.8 Earthquake in Maule, Chile on 27th February 2010 (Pollitz et al. (2011)), this consisted of co-seismic slip linked with a long period of post seismic deformation. There is also a change in the up velocity at the beginning of 2008 with undetermined origin. There are a large number of such sites deemed suitable for use in this study

(Figure 34), which are located in the predicted plate deformation zones. It is not possible to guarantee that these time series are free from linear or non-linear site motions caused by plate boundary processes. A large amount of work and assumptions would be required to check all boundary sites for simple offsets, (which have no associated transient deformation) caused by geophysical processes. The decision was taken to prevent any contamination of station velocities from non-linear plate boundary processes, by removing plate boundary sites from any further analysis. This is done prior to velocity estimation to save the trouble of cleaning up time series when they are never used. The removal of boundary stations leaves 172 sites (red, Figure 34); these sites form the core set which will be used to calculate this study's kinematic solution. A large number of these sites are situated on the Eurasian and North American plates but there are still sufficient sites on seven other major plates to be able to estimate plate tectonic velocities (Table 18).

Now that I have estimated the station coordinate time series, section (4.1), it is possible to estimate secular (linear) station velocities. The estimated linear station velocity arises from plate tectonics, GIA, secular changes in surface mass loading, and any other undetermined secular motion. In section (5.2) I discuss the estimated linear trend of plate tectonics after accounting for an a priori GIA model.

4.3 Offsets and Outlier Detection

Even with the homogeneous reprocessed time series which has had gross outliers removed from individual AC solutions, there will still be outliers and offsets due to data mismanagement (wrong station names, incorrectly recorded equipment changes…), geophysical (earthquakes, snow accumulation…) and other unexplainable causes. To be able to fully develop a global kinematic solution it is important to filter out any station outliers and offsets which have managed to pass through the data snooping routine of the weekly combination, section (4.2.1).

4.3.1 *Outliers*

Outliers are characterised as one-off deviations away from the trend of the station coordinates. In a long term solution these deviations may have only a small effect upon the overall time series, but for an individual weekly combination they can cause a large bias to the final solution. There are two

separate stages of outlier detection applied during the data process leading up to a kinematic solution. The first has already been discussed in section (4.2.1). The second data quality testing occurs when producing the kinematic solution which deals with individual station time series (along the row, Table 17). Working along a station time series, only if there are sufficient weekly estimations of the station's position (2.5 years and 104 observations) is a kinematic velocity calculated. For all included stations the weekly positional residual is calculated, if this is outside a predefined value then it is excluded from the solution and is recalculated. Iteration begins at $>6\sigma$ which iterates down to 3σ. The solution iterated over 80 times for this study; only when there are no more detectable outliers at the current residual level will the software reduce the σ threshold and begin rejecting smaller station outliers. Figure 36 shows detected outliers circled in red, for YELL, which are clear deviations from the expected value; these observations would be removed during the iterative processing of data along with other unobservable (humanly) but still statistically significant outliers.

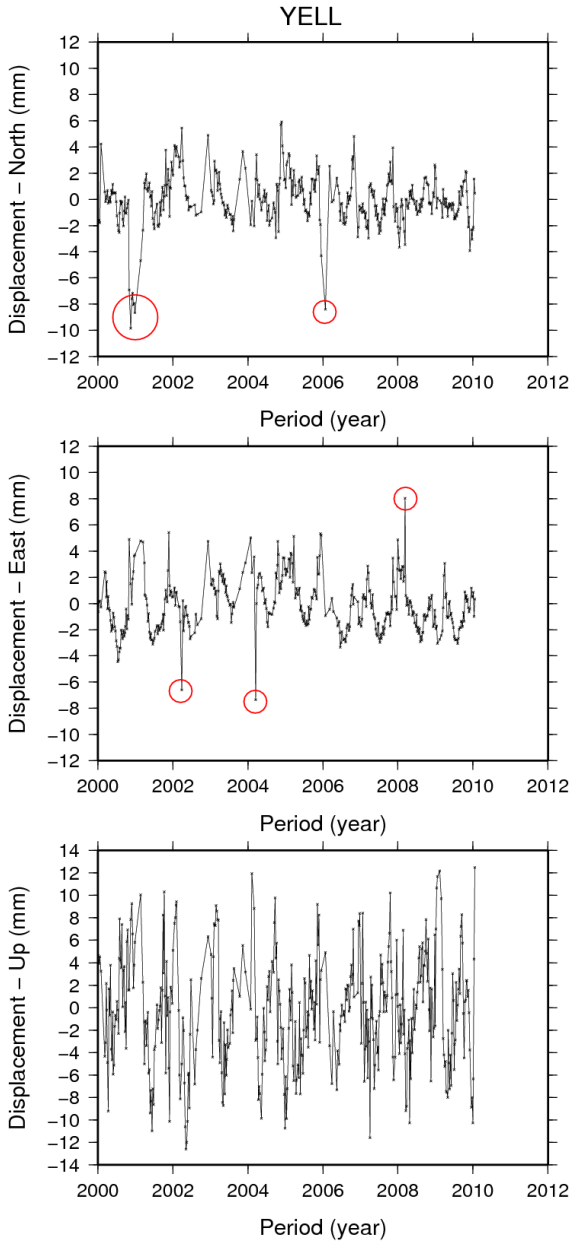

Figure 36: IGS Station YELL with outliers circled in red

4.3.2 *Offsets*

Offsets have to be handled differently to outliers; they cannot be identified in the AC combination as this is only concerned with the stability of the weekly network solution and carries out no inter-week data testing. The presence of an offset can be detected in the combination as it will materialise as a degradation of a station's RMS when aligned to a reference frame; however when they occur cannot always be so readily identified. Automation is not currently possible for offsets as they will appear as an apparent deviation of a station position from its mean which does not return to the original trend the following week. This deviation effectively offsets the mean reference value and must be taken as the new mean value for detecting outliers; as if post offset data are

treated as outliers large amounts of data will incorrectly be rejected. Currently there is no established automatic process to detect offsets; it must be achieved manually through visual interrogation which is subjective and very time consuming. Currently a pilot study, led at Newcastle is investigating automatic offset detection. This has begun to produce results, and is summarised in an IUGG poster (King and Williams (2011)) and at (http://www.cost-es0701.geoenvi.org/working-groups/working-group-3). The process of estimating offsets effectively introduces a new station estimate into the solution with the same velocity but with an additional coordinate estimate. This “new” station is still subjected to the same criteria of data span and number of observations; in principle any number of offsets can be introduced to a station time series, but the addition of additional offsets will weaken the overall solution. If a segment does not reach the specified criteria then it is excluded from any estimation. Once an offset has been identified then it is beneficial to determine the cause. An equipment change would cause the offset at the epoch of change and should not affect the post offset velocity and therefore the linear velocity estimation. An offset caused by seismic activity would not only comprise an instantaneous seismic deformation but potentially also an associated pre-seismic stress accumulation and post-seismic deformation which would appear as a transient motion to the station position (Pollitz et al. (2011)); this provides no valid data for long term studies. Earthquakes can be identified via an earthquake catalogue which categorises all major quakes, and if possible a large chunk of data must be excluded where transient motion is present. Figure 35 is a classic example of a station with clear offsets and two very different velocities either side of the offset.

In total 70 offsets have been estimated, of which all meet the data span criteria, (Appendix B). It is possible that as I am only estimating a single velocity for each station that the length of data and number of observations required does not need to be as stringent as the criteria set by Blewitt and Lavallée, but in the interest of quality I will still apply these checks. If individual velocities between offsets were estimated, to study transient velocities, then the Blewitt and Lavallee (2002) and Lavallee et al. (2006) criteria must still be applied. Even after accounting for these offsets there is still sufficient data for all 172 stations, albeit some with multiple segments.

4.4 Site Velocity Model

After several iterations of the model, I can be confident that the coordinate time series will be free from outliers. By estimating position offsets, section (4.3.2), I can be confident in the quality of data for estimating velocities using (4.1)-(4.8). As the number of station observations increases in time so does the redundancy of the solution; this strengthens the velocity estimation and the confidence that can be put behind it. The velocity estimation is a weighted LS linear fit through all station records which minimises the error of all estimates (4.1). Figure 37 shows the estimated horizontal and vertical velocities from the reprocessed data after estimating any linear offsets, assuming Gaussian white noise and coloured noise scaling factor, section (4.4.2). A full description of the handling of uncertainties can be found in section (2.8). These velocities are the secular motion of each station estimated from the time series of station coordinates; see Appendix A for a full breakdown of station velocities. Although not the focus of this study I will briefly discuss the presence of periodic variations on the velocity estimate in section (4.5) as there are some interesting results emerging from the reprocessed data, however the focus of the thesis will remain upon the secular trends.

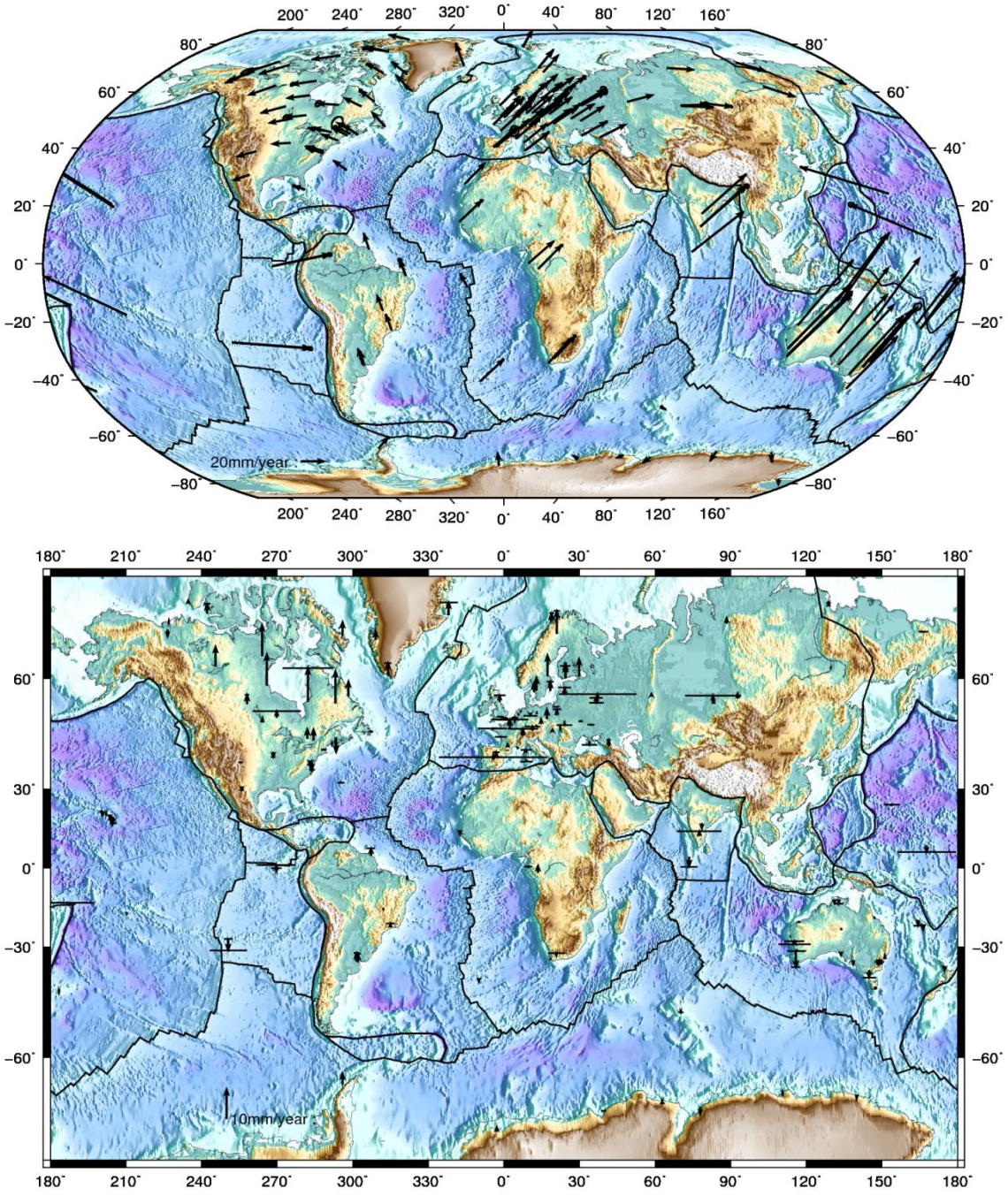

Figure 37: Raw velocity estimation at selected study sites with the modelled plate boundaries and associated error ellipses scaled as described in section (4.4.2). The top panel is the estimated horizontal velocity and the bottom panel is the estimated vertical velocity for every study site. The black lines are the mapped plate boundary zones. All horizontal plots are displayed in the Robinson projection and vertical plots are on a Mercator to ease reader viewing.

4.4.1 *Discussion of Raw Site Velocities*

Examination of site velocities will distinguish between the horizontal and vertical components. Observing the solution as a global model it is clear that stations which have been assigned to a tectonic plate tend to move with a common horizontal trend. There are two linear trends which will be considered as error in

the time series, these are GIA, section (2.4) and plate tectonic motion, section (2.5). In Chapter 5 I will be discussing the removal of GIA trends and the estimated Euler pole/plate tectonic velocity models. These global GIA/plate models will be evaluated and tested to see which improves the goodness of fit of the global vertical trends and the effect they have on the horizontal fit. Once the horizontal and vertical velocities for each site due to GIA and plate rotation have been estimated, it is possible to remove these from the site velocity. Any remaining secular trend will be due to present day secular loading or GIA model error Chapter 6.

4.4.2 *Estimation of Station Noise*

As discussed in section (2.8), estimation of station uncertainties in the kinematic solution assuming WN will underestimate the true influence. Santamaria-Gomez et al. (2011) determined that for ~13 years of reprocessed GPS data the mean power law noise amplitude is $5.8 mm / yr^{-k/4}$, with vertical velocity uncertainties ranging from 0.1-3.3mm/yr. Using this amplitude, with a sampling frequency of 7 days and the number of observations as 572, as input into Equation 32 of Bos et al. (2008) it is possible to determine the expected FN amplitude of ~1.37mm/yr for the NC1 kinematic solution. This is only a slightly larger value when comparing to the actual calculated vertical uncertainties in the kinematic solution (0.02-0.83mm/yr). This leads to a scaling factor of between (68.5-1.65), with the mean velocity uncertainty (0.11mm/yr), a scaling factor of (13) and the RMS of uncertainties (0.13mm/yr), a scaling factor of (10.5). However these values were determined assuming that all data sets have 572 observations and were free from offsets. By repeating the calculations after excluding sites with offsets and factoring in time series length produces the FN amplitude of ~2.62mm/yr. This leads to a range of scale factor values of 131-3.56, the mean scale factor is now 25.2 and the RMS derived scaling factor is 20.2.

All of the above scale factors fall within the expected range of Argus and Peltier (2010). By attempting to take into account individual station length and excluding offsets the scaling factor could almost double, but this could be due to a small number of stations with very short time series compared to the rest of the sample. It is for this reason that I will use a variance scaling factor of 20 when determining the uncertainties due to FN of the NC1 kinematic solution.

4.5 Periodic Site Displacements

Real periodic variations to a station's position are caused by the transportation of mass over the surface of the Earth. These signals appear in the station's time series and the magnitude and phase depends on the sites location e.g. strong hydrological signals in tropical river basins (Crowley et al. (2008)) or annual snow fall at high latitudes (Lidberg et al. (2007)).

It is not the aim of this thesis to investigate the source of this potential error, only to note that it is present to some extent in all IGS products. Due to the sampling frequency of the reprocessed submissions (weekly) it may not be possible to distinguish between the draconitic and solar annual periods, but higher harmonics should be identifiable.

Periods which are common to all sites, irrespective of location, may factor into the reprocessed station time series in addition to geophysical seasonal periods. The examination of individual station time series will not provide any information about systematic errors in the GPS time series as each time series will be a composition of station specific and global system effects. Dong et al. (2002) estimated that approximately half of the power in GPS time series is driven by real seasonal signals, leaving the remaining 50% unaccounted for. Ray et al. (2008) stacks multiple global station time series power spectra from operational data with the aim of eliminating localised geophysical signals, highlighting common (global) higher order draconitic spikes emerging above the background noise. Ray et al. (2008) found power at 1 cycle per year (cpy) up to the 6^{th} harmonic, however these periods are not strictly harmonics of 1cpy. These peaks could also explained by the draconitic year of 1.040±0.008cpy and its harmonics. Ray et al. (2008) and Collilieux et al. (2007) both find no evidence of similar high periodic signals (3^{rd}+) in results from VLBI, SLR or loading models, suggesting that it is a problem with the GPS system opposed to a geophysical signal.

The spectra of station time series from the NC1 combination were stacked (Clarke (2012)), to enable this, a single time series was taken and all other station time series values were interpolated to this single time series; the results are plotted in Figure 38. There is clear power at the annual solar period and potentially at the semi-annual which corresponds to the global nature of the seasonal transportation of surface mass (1.0 cpy), after which it becomes increasingly difficult to explain the higher harmonics at 1.0cpy. Using

operational data Ray et al. (2008) fits an annual and semi-annual sinusoid (1.0cpy) and presents the case that it is possible to remove these two main feature without affecting the higher harmonic peaks. Through closer examination of the strong peaks (4^{th} harmonic UNE and 6^{th} harmonic NE), Ray et al. (2008) demonstrates these can be explained by using 1.04 cpy instead of 1 cpy, also there is also some suggestion of power at the 5^{th}, 7^{th} and 8^{th} harmonics of 1.04cpy.

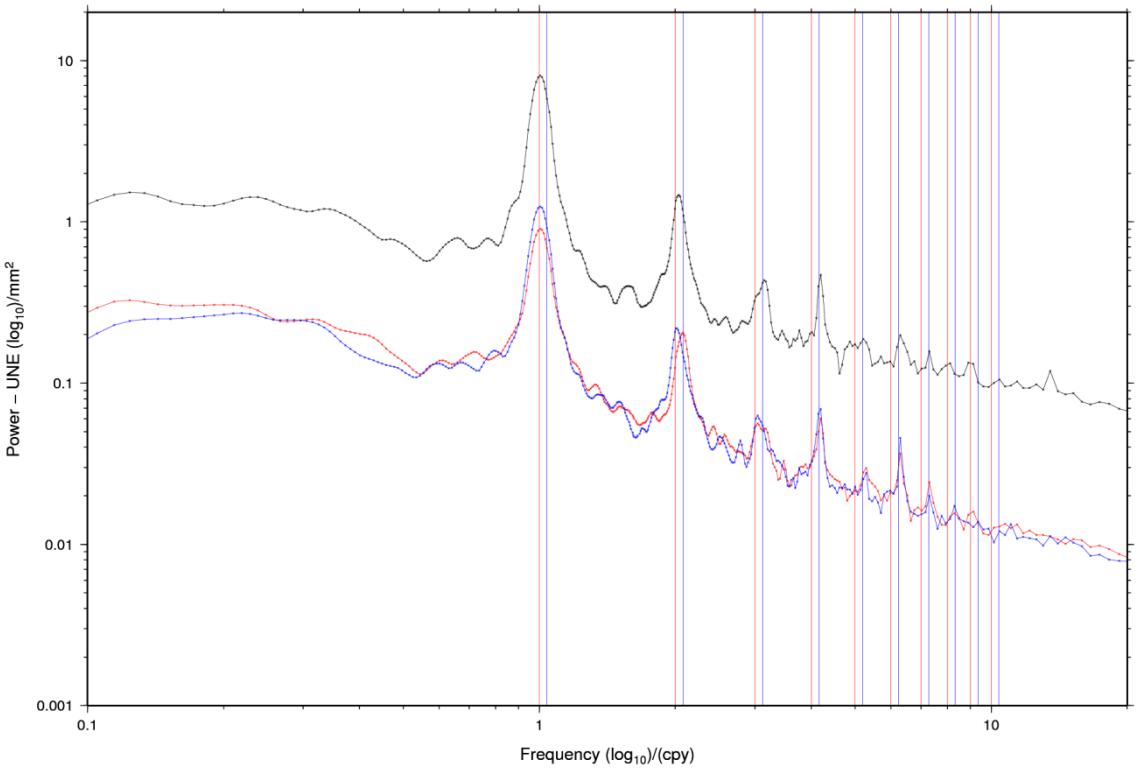

Figure 38: Stacked periodograms of non-linear station positions. Black line (Up component), Red line (East) and Blue line (North). The vertical red and blue line represents 1.0cpy and 1.04cpy periods and their first 10 harmonics respectively.

Figure 38 displays significant power at 1 and 2 cpy, 1 cpy appears to fall on the solar period for all components but it is not possible to determine whether 2cpy falls on the solar, draconitic period or both. Using the reprocessed data set strong peaks appear at higher frequency periods (3^{rd}, 4th and 6^{th} harmonics), with less distinct peaks at the 5^{th} and 7^{th} harmonics. At higher frequencies it becomes increasingly likely that these spikes appear as harmonics of 1.04 cpy (draconitic) instead of 1.00cpy (solar). Collilieux et al. (2011) analyses individual reprocessed AC solutions and determines periods of the 4^{th} draconitic harmonic in the scale parameter and 3^{rd} and 4^{th} harmonics in the Z translation, which in turn could pollute the annual period.

Ray et al. (2008) and Collilieux et al. (2007) that as a similar signal has not been detected in other geodetic techniques and that the peaks tend to coincide with a period equivalent to the repeat of the GPS satellite constellation then this would suggest a systematic error in the processing of the GPS orbits. It appears that these draconitic signals remain a problem to be addressed (hopefully) in future IGS reprocessing campaigns; however, their presence should not affect secular velocity estimates which are the main focus of this thesis.

4.6 Summary

In this chapter I have estimated coordinate time series and linear velocities of the selected tracking stations. Once these results have been iterated I can be confident in the quality of the estimated velocity with which I intend to study the secular rates of the Earth's surface. I intend to focus on the vertical and horizontal components individually and as a 3-dimensional network. In the next chapter I will develop a 3-dimensional model by combining a GIA model with the corresponding plate tectonic estimate. Using this model, instead of just estimating a linear velocity which would remove all secular trends, I can focus on evaluating the velocity residuals to this chosen velocity model which will represent secular changes in surface mass loading. I have confirmed the presence of periodic errors in the IGS analysis which have previously been presented by both Ray et al. (2008) and Collilieux et al. (2007) for operational products and reprocessed analysis Collilieux et al. (2011).

Chapter 5. Estimating a Combined Velocity Model

In Chapter 3 and Chapter 4 individual AC submissions were combined into weekly combined networks, which in turn were combined into station time series with estimated velocities. These linear velocities arise from a combination of factors including GIA and plate tectonics which are regarded here as a source of error. This chapter is concerned with the quantification and removal of both these sources of error. A range of GIA models will be evaluated and utilised prior to plate velocity estimation; combining these GIA and plate velocities will form the model. Figure 37 shows the estimated vertical and horizontal station velocities.

In work by Lavallee (2000) the focus was solely on the motions of the tectonic plates, so any vertical velocities were disregarded from the estimation and the horizontal velocity was assumed to be solely due to plate tectonic rotation (outside of plate boundary zones). It is the intent of this study to include an estimation of vertical velocities in the linear estimation, as the surface mass loading signal is greatest in the vertical. Until recently most previous studies of secular motion only accounted for plate motions (Kogan and Steblov (2008), Sella et al. (2002), Lavallee (2000), Argus and Heflin (1995)) or uplift from GIA (Bradley et al. (2009), Sella et al. (2007), Johansson et al. (2002)) separately, and there had been little in the way of study of the combined effects of GIA and plate tectonics. More recently Wu et al. (2010) attempted to simultaneously estimate PDMT and GIA values and Argus and Peltier (2010) constrained GIA models using geodetic observations.

Plate tectonics will only move sites in the horizontal plane, following Euler's rigid body rotation theory (Palais et al. (2009)). GIA and surface mass loading will influence the deformation in all directions. This study will attempt to remove the modelled vertical and horizontal velocities due to GIA prior to the estimation of plate motions by combining the GIA model with the estimation of plate tectonic rotations; thus producing the desired unified model.

5.1 Benefits of Integrating Plate Estimation with a GIA Model

The position at any time of a station is the summation of several factors,

$$X_{t_i} = X_{t_0} + \dot{X}_{GIA}(t_i - t_0) + \dot{X}_{Plate}(t_i - t_0) + \dot{X}_{other}(t_i - t_0) + \sum X_{S.M.L}(t_i - t_0) \qquad (5.1)$$

where X is a 3×1Cartesian coordinate and $\sum X_{S.M.L}$ is a summation of all components due to surface mass loading. This chapter attempts to account for $\dot{X}_{GIA}$ and $\dot{X}_{Plate}$ velocities. If a single linear trend is estimated then all secular trends will be absorbed into this term with no possible way of separating them into each term in (5.1).

$$X_{t_i} - \dot{X}_{GIA}(t_i - t_0) - \Omega \wedge r(t_i - t_0) = \sum X_{S.M.L.} + \varepsilon \qquad (5.2)$$

By implementing a GIA model with its associated plate velocity ($\Omega \wedge r(t_i - t_0)$) in the station displacement estimation instead of a single linear velocity, and assuming that $\dot{X}_{other}$ is zero, (5.2) suggests it is possible to interpret the residual trends as present day elastic deformation. I will then interpret this alongside models of surface mass loading.

5.1.1 *Construction of Combined Model*

Current processing techniques were designed to remove all horizontal and vertical velocities from the station time series; this process has been modified to use the estimated combined (tectonic plus GIA) station velocities as a substitute. The process of estimating this model velocity is laid out in Figure 39.

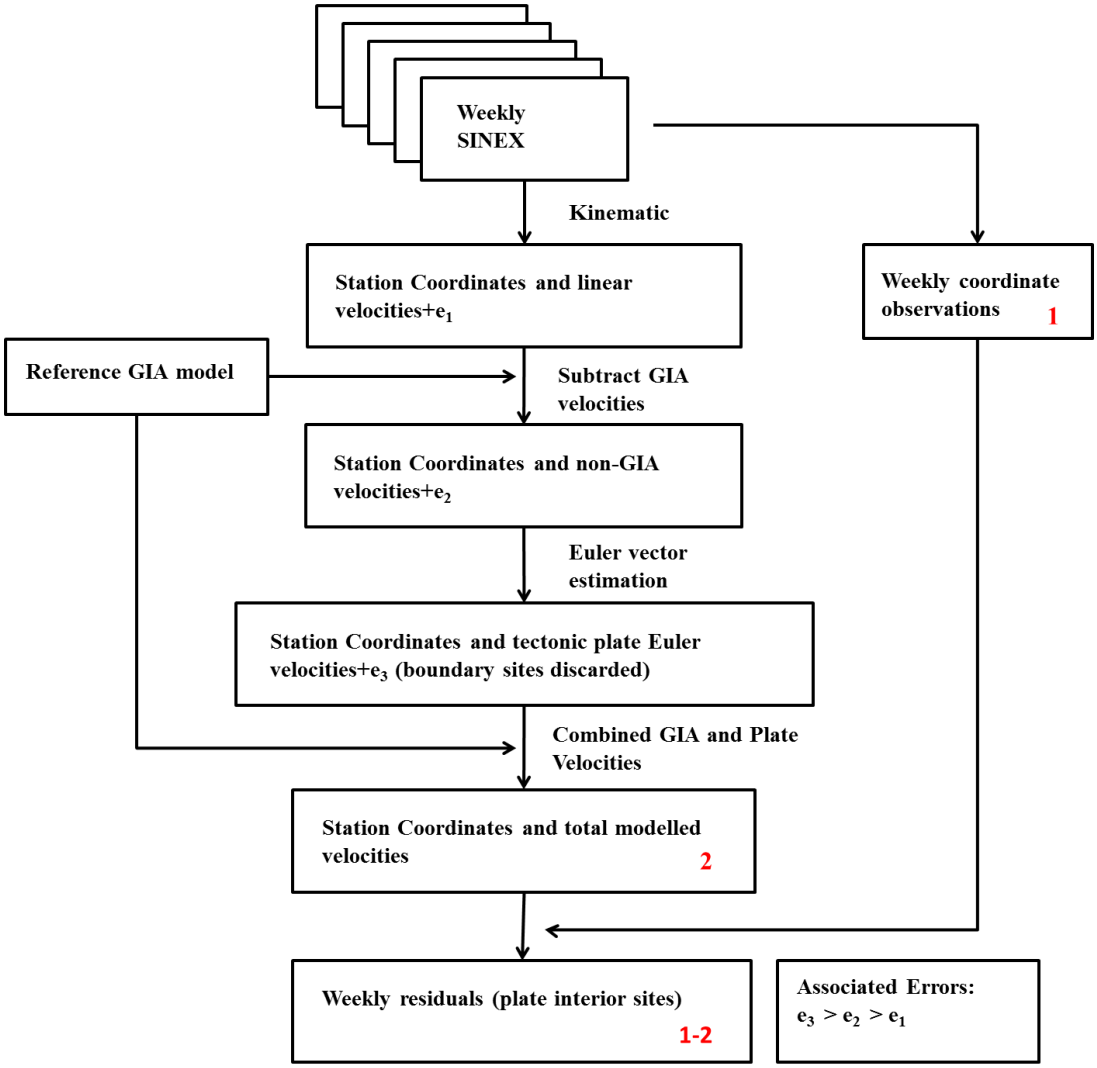

Figure 39: Schematic of modelled velocity estimation and the production of residual station velocities.

This combined model has to be created; the first step is to compute the horizontal and vertical velocities at each station from the chosen GIA model. This computed velocity is removed from the raw station velocities prior to the plate velocity estimation. Then combining the GIA modelling with the respective plate estimation produces the required combined model.

5.1.2 *Null-GIA Estimation*

In this section I will present the results without taking a GIA model into consideration, this will be known as the “null-GIA” hypothesis.

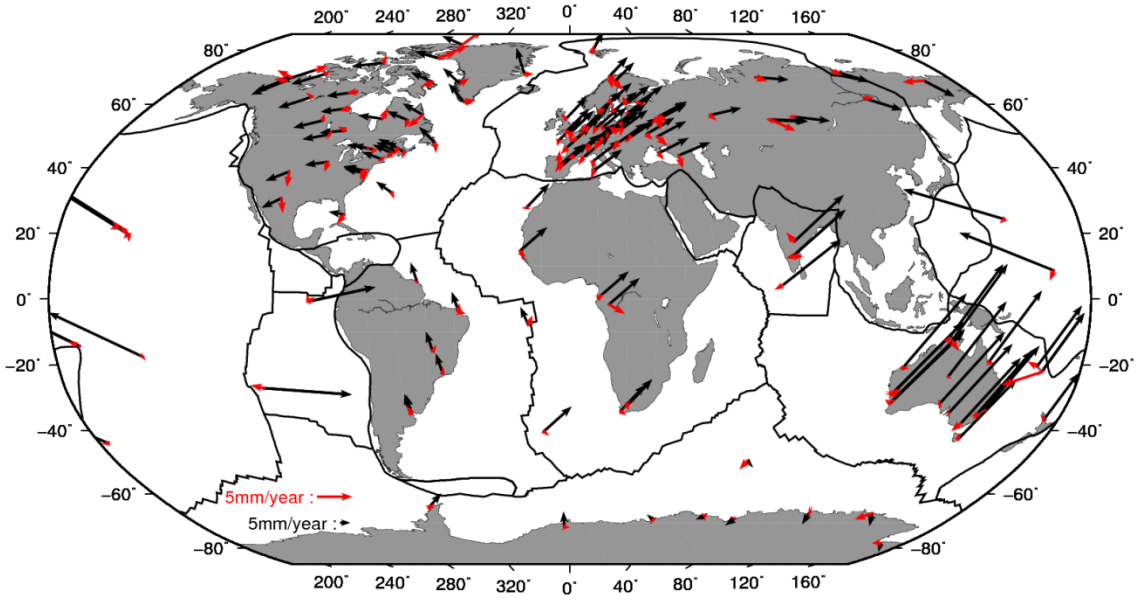

Figure 40: Estimated plate tectonic velocities for the null-GIA scenario. Tectonic plate velocity component in black and the residual component in red for each study site.

Figure 40 is an estimation of horizontal plate tectonic velocities at the chosen study sites; this reconstructs the method followed by Lavallee (2000). The horizontal fit of the estimated plate tectonic velocity component accounts for nearly all of the observed horizontal velocity at most sites. I will compare this to the four GIA scenarios to quantify the influence of these GIA models on the horizontal velocity estimation and the subsequent Euler pole estimation.

5.1.3 *Tectonic Plate Designation*

Following the strategy of section (2.5.5), I have designated each station to a tectonic plate, with Table 18 showing the number of plates on the rigid interior which will be used for the plate rotation estimate:

Table 18: Number of stations and their distribution on the tectonic plates

Plate	Number of Stations
Antarctica	9
Australia	24
Eurasia	62
India	4
Nazca	4
North America	41
Nubia	8
Pacific	12
South America	8
Total = 9	Total = 172

5.1.4 *GIA Velocity Models*

The null-GIA estimation, section (5.1.2), as discussed will not account for any vertical velocity in the overall estimation. To account for the GIA influence at each site I have the four GIA models previously introduced, section (2.4.4). Each of these models will provide a different interpretation of GIA influenced station velocities and therefore produce different Euler vector and residual secular velocity results. Figure 8 and Figure 9 show the modelled GIA vertical and horizontal velocities which I will be using to make the combined loading model.

The differences between these models will allow the evaluation of the effectiveness and impact of the different GIA models within the limitations of a small set of models. It is incorrect to assume that the model that minimises the residuals is the truth. There is no conclusive “true” estimate of present day elastic deformation so any errors in a chosen GIA model may be absorbed as unknown errors in the estimation of present day surface mass loading, see Table 20 for plate estimation RMS.

5.2 Removal of Ensemble of GIA Model Combinations

The GIA models were provided as a regular grid; using bicubic interpolation between these points it is possible to estimate each station’s GIA velocity component, Figure 8 and Figure 9. By forming the vector of velocities they can be subtracted from the raw station velocities.

$$\begin{pmatrix} x \\ y \\ z \\ \dot{x} \\ \dot{y} \\ \dot{z} \end{pmatrix}_{Non\ GIA} = \begin{pmatrix} x \\ y \\ z \\ \dot{x} \\ \dot{y} \\ \dot{z} \end{pmatrix}_{Raw} - \begin{pmatrix} 0 \\ 0 \\ 0 \\ \dot{x} \\ \dot{y} \\ \dot{z} \end{pmatrix}_{GIA} \tag{5.3}$$

The GIA models are only predictions of what is believed to be the isostatic response; they are assumed to be error free so there is no covariance information. To complete the calculation in TANYA a nominal covariance matrix of zeroes is implemented, but any further analysis of covariance will not be a true test of the stations' covariance. Horizontally there is very little difference to the raw observed station velocities with the addition of a GIA model. However the GIA models account for a large proportion of the observed vertical velocities. Examining the residual values there are still some vertical velocities after removal of each of the proposed models. This could either be caused by present day secular loading or by unaccounted GIA.

5.2.1 *Plate Estimation After GIA Removal*

Working with Cartesian coordinates, the rotation axis can be described by a 3x1 Euler vector. By using the linear velocities of all sites on a particular plate it is possible to estimate the absolute Euler vectors using Least Squares techniques. If there are systematic errors in the GIA model used, these may result in systematic horizontal rotation in a particular area and this may be aliased into the plate estimation. However the estimated horizontal GIA velocities are small in comparison to the potential velocity influence of the movement of the tectonic plates. The effect of only modelling a 1D earth has the potential to introduce errors into the estimation of horizontal rates, see section (2.4.5).

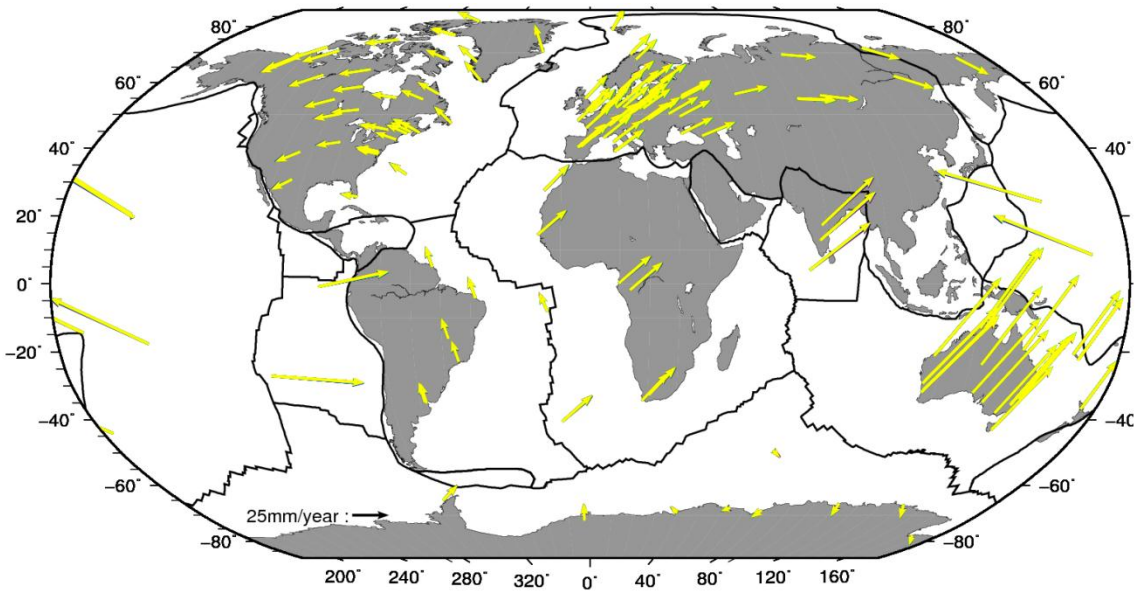

Figure 41: Estimation of nine major horizontal plate velocities for null GIA and four scenarios. Null (black), ICE5G-VM2 (Peltier (2004)) (red), ICE5G-VM4 (Peltier (2004)) (blue), Schotman (Schotman and Vermeersen (2005)) (green), Alternate Schotman (Schotman and Vermeersen (2005)) (yellow)

Figure 41 shows the null-GIA and four GIA horizontal plate estimations. Visually there is very little difference between the different plate velocity estimates after accounting for the horizontal velocity due to GIA. By using a suite of GIA models it is possible to produce four different scenarios plus a null GIA to evaluate the effectiveness of removing a secular term due to GIA. From the GIA altered velocity it is possible to estimate a GIA adjusted plate model. Section (5.2.2) describes the combination of the two respective models.

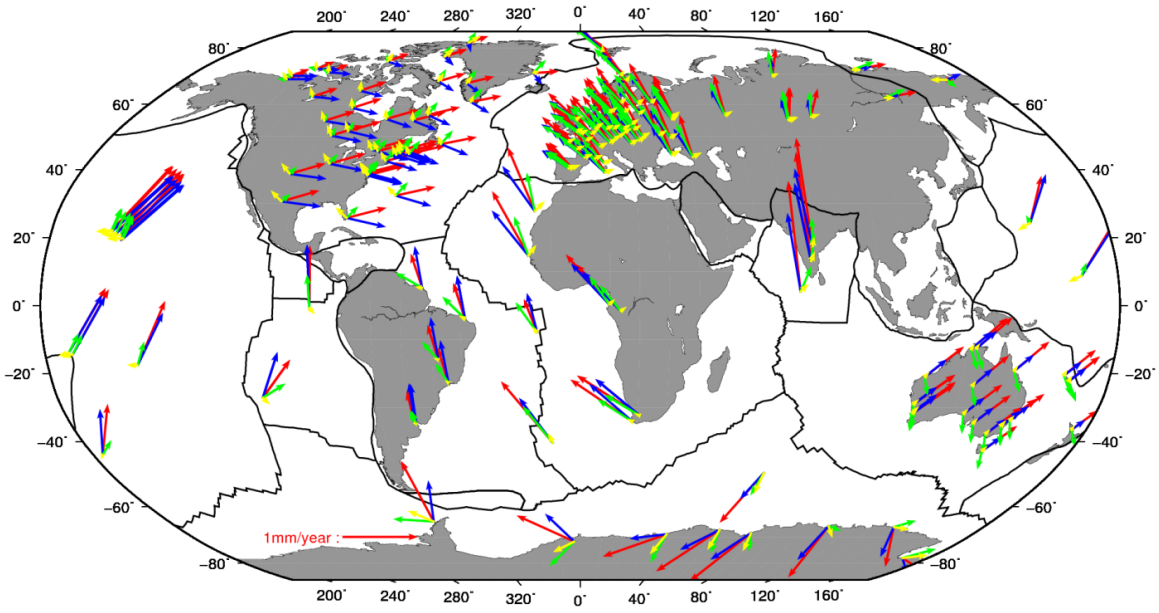

Figure 42: Difference at each station of estimated plate rotation between the null GIA model and the four GIA models. ICE5G-VM2 (Peltier (2004)) (red), ICE5G-VM4 (Peltier (2004)) (blue), Schotman (Schotman and Vermeersen (2005)) (green), Alternate Schotman (Schotman and Vermeersen (2005)) (yellow)

What Figure 42 shows is that the inclusion of the GIA model prior to plate velocity estimation makes very little differences to the overall plate estimation, with the residuals only ~1mm/yr different to the null-GIA estimation. This is a very small percentage of the overall plate velocities. There are however some distinct orientation differences between the two families of GIA model, especially over North America, the Pacific and Australia. It is these differences that the final chapter intends on exploiting when investigating present day mass trends. These small alterations are demonstrated further in (Table 20).

5.2.2 *Absolute Euler Poles*

Several studies Altamimi et al. (2011), Argus et al. (2011), Argus et al. (2010), DeMets et al. (2010), Altamimi et al. (2007), Sella et al. (2002), Lavallee (2000), Cretaux et al. (1998) and Larson et al. (1997) have all attempted to estimate the absolute Euler poles by aligning them to a NNR frame such as NNR-NUVEL-1A or the more recent NNR-MORVEL by applying a Helmert transformation. This allows for the comparison of absolute Euler poles estimated by different authors as all use slightly different realisations of the ITRF/IGS. Larson et al. (1997) determined that horizontal accuracies of 1.2-5mm/yr in velocity are attainable via GPS measurements. Early studies such as Larson et al. (1997) and Lavallee (2000) attempted to calculate the velocity of eight major plates using limited GPS data with an uneven distribution. More recently there have been

studies which have had a much larger data set at their disposal. Sella et al. (2002) presented the REVEL model which describes the relative velocities of 19 plates, Sella et al. (2002) used operational GPS data from between 1993-2000, (reprocessed at the time to limit inconsistencies) using 200 GPS stations. Instead of applying a particular GIA model, Sella et al. (2002) removed any sites deemed to be affected by GIA, this is achieved using the ICE4G model (Peltier (1994)) and rejecting any sites with modelled horizontal rates of ≥0.7mm/yr and vertical rates of ≥3mm/yr. Sites are rejected in North America, Eurasia and Antarctica. Even more recent is the NNR-MORVEL56 model Argus et al. (2011) which defines the angular velocities of 56 plates in a NNR reference frame. This model comprises of 25 plates from the MORVEL model (DeMets et al. (2010)) and 31 minor/micro plates from Bird (2003). The addition of Bird's 31 plates increases the coverage of the Earth's surface by 2.8%.

Comparing this frame to the results presented in this study enables the comparison of two different NNR realisations, ITRF2005 (this study) and Argus' own frame. Altamimi et al. (2007) estimates 15 major plates from a velocity field of 152 sites which have horizontal velocity errors of less than 1.5mm/yr and are located on the rigid plate interior and have 3+ years of data.

Table 19 lists the common estimated absolute Euler poles plus associated error ellipses. Each of these studies is supposed to meet the NNR condition; however each of these solutions is aligned to a different reference frame. Although these should fulfil the NNR, there will be slight variations to the reference frame realisations. There are large improvements to the formal errors for the Nubian, South America and Pacific plates which are down to the increased number of stations assigned to each plate from early studies (Lavallee (2000), Larson et al. (1997)) to the more recent studies (Altamimi et al. (2007), Sella et al. (2002)). The size of the error ellipse depends on both the error estimation from each input AC but also the noise model used in the kinematic estimation, section (2.8). The preliminary noise model used to estimate error ellipses in the NC1 solution assumes white noise only, which decreases in size as the number of observations increases until they become unrealistic. However this should have been accounted for by scaling the uncertainties, section (4.4.2). Altamimi et al. (2007) also assumes a WN model, Altamimi et al., (2007) also uses the operational data which has approximately half the available reprocessed

observations. Below, Table 19/Figure 43 shows a comparison of the NC1 solution (scaled) and other modern solutions.

Table 19: Calculated absolute Euler poles, Green (Sella et al. (2002)), Blue ITRF2005 (Altamimi et al. (2007)), Orange (Argus et al. (2011)), Red this study (null-GIA)

Plate	#	Latitude	Longitude	Error Ellipse			Rotation Rate	
		φ°	λ°	η° major Azimuth	σ_{maj}	$\sigma_{\min}$	ω $^\circ/Ma$	σ_ω
Antarctica	7	58.480	226.000	32.0	1.600	1.00	0.226	0.010
ITRF2005	8	59.813	234.685	0.0	0.864	1.68	0.223	0.007
Argus		65.420	241.89				0.250	0.008
Booker	9	58.370	232.940	4.7	0.240	0.14	0.213	0.0018
Australia	11	34.860	38.260	-65.0	1.200	0.40	0.627	0.004
	14	32.407	37.367	0.0	0.267	0.36	0.628	0.003
		33.860	37.940				0.632	0.017
	24	32.400	38.030	-16.9	0.070	0.04	0.634	0.0010
Eurasia	15	58.270	257.790	34.0	1.500	0.40	0.257	0.003
	41	56.330	264.021	0.0	0.549	0.97	0.261	0.003
		48.850	253.500				0.223	0.009
	62	54.460	259.440	32.0	0.130	0.07	0.250	0.0006
India	3	53.650	346.01	80.0	11.70	0.50	0.483	0.013
	3	49.823	21.841	0.0	6.628	24.5	0.614	0.108
		50.370	356.710				0.544	0.010
	4	54.580	1.550	-2.3	2.27	0.12	0.531	0.0092
Nazca	5	44.450	260.510	5.0	2.900	0.60	0.647	0.011
	3	45.101	259.559	0.0	1.856	0.75	0.642	0.015
		46.230	258.940				0.696	0.029
	4	45.950	256.700	-88.4	0.35	0.15	0.631	0.0042
N America	64	-2.390	280.92	-6.0	0.800	0.30	0.199	0.002
	30	-4.921	272.615	0.0	0.861	0.57	0.192	0.002
		-4.850	279.360				0.209	0.013
	41	-4.070	274.680	-88.5	0.15	0.08	0.195	0.0008
Nubia	5	52.250	279.82	-83.0	1.600	0.90	0.253	0.004
	13	49.955	277.499	0.0	0.483	1.26	0.269	0.003
		47.680	291.560				0.292	0.007
	8	49.210	279.190	-1.3	0.29	0.10	0.269	0.0012
Pacific	9	-64.210	112.740	75.0	0.700	0.40	0.655	0.004
	10	-62.569	112.873	0.0	0.222	0.74	0.682	0.004
		-63.580	114.700				0.651	0.011
	12	-62.390	111.250	-0.1	0.16	0.04	0.684	0.0010
S America	11	-25.830	224.62	-80.0	7.700	2.80	0.106	0.003
	9	-16.800	230.369	0.0	1.593	2.05	0.121	0.003
		-22.620	247.170				0.109	0.011
	8	-18.680	229.990	-17.9	0.66	0.24	0.129	0.0014

Antarctica

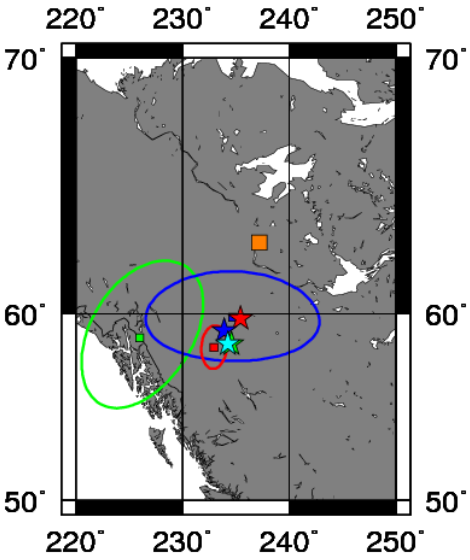

Australia

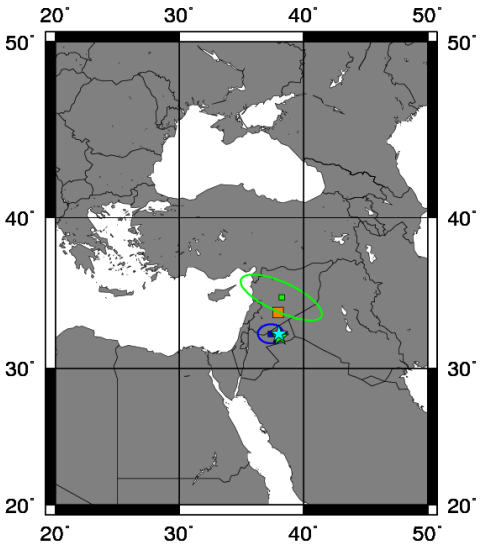

Eurasia

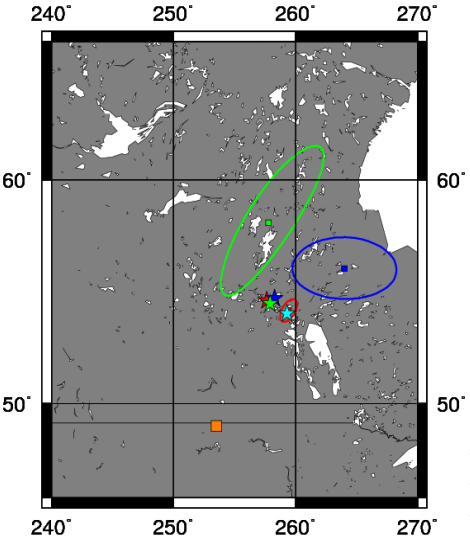

India

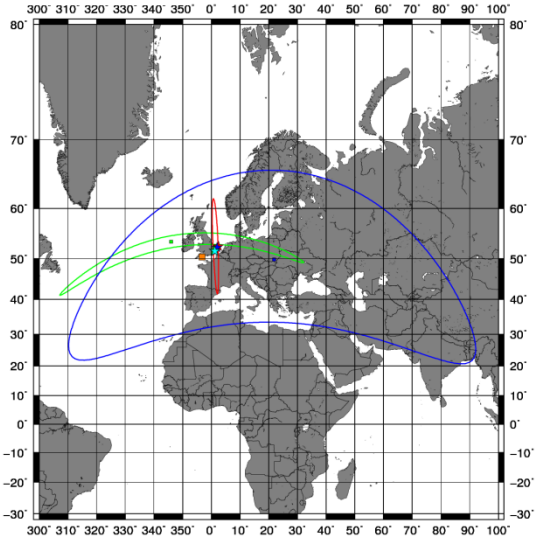

Nazca

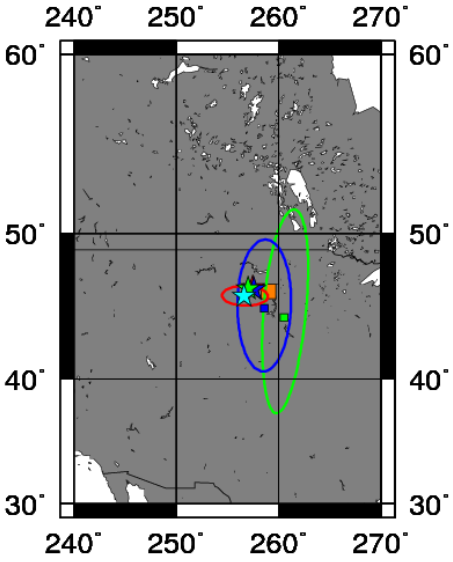

North America

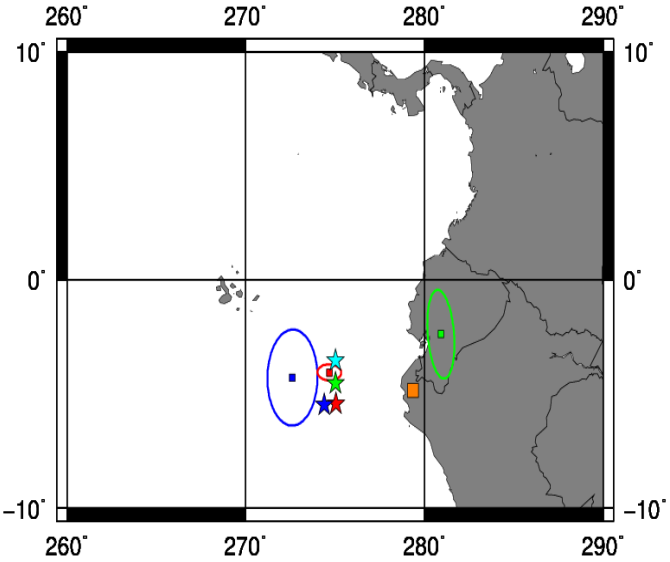

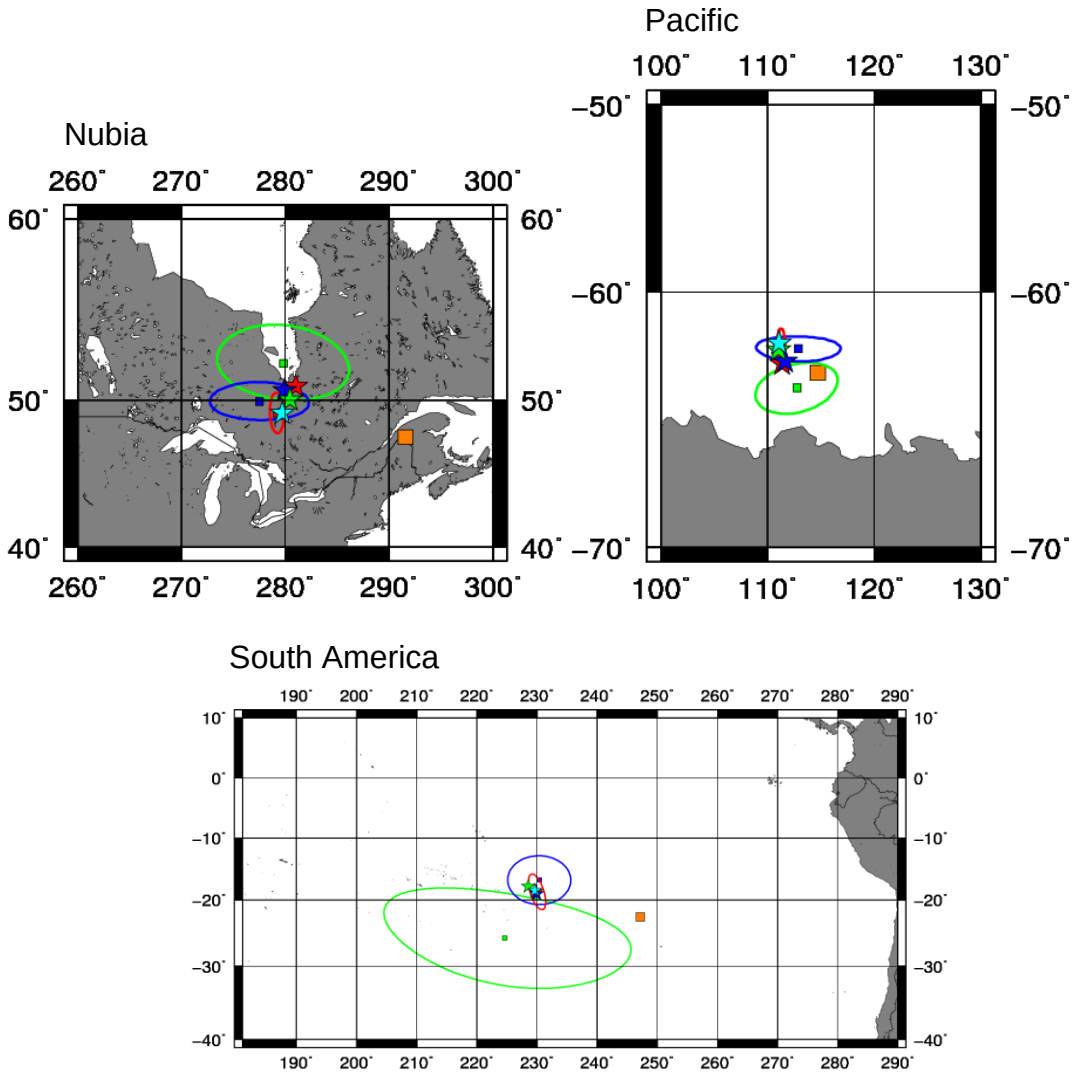

Figure 43: Absolute Euler pole and error ellipse. Red this study (null-GIA) accounting for WN+CN scaling, Blue ITRF2005 (Altamimi et al. (2007)) Green REVEL (Sella et al. (2002)) and Orange NNR-MORVEL56 (no error ellipse information published) (Argus et al. (2011)). 95% confidence. Stars represent the GIA adjusted plate models, ICE5G-VM2 (Red), ICE5G-VM4 (Blue), Schotman (Green) and Schotman Alternative (Cyan).

As a whole the NC1 solution tends to show agreement with the solution of Altamimi et al. (2007) but with significantly reduced error ellipses due to the improvement to the GPS time series and the additional stations in the solution. For plates which have fair-to-good coverage the three GPS solutions (NC1, ITRF2005 and REVEL) tends to show agreement with error ellipses. For GIA affected plates the REVEL model attempts to account for GIA by removing sites which are deemed to be affected by GIA, this different method is most notable in the determination of the North America Euler Pole, less so for Eurasia and Antarctica. The geological model NNR-MORVEL56 only shows a loose agreement with ~50% of the plate poles.

Table 20 lists the absolute Euler poles of the nine plates listed above as in Table 19, but after accounting for the various GIA models (stars in Figure 43),

section (2.4.4). The largest variation occurs on plates which have been subjected to previous glaciation e.g. Antarctica, Eurasia and North America, with plates such as Australia and the Pacific showing very little variation with the introduction of a GIA model. Even the largest variation is only (±3°) of the null-GIA model.

Table 20: Estimated Absolute Euler poles, Red - ICE5g-VM2, Blue - ICE5G-VM4, Green - Schotman, Yellow - Alternative Schotman, White null-GIA

	Latitude	Longitude	Error Ellipse			Rotation Rate			Horizontal		Vertical
Plate	φ°	λ°	η° Major Azimuth	σ_{maj}	$\sigma_{\min}$	ω° / *Ma*	σ_ω	Sites	RMS (mm)	RMS Prior	RMS (mm)
Antarctica	59.76	235.42	3.9	0.26	0.14	0.209	0.0018	9	0.6	7.1	1.9
	59.20	233.90	4.2	0.26	0.14	0.208	0.0018	9	0.6	7.2	1.4
	58.54	234.58	4.4	0.24	0.12	0.217	0.0018	9	0.9	7.7	2.5
	58.55	234.24	4.5	0.24	0.14	0.214	0.0018	9	0.8	7.6	2.6
	58.37	232.94	4.7	0.24	0.14	0.213	0.0018	9	0.7	7.6	1.8
Australia	32.27	38.02	-17.0	0.07	0.04	0.629	0.0010	24	0.9	43.8	1.4
	32.32	38.05	-17.0	0.07	0.04	0.631	0.0010	24	0.9	43.9	1.4
	32.20	38.12	-17.1	0.07	0.04	0.636	0.0010	24	1.0	44.6	1.5
	32.40	38.01	-16.9	0.07	0.04	0.634	0.0010	24	1.0	44.3	1.5
	32.40	38.03	-16.9	0.07	0.04	0.634	0.0010	24	1.0	44.2	1.4
Eurasia	54.91	257.65	32.2	0.13	0.07	0.249	0.0006	62	0.8	16.9	2.0
	55.02	258.30	31.7	0.13	0.07	0.250	0.0006	62	0.8	17.1	2.2
	54.78	257.90	32.3	0.13	0.07	0.249	0.0006	62	0.6	17.1	2.1
	54.33	259.30	32.3	0.13	0.07	0.249	0.0006	62	0.6	17.1	2.3
	54.46	259.44	32.0	0.13	0.07	0.250	0.0006	62	0.7	17.1	2.7
India	52.73	2.45	-3.0	2.39	0.14	0.525	0.0092	4	0.8	39.2	2.1
	52.45	2.00	-2.7	2.37	0.14	0.527	0.0092	4	0.8	39.4	2.1
	51.83	0.91	-2.1	2.31	0.14	0.527	0.0092	4	0.8	39.7	1.9
	51.64	1.20	-2.2	2.31	0.12	0.530	0.0092	4	0.8	39.7	1.9
	51.58	1.55	-2.3	2.27	0.12	0.531	0.0092	4	0.8	39.8	2.0

Nazca	46.53	257.44	-89.6	0.35	0.15	0.625	0.0042	4	0.7	42.5	2.7
	46.40	257.53	-89.8	0.35	0.15	0.627	0.0042	4	0.6	42.6	2.7
	46.42	257.01	-88.9	0.35	0.15	0.626	0.0042	4	0.7	42.7	2.2
	45.94	256.62	-88.3	0.35	0.15	0.630	0.0042	4	0.7	42.7	2.1
	45.95	256.70	-88.4	0.35	0.15	0.631	0.0042	4	0.6	42.7	2.2
North America	-5.44	275.05	-88.3	0.15	0.08	0.196	0.0008	41	2.3	13.8	3.5
	-5.48	274.39	-88.8	0.15	0.08	0.196	0.0008	41	2.2	13.7	3.1
	-4.55	275.03	-88.2	0.15	0.08	0.194	0.0008	41	1.2	13.2	2.6
	-3.55	275.03	-88.2	0.15	0.08	0.195	0.0008	41	0.9	13.1	3.9
	-4.04	274.68	-88.5	0.15	0.08	0.195	0.0008	41	1.1	13.1	4.6
Nubia	50.89	280.98	-2.3	0.29	0.10	0.268	0.0012	8	1.0	19.1	1.1
	50.63	279.93	-1.8	0.29	0.10	0.270	0.0012	8	0.9	19.1	1.1
	50.05	280.42	-2.0	0.29	0.10	0.269	0.0012	8	1.2	19.1	1.0
	49.22	279.68	-1.5	0.29	0.10	0.269	0.0012	8	0.8	19.0	1.0
	49.21	279.19	-1.3	0.29	0.10	0.269	0.0012	8	0.8	19.0	1.1
Pacific	-63.20	111.32	-0.1	0.18	0.04	0.686	0.0010	12	0.8	50.3	1.1
	-63.10	111.60	0.0	0.18	0.04	0.683	0.0010	12	0.7	50.4	1.1
	-62.62	111.00	-0.2	0.16	0.04	0.684	0.0010	12	0.6	50.4	1.2
	-62.32	111.08	-0.2	0.16	0.04	0.683	0.0010	12	0.5	50.4	1.3
	-62.39	111.25	-0.1	0.16	0.04	0.684	0.0010	12	0.5	50.4	1.3
South America	-18.71	229.84	-17.9	0.70	0.24	0.125	0.0014	8	0.5	9.5	1.2
	-19.03	229.94	-17.8	0.70	0.24	0.124	0.0014	8	0.5	9.4	1.2
	-17.84	228.55	-18.5	0.70	0.24	0.126	0.0013	8	0.6	9.6	1.6
	-18.47	229.67	-18.1	0.68	0.24	0.129	0.0014	8	0.5	9.5	1.5
	-18.68	229.99	-17.9	0.66	0.24	0.129	0.0014	8	0.5	9.5	1.6

Table 20 lists the estimated absolute Euler poles after removal of each of the four GIA models and the null GIA model, with the respective rotation rates, horizontal and vertical RMS. Next to the horizontal RMS values are the RMS values prior to plate estimation.

The horizontal RMS values are significantly reduced after a plate model has been estimated. The introduction of a GIA model prior to plate estimation has very little effect on the horizontal RMS (±0.1) except for the North American plate, which has a distinct divide between the two different families of GIA models. Both the Schotman models only vary the horizontal RMS for North America (±0.2) versus the null-GIA model, however both of Peltier's models doubles the horizontal RMS. Argus and Peltier (2010) suggest that the present-day GIA motion is somewhere in between the ICE4G (not shown) and ICE5G models and that the VM2 model is a poor horizontal fit to recent observations in particular over North America which would be one explanation for the values in Table 20.

Vertically the RMS clearly shows the influence that introducing a GIA model has on the estimation. First focussing on areas of known previous glaciation there is a reduction of RMS for all models in North America (15%-44%) and Eurasia (15%-25%), this greater reduction over North America is most likely due to the higher percentage of North America covered by the Laurentia ice sheet compared to the more limited Fennoscandian ice sheets coverage of Eurasia. There is some disagreement over Antarctica (-22% to +45%) with no pattern to GIA family, this highlights the need to improve the understanding of GIA over Antarctica (Thomas et al. (2011)). Of the plates with "no" GIA the majority unsurprisingly show little to no change to the vertical RMS with the addition of a GIA models. This is true for Australia (7%), India (5%), Nubia (9%) and Pacific (15%, very small initial values), though there is a distinct divide between the vertical RMS for Nazca (+23%) and South America (-25%) for the Peltier models (-5% and -6% for Schotman). This small variation suggests some mismodelling of Peltier's GIA models either over South America (Chilean glaciation) or North America affecting the far field (King et al. (2012)).

5.2.3 *Secular Velocity Model Combination*

After estimating the GIA adjusted plate tectonic velocities the two components of the secular velocity model are now in place, one being the given GIA model and the second the associated estimated tectonic plate model. These provide velocities for each of the study sites which can be summed (5.4) to produce the required model.

$$\begin{pmatrix} x \\ y \\ z \\ \dot{x} \\ \dot{y} \\ \dot{z} \end{pmatrix}_{model} = \begin{pmatrix} x \\ y \\ z \\ \dot{x} \\ \dot{y} \\ \dot{z} \end{pmatrix}_{GIA} + \begin{pmatrix} 0 \\ 0 \\ 0 \\ \dot{x} \\ \dot{y} \\ \dot{z} \end{pmatrix}_{plate(GIA\ free)} \tag{5.4}$$

The estimated horizontal GIA velocities are never more than ~15% of the corresponding plate velocities so the removal of these should only make slight variations to the residual horizontal velocities. However the residual velocities are also ~15% of the estimate plate velocities, suggesting that the plate residuals could either be due to present day surface mass loading, GIA model error or a combination of the two.

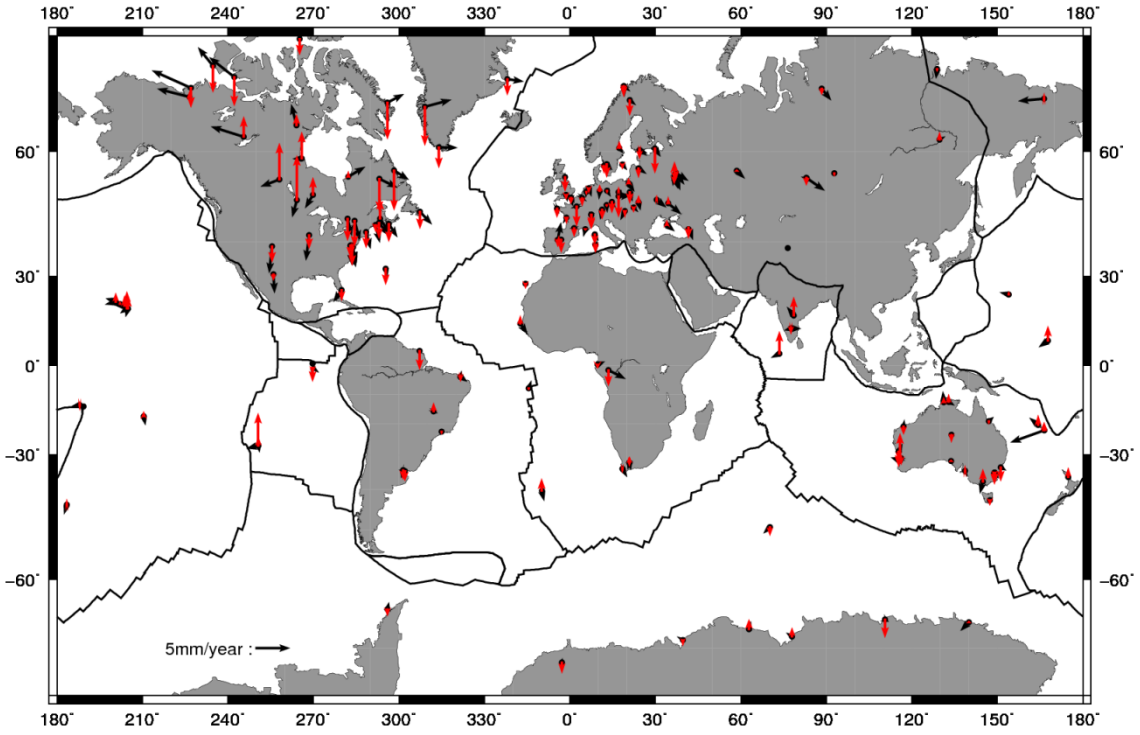

Figure 44: Station displacement residual velocities (tectonic and GIA free), horizontal (black), vertical (red). Peltier's ICE5G-VM2 (Peltier (2004))

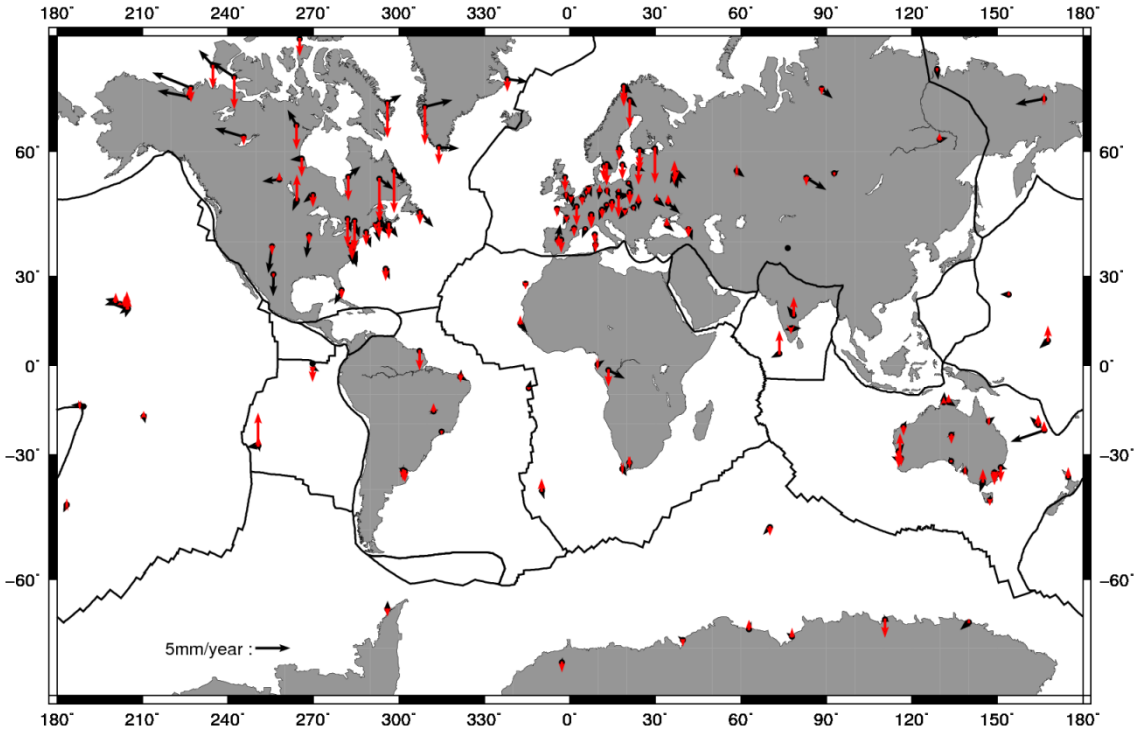

Figure 45: Station displacement residual velocities (tectonic and GIA free), horizontal (black), vertical (red). Peltier's ICE5G-VM4 (Peltier (2004))

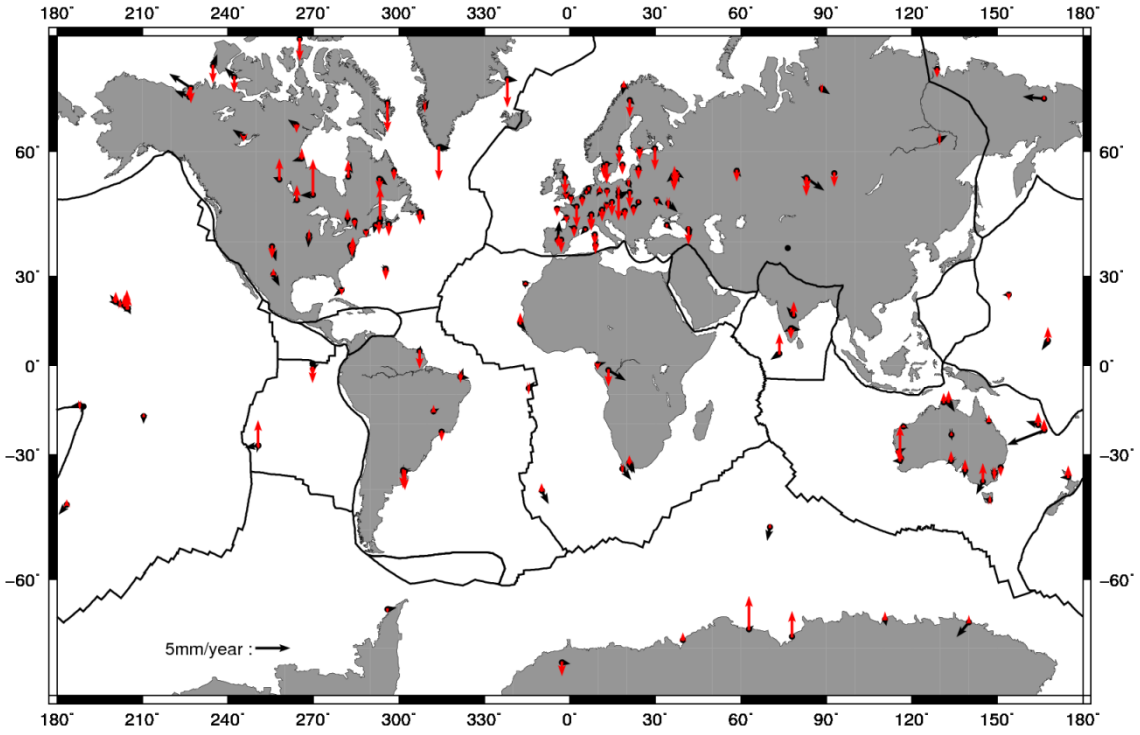

Figure 46: Station displacement residual velocities (tectonic and GIA free), horizontal (black), vertical (red). Schotman (Schotman and Vermeersen (2005))

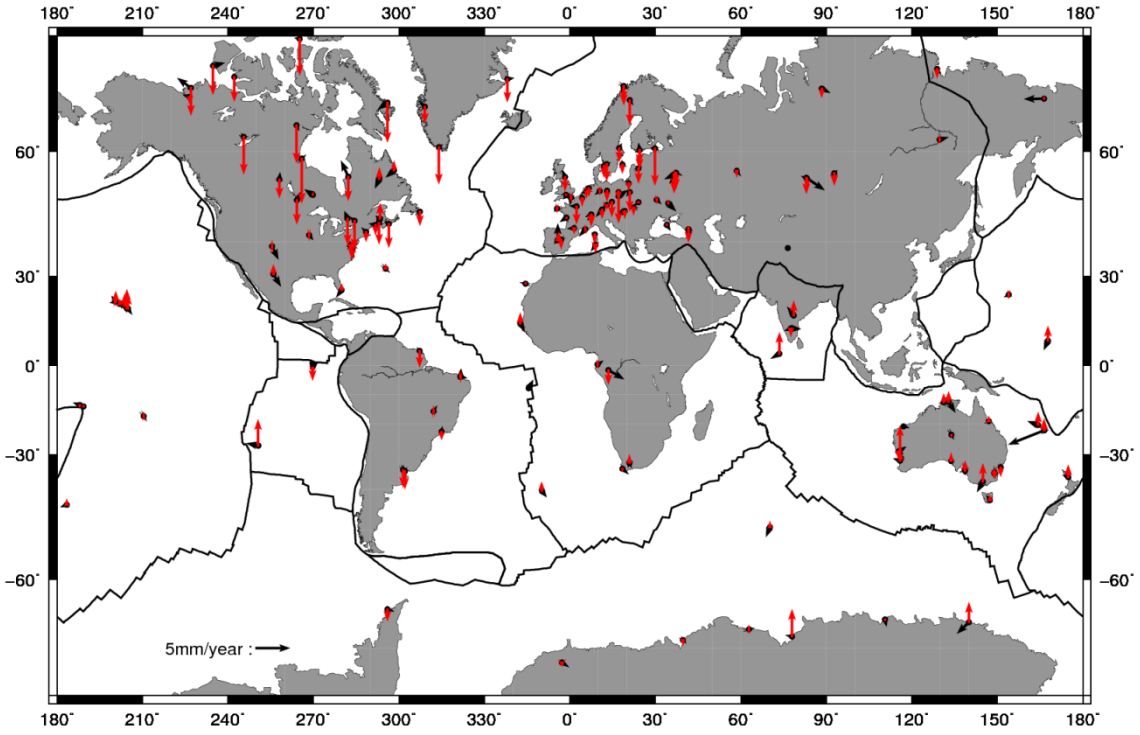

Figure 47: Station displacement residual velocities (tectonic and GIA free), horizontal (black), vertical (red). Schotman Alternative (Schotman and Vermeersen (2005))

5.2.4 *Visual Inspection of Models*

The residual velocities will highlight expected areas of present day surface mass loading and/or model errors (Figure 44-Figure 47). Visually inspecting the residuals to each model can highlight some interesting facts. Both Peltier models seem to leave a systematic residual movement of stations situated around Hudson Bay in the horizontal plane. This could well be caused by systematic mismodelling; large areas of Hudson Bay are covered by water and as such there is a limited amount of continental land with which a surface load can accumulate/disperse in turn inducing an elastic response. This could also have an effect in Fennoscandia to a lesser degree as there is a higher ratio of land to water which is able to contain a surface load and hence a greater probability that terrestrial water storage could explain these residuals instead of model errors but due to the limited number of stations in the area is difficult to quantify.

5.2.5 *Statistical Testing of Models*

A χ^2/dof test will attempt to surmise the suitability of each model produced in this chapter. As discussed for the horizontal components GIA is a small component of the overall observed velocity compared to plate tectonics; and a large percentage of observed velocity due to vertical GIA. The impact of introducing the GIA model will best be seen in the vertical component, whereas an improvement may not be so apparent in the horizontal plane. The test statistic is calculated in the vertical and horizontal velocities. This test is unweighted as the GIA models errors are unquantified and considered uniform and error free.

$$\begin{aligned}\frac{\chi^2}{dof} &= \sum_i \frac{\left(\dot{u}^i_{obs} - \dot{u}^i_{model}\right)^2}{dof} \\ \frac{\chi^2}{dof} &= \sum_i \frac{\left(\left(\dot{n}^i_{obs} - \dot{n}^i_{model}\right)^2 + \left(\dot{e}^i_{obs} - \dot{e}^i_{model}\right)^2\right)}{dof}\end{aligned} \tag{5.5}$$

where $\dot{u}\dot{n}\dot{e}_{obs}$ and $\dot{u}\dot{n}\dot{e}_{model}$ are the velocities of stations $i = 172$, DOF are the degrees of freedom of the estimation. Vertically $DOF = N - 1$ and horizontally $DOF = 2N - 2P - 1$, where N is the number of sites and P are the number of plates estimated. The purpose of this test is to compare the various GIA modes, the results of which are present in Table 21

Table 21 Chi Square test of vertical and horizontal velocities, highlighted boxes are the smallest value for each test.

Model	3D	Vertical	Horizontal
Null-GIA	3.12	8.84	0.53
ICE5G-VM2	2.07	5.31	1.36
ICE5G-VM4	1.96	5.05	1.25
Schotman	1.57	4.33	0.60
Schotman Alternate	2.39	6.75	0.45

To compare the improvement made from the inclusion of a GIA model the statistics are first calculated for the null-GIA method, followed by the four GIA methods. Vertically the inclusion of all GIA models reduces the χ^2/dof value by ~25-50% which was expected as the null-GIA model makes no consideration for the large vertical velocities due to GIA. Horizontally both Peltier's models (156% and 135%) and to a much lesser extent the primary Schotman model (13%) degrade the χ^2/dof fit; only the alternative Schotman model improves the horizontal fit (15%), due to poor North American plate agreement (Table 20). However, the alternative Schotman model also happens to have the least beneficial effect on the vertical χ^2/dof fit, (23%). It should be noted that even though Peltier's models significantly increase the horizontal χ^2/dof they will not be discarded as it is possible that the null-GIA method is absorbing some of the horizontal GIA velocity into the tectonic velocity or there is an error in the model over North America and retaining them will provide an interesting comparison of potential secular mass loading.

5.3 Summary

In this chapter I have presented the processes used to produce the combined model of estimated secular velocities due to GIA and plate tectonics. The residual velocities to each of these models are the potential result of present day secular loading. The introduction of Schotman's primary model gives the best improvement over the null-GIA estimate, however all models will still be considered. In Chapter 6 I will present an estimation of loading by attempting to fit a set of modified spherical harmonics and evaluate the suitability of each model for quantifying the calculated mass change of selected areas.

Chapter 6. Secular Loading

The previous chapter describes the construction of the surface velocity model (GIA and plate rotation). Once this modelled velocity has been removed from the raw observations, the residual velocities are assumed to result from present day secular surface mass loading. To fully understand and interpret the residual velocities, a modified spherical harmonic estimation, section (2.3.1), of the secular surface mass loading will be produced. As the degree of estimation increases, the spatial resolution becomes finer which allows for the detection of smaller-scale loading signals. As a rough guide, it is possible to estimate the spatial scale of each basis function level n.

$$res = \frac{20000km}{n} \tag{6.1}$$

Table 22: Estimated spatial resolution of each basis function level.

Basis Function Level n	Resolution (km)
1	20000
2	10000
3	6700
4	5000
5	4000
6	3300
7	2900
8	2500

To avoid confusion, the terms “degree” and “order” refer to the standard spherical harmonic degree and order. The term “level” refers to the spherical harmonic degree from which the alternative basis functions are derived (Clarke et al. (2007)). The estimated basis function coefficients are reconstituted into spherical harmonic coefficients (to maximum degree and order 45, i.e. a spatial resolution of 440 km). The level of estimation can be increased until ultimately there are too many parameters and not enough independent observations to calculate a solution. It is important to ascertain the maximum level estimable from the available data sets as the distribution of stations, able to constrain the inversion, is uneven; which means the effective maximum level for each region is not the same and therefore the maximum global level must account for this. There is no definitive method to determine the correct level to estimate a

loading fit. Methods include comparing the spatially re-constructed estimated load with a “true” model of the predicted surface loads, but in practice there is no way to determine the true value of loading. A second method would examine the smoothness of fitted coefficients week to week, but again this is not a rigorous quantitative measure of truth, as it is clear that surface loads cannot move instantaneously from one location to another. Thirdly, as described below, it would be possible to examine the goodness of fit of a particular estimate to the observational data. A final method, and the one used ultimately in this thesis, would be to create a synthetic data set from a realistic loading model, and test the ability of the fitted coefficients to recover the known load.

6.1 Goodness of Fit of Basis Functions

One possible statistical measure to assess the appropriate basis function level would examine the residuals from the basis function estimation. For each GIA/plate scenario this would show the goodness of fit for each maximum basis function level. By calculating a χ^2/dof it may be possible to determine the optimum level, as an impossibly perfect fit would return a value of zero, values between 0.1 – 10 would represent a fair estimation with slight over- or under-fitting, and anything higher than this would be a poor estimation. The main hurdle arises when calculating the effective Degree of Freedom (*dof*). As with all estimations, a greater number of parameters require a greater number of observations, thus reducing the *dof*. As there is not a uniform distribution of sites then some areas will be light in station data (Pacific, Africa) so the loading estimation is free to deviate in order to produce a smooth fit over other areas that are well observed (North America, Europe). Hence the global *dof* does not reflect this spatial variability of information content. Table 23 shows the χ^2/dof values of basis function fit (X_{basis}) to the residual velocities (X_{obs}), equation (5.5) for a chosen level and model, where i is the epoch and s are the stations.

$$\chi^2/dof = \sum_i \sum_s \left(\frac{\left(X_{obs} - X_{basis}\right)^2}{\sigma_s^2} \right) \Big/ dof \qquad (6.2)$$

Once the χ^2/dof for each model at each level has been calculated then it will be possible to determine the optimum global level estimable.

Table 23: 3D χ^2/dof , all levels have 188013 observations.

Level	1	2	3	4	5	6	7	8
3D DOF	185789	182974	179033	174019	167820	160518	152141	142607
Non-GIA	0.69	0.65	0.66	0.66	0.67	0.60	0.56	0.54
ICE5G-VM2	1.39	1.38	1.34	1.30	1.16	1.03	0.99	0.86
ICE5G-VM4	1.31	1.31	1.30	1.29	1.22	1.10	1.03	0.93
Schotman	1.02	0.99	0.99	0.98	0.95	0.85	0.86	0.85
Schotman Alt.	0.48	0.46	0.46	0.46	0.45	0.40	0.41	0.41

The above table is calculated using all the observations; this global statistic however implicitly assumes that the stations are evenly distributed over the surface of the Earth, which is not the case. This test shows that the increasing level of basis function globally fits the data roughly equally well for each maximum level, and within the expected range of goodness of fit, (Figure 48). The introduction of a GIA model is having a quantifiable effect at all levels; however, it is not possible to reject any particular basis function level as an implausibly good or bad fit globally.

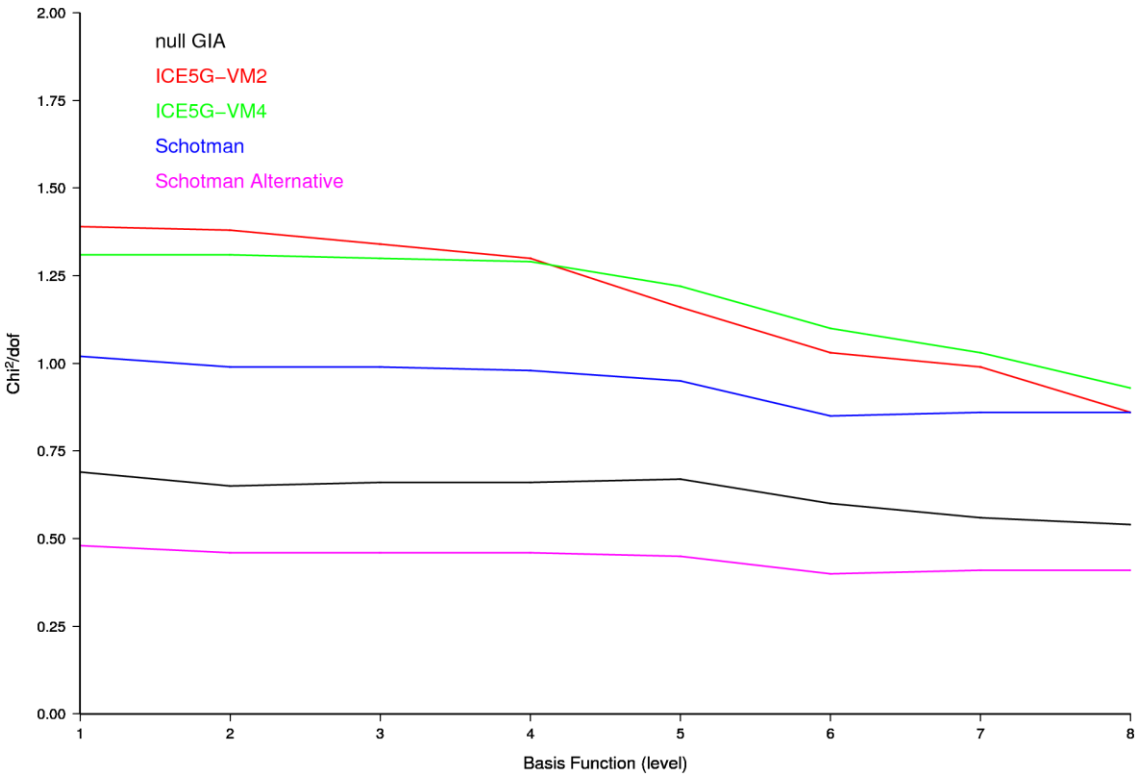

Figure 48: Calculated 3D χ^2/dof for each of the tested scenarios.

Realistically the global *dof* will not represent the true level of constraint imposed by the data over the different regions. Over-fitting in one region may be

compensated by under-fitting elsewhere. Section (6.2) shows how this may happen.

6.2 Synthetic Data Analysis

To test the effectiveness of the basis functions, a realistic synthetic data set has been created. The data set has been created from the combined loading model of atmosphere, National Centre for Environmental Prediction (NCEP) reanalysis (Kalnay et al. (1996)), the Land Dynamics (LaD) continental water storage (Milly and Shmakin (2002)) and OBP from the Estimating the Circulation and Climate of the Ocean (ECCO) general circulation model (http://www.ecco-group.org). Clarke et al. (2005) described how the annual cosine load corresponds to the seasonal inter-hemispheric changes associated with ocean-continent mass transfer and that the annual sine component corresponds to tropical monsoon changes with very little oceanic mass change.

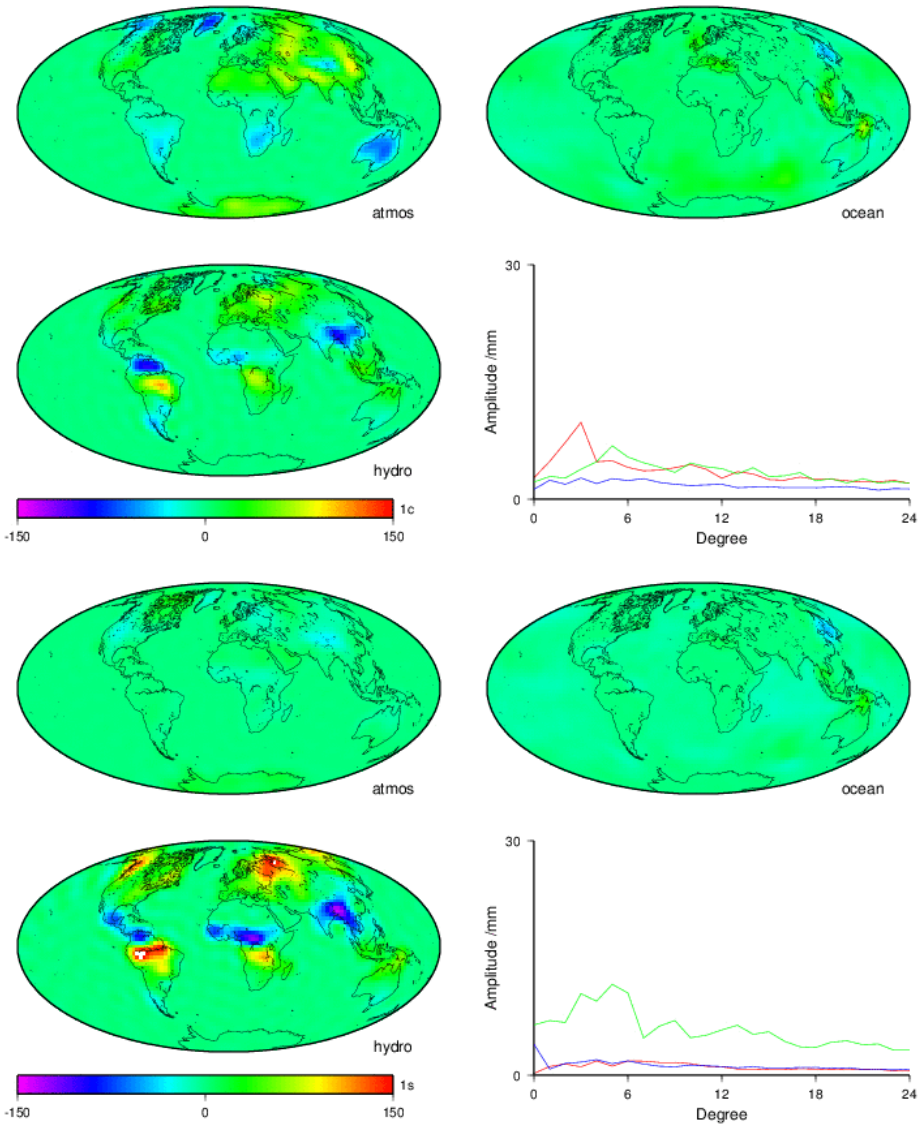

Figure 49: Total modelled seasonal load cosine top, sine bottom with degree/amplitude graphs for atmosphere (red), oceans (blue) and continental water (green), these are combined into a single value see Clarke et al. (2005)

This total seasonal load takes the form of an annual sine and cosine grid (Figure 49). To create a realistic loading displacement at a station then the data must be converted to a total load $T(\Omega)$, equation (6.3), then to an equivalent height and lateral displacement using the load Love numbers, section (2.2),.

$$T(\Omega) = \left(T_{\cos}(\Omega) \times \cos\left(\frac{doy}{365.25}\right)\right) + \left(T_{\sin}(\Omega) \times \sin\left(\frac{doy}{365.25}\right)\right) \qquad (6.3)$$

Where Ω is the geographical location and $T_{\cos}, T_{\sin}$ are the cosine and sine coefficients of the load. (6.3) also interpolates the UNE displacement value for each station used in this study for a single year which is repeated to produce a decadal time series. This time series is converted into a corresponding TANYA block (GPS week 1000-1570), equivalent to the loading displacements

produced as part of the kinematic estimate, section (4.4). The purpose of this synthetic data set is to test the sensitivity of the basis function routine to white noise and velocity biases.

This “true” data set is corrupted by adding synthesised Gaussian white noise to each weekly block, with magnitude given by each station’s scaled formal position error in that weekly block. A second simulation has been compiled which additionally introduces a velocity bias; this has been achieved by producing a random set of velocity biases which have a mean of zero and standard deviations of 0.2mm/yr and 1mm/yr in the horizontal and vertical respectively. The actual range of random velocity error in each of the simulations is ±0.6mm/yr in the horizontal and ±3mm/yr in the vertical.

The data set described above and the tests below are an attempt to produce some indication of the inversion error of the basis functions. However the reader should be made aware of a few limitations of the synthetic tests.

It must be noted that the synthetic data set (Clarke et al. (2005)) does not contain any substantial mass change over the Antarctic region as the hydrological model omits it and the atmospheric component is very small. This lack of model data will hinder the ability of the inversion test to calculate a realistic error budget.

The data set is interpolated over the full network of 172 stations, in reality though the trends are calculated over a network which is constantly changing its size and distribution. This lack of temporal network variation will likely cause an underestimation of the true level of inversion artefacts. In an attempt to quantify the effect of this a reduced network was created (section 6.2.1). This reduced network size is an attempted recreation of the early GPS network to determine the effects on the final inversion. This however is only one test, in reality the very early GPS network was much smaller than the two tested here and latter weeks were much larger (Figure 14). The reader should be made aware that the estimated error budget calculated will underestimated the true error due to network evolution.

The tests below only consider random errors, but in reality it is highly likely that there is strong spatial correlation to these errors such as those due to GIA (King et al. (2010)). These small errors with a regional correlation can have a significant influence upon the final mass estimate, by comparing the Peltier and Schotman models over North America which has a distinctly different spatial

pattern the reader can begin to understand the effect that small regionally correlated errors can have on the final solution.

6.2.1 *White Noise*

For the weekly white noise simulation there should be no secular trend present at any station's loading displacements, therefore the basis function estimation should also contain no trends in any of the reconstituted spherical harmonic coefficients.

One simulation would not be statistically sufficient, several (four) syntheses were compiled, inverted and the RMS of each level's (4-6) trend was calculated, Figure 50, a contour of 3mm/yr has been chosen to highlight the regions of confidence, this value has been chosen subjectively to represent what I believe to be a sensible value separating what is real and what is an artefact. Levels 4 and 5 of Figure 50 does not have a contour line highlighting the confidence across the entire solution, however for a level six estimation two small contours appear in Madagascar and North India.

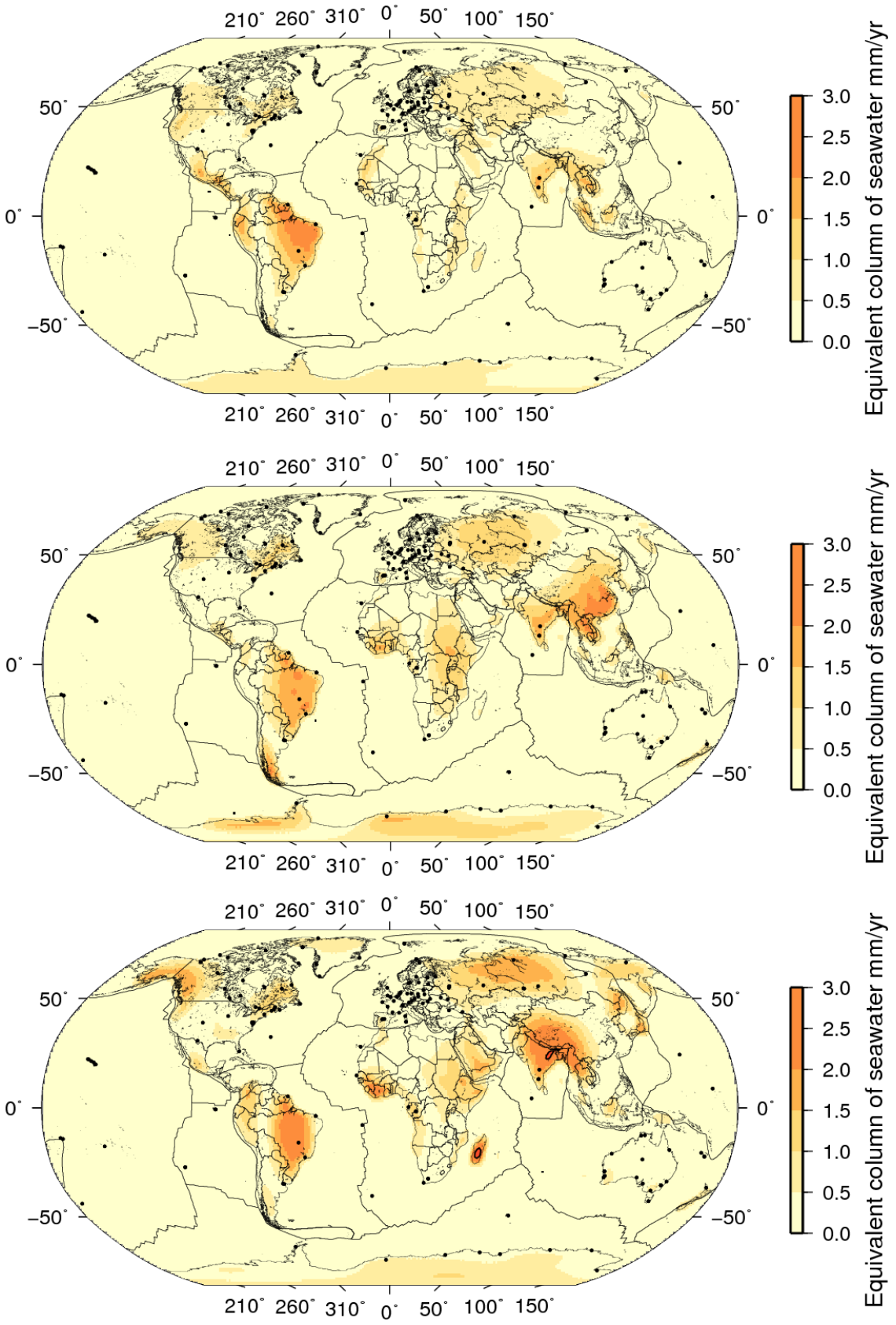

Figure 50: Synthetic data set RMS; White Noise adjusted Levels 4, 5 and 6, (four simulations). GPS stations shown as black dots, regions greater than 3mm/yr inside black contour. Regions above the threshold are not represented on the scale bar.

Small trends of ±3mm/yr exist in the reconstituted loads especially at higher levels and in areas with fewer GPS stations. These trends can be thought of as the precision or numerical error of the basis function estimations.

6.2.1 *Network Distribution*

The conclusions stated above are for a particular network geometry using the same synthetic load. Network geometry has been shown to be a potential source of error when estimating a loading inversion (Wu et al. (2002)), especially the bias of stations towards the Northern Hemisphere. To test this hypothesis, a thinned network of study sites has been produced; this was achieved using Delaunay triangulation to maximise inter-site distance. Specifically, the inter-site distances for the original network were calculated and if a site appeared within 200km of another site it was flagged. The site with the most vectors less than this threshold was then removed. This procedure was iterated until no vectors fell below the threshold (some discretion was used over southern hemisphere sites), at which point the threshold was increased by 100 km and the procedure repeated until a network of ~80 sites remained (at a final threshold of 500 km). The new network maintains a global distribution but evens out the distribution of sites between continents and especially along the Z-axis. Following the same methods as above a set of plots (Figure 51) was created which represents the RMS of four synthetic data sets with white noise, these solutions show more regions of uncertainties but again these are very small and disperse.

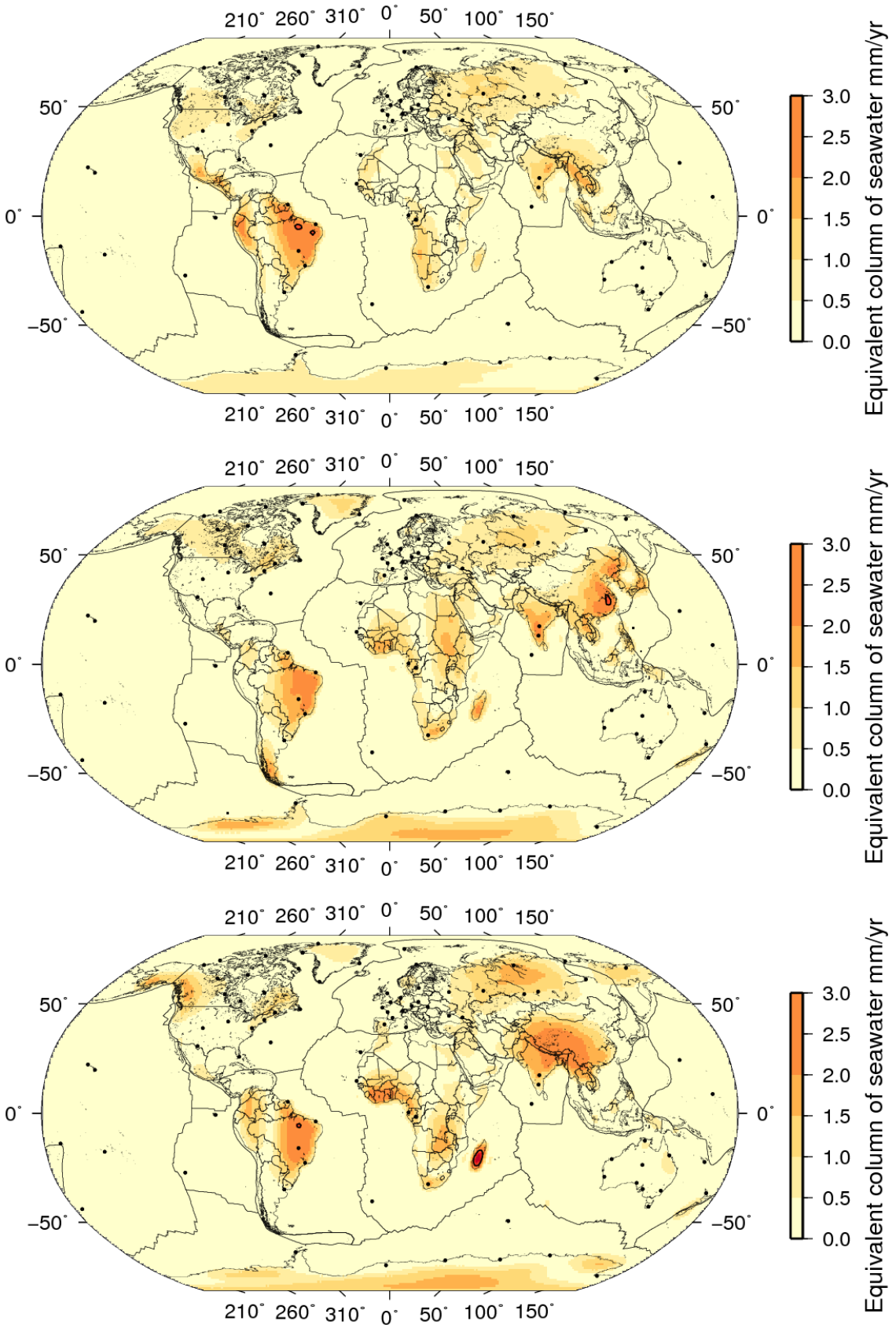

Figure 51: Levels 4, 5 and 6 RMS of four simulations of WN adjusted synthetic data set for a ~80 station network. GPS stations shown as black dots, regions greater than 3mm/yr inside black contour. Regions above the threshold are not represented on the scale bar.

Again, it would be expected that there should be no trends anywhere, but as shown by Figure 51, for a thinned out network the basis function estimation accumulates in areas which are poor in spatial coverage (e.g. Madagascar, Himalayas, no sites). However, the maximum error for all tested levels never reaches greater than ~3mm/yr globally, apart from Madagascar.

6.2.2 *Velocity Bias*

For the data set which has had a velocity bias added then each station will have a random trend added; these trends will be recovered by the basis function estimation and appear as (erroneous) trends in the reconstituted spherical harmonic coefficients. Again several (four) syntheses were compiled, inverted and the RMS of each level's (4-7) trend was calculated, Figure 52-Figure 54. Again a contour has been chosen, this time 40mm/yr, to highlight the regions of confidence. This value is also subjective to reflect the potential divide between real and artefacts. Figure 52 does not have a contour line highlighting the confidence across the entire solution, however as the level of estimation increases the regions of uncertainties increase in area.

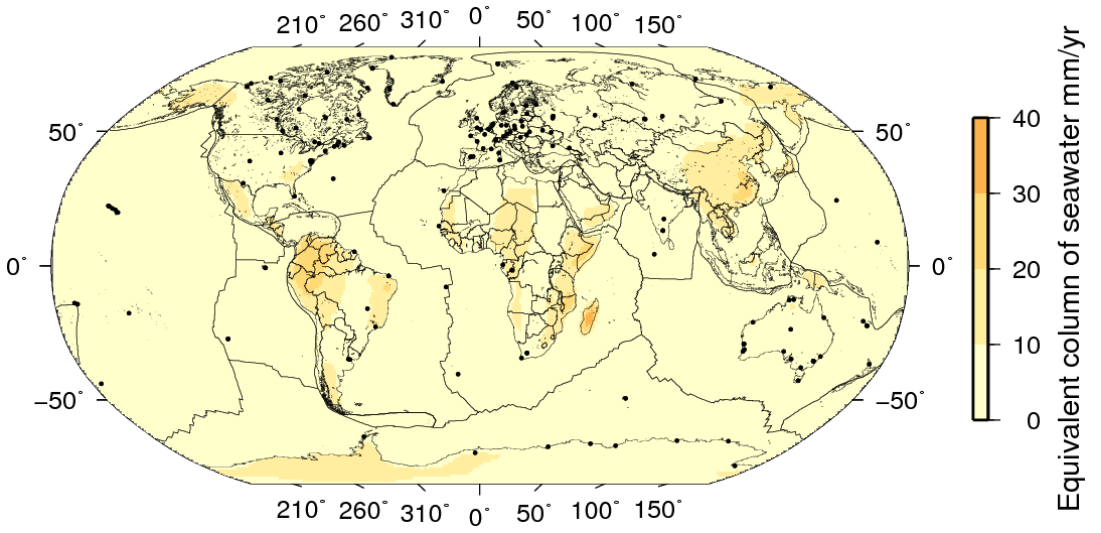

Figure 52: Velocity biased RMS of four syntheses at level 4, GPS stations (black dots). Regions greater than 40mm/yr inside contour and are not represented on the scale bar.

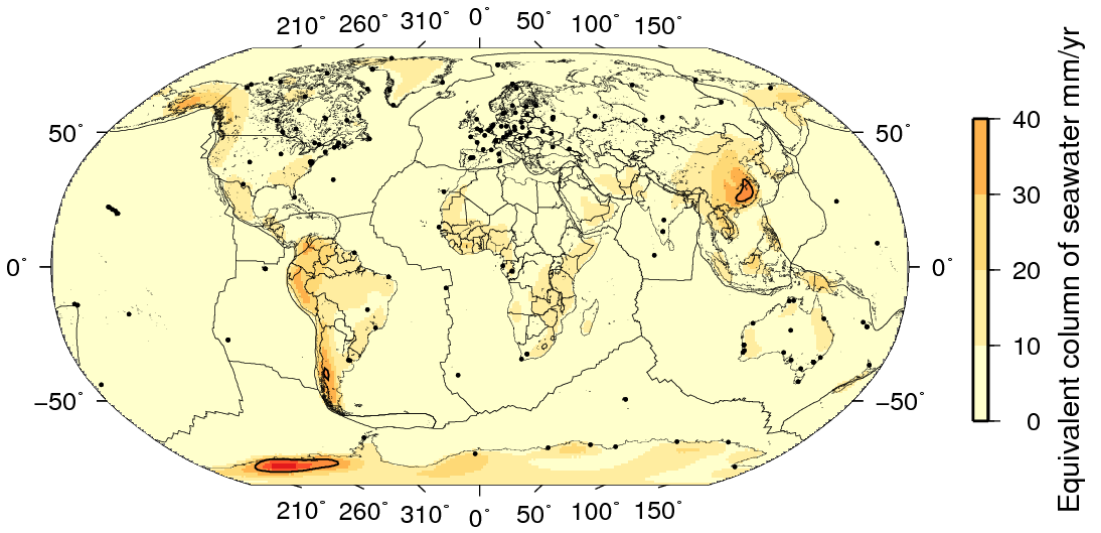

Figure 53: Velocity biased RMS of four syntheses at level 5. Regions above the threshold are not represented on the scale bar.

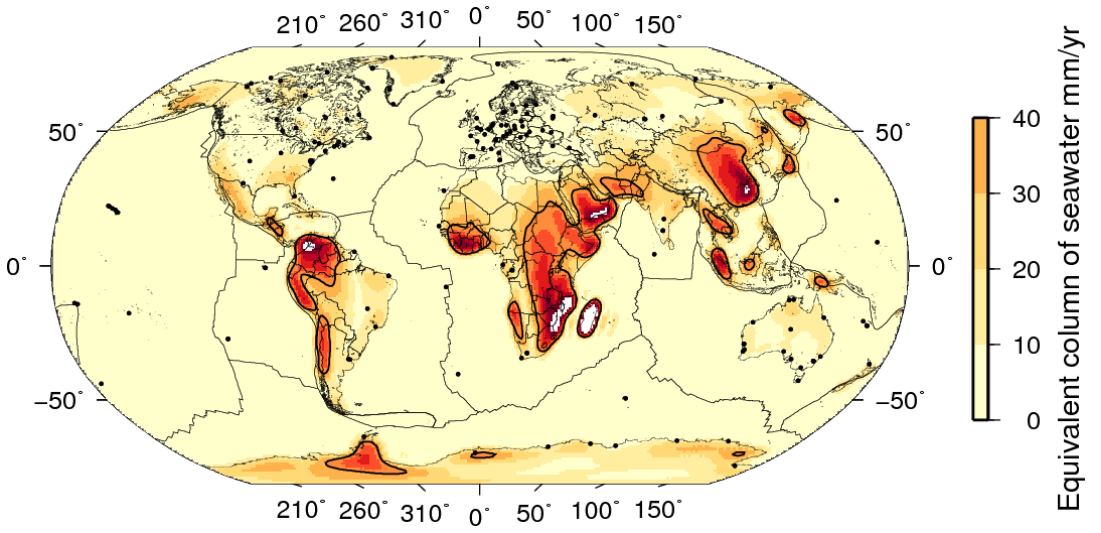

Figure 54: Velocity biased RMS of four syntheses at level 6. Regions above the threshold are not represented on the scale bar.

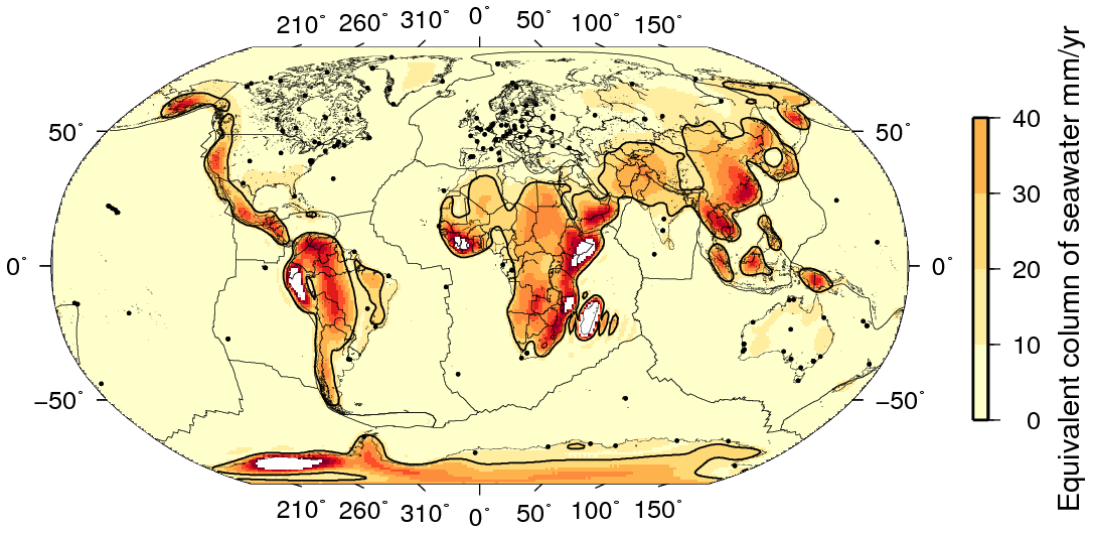

Figure 55: Velocity biased RMS of four syntheses at level 7. Regions above the threshold are not represented on the scale bar.

Figure 52- Figure 55 represent the synthetic velocity RMS for levels (4-7). Up to a level 5 estimation, the maximum trend is less than ~40mm/yr, in areas which have poor spatial coverage of tracking sites, but generally the secular loading error is less than ~20mm/yr. For a level 6 and 7 estimation however this value has risen to over 90mm/yr and 160+mm/yr in similar areas. The general pattern of this error tends to accumulate in areas where there is a lack of IGS stations providing constraints, which often coincide approximately with the plate boundary deformation zones (Kreemer et al. (2003)). The same velocity bias synthesis was applied to the reduced network to investigate the effect of network distribution for levels four to six (Figure 56-Figure 58).

Any areas which have shown potential artefacts from the very small synthetic velocity trend, Figure 52-Figure 55, must be regarded as unreliable in the real data set; conversely, areas which do not show artefacts in the synthetic test may be interpreted more confidently; these regions are divided by a contour line at 40mm/yr. A similar pattern of growth of the regions of uncertainty to the full network velocity bias is observed.

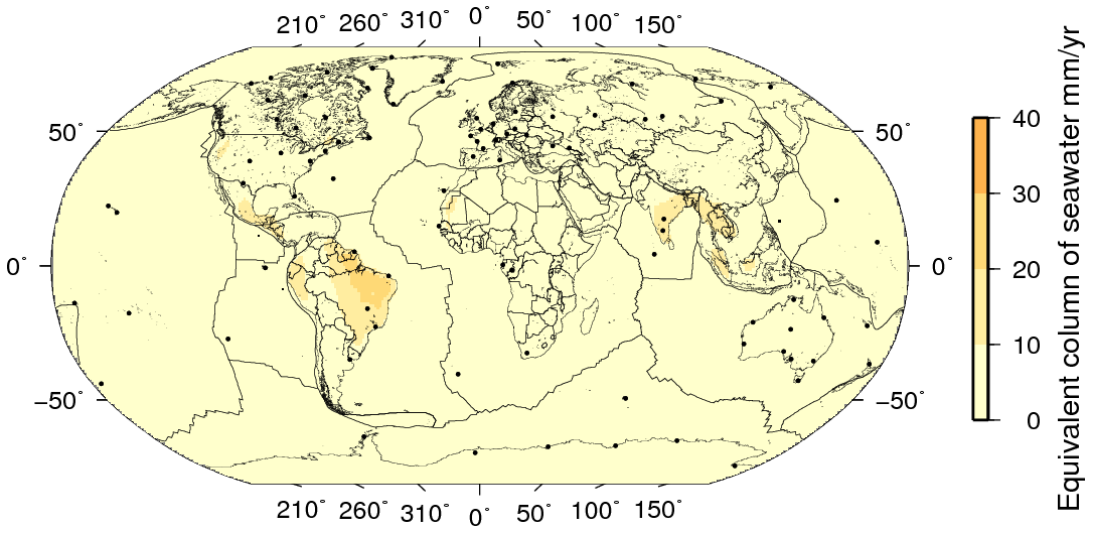

Figure 56: Velocity bias RMS of four syntheses, level 4, GPS stations (black dots) reduced network. Regions >40mm/yr inside contour and not represented on the scale bar

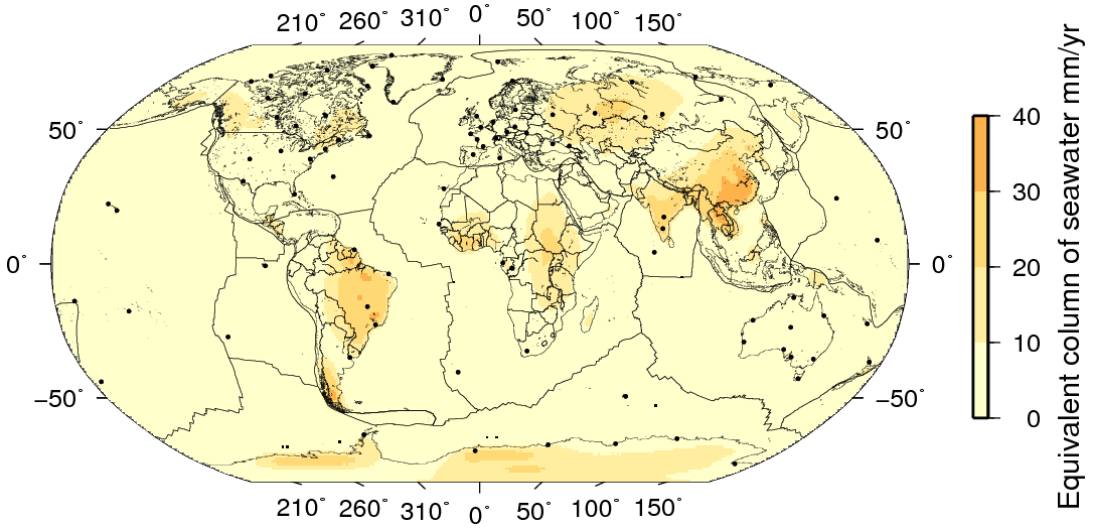

Figure 57: Velocity bias at level five of four syntheses, but with a reduced network. Regions >40mm/yr inside contour and are not represented on the scale bar.

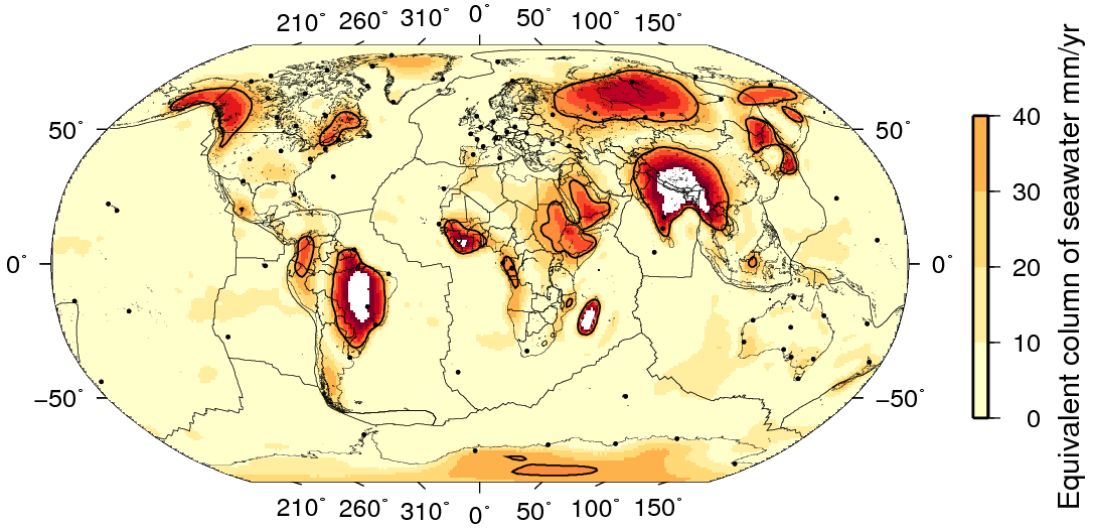

Figure 58: Velocity bias at a level six of four syntheses, but with a reduced network. Regions >40mm/yr inside contour and are not represented on the scale bar.

The conclusions to be taken from the synthetic data set for the networks and geometry shown are:

- Level 5 is the maximum global level estimable without introducing major artefacts, however areas with a good network coverage should be reliable for estimates to a higher level (7)
- The areas susceptible to basis function estimation are those that are lacking tracking stations (or have had them excluded because they are in a plate boundary zone)
- The artefacts begin to appear as the distance to the tracking stations is approximately equal to or greater than the spatial resolution of the basis function level (Table 22).
- Varying the network distribution does vary the manifestation of artefacts, on the whole these appear in similar areas with a similar magnitude; notable is Alaska which is more susceptible to artefacts at a lower level (possibly due to the reduction of North American stations).
- The full network velocity biased solutions will be used to create a mask highlighting the regions of confidence for the real solutions, section 6.4.

6.3 Seasonal Basis Function Estimations

Each week a loading inversion is calculated from which a linear trend is fitted to each coefficient to produce the secular estimation. This however disregards any seasonal variation which in itself is an interesting point of study. This section is a small deviation away from secular loading before returning to the main focus of the study in section (6.4).

Each week a basis function estimation for a particular level is calculated, from this a weekly grid can be produced which is representative of the seasonal variation of surface mass loading. By varying the level of the basis functions it is possible to observe the very large scale hemispherical mass redistribution to the smaller scale pockets of river basins and monsoon regions. The plots below are plots of a representative epoch for a northern hemisphere winter 2004.0137 (GPS week 1252) and summer 2004.6270 (GPS week 1284), illustrated by the grey bar in each plot.

The level-one estimation calculates four parameters and has a very coarse spatial resolution. The signal is driven by an excess of mass in one of the hemisphere causing a displacement of the centre of mass. Plotted in Figure 59

are the level-one and level-two estimates for the Northern hemisphere winter (top) and summer (bottom).

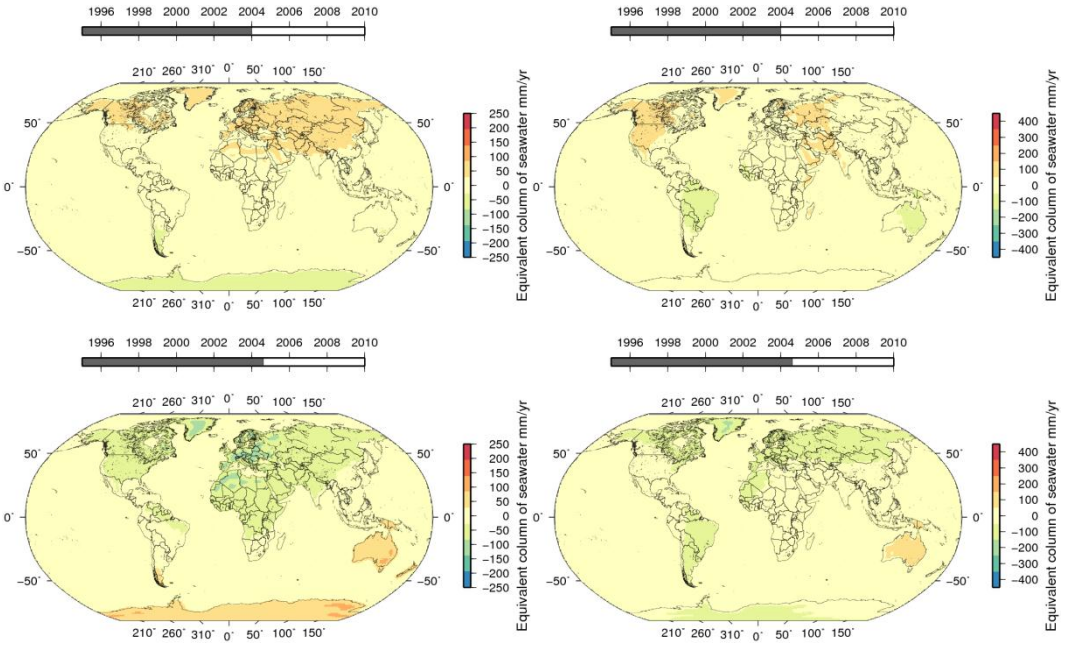

Figure 59: Level-One estimation, top left pane Northern Hemisphere winter and bottom left pane summer. Level-Two estimation, top right winter, bottom right summer. Grey bar indicates the epoch for each plot. Note different scale to other seasonal plots for level-one.

It is clear that in winter there is an excess of mass in the Northern hemisphere which corresponds to the accumulation of surface water, predominantly snow and ice. This trend is reversed in the summer months where there is a mass deficit in the North. This is documented by Lavallee and Blewitt (2002) who find a degree-1 signal. However Figure 59 is based on a very low resolution estimate and in reality there is unlikely to be a uniform mass transfer across the entirety of Europe and Africa; to identify the pockets of seasonal mass variation, higher level must be estimated. Moving to a level two estimation (estimating nine parameters) Figure 59 reveals mass variation are concentrated in smaller areas as the increased level of estimation refines the spatial resolution. As the level of estimation increases, the combination of the non-secular higher degree coefficients paints a picture of what seasonal surface mass exchange is occurring.

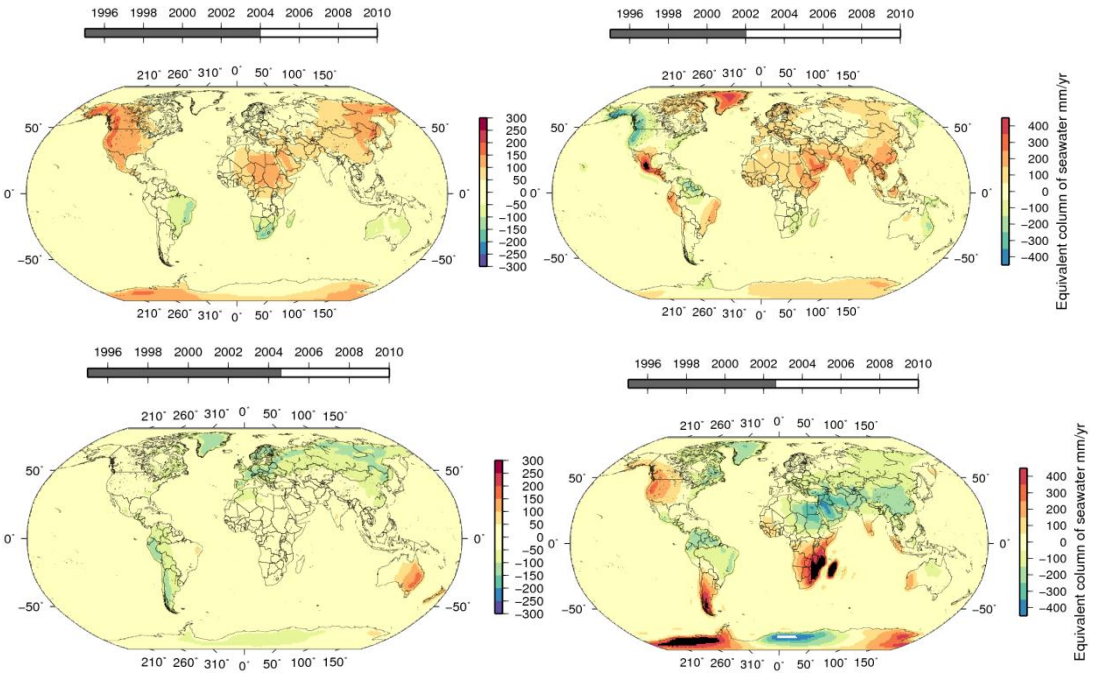

Figure 60: Level three (left) and Level four (right) estimation, northern hemisphere winter (top), summer (bottom).

As the level of estimation is increased the ability to fit the load to finer detail increases. Figure 60 estimate 16 and 25 parameters per epoch respectively. It is apparent that the higher level estimates are beginning to define distinct locations of periodic surface loading on the surface of the Earth. Discrete pockets are appearing around large river basins (Amazon) which are comparable to GRACE results (Crowley et al. (2008)) and tropical regions which receive strong monsoon rainfall (South East Asia). But there are also the same distinct artefacts appearing in similar areas (e.g. Madagascar, East Africa and South East Asia) that were also present in the synthetic data analysis, section (6.2.2).

6.4 Secular Surface Mass Loading

By calculating a simple weighted linear regression of each basis function or spherical harmonic coefficient it is possible to isolate the respective secular loading value. It is this information that I will use in this final section to investigate any present day secular loading. I will do this for the case of removing each of the four previously-described global GIA models and for the null GIA model. For each scenario I will evaluate basis functions from level four up to a maximum of level seven, but focus on a level five and six estimation as the synthetic tests have shown that the low level estimations have too broad a spatial resolution and higher level estimations (8-12, not shown) become

unstable in several regions. It may be expected to see a residual loading signal around the regions which have a significant modelled GIA velocity, e.g. Hudson Bay, Fennoscandia and Antarctica (this could be real or the result of potential GIA model error). Any other signal could be a result of present day surface loading (secular changes due to thinning/thickening of glaciers/ice sheets and the increased/decreased storage of water in river basins) or by the over-fitting of the basis function coefficients in poorly constrained areas at higher levels causing anomalously high estimates, also highlighted by the synthetic data analysis, section (6.2).

The first case presented is the estimated loading without the introduction of a GIA model, i.e. only plate velocities removed. Following this are the results from applying the four respective GIA models; the aim is to highlight areas of improvement and any present day secular surface mass loading free of GIA and tectonics.

6.4.1 *Null-GIA*

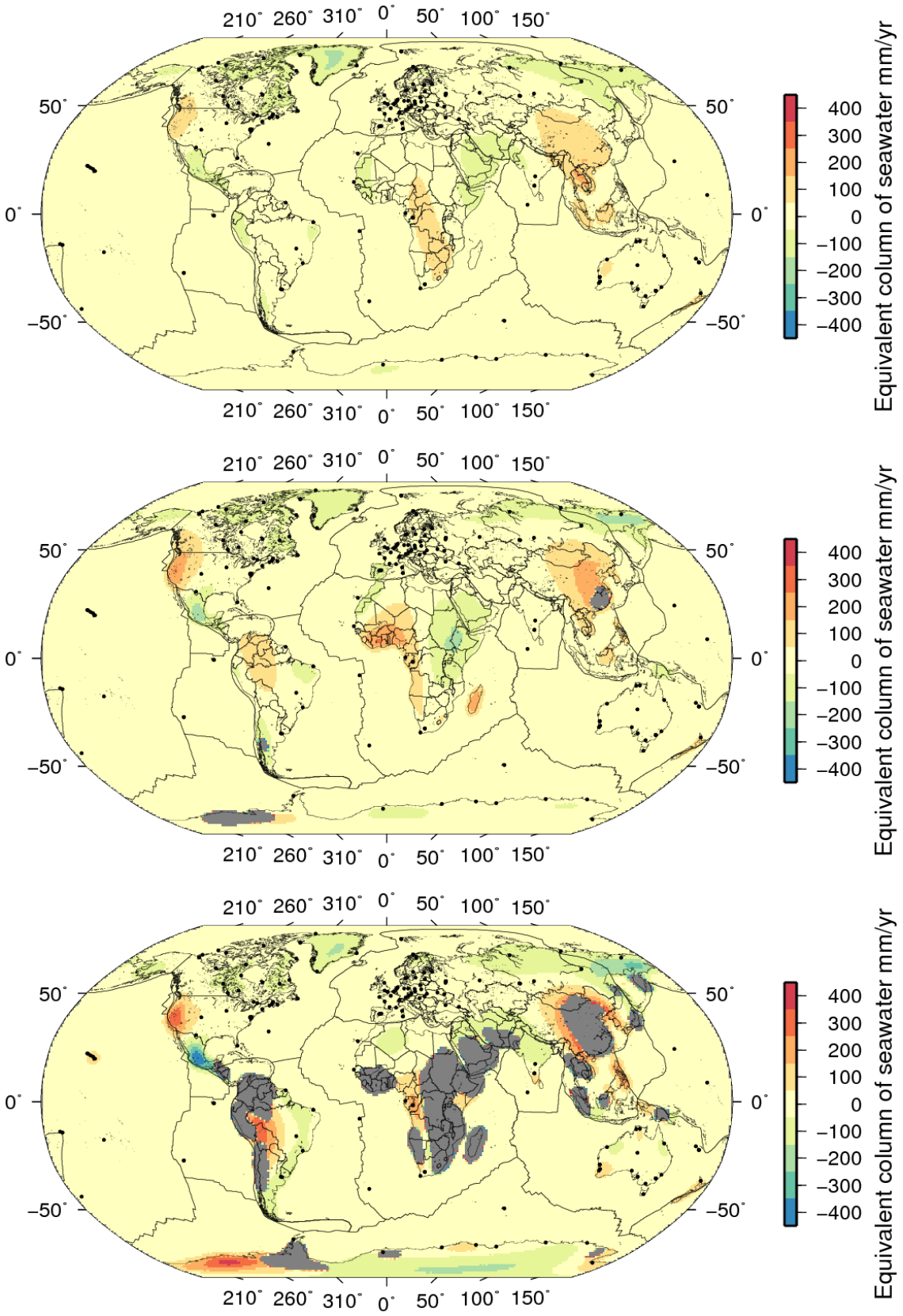

Figure 61: Level four (top), Level five (middle) and Level six (bottom) secular loading rate estimation, null GIA model, station network black dots. Grey mask covering areas of uncertainties, taken from synthetic solution (>40mm/yr).

Figure 61 shows unloading in high latitude areas which have a history of glaciation (North America, Fennoscandia, Siberia), however as the estimation increases to level 6 there is a similar pattern of artefacts emerging elsewhere to that seen in the synthetic studies in section (6.2). With the inclusion of a GIA model in the velocity model (Figure 62 to Figure 64), the areas of GIA-related deformation should be accounted for, leaving only present day surface mass loading but with possible inversion artefacts due to poor spatial coverage remaining in certain areas. A confidence mask has been applied; this has been created from the velocity biased synthetic data set covering all areas which showed trends of greater than 40mm/yr for each level considered.

6.4.2 *Level Four Estimation (GIA)*

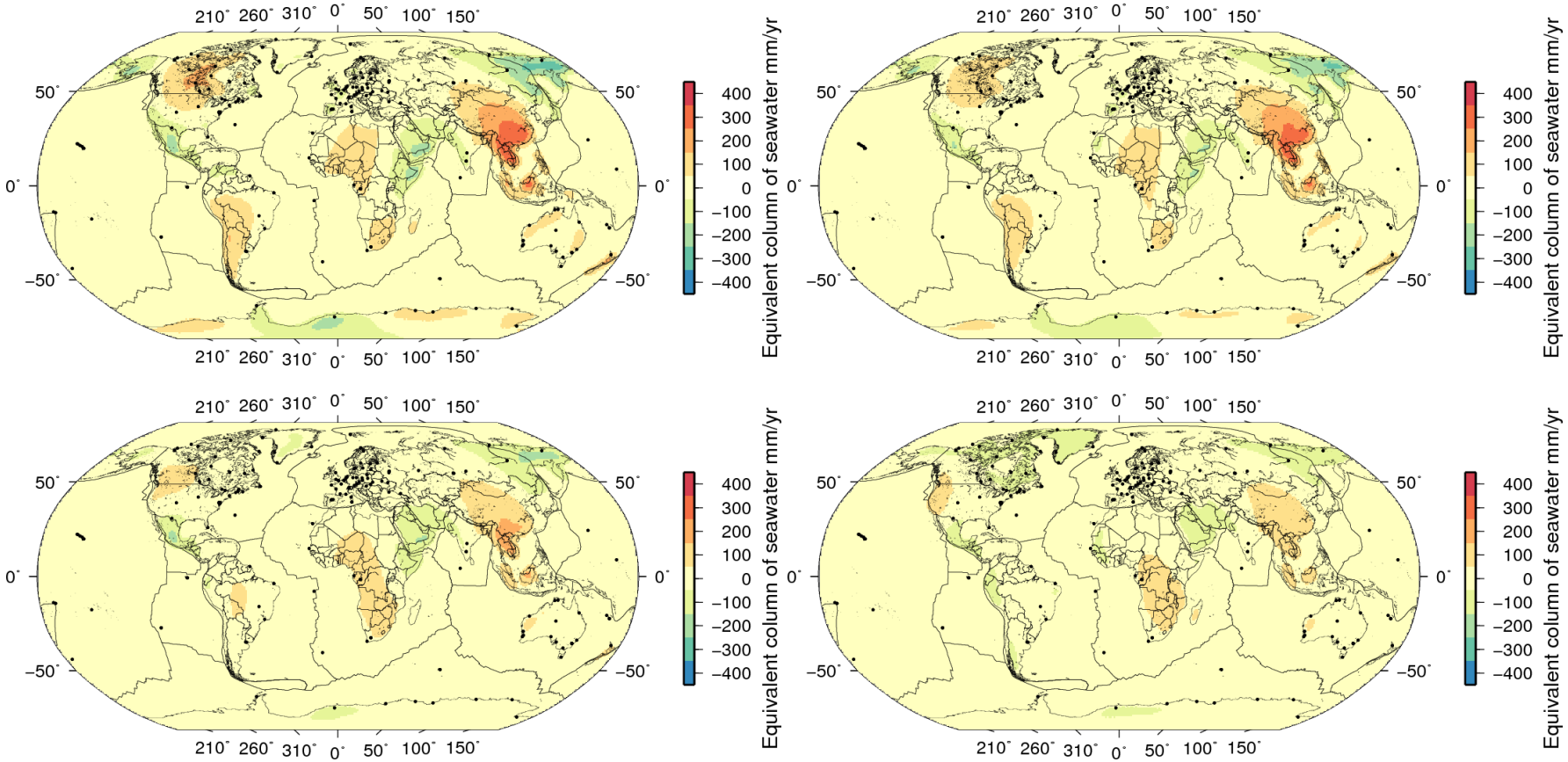

Figure 62: Level four estimation for each GIA velocity model, network sites plotted in black. Top left ICE5G-VM2, top right ICE5G-VM4 (Peltier, 2004), bottom left Schotman, and bottom right Schotman Alternate (Schotman and Vermeersen, 2005). Grey mask covering areas of uncertainties, taken from synthetic solution (>40mm/yr).

6.4.3 *Level Five estimation (GIA)*

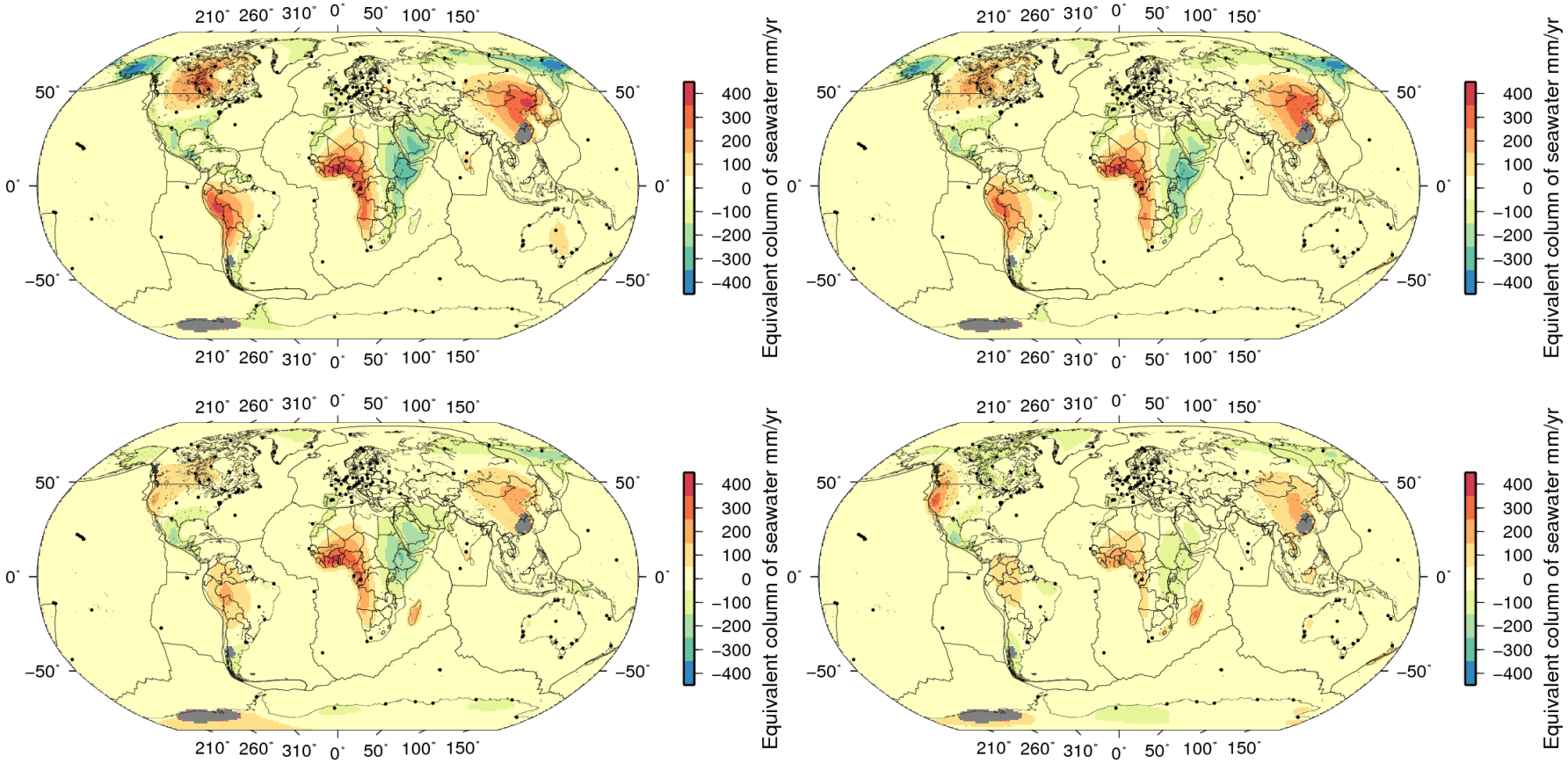

Figure 63: Level five estimation for each GIA velocity model, network sites plotted in black. Top left ICE5G-VM2, top right ICE5G-VM4 (Peltier, 2004), bottom left Schotman, and bottom right Schotman Alternate (Schotman and Vermeersen, 2005). Grey mask covering areas of uncertainties, taken from synthetic solution (>40mm/yr).

6.4.4 *Level Six estimation (GIA)*

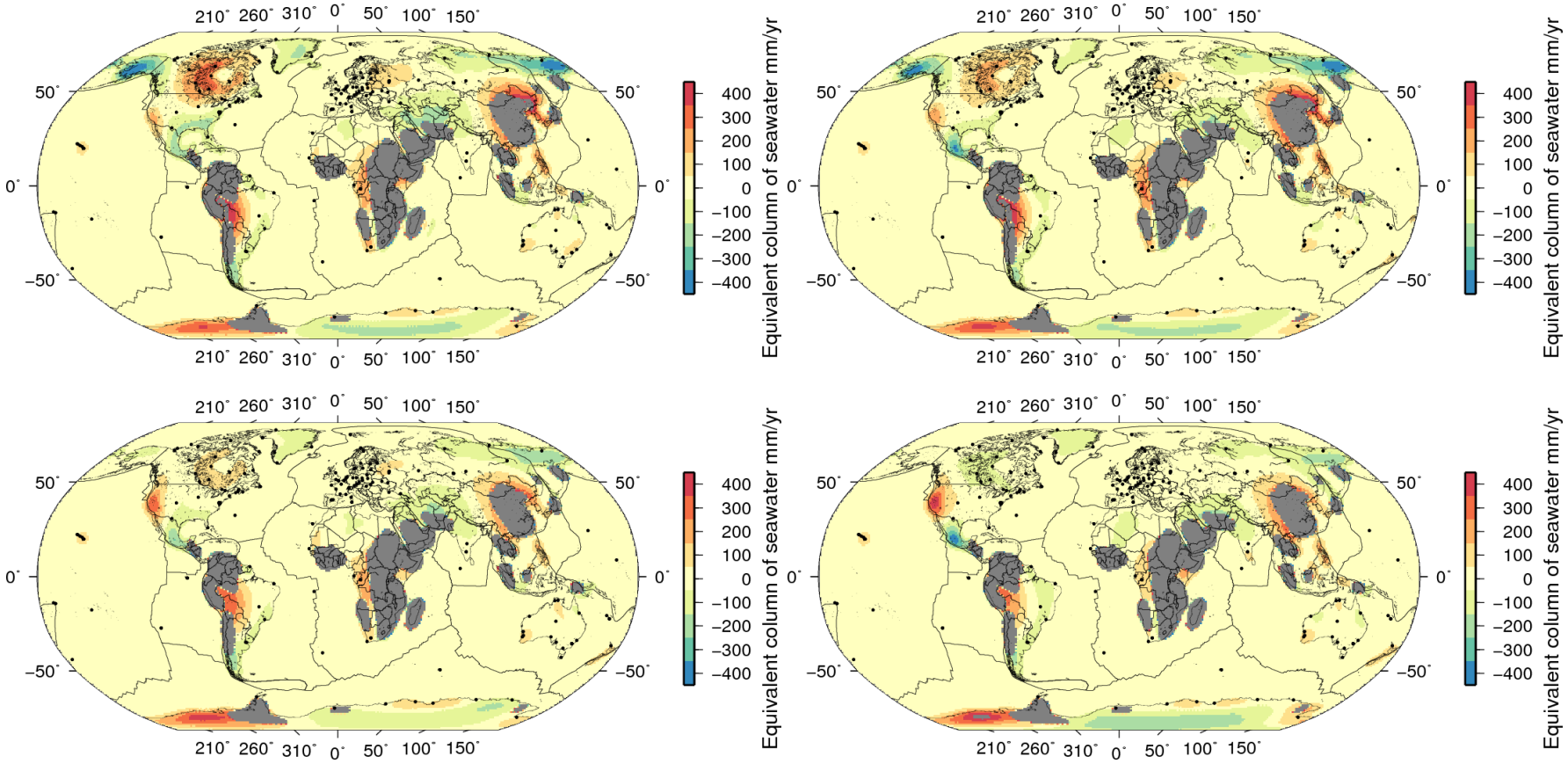

Figure 64: Level six estimation for each GIA velocity model, network sites plotted in black. Top left ICE5G-VM2, top right ICE5G-VM4 (Peltier, 2004), bottom left Schotman, and bottom right Schotman Alternate (Schotman and Vermeersen, 2005). Grey mask covering areas of uncertainties, taken from synthetic solution (>40mm/yr).

Each GIA model will have a different set of specific site velocities, which in turn will imply a different pattern of secular loading trends. Fitting basis function levels four (Figure 62), level five (Figure 63) and level six (Figure 64) should begin to highlight areas which are common artefacts to all models, section (6.2) and what are genuine geophysical signals. In general the artefacts appear in areas which have sparse data coverage; this mostly leaves higher latitude sites as candidates for real geophysical signals.

There is disagreement over continental North America as to the magnitude and spatial distribution of the effects of GIA, also seen in section (5.2.2) and the differences between the two families of GIA models. The residuals to the Peltier model predict large areas of loading over Hudson Bay, for all levels (Figure 62-Figure 64). This is unlikely to be a real signal as it only seems to radiate around Hudson Bay; but is more likely an artefact or a GIA error. I would suggest this is a GIA model error as in the synthetic tests; loading over North America is very well constrained and has shown no tendency to produce artefacts over Hudson Bay. The Schotman models show a mixture of loading and unloading but at a fraction of the magnitude of the Peltier models suggesting a better modelling of the North American GIA effect, presenting an improved picture of the potential present day loading. Greenland and Western Europe appears to be much more robust for all GIA models and levels presented, with Antarctica and Alaska becoming more susceptible to artefacts as the estimated level increases.

Summation of the grid values over selected areas for each model will yield a range of estimated mass change rates which can be compared to other studies. Assuming that there are real signals in areas which are well constrained, then there is possible secular mass unloading over Alaska/Bering straits, Greenland and the Antarctic Peninsula detectable at different basis function levels. Other methods (Wu et al. (2010)) and other systems such as GRACE (Tapley et al. (2004)) have been used to determine similar trends of surface mass loss. GRACE, as with GPS, cannot distinguish between mass loss due to present day trends and those caused by GIA and therefore GRACE is as dependent upon the choice of GIA model as GPS is.

6.5 Predicting Mass Loss from Secular Trends

Through the process described in this thesis it should be possible to detect mass loss in the same regions as those detected by GRACE, through the surface deformation of the Earth.

6.5.1 *GRACE Surface Mass Observations*

One of the products from the GRACE mission is an estimation of the variation of surface masses. By calculating the trend from the monthly GRACE estimates a picture of secular mass variation begins to emerge. Figure 65 is a picture of present day secular mass change from GRACE without any consideration of GIA. The main areas of change occur under the former Laurentian ice dome, Greenland, Alaska, Western Antarctica and the Amazon Basin.

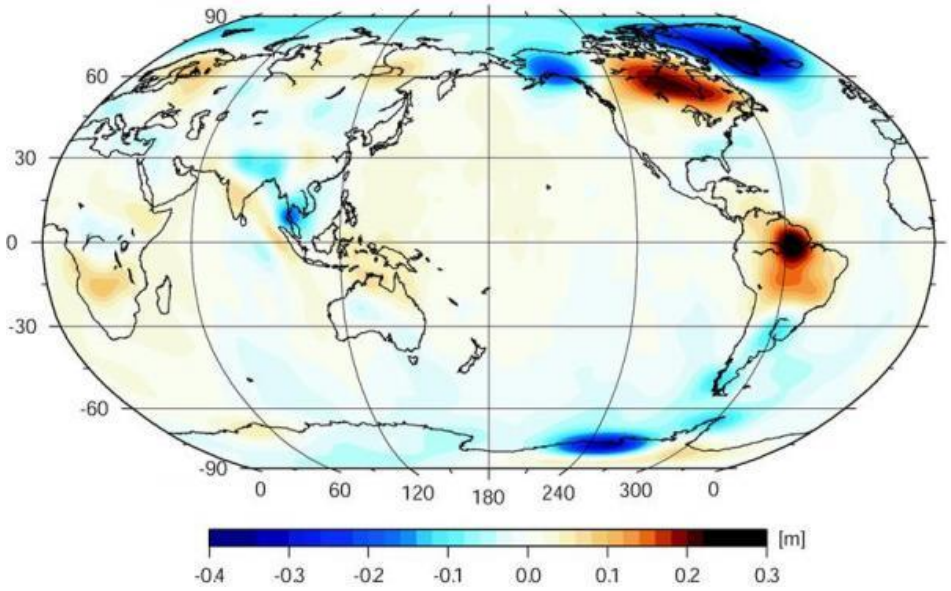

Figure 65: GRACE present day secular mass gain/loss, no GIA accounted for (m) averaged over 2003-2009, taken from Baur et al. (2009)

Baur et al (2009) proceeded to correct these values, accounting for GIA by subtracting a GIA model (Paulson et al. (2005)) from the signal. This produces a GIA-corrected estimate of present day secular mass variation (Figure 66).

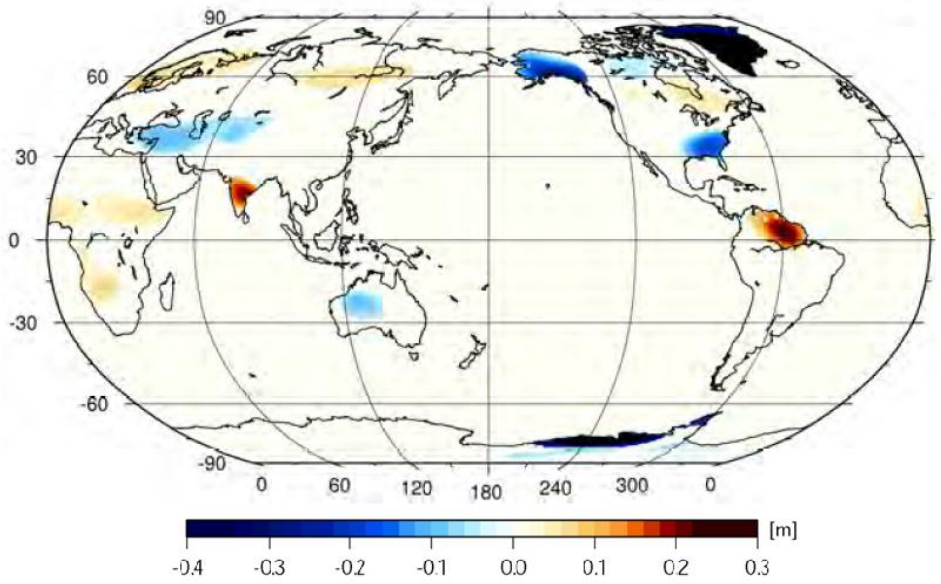

Figure 66: GIA corrected secular mass change, equivalent column of seawater (m) averaged over 2003-2009, taken from Baur et al. (2009)

Figure 66 shows a present day loss of mass in Alaska, Greenland, along the Antarctic Peninsula and over Pine Island and Amundsen Sea Coast. There is also secular mass gain in the Amazon basin and India suggesting these areas are getting wetter. Comparing the GRACE GIA adjusted Figure 66 with our GPS estimates and accounting for areas which have shown susceptibility to artefacts, focus will be upon three areas which have shown recent acceleration of mass loss but have a variety of different surface areas and data coverage (Alaska, Antarctic Peninsula and Greenland) (Rignot et al. (2011), Chen et al. (2009a), Velicogna and Wahr (2006a)), plus a benchmark area (Australia).

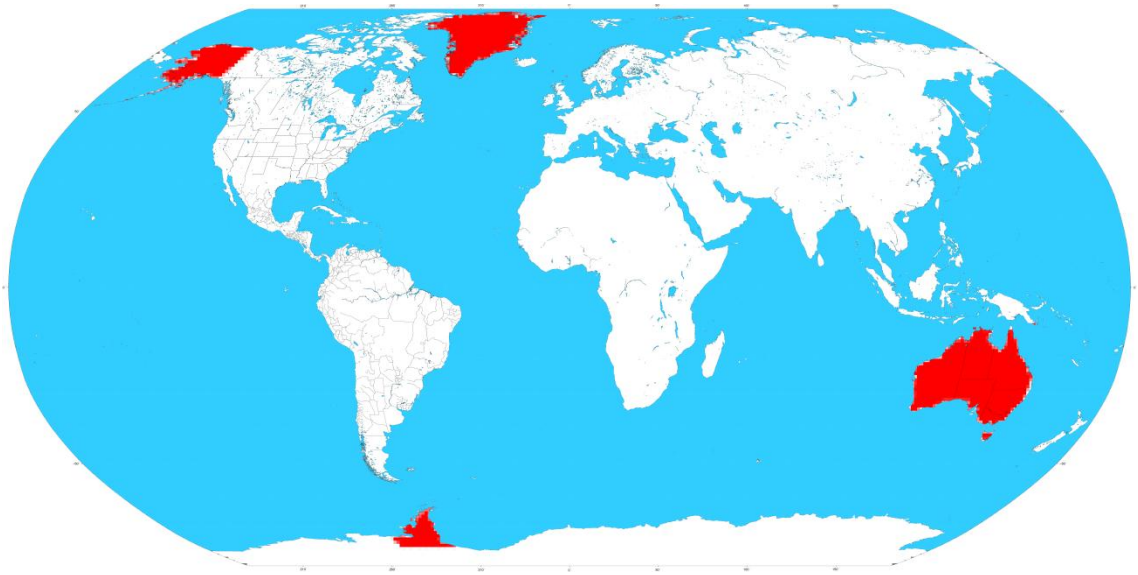

Figure 67: Areas of interest and the exact extent of land mask used in calculations

With the following land surface areas and the number of stations in the region:

- Alaska – $1.48 \times 10^6 km^2$ (0)
- Antarctic Peninsula – $1.06 \times 10^6 km^2$ (1)
- Greenland – $2.17 \times 10^6 km^2$ (4)
- Australia – $7.70 \times 10^6 km^2$ (20)

Below, Table 24 to Table 27 shows the estimated mass loss values for the respective regions from fitting a weighted linear regression. The propagation of errors through the inversion process will bias the estimation of secular surface mass loading. To account for this fact an associated error budget for each level has been calculated using the same inversion methods but using the RMS of the velocity biased trends from section (6.2.2) as the input for each level.

6.5.1 *Alaska*

Table 24: Estimated mass loss for respective levels and models in Gt/yr for Alaska. The numbers in the brackets are the equivalent trend errors (1σ) from section (6.2) represented in terms of mass change in Gt/yr.

	Level			
Alaska	4 (±18)	5 (±29)	6 (±31)	7 (±80)
null	-41	-57	-68	-123
ICE5G-VM2	-130	-400	-420	-371
ICE5G-VM4	-129	-324	-339	-313
Schotman	-49	-114	-56	-70
Schotman Alternative	-37	-25	-35	-105
Wu et al. (2010)	-101±23			

Although there are no stations located directly in the proposed study area, there is a very strong network in North America to constrain the inversion. However the south coast of Alaska runs very close to an active deformation zone which could contaminate the solution. Alaska has also shown a tendency for higher level estimation artefacts. The size and shape of the Alaskan area makes it more suitable to lower level estimation than the Antarctic Peninsula, section (6.5.2).

From the synthetic analysis, Alaska seems to be resilient to gross artefacts up to a maximum level 6 which is reflected in the error budget. Accounting only for tectonic motion there is a small net loss up to a level 6 estimation (-68±31Gt/yr), once a GIA model has been introduced then there are two very distinct

solutions relating to the two GIA model families. Peltier's models suggest GIA had a large influence over the net mass change and was masking the true extent of present day mass loss. This again seems indicative of the unrealistic nature of Peltier's models over North America, section (5.2.2). If however the Schotman family are considered correct then GIA has a significantly smaller influence over the net mass change suggesting that Alaska was outside or on the peripheral bulge of the Laurentian Ice complex and will only explain a small part of the mass loss, with present day melt explaining the rest. Based on the Schotman model, (discounting the level five value) the preponderance of the results are in the range of -25 to -56Gt/yr with errors in the order of ±30Gt/yr assuming that Alaska it resistant to major artefacts up to a level five or six estimation and rejecting both of Peltier's models.

6.5.2 *The Antarctic Peninsula*

Table 25: Estimated mass loss for respective levels and models in Gt/yr for Antarctic Peninsula. The numbers in the brackets are the equivalent trend errors (1σ) from section (6.2) represented in terms of mass change in Gt/yr. Levels 6 and 7 are added for consistency but are within the area of uncertainty, Figure 54 and Figure 55 respectively.

	Level			
Antarctica	4 (±6)	5 (±7)	6 (±25)	7 (±45)
Null	-12	15	-11	48
ICE5G-VM2	-36	-53	29	26
ICE5G-VM4	-34	-29	2	33
Schotman	-12	12	53	90
Schotman Alternative	-10	7	18	64
Wu et al. (2010)	-64±32			

Estimates of the Peninsula suffers from several factors, first it is very long and narrow which means that the lower level solutions generalise over a large area. A higher level solution would be ideal, increasing the spatial resolution, except that there is insufficient data to be able to constrain the inversion: currently only one station is included on the Peninsula and all other Antarctic stations are located along the coastlines. Using the synthetic analysis as a guide then a maximum estimation of levels four or potentially five can be considered. As there are no stations to the west of the Peninsula, artefacts become large and leak into the Peninsula biasing the estimation of mass loss.

There is a mixture of estimates even at low levels with the introduction of a GIA model. The Peltier estimates of mass loss appear to be ~3 times larger than the Schotman models at level four, but with good agreement within each GIA family. I suggest a potential present day mass loss of the interior, of somewhere in between the two models -24±6Gt/yr, which is significant at 2σ but there is such a scatter of results and as noted in section (5.2.2), Antarctica GIA remains a significant uncertainty.

6.5.3 *Greenland*

Table 26: Estimated mass loss for respective levels and models in Gt/yr for Greenland. The numbers in the brackets are the equivalent trend errors (1σ) from section (6.2) represented in terms of mass change in Gt/yr.

	Level			
Greenland	4 (±12)	5 (±22)	6 (±22)	7 (±35)
null	-245	-194	-226	-195
ICE5G-VM2	-47	-124	-229	-239
ICE5G-VM4	-56	-64	-136	-138
Schotman	-90	-79	-140	-135
Schotman Alternative	-188	-113	-148	-135
Wu et al. (2010)	-104±23			

Greenland is a much better candidate for this method as it is both bigger than either the Antarctic Peninsula or Alaska and there are multiple sites able to constrain the inversion on Greenland itself and large networks either side in North America and Europe. The null-GIA calculation estimates a large mass loss (comparable with the higher end of the GRACE value, see below Table 28), but the introduction of a GIA model at the lower level estimation removes a significant amount of mass loss, suggesting that Greenland is partly subsiding due to the Laurentian adjustment. Greenland has shown strong resilience to artefacts at all levels tested, such that a higher level estimate can be calculated (finer resolution) with greater confidence. There is some disagreement over lower levels but for a level six and seven the general consensus is that GIA can explain some of the signal with all the models apart from ICE5G-VM2 settling on a mass loss value in the region of -140±30Gt/yr which is strongly significant at the 2σ level. Once again the ICE5G-VM2 model suggests a significantly

different answer to the other GIA models presented here. A much more detailed discussion and comparison of Greenland is conducted below, section (6.6).

6.5.4 *Australia*

Table 27: Estimated mass loss for respective levels and models in Gt/yr for Australia. The numbers in the brackets are the equivalent trend errors (1σ) from section (6.2) represented in terms of mass change in Gt/yr.

	Level			
Australia	4 (±45)	5 (±59)	6 (±83)	7 (±138)
Null	128	134	58	44
ICE5G-VM2	242	224	158	156
ICE5G-VM4	195	179	103	93
Schotman	183	183	127	111
Schotman Alternative	139	117	44	33

As a benchmark the mass change estimation was calculated for Australia as it is similar in shape and has a similar network distribution to Greenland although it is considerably larger. Here one would expect relatively little secular mass change due to the arid nature of the region. If any, (Baur et al. (2009)) Figure 66, displays a small mass loss over Western Australia. The lower level results for the null GIA model show unexpected artefacts, and only once the level estimation increases do the estimated net mass change values drop down below the predicted noise values (58±83Gt/yr). The introduction of a GIA model tends to confuse matters even at high levels (103-242Gt/yr), apart from Schotman's alternative model. This suggests that a mid-range, level 5, mass gain in the order of 175Gt/yr but with errors bounds of ±59Gt/yr and is therefore not significant at the 2σ confidence level. In an attempt to explain this, closer examination of the basis function estimation residuals reveal an unrecovered signal at Alice Springs which is the only site in the interior of Australia. This could potentially dominate at the lower level estimates due to the broader resolution, but once the spatial resolution become finer the area of influence of Alice Springs is reduced. The size of Australia plays a part in this unexpected result, as small systematic errors will accumulate especially in the synthetic analysis when assessing the RMS. Closer inspection of the GIA models used shows a distinct SW motion of Australian sites in the Schotman models, with the

main Schotman model slightly more pronounced; these motions are not present in Peltier's model.

6.6 Comparisons of Mass Loss Estimates

Discussed above consider the various secular mass estimates over selected area with different GIA models introduced. All have shown potential for observing present day mass loss but some have also shown a susceptibility to inversion artefacts (Alaska and the Antarctic Peninsula). It should be noted that the Antarctic Peninsula is approximately half the size of Alaska and Greenland, and the approach is unable to produce consistent results. To be able to put any confidence into an Antarctic Peninsula mass loss estimate, a much denser station network is required; the POLENET campaign (www.polenet.org) is achieving this but it will take several years before any estimation of secular rates can be made.

The methods used in this study are offered as an alternative to compare with other GPS results (Wu et al. (2010)) or with alternate systems such as GRACE (Tapley et al. (2004)). Wu et al. (2010) attempted to estimate a GIA adjusted mass loss and for the three areas identified calculated the following values: -101±23Gt/yr Alaska, -64±32Gt/yr West Antarctica and -104±23Gt/yr Greenland. Using GRACE, Velicogna (2009) observed different secular rates over different data spans. A secular mass loss over Greenland of -137Gt/yr and -248Gt/yr over the periods 2002-2003 and 2007-2009 respectively is observed, suggesting an increasing in mass loss, with an overall trend of -230±33Gt/yr. Velicognia also calculates a mass change of -143±73Gt/yr over the entire Antarctic ice sheet. A range of values from a variety of authors spans from -66±49Gt/yr to -248±36Gt/yr for Greenland (Table 28).

Table 28: Secular ice mass variations over Greenland, Gt/yr. Mass loss values are corrected for the GIA model stated. *Pritchard et al. (2010) does not explicitly state the GIA model used but states that it is a continuation of the work from Luthcke et al. (2008).

Study	GIA model	Period	Mass loss (Gt/yr)
Velicogna and Wahr (2005)	ICE5G-VM2	Apr2002-Jul2004	-82 ± 28
Velicogna and Wahr (2006a)	ICE5G-VM2	Apr2002–Apr2006	-248 ± 36
Chen et al. (2006c)	ICE5G-VM2	Apr2002–Nov2005	-234 ± 24
Luthcke et al. (2006)	ICE5G-VM2	Jul2003–Jul2005	-113 ± 17
Ramillien et al. (2008)	ICE4G-VM2	Jul2002–Mar2005	-141 ± 16
Wouters et al. (2008)	Paulson et al. (2005)	Feb2003–Jan2008	-179 ± 25
Velicogna (2009)	ICE5G-VM2	Apr2002–Feb2009	-230 ± 33
Pritchard et al. (2010)	ICE5G-VM2*	2004-2009	-66 ± 49
NC1 (Level 7)	ICE5G-VM2	1999-2010	-239 ± 35
NC1 (Level 7)	Schotman/ ICE5G-VM4	1999-2010	-140 ± 30

The solutions presented in this study (-135±22 to -148±35Gt/yr) fit within mass loss estimates from GRACE (-66±49 to -248±36Gt/yr) over Greenland. However it is clear that there is as yet no definitive value of secular mass loss; the range varies dramatically due to the very different time periods used and the inclusion of different GIA models. Comparing the NC1 results with the more recent published results over a similar time period (Velicogna (2009), Wouters et al. (2008)) shows that the results which rely on the ICE5G-VM2 model are comparable within errors and the results which use an alternative GIA model are approximately equivalent within the error budgets.

An altimetric study of Alaska Arendt et al. (2002) suggests a mass loss of ~96±35Gt/yr, and Wu et al. (2010) obtained a mass loss of 101±23Gt/yr. In comparison a level 4 estimate for the NC1 results of (-25 to -56±30Gt/yr).

However the NC1 result agrees with Wu et al. (2010) if we consider the GRACE only values, -68±28Gt/yr and -71±6Gt/yr (Luthcke et al. (2008)). This lower estimate could be explained by the lack of stations within the study area, the choice of GIA model used or, as the region is close to a deformation zone. All of these reasons make it increasingly difficult to estimate consistent results due to inversion artefacts.

6.7 Summary

In this chapter I have shown that it is possible to fit a set of modified basis functions to enable an estimate of present day surface mass loading, although the solution is unstable in areas of poor spatial coverage. This increases the likelihood of artefacts masking real geophysical signals. Converting these results, which are represented as equivalent columns of sea water, into an estimated mass loss in Gt/yr it is possible to compare the results to a completely independent estimate of present day mass loss in areas which show stability in the synthetic data analysis. Estimates from the GRACE satellite system are used for comparison; values vary dramatically due to different study periods and GIA model adjustments. The results presented from this study fit within the range of published estimates, but there is no one GRACE value which the results presented in this study agrees with. This is most likely due to the variations in data span and GIA model used.

Chapter 7. Conclusions

The precision of station coordinate estimates from GPS measurements is continually improving. This is due to the on-going efforts to improve processing strategies and models, section (3.3). The computed combination of reprocessed data contains ~80 extra stations (GPS week 1000-1300) and has shown great improvement over the operational data, sections (3.6.6, 3.6.7); this is highlighted by the reduced WRMS, Figure 26. This improvement has allowed the construction of an improved global kinematic solution, section (4.1) which is fundamental to the estimation of plate tectonic rotations, section (2.5.3) and surface mass loading, section (2.3).

7.1 Reprocessed Data Series

This study pays careful attention to the quality of the weekly combined solution and the kinematic station estimates, Chapter 3 and Chapter 4. The best measures of quality can be concluded by comparing the reprocessed dataset to its predecessor.

- The number of stations included in the weekly estimates has increased dramatically, especially in the early weeks (1000-1300) of the data sets (Figure 22). This results in an increased number of stations suitable for inclusion in the kinematic estimation, section (4.1).
- The WRMS of each AC and of the combined solution shows a dramatic reduction, ~50% in comparison to the operational series, when aligned to the chosen reference frame (Figure 24, Figure 25 and Figure 26).
- The estimated seven parameter Helmert transformation variations are reduced by ~75% across the board. This reduction is even greater for some AC solutions in the very early weeks (Table 16).
- The most important improvement seen between the operational and reprocessed data sets is the removal of systematic offsets (Figure 27, Figure 28 and Figure 29) and noise (Figure 30 and Figure 31) which was the primary aims of the IGS reprocessing campaign.
- By only including stations with over 2.5 years of data (following recommendations of Blewitt and Lavallee (2002), with the majority of included station having a much longer data span, station velocities, section (4.4), are now estimated with sub-millimetric formal errors,

(Appendix A), even after accounting for an appropriate noise model, section (4.4.2).

7.2 Model Estimation

A large section of this work has been the development of an integrated 3D displacement model, section (5.2). A by-product of this is an estimation of the tectonic plates' absolute Euler poles, section (5.2.2). As the solutions presented here are aligned to the IGS05 it is possible to directly compare the NC1 model with other studies, section (5.2.2). There are differences between the estimated Euler pole locations and error ellipses calculated here and those from previous studies, section (5.2.2); this is most likely due to the different data spans and analysis used (operational versus reprocessed).

The introduction of a suite of GIA models into the station displacement model, section (5.1.4), has very little effect upon the estimation of the horizontal tectonic plate models (<3mm/yr residual compared to null-GIA estimate, based on King et al. (2010)), (Figure 43). This allows for the removal of a range of a priori GIA trends from the raw velocities, section (5.2), although these small changes have an important effect upon the final estimates. Shows sensitivity to small regionally correlated velocity errors It should be noted that the GIA models used only represent a 1D Earth model and the introduction of a 3D model could potentially introduce horizontal velocities different by ~1-2mm/yr (Latychev et al. (2005a)), which would influence the tectonic plate estimation, but until a 3D GIA model becomes publically available this influence can only by hypothesised.

The use of a combined GIA and plate tectonic velocity model in place of a linear velocity estimate produces residuals which should be due to present day secular surface mass loading and model error. The final stage of work, Chapter 6, fits a set of modified spherical harmonic functions to the residual at different levels; this method models and recover the remaining trends.

One of the aims of this study was to determine the maximum level of basis function estimable; preliminary investigations showed that higher level inversions (7-12) were prone to spurious signals, so two tests of global inversion quality were carried out. The first used a global χ^2/dof to test if there were any indication of a fall in inversion quality as the inversion level increased. Of the levels tested (1-8) there was no indication that the higher levels were

indeed a poor fit with all values falling within the expected χ^2/dof range (Table 23).

The second test used a trend free synthetic data set, section (6.2), to which several scenarios of random white noise (WN) and coloured noise as a velocity bias (VB) were added. The inversion was completed as with the real data sets and the RMS of WN and VB results were produced. The WN test shows that for levels (4-6), with no trend was expected, there is only a very small loading trend of 2-3mm/yr introduced through the inversion process which is deemed to be the random error of the basis function estimation.

For the WN+VB synthesis which has a small velocity bias added (standard deviation of 0.2mm/yr and 1mm/yr for horizontal and vertical components respectively), as the basis function level increases, there is a growing susceptibility to inversion artefacts for regions at different levels. These artefacts tend to appear where the spatial data coverage is sparse, Figure 55, whereas areas which are, in or around, dense GPS network coverage show resilience to inversion artefacts. This synthesis indicates which observed loading signals are potentially real, and provides an estimation of the inversion error. The same VB test but using the reduced network shows similar spatial pattern and magnitude of inversion error, section (6.2.2).

Despite the different GIA models, section (2.4.4), similar areas of present day mass loss become apparent at the maximum reliable inversion level Alaska (level six), Antarctic Peninsula (level four) and Greenland (level seven), Figure 62-Figure 64, with an expected low to zero benchmark test of Australia (level seven). There are some differences between the GIA adjusted estimated load in both spatial distribution and magnitude. Alaska and the Antarctic Peninsula tend to suffer from inversion artefacts at a lower level compared to Greenland which is, in part, due to the latter's size, shape and data coverage. This again reiterates the method's reliance upon global data coverage.

Calculation of the total mass change in the selected areas over all levels produces an initial mixed message of mass loss and gain, but when accounting for the maximum reliable inversion level for the selected areas (Alaska, Antarctic Peninsula and Greenland), the message becomes one of clear mass loss, (Table 24-Table 27), with Australia showing a small mass gain within the inversion error.

There have been several studies of mass loss using GRACE (Baur et al. (2009), Velicogna (2009), Luthcke et al. (2008), Velicogna and Wahr (2005)), section (6.5.1) and some using GPS in addition to GRACE (Wu et al. (2010)). These offer an independent assessment of global mass change which can be compared to the NC1 estimation. Greenland has by far the most investigations, and also happens to be the best candidate for this method especially at the higher basis function levels. Apart from the ICE5G-VM2 model, there is good agreement at levels six and seven of a value ~-140±30Gt/yr, with the ICE5G-VM2 model giving an estimated value of -234±30Gt/yr. GRACE, as with GPS, is dependent upon GIA model choice. Table 28 shows the wide ranging values of GRACE mass change estimates over Greenland with some of the ICE5G-VM2 adjusted estimates estimating mass change of -234±24 to -248±36Gt/yr, (Chen et al. (2006c), Velicogna and Wahr (2006a)) which are similar to the NC1 ICE5G-VM2 estimate. Considering the various studies over Greenland which range from -66±49Gt/yr to -248±36Gt/yr the NC1 solutions fit well within this range for three out of the four models used with the fourth (ICE5G-VM2) at the higher end of values.

Comparing values over Alaska at a lower level to other studies we find our estimates are ~50% less, this could be due to the “true” loading being contaminated by inversion artefacts, tectonic deformation or network coverage. Synthetic tests would suggest that the processes is mainly affected by station coverage, combined with residual GIA as being the cause for this reduced value over Alaska. As for the Antarctic Peninsula the level four values suggests a small mass loss but this quickly becomes biased by artefacts and is highly unstable between levels. There is no real comparable study for the Antarctic Peninsula on its own.

7.3 Future Work and Recommendations

The kinematic solution and suite of global secular loading models presented here are a valuable source of data for scientific research and I have only followed one line of investigation. Even with all considerations there are still components of this study which could be further extended. In the future additional GNSS data sets will become available (e.g. GLONASS in some AC solutions). The addition of these data sets will continually increase the length and number of stations available for study, and may reduce technique-specific

errors. The improvement of the IGS reprocessing campaign's first round is highlighted by the vast increase in the precision compared to the historic operational processing. Although such a dramatic improvement of any further rounds of reprocessing might not be as apparent. The first recommendation made is that these reprocessing campaigns are a valid and valuable use of resources and that future campaigns should be considered as new model improvements come to light. One of the main limitations of this study is the number of stations available, especially in the southern hemisphere. One of the main improvements is due to the densification of the available network especially in early weeks. It cannot be stressed enough the importance of including previously unused stations which has shown to be a factor throughout this study. This should partly be address through the second round of reprocessing is already in the pipeline and also intends to include:

- Other GNSS solutions
- TIGA solutions
- Reprocessed regional and external global networks
- P2-C2 satellite bias correction
- Adoption of IGS08 reference frame, with increased number of sites in comparison to IGS05
- Updated antenna calibrations
- Updated geopotential model
- Improved satellite attitude modelling
- Updated albedo accelerations model

The list is long, and if all of the proposed updates are included then the improvement to the entire data series would warrant a second kinematic solution being produced. Steps have been taken to include the ERPs as with the IGS official combined product; investigations into the numerical instabilities and future inclusion of ERPs would provide a separate data series to compare with this study.

The consideration of vertical station motion in this study has been achieved by employing a limited number of global GIA models which use a 1D Earth model. The inclusion of these models has been shown to reduce the vertical residuals of the secular loading model. The included models have known deficiencies, especially around Antarctica. The second recommendation is twofold, first to

extend the range of GIA models used, focussing upon Antarctica, and second to introduce a GIA model based on a 3D earth model.

This initial kinematic solution assumes a white noise station velocity error model which is insufficient to account for the known correlations between weekly GPS observations, individual tracking stations' monument motion or any other low frequency systematic noise. To account for this a uniform variance scaling factor has been applied to the kinematic solutions uncertainties based on work by Santamaria-Gomez et al. (2011) and Bos et al. (2008). The third recommendation would encourage a more in-depth investigation of individual station coloured noise components using the reprocessed data and a more through implementation of these into the kinematic velocity estimation.

This study has only used data from one spaceborne geodetic technique with a limited set of GIA models, and carried out the inversion using basis functions. The method has been shown to suffer from inversion artefacts over regions with sparse data coverage; the inclusion of additional sites (e.g. relaxing inclusion criteria) would allow additional stations to aid the inversion. The inclusion of data from other missions such as GRACE or sea-surface altimetry (corrected for steric ocean changes) would increase the redundancy of the solution and strengthen any inferences made about present day surface mass changes. The residual loading harmonic estimation only uses continental basis functions. The inclusion of oceanic basis functions, which account for the redistribution of masses within the ocean due to circulation currents, might improve the estimation of loading slightly. This again would provide a better picture of global mass redistribution.

The methods described in this study are presented as an alternative which only uses deformation data. This is an advantage as it is neither dependent upon a particular ocean model output nor dependent upon assumed covariance between GIA deformation fields. This produces a much clearer and more transparent method, i.e. when using model A the predicted mass change is X Gt/yr with a known ocean effect. The limitations of this study are imposed from the size and distribution of the station network and the limited nature of the GIA model which should improve with time.

Appendix A. Raw Station Velocities

Site	Latitude	Longitude	Height	Velocity (mm/yr)			1σ					
	ϕ°	λ°	(m)	Up	North	East	ϕ°	λ°	Height	Up	North	East
ade1	-34.73	138.65	38.06	-1.19	58.72	24.80	0.72	0.67	2.48	0.35	0.10	0.10
ajac	41.93	8.76	98.77	0.74	16.03	20.42	1.14	0.96	3.73	0.77	0.23	0.20
algo	45.96	281.93	200.90	3.15	2.58	-16.23	0.48	0.39	1.51	0.44	0.14	0.11
alic	-23.67	133.89	603.26	0.18	59.42	32.03	0.45	0.45	1.64	0.27	0.07	0.08
alrt	82.49	297.66	78.10	5.60	5.50	-20.80	0.87	0.78	5.30	0.84	0.14	0.12
amc2	38.80	255.48	1911.40	0.07	-4.92	-14.46	1.20	1.04	4.02	0.32	0.10	0.08
aoml	25.73	279.84	0.10	-0.24	3.14	-9.95	0.69	0.72	3.05	1.56	0.34	0.36
artu	56.43	58.56	247.57	0.74	6.34	24.59	0.46	0.35	1.34	0.24	0.08	0.06
asc1	-7.95	345.59	105.12	0.00	11.18	-5.85	0.65	0.77	2.33	0.72	0.19	0.23
aspa	-14.33	189.28	53.65	-0.15	34.65	-63.51	0.95	1.13	4.08	0.75	0.17	0.20
auck	-36.60	174.83	132.71	-1.42	40.27	5.20	0.48	0.49	1.51	0.24	0.08	0.08
bake	64.32	264.00	4.38	10.45	-3.82	-18.62	3.93	2.91	13.63	2.70	0.77	0.57
ban2	13.03	77.51	831.87	1.36	35.85	43.82	3.81	4.96	17.04	3.15	0.70	0.90
barh	44.40	291.78	6.76	-0.53	6.99	-14.92	0.94	0.77	3.46	0.97	0.27	0.22
bili	68.08	166.44	456.14	0.10	-20.18	8.86	0.57	0.44	1.89	0.66	0.19	0.15
bor1	52.28	17.07	124.36	0.06	14.70	19.77	0.54	0.42	1.72	0.27	0.09	0.07
braz	-15.95	312.12	1106.02	-0.39	12.92	-4.25	0.51	0.55	1.77	0.31	0.09	0.09
brft	-3.88	321.57	21.68	0.31	13.81	-5.34	3.02	3.45	12.58	1.87	0.45	0.51
brmu	32.37	295.30	-11.62	-0.16	8.18	-12.42	0.46	0.46	1.91	0.51	0.13	0.13
brst	48.38	355.50	65.83	0.22	16.54	16.45	1.66	1.32	5.81	2.01	0.58	0.46
brus	50.80	4.36	149.67	0.71	15.78	17.54	0.94	0.70	3.09	0.46	0.14	0.11
bue1	-34.57	301.48	48.66	2.62	13.14	-1.34	0.83	0.75	2.71	0.38	0.12	0.10
cagl	39.14	8.97	238.36	0.37	15.97	21.26	0.63	0.57	2.41	0.35	0.10	0.09
cagz	39.14	8.97	237.98	-0.08	16.07	21.35	1.80	1.61	6.66	0.85	0.23	0.20

cas1	-66.28	110.52	22.46	0.68	-10.00	1.80	0.56	0.45	1.54	0.27	0.10	0.08
cedu	-31.87	133.81	144.75	-0.92	58.99	29.15	0.45	0.43	1.49	0.26	0.08	0.07
chat	-43.96	183.43	57.99	-0.63	33.60	-40.52	0.61	0.59	1.99	0.35	0.12	0.10
chpi	-22.69	315.01	617.41	1.07	12.93	-3.87	1.12	1.15	4.39	0.59	0.15	0.15
chur	58.76	265.91	-19.40	10.48	-2.89	-18.05	0.49	0.36	1.43	0.24	0.08	0.06
crao	44.41	33.99	365.80	-0.45	12.18	23.61	1.52	1.29	5.75	1.07	0.28	0.24
daka	14.68	342.53	46.20	-1.40	18.42	19.10	1.70	1.99	7.44	1.51	0.34	0.40
darw	-12.84	131.13	125.12	-0.93	59.05	35.93	0.53	0.58	2.12	0.63	0.15	0.16
dav1	-68.58	77.97	44.42	-2.19	-5.37	-2.81	0.63	0.52	1.90	0.44	0.14	0.11
dubo	50.26	264.13	245.29	1.22	-4.30	-17.30	1.35	1.04	4.30	0.27	0.09	0.07
dum1	-66.67	140.00	-1.35	-1.23	-11.09	8.84	1.20	0.90	3.84	0.83	0.25	0.19
eisl	-27.15	250.62	114.55	-3.90	-5.54	68.42	1.03	1.18	4.29	2.60	0.61	0.71
eprt	44.91	293.01	30.38	0.63	6.93	-15.43	0.76	0.61	2.63	1.10	0.33	0.27
fale	-13.83	188.00	47.60	0.15	34.04	-62.82	0.80	0.95	3.10	3.26	0.79	0.93
flin	54.73	258.02	311.50	2.99	-6.96	-17.47	0.58	0.43	1.71	0.29	0.10	0.07
fort	-3.88	321.57	19.47	0.49	12.69	-4.67	1.35	1.83	6.64	1.78	0.36	0.46
gala	-0.74	269.70	7.44	1.69	10.34	51.22	0.94	1.10	3.57	2.63	0.63	0.77
glps	-0.74	269.70	1.79	0.65	10.54	50.45	1.04	1.19	3.49	0.72	0.21	0.25
glsv	50.36	30.50	226.32	0.12	12.79	22.03	0.46	0.36	1.33	0.30	0.10	0.08
gode	39.02	283.17	14.51	-0.95	4.20	-14.62	0.49	0.44	1.70	0.28	0.08	0.07
gope	49.91	14.79	592.58	1.53	14.85	19.97	4.34	3.14	14.92	0.99	0.31	0.23
goug	-40.35	350.12	81.26	-1.09	18.85	20.93	0.69	0.62	2.09	0.96	0.25	0.22
hers	50.87	0.34	76.51	0.34	16.35	16.61	0.73	0.57	2.45	0.45	0.14	0.11
hert	50.87	0.33	83.33	-0.10	16.86	16.73	2.18	1.69	6.83	0.95	0.30	0.24
hilo	19.72	204.95	29.31	-1.91	36.04	-63.02	0.74	0.83	3.01	0.49	0.12	0.14
hlfx	44.68	296.39	3.11	0.02	8.58	-15.05	1.25	0.97	4.06	0.62	0.19	0.15
hnlc	21.30	202.14	21.97	-0.46	35.10	-62.71	0.52	0.57	2.08	0.37	0.09	0.11
hnpt	38.59	283.87	-27.96	-2.27	3.79	-14.31	0.80	0.70	3.24	0.43	0.11	0.10

hob2	-42.80	147.44	41.07	-0.43	55.32	14.72	0.48	0.43	1.38	0.23	0.08	0.07
holm	70.74	242.24	0.41	3.12	-11.93	-16.97	0.81	0.60	2.98	0.43	0.12	0.09
hrm1	51.45	358.72	163.02	0.08	16.53	16.30	0.59	0.45	1.76	0.45	0.15	0.11
hyde	17.42	78.55	441.71	-1.65	34.67	42.58	1.30	1.51	5.40	0.97	0.23	0.27
iisc	13.02	77.57	843.71	1.24	35.68	41.92	0.64	0.81	2.78	0.74	0.17	0.21
invk	68.31	226.47	46.38	-2.07	-16.31	-12.21	1.27	0.92	4.86	0.62	0.17	0.12
ispa	-27.12	250.66	112.50	-0.07	-5.15	66.81	1.21	1.32	4.30	0.59	0.17	0.18
jab1	-12.66	132.89	82.14	-1.18	60.66	34.88	0.64	0.73	2.76	0.65	0.16	0.17
joze	52.10	21.03	141.43	1.73	14.39	20.82	0.57	0.43	1.80	0.59	0.19	0.14
karr	-20.98	117.10	109.16	0.11	58.54	38.80	0.46	0.49	1.63	0.52	0.13	0.14
kely	66.99	309.06	229.87	2.70	11.44	-17.74	1.11	0.83	3.80	0.57	0.16	0.12
kerg	-49.35	70.26	73.03	-0.50	-2.57	4.76	0.66	0.54	2.00	0.38	0.13	0.10
kiru	67.86	20.97	390.94	7.67	14.81	15.59	0.67	0.49	2.44	0.41	0.11	0.08
kokb	22.13	200.34	1167.36	-0.29	34.87	-62.17	0.55	0.61	2.26	0.57	0.15	0.16
kosg	52.18	5.81	96.85	-0.19	15.93	17.81	0.46	0.36	1.38	0.44	0.14	0.11
kouc	-20.56	164.29	84.16	-1.68	47.42	24.39	1.34	1.46	5.46	0.66	0.16	0.18
kour	5.25	307.19	-25.76	2.30	13.21	-4.68	0.55	0.62	2.11	0.56	0.13	0.15
kstu	55.99	92.79	210.04	1.54	-3.79	25.34	1.54	1.20	4.84	1.60	0.49	0.34
kuuj	55.28	282.25	-0.49	11.26	1.33	-18.39	6.15	4.51	18.71	3.55	1.18	0.86
kwj1	8.72	167.73	38.23	-1.98	30.64	-69.01	1.09	1.43	5.33	4.06	0.81	1.05
lama	53.89	20.67	187.03	0.01	14.21	19.96	0.97	0.72	2.88	0.49	0.16	0.12
lhue	21.98	200.66	46.00	-1.39	35.54	-61.96	1.01	1.13	4.55	1.73	0.40	0.44
lpgs	-34.91	302.07	29.86	2.70	12.13	-1.05	0.68	0.62	2.57	0.41	0.11	0.10
lroc	46.16	358.78	57.86	0.20	16.64	18.20	1.55	1.26	5.30	0.81	0.24	0.20
mad2	40.43	355.75	829.44	-0.09	14.00	18.31	1.70	1.41	6.68	7.57	1.90	1.54
madr	40.43	355.75	829.44	0.62	16.38	18.58	0.63	0.53	2.19	0.63	0.18	0.15
mald	4.19	73.53	-92.03	-3.12	35.48	46.35	0.89	1.05	3.45	1.18	0.24	0.31
mar6	60.60	17.26	75.41	7.01	13.81	17.52	0.67	0.49	2.03	0.34	0.12	0.09

mars	43.28	5.35	61.81	-0.29	16.45	20.19	3.32	2.72	11.32	1.77	0.52	0.44
mas1	27.76	344.37	197.15	-0.40	17.76	16.53	0.44	0.45	1.75	0.26	0.07	0.07
maui	20.71	203.74	3062.12	-1.49	35.08	-61.95	0.44	0.48	1.50	0.29	0.08	0.09
maw1	-67.60	62.87	59.14	-0.63	-2.43	-3.75	0.63	0.51	1.94	0.32	0.10	0.09
mcil	24.29	153.98	35.66	0.29	24.32	-71.58	2.37	2.38	9.34	1.15	0.29	0.30
mcm4	-77.84	166.67	98.00	-2.67	-11.37	10.09	0.70	0.61	3.21	0.47	0.10	0.09
mdo1	30.68	255.99	2004.50	-0.96	-4.93	-12.45	0.49	0.51	2.05	0.30	0.07	0.08
mdvj	56.02	37.21	257.12	0.37	11.86	22.29	1.20	0.86	3.78	0.54	0.17	0.12
mdvo	56.03	37.22	254.80	1.21	11.33	21.77	1.89	1.46	7.13	5.43	1.45	1.12
mets	60.22	24.40	94.59	4.80	12.65	19.57	0.46	0.34	1.34	0.23	0.08	0.06
metz	60.22	24.40	94.55	4.01	12.37	19.53	1.60	1.12	4.88	0.72	0.24	0.17
mkea	19.80	204.54	3754.70	-2.70	35.66	-62.63	0.55	0.61	2.19	0.54	0.13	0.15
mobn	55.11	36.57	182.66	1.26	11.88	22.96	1.78	1.29	5.65	0.90	0.30	0.22
mobs	-37.83	144.98	40.62	-2.35	58.04	19.99	1.80	1.57	6.89	0.92	0.24	0.21
morp	55.21	358.31	144.43	1.96	15.40	15.36	1.63	1.22	5.96	0.82	0.23	0.17
msku	-1.63	13.55	359.65	2.25	20.79	20.51	1.49	1.83	7.04	1.60	0.32	0.40
nain	56.54	298.31	32.75	4.87	10.44	-16.00	2.50	1.80	7.99	1.61	0.50	0.36
nklg	0.35	9.67	31.51	0.26	19.17	22.04	0.62	0.75	2.41	0.51	0.12	0.15
nlib	41.77	268.43	207.04	-1.45	-1.06	-15.47	0.55	0.51	2.18	0.33	0.09	0.08
nnor	-31.05	116.19	234.84	-0.28	58.23	38.53	1.82	1.77	9.03	1.32	0.27	0.27
noum	-22.27	166.41	83.07	-1.44	46.89	21.25	0.50	0.56	1.77	0.75	0.19	0.20
novj	55.03	82.91	125.92	2.18	0.89	23.44	5.46	4.03	19.68	3.89	1.05	0.77
nrc1	45.45	284.38	82.48	3.69	4.06	-16.09	0.47	0.38	1.49	0.25	0.08	0.06
nril	69.36	88.36	47.91	1.74	-1.84	21.74	0.61	0.47	2.10	0.34	0.10	0.08
nrmd	-22.23	166.48	160.35	-1.06	48.66	26.47	3.66	3.90	14.71	1.66	0.41	0.44
nvsk	54.84	83.24	123.09	1.17	-1.22	26.61	1.15	0.81	3.78	0.61	0.19	0.13
nya1	78.93	11.87	84.20	8.83	14.23	10.09	0.47	0.40	2.30	0.56	0.11	0.09
nyal	78.93	11.87	78.47	9.59	14.03	9.95	0.48	0.41	2.43	0.47	0.10	0.08

obe2	48.09	11.28	641.43	1.25	16.08	20.26	1.68	1.57	5.42	1.11	0.35	0.40
onsa	57.40	11.93	45.56	2.74	14.44	16.86	0.42	0.32	1.24	0.20	0.07	0.05
opmt	48.84	2.33	122.57	2.71	15.90	18.30	6.73	5.29	23.16	2.58	0.75	0.59
palm	-64.78	295.95	31.03	3.71	10.68	12.92	0.97	0.71	2.67	0.61	0.21	0.15
penc	47.79	19.28	291.73	0.79	14.84	22.19	0.59	0.47	1.92	0.40	0.12	0.10
pert	-31.80	115.89	12.74	-5.09	57.81	39.42	0.53	0.54	2.03	0.59	0.15	0.15
picl	51.48	269.84	315.10	2.01	-2.32	-16.65	6.07	4.55	17.90	3.38	1.15	0.86
polv	49.60	34.54	178.37	-0.08	12.57	22.26	0.89	0.66	2.64	0.49	0.17	0.12
pots	52.38	13.07	144.42	0.34	15.06	18.91	0.46	0.36	1.35	0.25	0.08	0.06
ptbb	52.30	10.46	130.25	-0.75	15.73	18.81	1.13	0.86	4.38	0.98	0.30	0.22
qaq1	60.72	313.95	110.40	4.09	13.41	-16.66	0.94	0.67	2.77	0.49	0.16	0.12
qiki	67.56	295.97	13.24	4.62	8.40	-18.07	2.23	1.70	7.82	1.00	0.28	0.22
reso	74.69	265.11	19.93	5.97	-4.88	-20.19	1.33	1.05	6.59	0.83	0.17	0.14
riga	56.95	24.06	34.71	1.92	13.25	19.85	0.83	0.67	2.58	0.92	0.29	0.22
sach	71.99	234.75	69.25	0.85	-14.62	-17.11	8.95	6.94	35.42	8.32	2.11	1.64
sch2	54.83	293.17	498.19	10.88	7.81	-17.63	0.49	0.37	1.46	0.24	0.08	0.06
scor	70.49	338.05	128.47	4.18	19.24	-10.62	2.75	1.98	10.61	1.29	0.34	0.24
simo	-34.19	18.44	39.50	0.17	19.69	16.45	1.87	1.81	7.09	1.08	0.28	0.28
sol1	38.32	283.55	-19.05	-2.18	4.31	-14.64	0.77	0.68	3.07	0.96	0.25	0.22
spt0	57.71	12.89	219.94	4.26	14.49	17.10	1.99	1.44	7.23	1.35	0.37	0.27
stjo	47.60	307.32	152.84	0.16	12.79	-14.80	0.84	0.69	2.78	0.29	0.09	0.07
str1	-35.32	149.01	799.94	0.86	55.90	18.52	0.66	0.61	2.36	0.47	0.13	0.12
str2	-35.32	149.01	802.49	0.01	55.73	18.63	1.55	1.40	5.50	0.78	0.22	0.20
sulp	49.84	24.01	370.53	-0.52	13.89	21.94	2.51	1.84	7.44	1.11	0.38	0.28
suth	-32.38	20.81	1799.77	-0.61	19.40	17.32	0.64	0.64	2.16	0.40	0.13	0.12
sutm	-32.38	20.81	1797.62	0.30	19.46	16.96	3.03	2.91	10.16	1.21	0.36	0.35
svtl	60.53	29.78	76.64	5.82	12.22	20.58	4.25	2.93	12.78	1.93	0.64	0.44
sydn	-33.78	151.15	85.59	1.17	54.83	18.33	11.47	10.39	48.28	6.23	1.48	1.34

syog	-69.01	39.58	50.01	0.07	2.69	-4.15	0.72	0.58	2.48	0.36	0.11	0.09
thti	-17.58	210.39	98.04	-0.31	35.08	-66.16	0.56	0.68	2.26	0.35	0.09	0.11
thu1	76.54	291.21	55.02	6.98	3.79	-23.04	0.64	0.55	2.73	3.43	0.78	0.62
thu2	76.54	291.17	36.09	5.21	4.78	-22.05	1.73	1.44	8.05	0.95	0.21	0.17
thu3	76.54	291.17	36.08	5.99	4.77	-22.13	1.10	0.87	5.13	1.01	0.22	0.17
tid1	-35.40	148.98	665.34	0.48	55.49	18.41	1.09	0.97	3.78	0.66	0.19	0.17
tid2	-35.40	148.98	665.34	0.60	55.51	18.41	0.80	0.77	3.02	0.73	0.18	0.17
tidb	-35.40	148.98	665.35	-0.03	55.36	18.36	0.63	0.58	2.19	0.42	0.12	0.11
tixi	71.63	128.87	47.06	1.04	-11.52	16.61	0.42	0.33	1.43	0.29	0.08	0.06
tlse	43.56	1.48	207.19	0.81	16.01	19.41	0.70	0.58	2.46	0.61	0.18	0.14
tow2	-19.27	147.06	88.13	-0.35	56.38	28.90	0.41	0.44	1.39	0.24	0.07	0.07
tro1	69.66	18.94	138.07	2.02	15.55	15.17	0.45	0.34	1.55	0.57	0.16	0.12
trom	69.66	18.94	132.45	2.63	14.84	14.54	0.57	0.43	1.99	0.32	0.10	0.08
tukt	69.44	227.01	-1.53	0.70	-17.32	-11.27	5.14	4.05	18.39	2.73	0.76	0.60
unb1	45.95	293.36	22.85	-4.90	7.66	-15.54	7.06	5.74	22.67	7.27	2.32	1.91
usna	38.98	283.52	-27.31	0.32	3.91	-14.92	0.79	0.68	2.90	0.97	0.26	0.22
usno	38.92	282.93	48.88	-0.91	4.10	-14.55	0.50	0.43	1.78	0.33	0.09	0.08
uzhl	48.63	22.30	232.01	0.65	13.72	21.66	0.92	0.72	3.24	0.74	0.20	0.16
vesl	-71.67	357.16	862.36	1.38	10.29	-0.70	0.59	0.52	1.91	0.31	0.10	0.08
vill	40.44	356.05	647.35	-0.39	16.58	18.80	0.51	0.44	1.81	0.57	0.16	0.13
vis0	57.65	18.37	79.80	2.81	13.65	18.80	1.06	0.80	3.14	0.51	0.19	0.14
wab2	46.92	7.46	611.18	2.00	15.81	19.65	5.48	4.28	18.61	2.12	0.63	0.49
wes2	42.61	288.51	85.02	0.11	5.32	-15.08	0.73	0.66	2.68	0.41	0.11	0.09
wroc	51.11	17.06	180.80	3.18	13.78	18.82	1.88	1.42	6.61	1.08	0.33	0.26
wsrt	52.91	6.60	82.28	-0.18	16.27	17.38	0.45	0.34	1.28	0.22	0.07	0.06
wtzr	49.14	12.88	666.03	0.20	15.42	20.03	0.46	0.36	1.38	0.22	0.07	0.06
yakt	62.03	129.68	103.39	0.34	-12.49	18.55	0.71	0.51	2.04	0.34	0.12	0.08
yar1	-29.05	115.35	241.29	0.07	57.36	38.49	0.61	0.65	2.37	2.23	0.52	0.55

yar2	-29.05	115.35	241.29	0.86	58.16	38.94	0.62	0.62	2.27	0.36	0.10	0.10
yarr	-29.05	115.35	241.36	1.06	58.24	39.06	1.71	1.73	7.33	1.33	0.31	0.31
yebe	40.52	356.91	972.75	1.58	16.35	18.74	0.70	0.60	2.29	0.47	0.14	0.12
yell	62.48	245.52	180.87	6.55	-11.05	-16.57	0.50	0.37	1.50	0.25	0.08	0.06
zeck	43.79	41.57	1166.27	2.02	11.59	24.95	0.56	0.45	1.89	0.29	0.09	0.07
zimm	46.88	7.47	956.33	1.64	16.16	19.45	0.50	0.40	1.61	0.26	0.08	0.07
zwe2	55.70	36.76	208.21	-1.29	12.48	22.62	2.71	1.79	7.97	1.03	0.35	0.23
zwen	55.70	36.76	204.99	0.84	11.76	23.62	0.75	0.55	2.33	0.96	0.30	0.22

Appendix B. Station Offsets

Site	Week	Lat	Long	Cartesian Offset (mm)						Geodetic Offset (mm)					
		ϕ°	λ°	X	Y	Z	σ_X	σ_Y	σ_Z	U	N	E	σ_U	σ_N	σ_E
algo	1340	45.76	281.93	0.44	-3.10	2.66	1.13	2.82	2.80	4.09	-0.39	-0.21	3.84	1.19	0.95
alrt	1509	82.44	297.66	-1.82	-1.31	5.35	1.54	1.70	10.18	5.34	0.39	-2.22	10.19	1.66	1.48
amc2	1024	38.62	255.48	-3.35	-2.21	-3.27	1.39	3.42	2.75	0.29	-4.41	-2.69	4.28	1.28	1.12
amc2	1447	38.62	255.48	4.03	4.51	2.17	1.12	2.78	2.21	-2.84	5.05	2.77	3.47	1.04	0.89
aspa	1490	-14.23	189.28	13.53	-2.97	6.32	8.06	2.66	2.91	-14.03	2.96	5.11	8.44	1.95	2.33
ban2	1309	12.95	77.51	-10.50	-7.57	-5.03	11.47	30.85	10.27	-10.54	-2.74	8.62	32.41	7.20	9.30
barh	1417	44.20	291.78	-2.10	8.15	-3.39	3.44	6.79	6.77	-8.34	3.39	1.07	9.58	2.67	2.19
bili	1286	67.94	166.44	-0.85	0.47	1.57	1.94	1.18	4.79	1.81	-0.28	-0.26	4.98	1.47	1.11
brft	1434	-3.85	321.57	-1.71	4.68	-8.22	16.58	13.72	5.15	-3.68	-8.49	2.61	20.78	5.00	5.72
brmu	1207	32.20	295.30	-0.35	-3.60	-0.55	1.78	3.28	2.32	2.34	-2.12	-1.85	4.14	1.06	1.02
brst	1422	48.19	355.50	-1.93	2.31	-5.47	12.31	4.08	13.01	-5.48	-2.07	2.15	17.25	4.92	3.96
brst	1484	48.19	355.50	-1.91	-5.44	4.11	17.60	5.85	18.61	2.08	3.84	-5.57	24.66	7.05	5.69
brus	1059	50.61	4.36	5.95	-0.10	0.72	2.51	0.85	2.85	4.31	-4.12	-0.56	3.63	1.11	0.83
brus	1189	50.61	4.36	-0.64	-1.35	1.13	2.57	0.91	3.01	0.40	1.29	-1.30	3.79	1.16	0.90
cagl	1121	38.95	8.97	-3.45	5.52	0.02	2.66	0.93	2.20	-1.97	1.61	5.99	3.35	0.93	0.82
chat	1141	-43.76	183.43	-2.81	-4.75	2.18	2.42	0.90	2.15	0.73	3.71	4.58	3.08	0.99	0.90
darw	1303	-12.76	131.13	2.44	-2.82	1.53	5.10	5.39	2.40	-3.98	0.67	0.02	7.40	1.66	1.79
darw	1316	-12.76	131.13	-3.33	5.12	0.17	5.95	6.29	2.81	5.85	1.50	-0.86	8.64	1.94	2.11
dav1	1439	-68.45	77.97	2.65	8.06	-5.00	1.16	1.88	4.52	7.75	6.00	-0.91	4.69	1.43	1.12
dubo	1026	50.07	264.13	3.84	18.79	-12.04	1.17	3.24	3.56	-21.48	6.91	1.90	4.60	1.45	1.12
eisl	1205	-26.99	250.62	1.25	-4.32	-1.86	4.81	10.51	6.22	4.10	0.00	2.61	12.38	2.86	3.29
eprt	1151	44.72	293.01	-0.65	7.05	-7.46	2.09	3.93	3.94	-10.04	-0.55	2.15	5.56	1.66	1.32
eprt	1276	44.72	293.01	2.54	15.52	-4.52	4.09	7.66	7.71	-12.63	6.14	8.41	10.84	3.25	2.61
fort	1054	-3.85	321.57	-4.77	7.51	-2.16	7.68	6.57	2.04	-8.25	-2.72	2.92	9.77	1.98	2.64
glps	1342	-0.74	269.70	0.73	7.74	-0.44	2.29	6.12	1.99	-7.74	-0.54	0.69	6.13	1.99	2.29

glsv	1453	50.18	30.50	-0.87	3.35	-7.96	2.08	1.41	2.61	-5.50	-5.83	3.32	3.34	1.12	0.85
gope	1034	49.72	14.79	5.34	7.02	0.98	11.40	4.26	12.73	5.24	-4.67	5.43	16.60	4.76	3.44
gope	1072	49.72	14.79	12.60	4.03	12.96	5.77	2.10	6.50	18.43	-1.69	0.68	8.46	2.34	1.70
gope	1384	49.72	14.79	-9.87	-5.91	-3.69	6.61	2.77	7.26	-9.96	6.05	-3.19	9.52	2.94	2.21
hers	1126	50.68	0.34	-14.93	-33.54	-12.28	2.57	0.89	2.88	-19.08	3.93	-33.45	3.69	1.15	0.89
hrm1	1485	51.27	358.72	1.51	0.43	-0.97	3.31	1.19	3.90	0.18	-1.77	0.46	4.86	1.60	1.19
hyde	1455	17.31	78.55	4.19	3.19	-7.04	3.30	9.70	3.97	1.68	-7.90	-3.47	10.32	2.47	2.86
iisc	1316	12.94	77.57	-17.69	-14.28	-6.76	2.19	5.73	1.92	-18.81	-2.61	14.20	6.01	1.45	1.79
jab1	1098	-12.58	132.89	-4.81	1.64	-6.46	3.18	3.26	1.46	5.77	-5.33	2.41	4.51	1.07	1.18
joze	1300	51.91	21.03	-0.82	-3.73	-2.35	3.20	1.74	4.01	-3.15	0.21	-3.19	5.05	1.58	1.17
karr	1316	-20.85	117.10	-0.41	0.96	0.76	2.16	3.56	1.87	0.70	1.08	-0.08	4.26	1.10	1.20
kely	1132	66.85	309.06	-20.99	23.19	-62.92	1.80	1.90	4.93	-70.14	3.99	-1.69	5.26	1.51	1.12
kokb	1160	21.99	200.34	-3.79	-0.34	2.42	5.14	2.50	2.63	4.32	0.87	-1.00	5.91	1.48	1.58
kokb	1272	21.99	200.34	-4.53	1.63	3.36	6.02	2.93	3.12	4.67	1.74	-3.11	6.91	1.79	1.91
kosg	1210	51.99	5.81	4.56	-2.67	-4.49	2.24	0.88	2.75	-0.91	-6.13	-3.12	3.38	1.13	0.85
kour	1384	5.22	307.19	-5.25	10.46	1.93	3.42	4.28	1.37	-11.29	2.97	2.14	5.30	1.28	1.47
kstu	1039	55.81	92.79	5.18	-5.94	-0.46	1.54	4.22	5.27	-3.86	4.86	-4.88	6.45	2.01	1.52
lama	1083	53.71	20.67	-2.32	-6.75	-9.56	2.34	1.27	3.17	-10.40	-1.98	-5.50	3.83	1.27	0.94
lama	1454	53.71	20.67	2.16	-0.07	10.46	3.25	1.79	4.49	9.61	4.58	-0.83	5.40	1.75	1.30
mad2	1037	40.24	355.75	-20.71	-45.97	14.13	9.39	2.51	8.06	-4.04	21.93	-47.38	12.03	2.94	2.44
madr	1244	40.24	355.75	1.26	-1.37	0.26	4.00	1.21	3.23	1.20	-0.68	-1.27	4.94	1.42	1.19
mald	1064	4.16	73.53	15.25	24.78	37.88	1.95	5.33	1.37	30.76	35.74	-7.60	5.48	1.27	1.57
mkea	1396	19.68	204.54	1.14	12.04	-1.07	4.00	2.43	2.05	-6.05	1.03	-10.47	4.77	1.22	1.36
nain	1404	56.36	298.31	-0.14	-0.19	0.18	5.37	8.37	13.65	0.21	0.02	-0.22	15.77	4.90	3.53
noum	1142	-22.14	166.41	6.85	-0.93	4.61	3.75	1.48	1.87	-8.11	1.68	-0.70	4.15	1.06	1.19
nya1	1460	78.86	11.87	-0.63	1.84	-3.81	1.26	1.01	5.99	-3.79	-0.50	1.93	6.01	1.21	0.99
nyal	1130	78.86	11.87	3.39	-0.05	-1.34	0.84	0.67	3.98	-0.68	-3.50	-0.74	4.00	0.79	0.65
pert	1316	-31.63	115.89	-1.13	4.35	-3.07	2.28	3.87	2.68	5.36	-0.30	-0.88	4.93	1.23	1.25

polv	1460	49.41	34.54	4.21	1.17	3.76	3.32	2.53	4.33	5.54	-0.69	-1.42	5.56	1.86	1.38
pots	1527	52.19	13.07	-4.36	-2.27	-1.96	2.49	1.11	3.08	-4.47	2.56	-1.22	3.80	1.27	0.95
ptbb	1237	52.11	10.46	4.88	-0.59	4.13	5.86	2.17	6.71	6.14	-1.16	-1.46	8.59	2.57	1.92
qaq1	1248	60.55	313.95	-1.84	-1.09	7.28	1.87	1.90	4.10	6.10	4.01	-2.08	4.52	1.52	1.09
riga	1306	56.77	24.06	-4.47	3.17	-3.76	3.61	2.13	5.64	-4.68	0.28	4.72	6.53	2.08	1.58
riga	1376	56.77	24.06	1.50	-4.47	-1.14	5.31	3.12	8.30	-1.20	-0.25	-4.69	9.60	3.04	2.30
sol1	1353	38.13	283.55	2.00	-1.72	2.73	2.30	6.34	4.97	3.37	0.82	1.54	7.91	2.09	1.80
stjo	1064	47.40	307.32	3.73	-1.56	1.06	1.58	2.00	2.55	3.16	-1.86	2.02	3.35	1.04	0.84
suth	1155	-32.21	20.81	5.71	-2.84	-1.93	2.86	1.48	2.01	4.70	0.68	-4.68	3.49	1.09	1.03
sydn	1486	-33.60	151.15	2.24	-1.03	1.64	55.27	34.97	45.20	-2.96	0.00	-0.18	75.69	18.02	16.31
thu3	1404	76.45	291.18	0.50	-0.80	4.58	1.79	2.31	10.07	4.67	0.17	0.18	10.11	2.17	1.69
tidb	1435	-35.22	148.98	-0.01	0.13	1.20	3.38	2.34	2.82	-0.63	1.03	-0.11	4.67	1.30	1.18
tlse	1247	43.37	1.48	-3.44	2.98	-1.64	3.84	1.20	3.57	-3.57	1.11	3.06	5.04	1.47	1.19
tro1	1279	69.54	18.94	11.28	-5.30	5.63	1.61	1.02	4.41	8.40	-6.42	-8.68	4.54	1.27	0.93
unb1	1207	45.76	293.36	1.45	-3.76	3.37	14.98	27.10	28.54	5.22	-0.53	-0.16	38.98	12.34	10.07
vill	1289	40.25	356.05	-3.86	0.22	0.76	3.90	1.15	3.22	-2.46	3.08	-0.05	4.88	1.35	1.13
wes2	1076	42.42	288.51	-9.80	0.41	-2.04	1.21	2.91	2.55	-3.96	0.85	-9.16	3.82	1.03	0.90

References

Agnew, D. C. (1992) 'The time-domain behaviour of power-law noises', *Geophysical Research Letters,* 19, (4), pp. 333-336.

Altamimi, Z., Boucher, C. and Gambis, D. (2005) 'Long-term stability of the terrestrial reference frame', *Advances in Space Research,* 36, (3), pp. 342-349.

Altamimi, Z. and Collilieux, X. (2009) 'IGS contribution to the ITRF', *Journal of Geodesy,* 83, (3-4), pp. 375-383.

Altamimi, Z., Collilieux, X. and Boucher, C. (2008) 'Accuracy Assessment of the ITRF Datum Definition', in Xu, P. L. J. D. A.(ed), *Vi Hotine-Marussi Symposium on Theoretical and Computational Geodesy.* Vol. 132, pp. 101-110.

Altamimi, Z., Collilieux, X., Legrand, J., Garayt, B. and Boucher, C. (2007) 'ITRF2005: A new release of the International Terrestrial Reference Frame based on time series of station positions and earth orientation parameters', *Journal of Geophysical Research-Solid Earth,* 112, (B9).

Altamimi, Z., Collilieux, X. and Metivier, L. (2011) 'ITRF2008: an improved solution of the international terrestrial reference frame', *Journal of Geodesy,* 85, (8), pp. 457-473.

Altamimi, Z. and Dermanis, A. (2012) 'The Choice of Reference System in ITRF Formulation
VII Hotine-Marussi Symposium on Mathematical Geodesy', in Sneeuw, N., Novák, P., Crespi, M. and Sansò, F.(eds). Vol. 137 Springer Berlin Heidelberg, pp. 329-334.

Altamimi, Z., Sillard, P. and Boucher, C. (2002) 'ITRF2000: A new release of the International Terrestrial Reference frame for earth science applications', *Journal of Geophysical Research-Solid Earth,* 107, (B10).

Amiri-Simkooei, A. R., Tiberius, C. and Teunissen, P. J. G. (2007) 'Assessment of noise in GPS coordinate time series: Methodology and results', *Journal of Geophysical Research-Solid Earth,* 112, (B7), pp. 19.

Anderson, D. L. (2007) *New Theory of the Earth.* Cambridge University Press.

Angermann, D., Drewes, H., Gerstl, M., Kelm, R., Krugel, M. and Meisel, B. (2005) 'ITRF combination - Status and recommendations for the future', in Sanso, F.(ed), *Window on the Future of Geodesy.* Vol. 128, pp. 3-8.

Arendt, A. A., Echelmeyer, K. A., Harrison, W. D., Lingle, C. S. and Valentine, V. B. (2002) 'Rapid wastage of Alaska glaciers and their contribution to rising sea level', *Science,* 297, (5580), pp. 382-386.

Argus, D. F. (2007) 'Defining the translational velocity of the reference frame of Earth', *Geophysical Journal International,* 169, (3), pp. 830-838.

Argus, D. F. and Gordon, R. G. (1991) 'No-Net-Rotation Model of Current Plate Velocities Incorporating Plate Motion Model Nuvel-1', *Geophysical Research Letters,* 18, (11), pp. 2039-2042.

Argus, D. F., Gordon, R. G. and DeMets, C. (2011) 'Geologically current motion of 56 plates relative to the no-net-rotation reference frame', *Geochemistry Geophysics Geosystems,* 12.

Argus, D. F., Gordon, R. G., Heflin, M. B., Ma, C., Eanes, R. J., Willis, P., Peltier, W. R. and Owen, S. E. (2010) 'The angular velocities of the plates and the velocity of Earth's centre from space geodesy', *Geophysical Journal International,* 180, (3), pp. 913-960.

Argus, D. F. and Heflin, M. B. (1995) ' Plate Motion and Crustal Deformation Estimated with Geodetic Data from the Global Positioning System', *Geophysical Research Letters,* 22, (15), pp. 1973-1976.

Argus, D. F. and Peltier, W. R. (2010) 'Constraining models of postglacial rebound using space geodesy: a detailed assessment of model ICE-5G (VM2) and its relatives', *Geophysical Journal International,* 181, (2), pp. 697-723.

Argus, D. F., Peltier, W. R. and Watkins, M. M. (1999) 'Glacial isostatic adjustment observed using very long baseline interferometry and satellite laser ranging geodesy', *Journal of Geophysical Research-Solid Earth,* 104, (B12), pp. 29077-29093.

Arriagada, C., Arancibia, G., Cembrano, J., Martinez, F., Carrizo, D., Van Sint Jan, M., Saez, E., Gonzalez, G., Rebolledo, S., Sepulveda, S. A., Contreras-Reyes, E., Jensen, E. and Yanez, G. (2011) 'Nature and tectonic significance of co-seismic structures associated with the Mw 8.8 Maule earthquake, central-southern Chile forearc', *Journal of Structural Geology,* 33, (5), pp. 891-897.

Banerjee, P., Bürgmann, R., Nagarajan, B. and Apel, E. (2008) 'Intraplate deformation of the Indian subcontinent', *Geophys. Res. Lett.,* 35, (18), pp. L18301.

Baur, O., Kuhn, M. and Featherstone, W. E. (2009) 'GRACE-derived ice-mass variations over Greenland by accounting for leakage effects', *Journal of Geophysical Research-Solid Earth,* 114.

Benjamin, D., Wahr, J., Ray, R. D., Egbert, G. D. and Desai, S. D. (2006) 'Constraints on mantle anelasticity from geodetic observations, and implications for the J(2) anomaly', *Geophysical Journal International,* 165, (1), pp. 3-16.

Bennett, R. A. (2008) 'Instantaneous deformation from continuous GPS: contributions from quasi-periodic loads', *Geophysical Journal International,* 174, (3), pp. 1052-1064.

Bevis, M., Kendrick, E., Smalley, R., Jr., Dalziel, I., Caccamise, D., Sasgen, I., Helsen, M., Taylor, F. W., Zhou, H., Brown, A., Raleigh, D., Willis, M., Wilson, T. and Konfal, S. (2009) 'Geodetic measurements of vertical crustal velocity in West Antarctica and the implications for ice mass balance', *Geochem. Geophys. Geosyst.,* 10, (10), pp. Q10005.

Bianco, G., Devoti, R., Luceri, V. and Sciarretta, C. (2001) 'A review of SLR contributions to geophysics in Eurasia by CGS', *Surveys in Geophysics,* 22, (5-6), pp. 481-490.

Bird, P. (2003) 'An updated digital model of plate boundaries', *Geochemistry Geophysics Geosystems,* 4.

Blewitt, G. (1997) *GPS data processing methodology from theory to applications.* Springer.

Blewitt, G. (2003) 'Self-consistency in reference frames, geocenter definition, and surface loading of the solid Earth', *Journal of Geophysical Research-Solid Earth,* 108, (B2), pp. 10.

Blewitt, G., Bock, Y. and Kouba, J. (1994) *Densification of ITRF through Regional GPS Networks.* JPL, Nov30-Dec 2.

Blewitt, G. and Clarke, P. (2003) 'Inversion of Earth's changing shape to weigh sea level in static equilibrium with surface mass redistribution', *Journal of Geophysical Research-Solid Earth,* 108, (B6), pp. 23.

Blewitt, G., Heflin, M. B., Webb, F. H., Lindqwister, U. J. and Malla, R. P. (1992) 'Global Coordinates with Centimeter Accuracy in the International Terrestrial Reference Frame Using GPS', *Geophysical Research Letters,* 19, (9), pp. 853-856.

Blewitt, G. and Lavallee, D. (1999) 'Investigations of Plat Motions: Results from the IGS ITRF Densification project', *Eos, Transactions,* 79, (45).

Blewitt, G. and Lavallee, D. (2002) 'Effect of annual signals on geodetic velocity', *Journal of Geophysical Research-Solid Earth,* 107, (B7), pp. 11.

Blewitt, G., Lavallee, D., Clarke, P. and Nurutdinov, K. (2001) 'A new global mode of Earth deformation: Seasonal cycle detected', *Science,* 294, (5550), pp. 2342-2345.

Boehm, J., Niell, A., Tregoning, P. and Schuh, H. (2006a) 'Global Mapping Function (GMF): A new empirical mapping function based on numerical weather model data', *Geophysical Research Letters,* 33, (7).

Boehm, J. and Schuh, H. (2004) 'Vienna mapping functions in VLBI analyses', *Geophysical Research Letters,* 31, (1).

Boehm, J., Werl, B. and Schuh, H. (2006b) 'Troposphere mapping functions for GPS and very long baseline interferometry from European Centre for Medium-Range Weather Forecasts operational analysis data', *Journal of Geophysical Research-Solid Earth,* 111, (B2).

Bomford, G. (1980) *Geodesy.*4th ed: Oxford University Press.

Bos, M., Bastos, L. and Fernandes, R. M. S. (2010) 'The influence of seasonal signals on the estimation of the tectonic motion in short continuous GPS time-series', *Journal of Geodynamics*.

Bos, M. S., Fernandes, R. M. S., Williams, S. D. P. and Bastos, L. (2008) 'Fast error analysis of continuous GPS observations', *Journal of Geodesy,* 82, (3), pp. 157-166.

Boucher, C. (2001) *Terrestrial coordinate systems and frames.* Nature Publishing Group; and Bristol: Institute of Physics.

Bradley, S. L., Milne, G. A., Teferle, F. N., Bingley, R. M. and Orliac, E. J. (2009) 'Glacial isostatic adjustment of the British Isles: new constraints from GPS measurements of crustal motion', *Geophysical Journal International,* 178, (1), pp. 14-22.

Bullard, E. C. (1965) 'Fit of the Continents around the Atlantic', *Science (New York, N.Y.),* 148, (3670), pp. 664.

Calais, E. (1999) 'Continuous GPS measurements across the Western Alps, 1996-1998', *Geophysical Journal International,* 138, (1), pp. 221-230.

Calais, E. (2012) *http://web.ics.purdue.edu/~ecalais/projects/noam*. Available at: (Accessed: January).

Calais, E., Freed, A. M., Van Arsdale, R. and Stein, S. (2010) 'Triggering of New Madrid seismicity by late-Pleistocene erosion', *Nature,* 466, (7306), pp. 608-U2.

Cartwright, D. E. (2000) *Tides, a Scientific History*

Cazenave, A. and Chen, J. (2010) 'Time-variable gravity from space and present-day mass redistribution in the Earth system', *Earth and Planetary Science Letters,* 298, (3-4), pp. 263-274.

Chambers, D. P., Wahr, J. and Nerem, R. S. (2004) 'Preliminary observations of global ocean mass variations with GRACE', *Geophysical Research Letters,* 31, (13).

Chao, B. F., Wu, Y. H. and Li, Y. S. (2008) 'Impact of artificial reservoir water impoundment on global sea level', *Science,* 320, (5873), pp. 212-214.

Chen, C.-H., Yeh, T.-K., Liu, J.-Y., Wang, C.-H., Wen, S., Yen, H.-Y. and Chang, S.-H. (2011) 'Surface Deformation and Seismic Rebound:

Implications and Applications', *Surveys in Geophysics,* 32, (3), pp. 291-313.

Chen, J. L., Tapley, B. D. and Wilson, C. R. (2006a) 'Alaskan mountain glacial melting observed by satellite gravimetry', *Earth and Planetary Science Letters,* 248, (1-2), pp. 368-378.

Chen, J. L. and Wilson, C. R. (2003) 'Low degree gravitational changes from earth rotation and geophysical models', *Geophysical Research Letters,* 30, (24).

Chen, J. L. and Wilson, C. R. (2008) 'Low degree gravity changes from GRACE, Earth rotation, geophysical models, and satellite laser ranging', *Journal of Geophysical Research-Solid Earth,* 113, (B6).

Chen, J. L., Wilson, C. R., Blankenship, D. and Tapley, B. D. (2009a) 'Accelerated Antarctic ice loss from satellite gravity measurements', *Nature Geoscience,* 2, (12), pp. 859-862.

Chen, J. L., Wilson, C. R., Blankenship, D. D. and Tapley, B. D. (2006b) 'Antarctic mass rates from GRACE', *Geophysical Research Letters,* 33, (11).

Chen, J. L., Wilson, C. R. and Tapley, B. D. (2006c) 'Satellite gravity measurements confirm accelerated melting of Greenland ice sheet', *Science,* 313, (5795), pp. 1958-1960.

Chen, J. L., Wilson, C. R., Tapley, B. D., Blankenship, D. and Young, D. (2008) 'Antarctic regional ice loss rates from GRACE', *Earth and Planetary Science Letters,* 266, (1-2), pp. 140-148.

Chen, J. L., Wilson, C. R., Tapley, B. D., Blankenship, D. D. and Ivins, E. R. (2007) 'Patagonia icefield melting observed by gravity recovery and climate experiment (GRACE)', *Geophysical Research Letters,* 34, (22).

Chen, J. L., Wilson, C. R., Tapley, B. D., Yang, Z. L. and Niu, G. Y. (2009b) '2005 drought event in the Amazon River basin as measured by GRACE and estimated by climate models', *Journal of Geophysical Research-Solid Earth,* 114.

Clark, P. U., Dyke, A. S., Shakun, J. D., Carlson, A. E., Clark, J., Wohlfarth, B., Mitrovica, J. X., Hostetler, S. W. and McCabe, A. M. (2009) 'The Last Glacial Maximum', *Science,* 325, (5941), pp. 710-714.

Clarke, P. J. (2012) Personal Communication - Periodic stacking script "sidstack",

Clarke, P. J., Lavallee, D. A., Blewitt, G. and van Dam, T. (2007) 'Basis functions for the consistent and accurate representation of surface mass loading', *Geophysical Journal International,* 171, (1), pp. 1-10.

Clarke, P. J., Lavallee, D. A., Blewitt, G., van Dam, T. M. and Wahr, J. M. (2005) 'Effect of gravitational consistency and mass conservation on seasonal surface mass loading models', *Geophysical Research Letters,* 32, (8), pp. 5.

Collilieux, X. and Altamimi, Z. (2009) 'Impact of the Network Effect on the Origin and Scale: Case Study of Satellite Laser Ranging', *Observing Our Changing Earth,* 133, pp. 31-37.

Collilieux, X., Altamimi, Z., Coulot, D., Ray, J. and Sillard, P. (2007) 'Comparison of very long baseline interferometry, GPS, and satellite laser ranging height residuals from ITRF2005 using spectral and correlation methods', *Journal of Geophysical Research-Solid Earth,* 112, (B12).

Collilieux, X., Metivier, L., Altamimi, Z., van Dam, T. and Ray, J. (2011) 'Quality assessment of GPS reprocessed terrestrial reference frame', *GPS Solutions,* 15, (3), pp. 219-231.

Collilieux, X. and Woeppelmann, G. (2010) 'Global sea-level rise and its relation to the terrestrial reference frame', *Journal of Geodesy,* 85, (1), pp. 9-22.

Condie, K. C. (1997) *Plate Tectonics and Crustal Evolution.* Butterworth Heinemann.

Cox, C. M. and Chao, B. F. (2002) 'Detection of a large-scale mass redistribution in the terrestrial system since 1998', *Science,* 297, (5582), pp. 831-833.

Cretaux, J. F., Soudarin, L., Cazenave, A. and Bouille, F. (1998) 'Present-day tectonic plate motions and crustal deformations from the DORIS space system', *Journal of Geophysical Research-Solid Earth,* 103, (B12), pp. 30167-30181.

Cretaux, J. F., Soudarin, L., Davidson, F. J. M., Gennero, M. C., Berge-Nguyen, M. and Cazenave, A. (2002) 'Seasonal and interannual geocenter motion from SLR and DORIS measurements: Comparison with surface loading data', *Journal of Geophysical Research-Solid Earth,* 107, (B12).

Cross, P. A. (1992) *Working Paper 6: Advanced least squares applied to position fixing.* Polytechnic of East London Department of Land Surveying

Crowley, J. W., Mitrovica, J. X., Bailey, R. C., Tamisiea, M. E. and Davis, J. L. (2006) 'Land water storage within the Congo Basin inferred from GRACE satellite gravity data', *Geophysical Research Letters,* 33, (19).

Crowley, J. W., Mitrovica, J. X., Bailey, R. C., Tamisiea, M. E. and Davis, J. L. (2008) 'Annual variations in water storage and precipitation in the Amazon Basin', *Journal of Geodesy,* 82, (1), pp. 9-13.

Davies, P. and Blewitt, G. (1995) *The Newcastle Global Network Associate Analysis Center Annual Report 1995.*

Davies, P. and Blewitt, G. (2000) 'Methodology for global geodetic time series estimation: A new tool for geodynamics', *Journal of Geophysical Research-Solid Earth,* 105, (B5), pp. 11083-11100.

Davies, P. B. H. (1997) *Assembling the IGS polyhedron. A densified weekly GPS terrestrial reference frame.* thesis. Newcastle University.

Davis, J. E., Latychev, K., Mitrovica, J. X., Kendall, R. and Tamisiea, M. E. (2008) 'Glacial isostatic adjustment in 3-D earth models: Implications for the analysis of tide gauge records along the U.S. east coast', *Journal of Geodynamics,* 46, (3–5), pp. 90-94.

Davis, J. L., Elosequi, P., Mitrovica, J. X. and Tamisiea, M. E. (2004) 'Climate-driven deformation of the solid Earth from GRACE and GPS', *Geophysical Research Letters,* 31, (24).

DeMets, C., Gordon, R. G. and Argus, D. F. (2010) 'Geologically current plate motions', *Geophysical Journal International,* 181, (1), pp. 1-80.

Demets, C., Gordon, R. G., Argus, D. F. and Stein, S. (1990) 'Current Plate Motions', *Geophysical Journal International,* 101, (2), pp. 425-478.

Devoti, R., Luceri, V., Sciarretta, C., Bianco, G., Di Donato, G., Vermeersen, L. L. A. and Sabadini, R. (2001) 'The SLR secular gravity variations and their impact on the inference of mantle rheology and lithospheric thickness', *Geophysical Research Letters,* 28, (5), pp. 855-858.

Dickey, J. O., Marcus, S. L., de Viron, O. and Fukumori, I. (2002) 'Recent Earth oblateness variations: Unraveling climate and postglacial rebound effects', *Science,* 298, (5600), pp. 1975-1977.

Dietrich, R., Rulke, A., Ihde, J., Lindner, K., Miller, H., Niemeier, W., Schenke, H.-W. and Seeber, G. (2004) 'Plate kinematics and deformation status of the Antarctic Peninsula based on GPS', *Global and Planetary Change,* 42, (1-4), pp. 313-321.

Dixon, T. H. (1991) 'An Introduction to the Global Positioning System and Some Geological Applications', *Reviews of Geophysics,* 29, (2), pp. 249-276.

Dong, D., Dickey, J. O., Chao, Y. and Cheng, M. K. (1997) 'Geocenter variations caused by atmosphere, ocean and surface ground water', *Geophysical Research Letters,* 24, (15), pp. 1867-1870.

Dong, D., Fang, P., Bock, Y., Cheng, M. K. and Miyazaki, S. (2002) 'Anatomy of apparent seasonal variations from GPS-derived site position time series', *Journal of Geophysical Research-Solid Earth,* 107, (B4).

Dong, D., Yunck, T. and Heflin, M. (2003) 'Origin of the International Terrestrial Reference Frame', *J. Geophys. Res.,* 108, (B4), pp. 2200.

Dziewonski, A. M. and Anderson, D. L. (1981) 'Preliminary Reference Earth Model', *Physics of the Earth and Planetary Interiors,* 25, (4), pp. 297-356.

Eanes, R. J. and Schuler, A. (1999) 'An improved global ocean tide model from TOPEX/Poseidon altimetry: CSR4. *', EGS General Assembly.* The Hague, Netherlands, pp.

Egbert, G. D., Bennett, A. F. and Foreman, M. G. G. (1994) 'TOPEX/POSEIDON Tides Estimated Using a Global Inverse Model', *Journal of Geophysical Research-Oceans,* 99, (C12), pp. 24821-24852.

El-Fiky, G. and Kato, T. (2006) 'Secular crustal deformation and interplate coupling of the Japanese Islands as deduced from continuous GPS array, 1996-2001', *Tectonophysics,* 422, (1-4), pp. 1-22.

Elgered, G., Davis, J. L., Herring, T. A. and Shapiro, II. (1991) 'Geodesy by Radio Interferometry - Water Vapour Radiometry for Estimation of the Wet Delay', *Journal of Geophysical Research-Solid Earth and Planets,* 96, (B4), pp. 6541-6555.

Farrell, W. E. (1972) 'Deformation of Earth by Surface Loads', *Reviews of Geophysics and Space Physics,* 10, (3), pp. 761-&.

Farrell, W. E. and Clark, J. A. (1976) 'Postglacial Sea-Level', *Geophysical Journal of the Royal Astronomical Society,* 46, (3), pp. 647-667.

Ferland, R. (2006) 'Proposed IGS05 realisation', in IGS Mail 5447.

Ferland, R., Kouba, J. and Hutchison, D. (2000) 'Analysis methodology and recent results of the IGS network combination', *Earth Planets and Space,* 52, (11), pp. 953-957.

Ferland, R. and Piraszewski, M. (2009) 'The IGS-combined station coordinates, earth rotation parameters and apparent geocenter', *Journal of Geodesy,* 83, (3-4), pp. 385-392.

Fiedler, K. and Doll, P. (2007) 'Global modelling of continental water storage changes - sensitivity to different climate data sets', *Advances in Geosciences*, (11), pp. 63-68.

Fjeldskaar, W. (1994) 'The Amplitude and Decay of the Glacial Forebulge in Fennoscandia', *Norsk Geologisk Tidsskrift,* 74, (1), pp. 2-8.

Fjeldskaar, W., Lindholm, C., Dehls, J. F. and Fjeldskaar, I. (2000) 'Postglacial uplift, neotectonics and seismicity in Fennoscandia', *Quaternary Science Reviews,* 19, (14-15), pp. 1413-1422.

Frisch, W., Meschede, M. and Blakey, R. C. (2010) *Plate Tectonics: Continental Drift and Mountain Building.* Springer.

Fritsche, M., Dietrich, R., Knofel, C., Rulke, A., Vey, S., Rothacher, M. and Steigenberger, P. (2005) 'Impact of higher-order ionospheric terms on GPS estimates', *Geophysical Research Letters,* 32, (23).

Gasperini, P. and Sabadini, R. (1989) 'Lateral heterogeneities in mantle viscosity and post-glacial rebound', *Geophysical Journal International,* 98, (3), pp. 413-428.

Gasperini, P. and Sabadini, R. (1990) 'Finite element modeling of lateral viscosity heterogeneities and post-glacial rebound', *Tectonophysics,* 179, (1–2), pp. 141-149.

Ge, M., Gendt, G., Dick, G., Zhang, F. P. and Reigber, C. (2005) 'Impact of GPS satellite antenna offsets on scale changes in global network solutions', *Geophysical Research Letters,* 32, (6).

Gordon, R. G. and Stein, S. (1992) 'Global Tectonics and Spcae Geodesy', *Science,* 256, (5055), pp. 333-342.

Griffiths, J. and Ray, J. R. (2009) 'On the precision and accuracy of IGS orbits', *Journal of Geodesy,* 83, (3-4), pp. 277-287.

Gripp, A. E. and Gordon, R. G. (1990) 'Current Plate Velocities Relative to the Hotspots Incorporating the NUVEL-1A Global Plate Motion Model', *Geophysical Research Letters,* 17, (8), pp. 1109-1112.

Heki, K. (2003) *23rd General Assembly of the International-Union-of-Geodesy-and Geophysics.* Sapporo, JAPAN, Jul.Amer Geophysical Union.

Hess, H. H. (1962) 'History Of Ocean Basins', in eScholarship Repository.

Hoffman-Wellenhoff, B., Lichtenegger, H. and Collins, J. (1994) *GPS Theory and Practice.*3rd ed New York: Springer-Verlag.

IGSCB (2012) *Section 2.3*. Available at: http://igscb.jpl.nasa.gov/network/guidelines/guidelines.html (Accessed: 01/05/2012).

Ilk, K. H., Flurt, J., Rummel, R., Schwintzer, P., Bosch, W., Haas, C., Schroter, J., Stammer, D., Zahel, W., Miller, H. L., Dietrich, R., Huybrechts, P., Schmeling, H., Gotze, H., Riegger, J., Bardossy, A., Guntner, A. and Gruber, T. (2005) *Mass transport and mass distribution in the Earth system.* GOCE_Project Bureau TU Munich, GFZ Potsdam

Ivins, E. R. and James, T. S. (2004) 'Bedrock response to Llanquihue Holocene and present-day glaciation in southernmost South America', *Geophys. Res. Lett.,* 31, (24), pp. L24613.

Ivins, E. R. and James, T. S. (2005) 'Antarctic glacial isostatic adjustment: a new assessment', *Antarctic Science,* 17, (4), pp. 541-553.

Jacob, T., Wahr, J., Pfeffer, W. T. and Swenson, S. (2012) 'Recent contributions of glaciers and ice caps to sea level rise', *Nature,* advance online publication.

Jayles, C., Nhun-Fat, B. and Tourain, C. (2006) 'DORIS: System description and control of the signal integrity', *Journal of Geodesy,* 80, (8-11), pp. 457-472.

Johansson, J. M., Davis, J. L., Scherneck, H. G., Milne, G. A., Vermeer, M., Mitrovica, J. X., Bennett, R. A., Jonsson, B., Elgered, G., Elosegui, P., Koivula, H., Poutanen, M., Ronnang, B. O. and Shapiro, II. (2002) 'Continuous GPS measurements of postglacial adjustment in Fennoscandia - 1. Geodetic results', *Journal of Geophysical Research-Solid Earth,* 107, (B8).

Johnson, H., Agnew, D. C., University of California, S. D. I. o. G., Planetary, P. and Geological, S. (2000) *Correlated noise in the geodetic time series.* La Jolla, Calif.: The University.

Johnson, H. O. and Agnew, D. C. (1995) 'Monument Motion and Measurements of Crustal Velocities', *Geophysical Research Letters,* 22, (21), pp. 2905-2908.

Kalnay, E., Kanamitsu, M., Kistler, R., Collins, W., Deaven, D., Gandin, L., Iredell, M., Saha, S., White, G., Woollen, J., Zhu, Y., Chelliah, M., Ebisuzaki, W., Higgins, W., Janowiak, J., Mo, K. C., Ropelewski, C., Wang, J., Leetmaa, A., Reynolds, R., Jenne, R. and Joseph, D. (1996) 'The NCEP/NCAR 40-year reanalysis project', *Bulletin of the American Meteorological Society,* 77, (3), pp. 437-471.

Kaufmann, G. (2005) 'Geodetic signatures of a Late Pleistocene Tibetan ice sheet', *Journal of Geodynamics,* 39, (2), pp. 111-125.

Kaufmann, G. and Lambeck, K. (1997) 'Implications of Late Pleistocene Glaciation of the Tibetan Plateau for Present-Day Uplift Rates and Gravity Anomalies', *Quaternary Research,* 48, (3), pp. 267-279.

Kaufmann, G. and Wu, P. (2002) 'Glacial isostatic adjustment in Fennoscandia with a three-dimensional viscosity structure as an inverse problem', *Earth and Planetary Science Letters,* 197, (1–2), pp. 1-10.

Kaufmann, G., Wu, P. and Li, G. (2000) 'Glacial isostatic adjustment in Fennoscandia for a laterally heterogeneous earth', *Geophysical Journal International,* 143, (1), pp. 262-273.

Kearey, P., Klepeis, K. A. and Vine, F. J. (2009) *Global Tectonics.* Wiley-Blackwell.

Kedar, S., Hajj, G. A., Wilson, B. D. and Heflin, M. B. (2003) 'The effect of the second order GPS ionospheric correction on receiver positions', *Geophysical Research Letters,* 30, (16).

Kendall, R. A., Latychev, K., Mitrovica, J. X., Davis, J. E. and Tamisiea, M. E. (2006) 'Decontaminating tide gauge records for the influence of glacial isostatic adjustment: The potential impact of 3-D Earth structure', *Geophysical Research Letters,* 33, (24).

Kenyeres and Bruyninx. (2006) 'Noise and Periodic Terms in the EPN Time Series', *Geodetic Reference Frames,* 134, (3), pp. 5.

Khan, S. A., Wahr, J., Leuliette, E., van Dam, T., Larson, K. M. and Francis, O. (2008) 'Geodetic measurements of postglacial adjustments in Greenland', *Journal of Geophysical Research-Solid Earth,* 113, (B2), pp. 16.

King, M. A., Altamimi, Z., Boehm, J., Bos, M., Dach, R., Elosegui, P., Fund, F., Hernandez-Pajares, M., Lavallee, D., Cerveira, P. J. M., Penna, N., Riva, R. E. M., Steigenberger, P., van Dam, T., Vittuari, L., Williams, S. and Willis, P. (2010) 'Improved Constraints on Models of Glacial Isostatic Adjustment: A Review of the Contribution of Ground-Based Geodetic Observations', *Surveys in Geophysics,* 31, (5), pp. 465-507.

King, M. A., Keshin, M., Whitehouse, P. L., Thomas, I. D., Milne, G. and Riva, R. E. M. (2012) 'Regional biases in absolute sea-level estimates from tide gauge data due to residual unmodeled vertical land movement', *Geophys. Res. Lett.,* 39, (14), pp. L14604.

King, M. A. and Watson, C. S. (2010) 'Long GPS coordinate time series: Multipath and geometry effects', *Journal of Geophysical Research-Solid Earth,* 115.

King, M. A. and Williams, S. D. P. (2009) 'Apparent stability of GPS monumentation from short-baseline time series', *Journal of Geophysical Research-Solid Earth,* 114.

King, M. A. and Williams, S. D. P. (2011) 'Detection of Offsets in GPS Experiment (DOGEx)', in Newcastle University / National Oceanographic Centre, Liverpool.

Klemann, V. and Martinec, Z. (2009) 'Contribution of glacial-isostatic adjusment to the geocenter motion', *Tectonophysics*.

Klemann, V., Martinec, Z. and Ivins, E. R. (2008) 'Glacial isostasy and plate motion', *Journal of Geodynamics,* 46, (3-5), pp. 95-103.

Kogan, M. G. and Steblov, G. M. (2008) 'Current global plate kinematics from GPS (1995-2007) with the plate-consistent reference frame', *Journal of Geophysical Research-Solid Earth,* 113, (B4), pp. 17.

Kollo, K. and Vermeer, M. (2010) 'Lithospheric thickness recovery from horizontal and vertical land uplift rates', *Journal of Geodynamics,* 50, (1), pp. 32-37.

Kreemer, C., Haines, J., Holt, W. E., Blewitt, G. and Lavallee, D. (2000) 'On the determination of a global strain rate model', *Earth Planets and Space,* 52, (10), pp. 765-770.

Kreemer, C., Holt, W. E. and Haines, A. J. (2003) 'An integrated global model of present-day plate motions and plate boundary deformation', *Geophysical Journal International,* 154, (1), pp. 8-34.

Kreemer, C., Lavallee, D. A., Blewitt, G. and Holt, W. E. (2006) 'On the stability of a geodetic no-net-rotation frame and its implication for the International Terrestrial Reference Frame', *Geophysical Research Letters,* 33, (17), pp. 5.

Lambert, A., Courtier, N., Sasagawa, G. S., Klopping, F., Winester, D., James, T. S. and Liard, J. O. (2001) 'New constraints on Laurentide postglacial rebound from absolute gravity measurements', *Geophys. Res. Lett.,* 28, (10), pp. 2109-2112.

Lambert, A., Liard, J. O., Courtier, N., Goodacre, A. K., McConnell, R. K. and Faller, J. E. (1989) 'Canadian Absolute Gravity Program: Applications in geodesy and geodynamics', *Eos Trans. AGU,* 70, (44), pp. 1447-1459.

Langbein, J. and Johnson, H. (1997) 'Correlated errors in geodetic time series: Implications for time-dependent deformation', *Journal of Geophysical Research-Solid Earth,* 102, (B1), pp. 591-603.

Larsen, C. F., Motyka, R. J., Freymueller, J. T., Echelmeyer, K. A. and Ivins, E. R. (2004) 'Rapid uplift of southern Alaska caused by recent ice loss', *Geophysical Journal International,* 158, (3), pp. 1118-1133.

Larson, K. M., Freymueller, J. T. and Philipsen, S. (1997) 'Global plate velocities from the Global Positioning System', *Journal of Geophysical Research-Solid Earth,* 102, (B5), pp. 9961-9981.

Larson, K. M. and van Dam, T. (2000) 'Measuring postglacial rebound with GPS and absolute gravity', *Geophysical Research Letters,* 27, (23), pp. 3925-3928.

Latychev, K., Mitrovica, J. X., Ishii, M., Chan, N.-H. and Davis, J. L. (2009) 'Body tides on a 3-D elastic earth: Toward a tidal tomography', *Earth and Planetary Science Letters,* 277, (1–2), pp. 86-90.

Latychev, K., Mitrovica, J. X., Tamisiea, M. E., Tromp, J. and Moucha, R. (2005a) 'Influence of lithospheric thickness variations on 3-D crustal velocities due to glacial isostatic adjustment', *Geophys. Res. Lett.,* 32, (1), pp. L01304.

Latychev, K., Mitrovica, J. X., Tromp, J., Tamisiea, M. E., Komatitsch, D. and Christara, C. C. (2005b) 'Glacial isostatic adjustment on 3-D Earth

models: a finite-volume formulation', *Geophysical Journal International,* 161, (2), pp. 421-444.

Lavallee, D. and Blewitt, G. (2000) 'Constraint on integrated deformation across plate boundaries: Results from the IGS Densification project', *Eos, Transactions,* AGU Spring Meeting Supplement.

Lavallee, D. and Blewitt, G. (2002) 'Degree-1 Earth deformation from very long baseline interferometry measurements', *Geophysical Research Letters,* 29, (20), pp. 4.

Lavallee, D. A. (2000) *Tectonic plate motions from global GPS measurements.* thesis. Newcastle University.

Lavallee, D. A., Clarke, P., Moore, P., King, M. and Penna, N. (2007) 'Improved constraints on global-scale hydrological change by determining secular geocenter motion and low degrees of the surface mass load with GPS, SLR and GRACE', in University of Newcastle: NERC.

Lavallée, D. A., Moore, P., Clarke, P. J., Petrie, E. J., van Dam, T. and King, M. A. (2010) 'J2: An evaluation of new estimates from GPS, GRACE, and load models compared to SLR', *Geophys. Res. Lett.,* 37, (22), pp. L22403.

Lavallee, D. A., van Dam, T., Blewitt, G. and Clarke, P. J. (2006) 'Geocenter motions from GPS: A unified observation model', *Journal of Geophysical Research-Solid Earth,* 111, (B5).

Lefevre, F., Yard, F. H., Le Provost, C. and Schrama, E. J. O. (2002) 'FES99: A global tide finite element solution assimilating tide gauge and altimetric information', *Journal of Atmospheric and Oceanic Technology,* 19, (9), pp. 1345-1356.

Leick. (1995) *GPS Satellite Surveying.*2 ed: Wiley.

Lemke, P. and Ren, J. (2007) *Observations: Changes in Snow, Ice and Frozen Ground.*

Lennon, G. W. and Baker, T. F. (1973) 'Earth Tide Signal and Its Coherency', *Quarterly Journal of the Royal Astronomical Society,* 14, (2), pp. 161-182.

Lidberg, M., Johansson, J. M., Scherneck, H.-G. and Davis, J. L. (2007) 'An improved and extended GPS-derived 3D velocity field of the glacial isostatic adjustment (GIA) in Fennoscandia', *Journal of Geodesy,* 81, (3), pp. 213-230.

Lidberg, M., Johansson, J. M., Scherneck, H.-G. and Milne, G. A. (2010) 'Recent results based on continuous GPS observations of the GIA process in Fennoscandia from BIFROST', *Journal of Geodynamics,* 50, (1), pp. 8-18.

Love, A. (1909) 'The yielding of the Earth to disturbing forces'.

Luthcke, S. B., Arendt, A. A., Rowlands, D. D., McCarthy, J. J. and Larsen, C. F. (2008) 'Recent glacier mass changes in the Gulf of Alaska region from GRACE mascon solutions', *Journal of Glaciology,* 54, (188), pp. 767-777.

Luthcke, S. B., Zwally, H. J., Abdalati, W., Rowlands, D. D., Ray, R. D., Nerem, R. S., Lemoine, F. G., McCarthy, J. J. and Chinn, D. S. (2006) 'Recent Greenland ice mass loss by drainage system from satellite gravity observations', *Science,* 314, (5803), pp. 1286-1289.

Lyard, F., Lefevre, F., Letellier, T. and Francis, O. (2006) 'Modelling the global ocean tides: modern insights from FES2004', *Ocean Dynamics,* 56, (5-6), pp. 394-415.

Mao, A. L., Harrison, C. G. A. and Dixon, T. H. (1999) 'Noise in GPS coordinate time series', *Journal of Geophysical Research-Solid Earth,* 104, (B2), pp. 2797-2816.

Matsumoto, K., Takanezawa, T. and Ooe, M. (2000) 'Ocean Tide Models Developed by Assimilating TOPEX/POSEIDON Altimeter Data into Hydrodynamical Model: A Global Model and a Regional Model around Japan ', *Journal of Oceanography,* 56, (5), pp. 14.

Matsuo, K. and Heki, K. (2010) 'Time-variable ice loss in Asian high mountains from satellite gravimetry', *Earth and Planetary Science Letters,* 290, (1-2), pp. 30-36.

McCarthy, D. and Petit, G. (2004) *IERS Conventions 2003.*

Meier, M. F., Dyurgerov, M. B., Rick, U. K., O'Neel, S., Pfeffer, W. T., Anderson, R. S., Anderson, S. P. and Glazovsky, A. F. (2007) 'Glaciers dominate Eustatic sea-level rise in the 21st century', *Science,* 317, (5841), pp. 1064-1067.

Miller, F. P., Vandome, A. F. and McBrewster, J. (2009) *Structure of the Earth: Terrestrial Planet, Lithosphere, Mantle (geology), Asthenosphere, Outer Core, Inner Core, Crust (geology), Seismology.* Alphascript Publishing.

Milly, P. C. D. and Shmakin, A. B. (2002) 'Global modeling of land water and energy balances. Part I: the land dynamics (LaD) model', *Journal of Hydrometeorology,* 3, (3), pp. 283-299.

Milne, G. A. (2012) *Glacial Isostatic Adjustment and coastline modelling*. Available at: ftp://krypton.dur.ac.uk/pub/dgl0gam/sweden/GIA.ppt (Accessed: 11th June).

Milne, G. A., Shennan, I., Youngs, B. A. R., Waugh, A. I., Teferle, F. N., Bingley, R. M., Bassett, S. E., Cuthbert-Brown, C. and Bradley, S. L. (2006) 'Modelling the glacial isostatic adjustment of the UK region', *Philosophical Transactions of the Royal Society a-Mathematical Physical and Engineering Sciences,* 364, (1841), pp. 931-948.

Mitrovica, J. X. and Forte, A. M. (2004) 'A new inference of mantle viscosity based upon joint inversion of convection and glacial isostatic adjustment data', *Earth and Planetary Science Letters,* 225, (1-2), pp. 177-189.

Mitrovica, J. X., Gomez, N. and Clark, P. U. (2009) 'The Sea-Level Fingerprint of West Antarctic Collapse', *Science,* 323, (5915), pp. 753.

Mitrovica, J. X., Milne, G. A. and Davis, J. L. (2001) 'Glacial isostatic adjustment on a rotating earth', *Geophysical Journal International,* 147, (3), pp. 562-578.

Mitrovica, J. X. and Peltier, W. R. (1993) 'Present-Day Secular Variations in the Zonal Harmonics of Earths Geopotential', *Journal of Geophysical Research-Solid Earth,* 98, (B3), pp. 4509-4526.

Mitrovica, J. X., Wahr, J., Matsuyama, I. and Paulson, A. (2005) 'The rotational stability of an ice-age earth', *Geophysical Journal International,* 161, (2), pp. 491-506.

Moore, P. and Wang, J. (2003) 'Geocentre variation from laser tracking of LAGEOS1/2 and loading data', *Integrated Space Geodetic Systems and Satellite Dynamics,* 31, (8), pp. 1927-1933.

Moore, P., Zhang, Q. and Alothman, A. (2005) 'Annual and semiannual variations of the Earth's gravitational field from satellite laser ranging and CHAMP', *Journal of Geophysical Research-Solid Earth,* 110, (B6).

Morel, L. and Willis, P. (2005) 'Terrestrial reference frame effects on global sea level rise determination from TOPEX/Poseidon altimetric data', in Moore, P.(ed), *Satellite Dynamics in the Era of Interdisciplinary Space Geodesy.* Vol. 36, pp. 358-368.

Niell, A. E. (1996) 'Global mapping functions for the atmosphere delay at radio wavelengths', *Journal of Geophysical Research-Solid Earth,* 101, (B2), pp. 3227-3246.

Niell, A. E. (2001) 'Preliminary evaluation of atmospheric mapping functions based on numerical weather models', *Physics and Chemistry of the Earth Part a-Solid Earth and Geodesy,* 26, (6-8), pp. 475-480.

Nocquet, J. M., Calais, E., Altamimi, Z., Sillard, P. and Boucher, C. (2001) 'Intraplate deformation in western Europe deduced from an analysis of the International Terrestrial Reference Frame 1997 (ITRF97) velocity field', *Journal of Geophysical Research-Solid Earth,* 106, (B6), pp. 11239-11257.

Olaizola, M., van de Wal, R. S. W., Helsen, M. and de Boer, B. (2011) 'Present-Day Mass Changes for the Greenland Ice Sheet and their Interactions with Bedrock Adjustment', *The Cryosphere,* 5, (6).

Palais, B., Palais, R. and Rodi, S. (2009) 'A Disorienting Look at Euler's Theorem on the Axis of a Rotation', *American Mathematical Monthly,* 116, (10), pp. 892-909.

Paulson, A., Zhong, S. and Wahr, J. (2007) 'Limitations on the inversion for mantle viscosity from postglacial rebound', *Geophysical Journal International,* 168, (3), pp. 1195-1209.

Paulson, A., Zhong, S. J. and Wahr, J. (2005) 'Modelling post-glacial rebound with lateral viscosity variations', *Geophysical Journal International,* 163, (1), pp. 357-371.

Pearlman, M., Noll, C., Dunn, P., Horvath, J., Husson, V., Stevens, P., Torrence, M., Vo, H. and Wetzel, S. (2005) 'The International Laser Ranging Service and its support for IGGOS', *Journal of Geodynamics,* 40, (4-5), pp. 470-478.

Peltier, W. R. (1984) 'The Thickness of the Continental Lithosphere', *J. Geophys. Res.,* 89, (B13), pp. 11303-11316.

Peltier, W. R. (1994) 'Ice-Age Paleotopography', *Science,* 265, (5169), pp. 195-201.

Peltier, W. R. (1996) 'Mantle viscosity and ice-age ice sheet topography', *Science,* 273, (5280), pp. 1359-1364.

Peltier, W. R. (2004) 'Global glacial isostasy and the surface of the ice-age earth: The ice-5G (VM2) model and grace', *Annual Review of Earth and Planetary Sciences,* 32, pp. 111-149.

Penna, N. T., King, M. A. and Stewart, M. P. (2007) 'GPS height time series: Short-period origins of spurious long-period signals', *Journal of Geophysical Research-Solid Earth,* 112, (B2).

Petrie, E. J., Hernandez-Pajares, M., Spalla, P., Moore, P. and King, M. A. (2011) 'A Review of Higher Order Ionospheric Refraction Effects on Dual Frequency GPS', *Surveys in Geophysics,* 32, (3), pp. 197-253.

Plag, H. P., Engineering, M. S. E. S. and Geology, N. B. M. (2006) *B112: National Geodetic Infrastructure--Current Status and Future Requirements:The Example of Norway.* NV Bureau of Mines & Geology.

Poirier, J. P. (2000) *Introduction to the Physics of the Earth's Interior.* Cambridge University Press.

Pollitz, F. F., Brooks, B., Tong, X., Bevis, M. G., Foster, J. H., Buergmann, R., Smalley, R., Jr., Vigny, C., Socquet, A., Ruegg, J.-C., Campos, J., Barrientos, S., Parra, H., Soto, J. C. B., Cimbaro, S. and Blanco, M. (2011) 'Coseismic slip distribution of the February 27, 2010 Mw 8.8 Maule, Chile earthquake (vol 38, L09309, 2011)', *Geophysical Research Letters,* 38.

Press, W. H., Teukolsky, S. A., Vetterling, W. T. and Flannerty, B. P. (1992) *Numerical Recipes in C: The art of scientific computing.*2nd Edition ed New York:

Pritchard, H. D., Luthcke, S. B. and Fleming, A. H. (2010) 'Understanding ice-sheet mass balance: progress in satellite altimetry and gravimetry', *Journal of Glaciology,* 56, (200), pp. 1151-1161.

Ramillien, G., Famiglietti, J. S. and Wahr, J. (2008) 'Detection of Continental Hydrology and Glaciology Signals from GRACE: A Review', *Surveys in Geophysics,* 29, (4-5), pp. 361-374.

Ray, J., Altamimi, Z., Collilieux, X. and van Dam, T. (2008) 'Anomalous harmonics in the spectra of GPS position estimates', *GPS Solutions,* 12, (1), pp. 55-64.

Ray, R. D. (1999) 'A Global Ocean Tide Model From TOPEX/POSEIDON Altimetry: GOT99.2'.

Reddy, C. D., Arora, S. K., Sunil, P. S. and Prajapati, S. K. (2011) 'Earthquake Related Deformation Cycle: Perspectives from 2004 Sumatra and 2010 Chile Mega-Earthquakes', *Disaster Advances,* 4, (2), pp. 13-21.

Reprocessing, I. (2012) *Reprocessing Campaign*. Available at: http://acc.igs.org/reprocessing.html (Accessed: 01/05/2012).

Rignot, E., Velicogna, I., van den Broeke, M. R., Monaghan, A. and Lenaerts, J. (2011) 'Acceleration of the contribution of the Greenland and Antarctic ice sheets to sea level rise', *Geophysical Research Letters,* 38.

Sabadini, R. and Vermeersen, B. (2004) *Global Dynamics of the Earth: Applications of Normal Mode Relaxation Theory to Solid-Earth Geophysics.* Kluwer Academic Publishers.

Santamaria-Gomez, A., Bouin, M.-N., Collilieux, X. and Woeppelmann, G. (2011) 'Correlated errors in GPS position time series: Implications for velocity estimates', *Journal of Geophysical Research-Solid Earth,* 116.

Scargle, J. D. (1982) 'Studies in Astronomical Time-Series Analysis - 2 Statistical Aspects of Spectral-Analysis of Unevenly Spaced Data', *Astrophysical Journal,* 263, (2), pp. 835-853.

Schaer, S. (2006) 'Determination and Use of GPS Differential Code Bias Values *', IGS Workshop.* ESOC, ESA, Darmstadt, pp.

Schmid, R., Mader, G. and Herring, T. (2005) 'From relative to absolute antenna phase centre corrections*', Celebrating a Decade of the International GPS Servie, Workshop and Symposium 2004.* Astronomical Institue, University of Berne, Berne Switzerland, Meindl, M., pp. 209-211.

Schmid, R., Steigenberger, P., Gendt, G., Ge, M. and Rothacher, M. (2007) 'Generation of a consistent absolute phase-center correction model for

GPS receiver and satellite antennas', *Journal of Geodesy,* 81, pp. 781-798.

Schotman, H. H. A. and Vermeersen, L. L. A. (2005) 'Sensitivity of glacial isostatic adjustment models with shallow low-viscosity earth layers to the ice-load history in relation to the performance of GOCE and GRACE', *Earth and Planetary Science Letters,* 236, (3-4), pp. 828-844.

Schotman, H. H. A., Wu, P. and Vermeersen, L. L. A. (2008) 'Regional perturbations in a global background model of glacial isostasy', *Physics of the Earth and Planetary Interiors,* 171, (1-4), pp. 323-335.

Sella, G. F., Dixon, T. H. and Mao, A. L. (2002) 'REVEL: A model for Recent plate velocities from space geodesy', *Journal of Geophysical Research-Solid Earth,* 107, (B4).

Sella, G. F., Stein, S., Dixon, T. H., Craymer, M., James, T. S., Mazzotti, S. and Dokka, R. K. (2007) 'Observation of glacial isostatic adjustment in "stable" North America with GPS', *Geophysical Research Letters,* 34, (2).

Shmakin, A. B., Milly, P. C. D. and Dunne, K. A. (2002) 'Global Modeling of land water and energy balances. Part III: Interannual variability', *Journal of Hydrometeorology,* 3, (3), pp. 311-321.

Silverstein, A., Silverstein, V. B., Silverstein, V. and Nunn, L. S. (2009) *Plate Tectonics.* Lerner Publishing Group.

Solomon, S., Qin, D., Manning, M., Chen, Z., Marquism, M., Averyt, K. B. and Tignor, M. (2007) *Contribution of Working Group I to the Fourth Assessment Report of the IPCC.*

Spada, G., Antonioli, A., Cianetti, S. and Giunchi, C. (2006) 'Glacial isostatic adjustment and relative sea-level changes: the role of lithospheric and upper mantle heterogeneities in a 3-D spherical Earth', *Geophysical Journal International,* 165, (2), pp. 692-702.

Steffen, H., Kaufmann, G. and Wu, P. (2006) 'Three-dimensional finite-element modeling of the glacial isostatic adjustment in Fennoscandia', *Earth and Planetary Science Letters,* 250, (1–2), pp. 358-375.

Steigenberger, P., Romero, I. and Fang, P. (2006a) *IGS Workshop 2006.* ESOC, ESA, Darmstadt,

Steigenberger, P., Rothacher, M., Dietrich, R., Fritsche, M., Rulke, A. and Vey, S. (2006b) 'Reprocessing of a global GPS network', *Journal of Geophysical Research-Solid Earth,* 111, (B5), pp. 13.

Steinberger, B. and Torsvik, T. H. (2008) 'Absolute plate motions and true polar wander in the absence of hotspot tracks', *Nature,* 452, (7187), pp. 620-623.

Tamisiea, M. E. and Mitrovica, J. X. (2011) 'The Moving Boundaries of Sea Level Change Understanding the Origins of Geographic Variability', *Oceanography,* 24, (2), pp. 24-39.

Tamisiea, M. E., Mitrovica, J. X. and Davis, J. L. (2007) 'GRACE gravity data constrain ancient ice geometries and continental dynamics over Laurentia', *Science,* 316, (5826), pp. 881-883.

Tamisiea, M. E., Mitrovica, J. X., Milne, G. A. and Davis, J. L. (2001) 'Global geoid and sea level changes due to present-day ice mass fluctuations', *Journal of Geophysical Research-Solid Earth,* 106, (B12), pp. 30849-30863.

Tamisiea, M. E., Mitrovica, J. X., Tromp, J. and Milne, G. A. (2002) 'Present-day secular variations in the low-degree harmonics of the geopotential: Sensitivity analysis on spherically symmetric Earth models', *Journal of Geophysical Research-Solid Earth,* 107, (B12).

Tanaka, Y., Klemann, V., Martinec, Z. and Riva, R. E. M. (2011) 'Spectral-finite element approach to viscoelastic relaxation in a spherical compressible Earth: application to GIA modelling', *Geophysical Journal International,* 184, (1), pp. 220-234.

Tapley, B. D., Bettadpur, S., Ries, J. C., Thompson, P. F. and Watkins, M. M. (2004) 'GRACE measurements of mass variability in the Earth system', *Science,* 305, (5683), pp. 503-505.

Teferle, F. N., Bingley, R. M., Orliac, E. J., Williams, S. D. P., Woodworth, P. L., McLaughlin, D., Baker, T. F., Shennan, I., Milne, G. A., Bradley, S. L. and Hansen, D. N. (2009) 'Crustal motions in Great Britain: evidence from continuous GPS, absolute gravity and Holocene sea level data', *Geophysical Journal International,* 178, (1), pp. 23-46.

Tesmer, V., Steigenberger, P., Rothacher, M., Boehm, J. and Meisel, B. (2009) 'Annual deformation signals from homogeneously reprocessed VLBI and GPS height time series', *Journal of Geodesy,* 83, (10), pp. 973-988.

Teunissen, P. J. G. and Amiri-Simkooei, A. R. (2008) 'Least-squares variance component estimation', *Journal of Geodesy,* 82, (2), pp. 65-82.

Thomas, I. D., King, M. A., Bentley, M. J., Whitehouse, P. L., Penna, N. T., Williams, S. D. P., Riva, R. E. M., Lavallee, D. A., Clarke, P. J., King, E. C., Hindmarsh, R. C. A. and Koivula, H. (2011) 'Widespread low rates of Antarctic glacial isostatic adjustment revealed by GPS observations', *Geophysical Research Letters,* 38.

Tiwari, V. M., Wahr, J. and Swenson, S. (2009) 'Dwindling groundwater resources in northern India, from satellite gravity observations', *Geophys. Res. Lett.,* 36, (18), pp. L18401.

Tolman, H. L. (2008) 'A mosaic approach to wind wave modeling', *Ocean Modelling,* 25, (1-2), pp. 35-47.

Tregoning, P., Ramillien, G., McQueen, H. and Zwartz, D. (2009a) 'Glacial isostatic adjustment and nonstationary signals observed by GRACE', *Journal of Geophysical Research-Solid Earth,* 114.

Tregoning, P. and van Dam, T. (2005a) 'Atmospheric pressure loading corrections applied to GPS data at the observation level', *Geophysical Research Letters,* 32, (22).

Tregoning, P. and van Dam, T. (2005b) 'Effects of atmospheric pressure loading and seven-parameter transformations on estimates of geocenter motion and station heights from space geodetic observations', *Journal of Geophysical Research-Solid Earth,* 110, (B3), pp. 12.

Tregoning, P. and Watson, C. (2010) 'Atmospheric effects and spurious signals in GPS analyses', *Journal of Geophysical Research-Solid Earth,* 114.

Tregoning, P. and Watson, C. (2011) 'Correction to “Atmospheric effects and spurious signals in GPS analyses”', *J. Geophys. Res.,* 116, (B2), pp. B02412.

Tregoning, P., Watson, C., Ramillien, G., McQueen, H. and Zhang, J. (2009b) 'Detecting hydrologic deformation using GRACE and GPS', *Geophysical Research Letters,* 36.

Trupin, A. S. (1993) 'Effects of polar ice on the Earth's rotation and gravitational potential', *Geophysical Journal International,* 113, (2), pp. 273-283.

Trupin, A. S., Meier, M. F. and Wahr, J. M. (1992) 'Effect of Melting Glaciers on the Earth's Rotation and Gravitational-Field - 1965-1984', *Geophysical Journal International,* 108, (1), pp. 1-15.

Tushingham, A. M. and Peltier, W. R. (1991) 'ICE-3G: A New Global Model Of Late Pleistocene Deglaciation Based Upon Geophysical Predictions Of Post-Glacial Relative Sea Level Change', *J. Geophys. Res.,* 96, (B3), pp. 4497-4523.

Urschl, C., Gurtner, W., Hugentobler, U., Schaer, S. and Beutler, G. (2005) 'Validation of GNSS orbits using SLR observations', in Moore, P.(ed), *Satellite Dynamics in the Era of Intredisciplinary Space Geodesy.* Vol. 36, pp. 412-417.

USGS *Inside the Earth*. Available at: http://pubs.usgs.gov/publications/text/inside.html (Accessed: 11th June).

Van Camp, M., Williams, S. D. P. and Francis, O. (2005) 'Uncertainty of absolute gravity measurements', *Journal of Geophysical Research-Solid Earth,* 110, (B5).

van Dam, T., Altamimi, Z., Collilieux, X. and Ray, J. (2010) 'Topographically induced height errors in predicted atmospheric loading effects', *Journal of Geophysical Research-Solid Earth,* 115.

van Dam, T., Wahr, J. and Lavallee, D. (2007) 'A comparison of annual vertical crustal displacements from GPS and Gravity Recovery and Climate Experiment (GRACE) over Europe', *Journal of Geophysical Research-Solid Earth,* 112, (B3).

van Dam, T., Wahr, J., Milly, P. C. D., Shmakin, A. B., Blewitt, G., Lavallee, D. and Larson, K. M. (2001) 'Crustal displacements due to continental water loading', *Geophysical Research Letters,* 28, (4), pp. 651-654.

van Dam, T. M., Blewitt, G. and Heflin, M. B. (1994) 'Atmospheric-Pressure Loading Effects on Global Positioning System Coordinate Determinations', *Journal of Geophysical Research-Solid Earth,* 99, (B12), pp. 23939-23950.

van Dam, T. M. and Francis, O. (1998) 'Two years of continuous measurements of tidal and nontidal variations of gravity in Boulder, Colorado', *Geophysical Research Letters,* 25, (3), pp. 393-396.

van Dam, T. M. and Wahr, J. (1998) 'Modeling environment loading effects: a review', *Physics and Chemistry of The Earth,* 23, (9–10), pp. 1077-1087.

van Dam, T. M., Wahr, J., Chao, Y. and Leuliette, E. (1997) 'Predictions of crustal deformation and of geoid and sea-level variability caused by oceanic and atmospheric loading', *Geophysical Journal International,* 129, (3), pp. 507-517.

Van Der Pluijm, B. A. and Marshak, S. (2004) *Earth Structure: An Introduction to Structural Geology and Tectonics.* W.W. Norton.

Velicogna, I. (2009) 'Increasing rates of ice mass loss from the Greenland and Antarctic ice sheets revealed by GRACE', *Geophysical Research Letters,* 36.

Velicogna, I. and Wahr, J. (2005) 'Greenland mass balance from GRACE', *Geophysical Research Letters,* 32, (18).

Velicogna, I. and Wahr, J. (2006a) 'Acceleration of Greenland ice mass loss in spring 2004', *Nature,* 443, (7109), pp. 329-331.

Velicogna, I. and Wahr, J. (2006b) 'Measurements of time-variable gravity show mass loss in Antarctica', *Science,* 311, (5768), pp. 1754-1756.

Wahr, J., Swenson, S., Zlotnicki, V. and Velicogna, I. (2004) 'Time-variable gravity from GRACE: First results', *Geophysical Research Letters,* 31, (11), pp. 4.

Wahr, J., van Dam, T., Larson, K. and Francis, O. (2001) 'GPS measurements of vertical crustal motion in Greenland', *Journal of Geophysical Research-Atmospheres,* 106, (D24), pp. 33755-33759.

Wang, H., Wu, P. and van der Wal, W. (2008) 'Using postglacial sea level, crustal velocities and gravity-rate-of-change to constrain the influence of thermal effects on mantle lateral heterogeneities', *Journal of Geodynamics,* 46, (3–5), pp. 104-117.

Wegener, A. (1912) 'Die Entstenchung der Kontinente', *Geologische Rundschau,* 3, (4), pp. 16.

Whitehouse, P. (2009) *Glacial Isostatic Adjustment and sea-level change state of the art report.* Durham University (TR-09-11).

Whitehouse, P., Latychev, K., Milne, G. A., Mitrovica, J. X. and Kendall, R. (2006) 'Impact of 3-D Earth structure on Fennoscandian glacial isostatic adjustment: Implications for space-geodetic estimates of present-day crustal deformations', *Geophys. Res. Lett.,* 33, (13), pp. L13502.

Williams, S. D. P. (2003a) 'The effect of coloured noise on the uncertainties of rates estimated from geodetic time series', *Journal of Geodesy,* 76, (9-10), pp. 483-494.

Williams, S. D. P. (2003b) 'Offsets in Global Positioning System time series', *J. Geophys. Res.,* 108, (B6), pp. 2310.

Williams, S. D. P., Bock, Y., Fang, P., Jamason, P., Nikolaidis, R. M., Prawirodirdjo, L., Miller, M. and Johnson, D. J. (2004) 'Error analysis of continuous GPS position time series', *Journal of Geophysical Research-Solid Earth,* 109, (B3).

Williams, S. D. P. and Penna, N. T. (2011) 'Non-tidal ocean loading effects on geodetic GPS heights', *Geophysical Research Letters,* 38.

Wouters, B., Chambers, D. and Schrama, E. J. O. (2008) 'GRACE observes small-scale mass loss in Greenland', *Geophysical Research Letters,* 35, (20).

Wouters, B., Riva, R. E. M., Lavallee, D. A. and Bamber, J. L. (2011) 'Seasonal variations in sea level induced by continental water mass: First results from GRACE', *Geophysical Research Letters,* 38.

Wu, X., Heflin, M. B., Schotman, H., Vermeersen, B. L. A., Dong, D., Gross, R. S., Ivins, E. R., Moore, A. and Owen, S. E. (2010) 'Simultaneous estimation of global present-day water transport and glacial isostatic adjustment', *Nature Geoscience,* 3, (9), pp. 642-646.

Wu, X. P., Argus, D. F., Heflin, M. B., Ivins, E. R. and Webb, F. H. (2002) 'Site distribution and aliasing effects in the inversion for load coefficients and

geocenter motion from GPS data', *Geophysical Research Letters,* 29, (24).

Wu, X. P., Heflin, M. B., Ivins, E. R., Argus, D. F. and Webb, F. H. (2003) 'Large-scale global surface mass variations inferred from GPS measurements of load-induced deformation', *Geophysical Research Letters,* 30, (14).

Wubbena, G., Schmitz, M., Mader, G. and Czopech, F. (2007) 'GPS Block II/IIA satellite antenna testing using the automated absolute field calibration with robot*', ION GNSS 20th International Technical Meeting of the Satellite Division.* Fort Worth, Texas, 25-28th September 2007*.* pp.

Wunsch, C. and Stammer, D. (1997) 'Atmospheric loading and the oceanic "inverted barometer" effect', *Reviews of Geophysics,* 35, (1), pp. 79-107.

Yoder, C. F., Colombo, G., Synnott, S. P. and Yoder, K. A. (1983) 'Theory of Motion of Saturns Co-Orbiting Satellites', *Icarus,* 53, (3), pp. 431-443.

Zerbini, S., Richter, B., Rocca, F., van Dam, T. and Matonti, F. (2007) 'A combination of space and terrestrial geodetic techniques to monitor land subsidence: Case study, the southeastern Po Plain, Italy', *Journal of Geophysical Research-Solid Earth,* 112, (B5).

Zhang, J., Bock, Y., Johnson, H., Fang, P., Williams, S., Genrich, J., Wdowinski, S. and Behr, J. (1997) 'Southern California Permanent GPS Geodetic Array: Error analysis of daily position estimates and site velocities', *Journal of Geophysical Research-Solid Earth,* 102, (B8), pp. 18035-18055.

Zhong, S., Paulson, A. and Wahr, J. (2003) 'Three-dimensional finite-element modelling of Earth's viscoelastic deformation: effects of lateral variations in lithospheric thickness', *Geophysical Journal International,* 155, (2), pp. 679-695.